frontiers | Research Topics

Smart stimuli-responsive biomaterials for programmed drug delivery, 2nd edition

Edited by
Seyed Morteza Naghib, Ali Maleki, Yasser Zare and Kyong Rhee

Published in
Frontiers in Bioengineering and Biotechnology
Frontiers in Molecular Biosciences

ISSN 1664-8714
ISBN 978-2-8325-5398-5
DOI 10.3389/978-2-8325-5398-5

About Frontiers

Frontiers is more than just an open access publisher of scholarly articles: it is a pioneering approach to the world of academia, radically improving the way scholarly research is managed. The grand vision of Frontiers is a world where all people have an equal opportunity to seek, share and generate knowledge. Frontiers provides immediate and permanent online open access to all its publications, but this alone is not enough to realize our grand goals.

Frontiers journal series

The Frontiers journal series is a multi-tier and interdisciplinary set of open-access, online journals, promising a paradigm shift from the current review, selection and dissemination processes in academic publishing. All Frontiers journals are driven by researchers for researchers; therefore, they constitute a service to the scholarly community. At the same time, the *Frontiers journal series* operates on a revolutionary invention, the tiered publishing system, initially addressing specific communities of scholars, and gradually climbing up to broader public understanding, thus serving the interests of the lay society, too.

Dedication to quality

Each Frontiers article is a landmark of the highest quality, thanks to genuinely collaborative interactions between authors and review editors, who include some of the world's best academicians. Research must be certified by peers before entering a stream of knowledge that may eventually reach the public - and shape society; therefore, Frontiers only applies the most rigorous and unbiased reviews. Frontiers revolutionizes research publishing by freely delivering the most outstanding research, evaluated with no bias from both the academic and social point of view. By applying the most advanced information technologies, Frontiers is catapulting scholarly publishing into a new generation.

What are Frontiers Research Topics?

Frontiers Research Topics are very popular trademarks of the *Frontiers journals series*: they are collections of at least ten articles, all centered on a particular subject. With their unique mix of varied contributions from Original Research to Review Articles, Frontiers Research Topics unify the most influential researchers, the latest key findings and historical advances in a hot research area.

Find out more on how to host your own Frontiers Research Topic or contribute to one as an author by contacting the Frontiers editorial office: frontiersin.org/about/contact

Smart stimuli-responsive biomaterials for programmed drug delivery, 2nd edition

Topic editors

Seyed Morteza Naghib — Iran University of Science and Technology, Iran
Ali Maleki — Iran University of Science and Technology, Iran
Yasser Zare — Breast Cancer Research Center, Motamed Cancer Institute, Iran
Kyong Rhee — Kyung Hee University, Republic of Korea

Citation

Naghib, S. M., Maleki, A., Zare, Y., Rhee, K., eds. (2024). *Smart stimuli-responsive biomaterials for programmed drug delivery, 2nd edition*. Lausanne: Frontiers Media SA. doi: 10.3389/978-2-8325-5398-5

Publisher's note: This is a 2nd edition due to an article retraction.

Table of contents

frontiers | Frontiers in Bioengineering and Biotechnology

TYPE Editorial
PUBLISHED 22 May 2023
DOI 10.3389/fbioe.2023.1222034

OPEN ACCESS

EDITED AND REVIEWED BY
Gianni Ciofani,
Italian Institute of Technology (IIT), Italy

*CORRESPONDENCE
Seyed Morteza Naghib,
Naghib@iust.ac.ir

RECEIVED 13 May 2023
ACCEPTED 16 May 2023
PUBLISHED 22 May 2023

CITATION
Naghib SM, Garshasbi HR, Maleki A, Zare Y and Rhee K (2023), Editorial: Smart Stimuli-responsive Biomaterials for Programmed Drug Delivery.
Front. Bioeng. Biotechnol. 11:1222034.
doi: 10.3389/fbioe.2023.1222034

Editorial: Smart Stimuli-responsive Biomaterials for Programmed Drug Delivery

Seyed Morteza Naghib[1]*, Hamid Reza Garshasbi[1], Ali Maleki[2], Yasser Zare[3] and Kyong Rhee[4]

[1]Nanotechnology Department, School of Advanced Technologies, Iran University of Science and Technology, Tehran, Iran, [2]Catalysts and Organic Synthesis Research Laboratory, Department of Chemistry, Iran University of Science and Technology, Tehran, Iran, [3]Biomaterials and Tissue Engineering Research Group, Department of Interdisciplinary Technologies, Breast Cancer Research Center, Motamed Cancer Institute, ACECR, Tehran, Iran, [4]Department of Mechanical Engineering (BK21 Four), College of Engineering, Kyung Hee University, Yongin, Republic of Korea

KEYWORDS

smart, stimuli-responsive polymer, biomaterials, drug delivery, programmed release system

Editorial on the Research Topic
Smart Stimuli-responsive Biomaterials for Programmed Drug Delivery

The nature of traditional chemotherapy payloads frequently results in substantial adverse effects on healthy tissues since they are not tumor-specific. To change the therapeutic qualities of medications and make them safer and more efficient, several drug delivery systems (DDSs) were created. For maximum effectiveness, high levels of patient compliance, and minimal adverse effects, local medication administration is a crucial strategy that lowers systemic drug exposure.

Smart drug delivery systems (SDDSs) have drawn much interest and opened the door for more successful patient care. The technique that prevents the payloads from being released before they reach the target spot distinguishes SDDSs with stimuli-responsive properties. The precise location of the cargo release is established by the triggered release, which results from changes in the nano/microcarrier chemistry and structure in response to endogenous and/or external stimuli.

The high surface-to-volume ratio, low density, and high hydrophilicity of halloysite nanotubes (HNTs)-polymer composites and the ease with which they may be disseminated in hydrophilic biopolymers have drawn considerable interest. Additionally, it has been proven that they can control the release of medications and carry enough of them. According to research, a gelatin-based scaffold containing a halloysite nanotube (HNT) can serve as a drug carrier. At the same time, zoledronic acid (ZA) sustains release. According to earlier research, administering ZA intravenously has serious drawbacks. However, the goal of the current study is to lessen the negative consequences of local delivery by focusing on the benefits of its osteogenesis. The proliferation of the human adipose stem cells (hASCs) was efficiently increased by the ZA, as demonstrated by the seeding of hASCs on the ready scaffolds. Abdulahy et al. findings suggest that the HNTs-loaded Gelatin scaffold may be able to regulate ZA release and localize its distribution to the defect location while simultaneously enhancing the mechanical and osteogenic potential of gelatin-based scaffolds (Abdulahy et al.).

There are no new, effective treatments for acute lung injury (ALI), which has a significant death rate. The expression of zinc finger E-box binding homeobox 1 and 2 (ZEB1/2), which is positively connected with the development of pulmonary fibrosis, is high in the early stages of ALI. Weng et al. created a nanoscale porphyrin metal-organic (ZPM) framework based on Zr (IV) to deliver tiny interfering ZEB1/2 (siZEB1/2) to treat early lung fibrosis during ALI. Additionally, the ZEB1/2 silencing resulted in higher E-cadherin and lower -SMA levels. An effective non-viral vector technology to distribute siRNAs to treat early lung fibrosis during ALI was the nano-ZPM system (Weng et al.).

An efficient method for targeted cancer therapy with little to no harm is to create nanotechnology-based gene delivery to bladder tumor locations. The c(RGDfK)-MSN NPs, which are mesoporous silica nanoparticles modified with c(RGDfK)-PLGA-PEG, were developed to simultaneously deliver siPD-L1 and miR-34a to bladder cancer cells and tissues. However, in the T24 cells and T24 mouse model, c(RGDfK)-MSN NPs may concurrently downregulate PD-L1 expression, upregulate miR-34a and increase anti-tumor activities *in vivo* and *in vitro*. Shahidi et al. findings provide fresh recommendations for enhancing focused therapy approaches with clear molecular goals for treating bladder cancer (Shahidi et al.).

Increased water solubility and bioavailability of curcumin are produced by its encapsulation in a nanoniosomal delivery system, which also boosts radiosensitivity. With irradiation, the curcumin-containing nanoniosome (Cur-Nio) can increase radiosensitivity. To evaluate cytotoxicity and apoptosis, breast cancer cells were treated with various radiation dosages and different concentrations of free curcumin and Cur-Nio. Additionally, compared to cells treated with pure curcumin, the rate of cytotoxicity and apoptosis in the combination of irradiation and curcumin-containing nanoniosomes was much greater. Afereydoon et al. results suggest that Cur-Nio pre-treatment as a radiosensitizer promotes irradiation-induced breast cancer cell death and is an efficient method to improve the efficacy of breast cancer therapy (Afereydoon et al.).

Using polycaprolactone (PCL) and chitosan (CS), Mosallanezhad et al. created wound dressings. Curcumin (Cur) and zinc oxide nanoparticles (ZnO) were embedded as antibacterial agents in PCL/CS electrospun nanofibers, and various features, including shape, physicomechanical, interaction with water, antibacterial effectiveness, and *in vitro* tests, were examined. The maximum water vapor transformation rate was achieved thanks to ZnO nanoparticles' facilitation of nanofibers' contact with water. Effective bacterial growth inhibition was achieved by incorporating CS, ZnO, and Cur together. *In vitro*, tests have revealed that a high Cur concentration reduces cell survival and attachment. The results from the constructed nanofibrous scaffolds showed they have the right qualities to use as a wound bandage (Mosallanezhad et al.).

This study compared the effects of Tween-80, Tween-60, cholesterol, and dioleoyl-3-trimethylammonium propane (DOTAP) on nanoscaled niosomal structures. Compared to free-dispersed Cur, the results showed that Curniosome had better cytotoxic action against cancer cells. Curniosome often demonstrates a sizable buildup of excellent anticancer characteristics. Similarly, miR-34a-niosome was more harmful to tumor cells than in its free form. The anticancer effects of gene/drug delivery were studied in the 4T1 xenografted Balb/C mouse tumor model. Considering this, it was determined that encapsulating genes in the nanoniosomal delivery system is a potential approach for curing cancer cells (Abtahi et al.).

Injectable, thermoresponsive hydrogels based on chitosan and silk fibroin have been created using the improved crosslinker system and new gelling agent combinations of glycerophosphate and sodium hydrogen carbonate as a delivery system for hepatocytes in cell therapy. Hydrogel scaffolds with the ideal gelling duration and pH were created by adjusting the polymer-to-gelling agent ratio and using a chemical crosslinker. Chitosan is neutralized by adding sodium hydrogen carbonate while retaining its thermoresponsive properties and having its glycerophosphate content drop from 60% to 30%. Hydrogel's mechanical qualities are improved by genipin without shortening the gel time. Materials containing genipin have a low swelling ratio, about six, compared to those without genipin, which have a swelling ratio of eight, because of their stable microstructure and reduced amine availability. Silk fibroin works well as a degradation inhibitor in formulations, including silk, since it degrades more slowly than chitosan. The optimized samples all revealed a lack of hemolytic properties. Compared to HepG2 grown alone, urea levels are greater in the encapsulation state. According to all the studies, the optimized system may be a good option for liver regeneration (Gholami et al.).

Given its distinct structural characteristics and promising biocompatibility, the Cu-BTC framework has lately attracted much interest as a potential drug carrier for cancer treatment. However, its inherent incapability for medical imaging may restrict its bioapplications; Using Fe_3O_4 nanoparticles as an imaging agent and porous isoreticular MOF $[Cu_3(BTC)^2$ as a drug carrier], a magnetic nano/microscale MOF that addresses this Research Topic has been effectively created by Gharehdaghi et al. With a good pH-responsive drug release, the produced magnetic MOFs have a high loading capacity (40.5%) toward the model anticancer DOX. Clinical applications are anticipated for the synthesized magnetic nano/micro composite. It may also be used as a platform for pH/GSH/photo-responsive nanocarrier and photoactive antibacterial treatment (Gharehdaghi et al.).

Author contributions

SN and HG wrote the editorial text. All authors contributed to the article and approved the submitted version.

Conflict of interest

The authors declare that the research was conducted in the absence of any commercial or financial relationships that could be construed as a potential conflict of interest.

Publisher's note

frontiers | Frontiers in Bioengineering and Biotechnology

ORIGINAL RESEARCH
published: 25 April 2022
doi: 10.3389/fbioe.2022.890583

Osteogenesis Improvement of Gelatin-Based Nanocomposite Scaffold by Loading Zoledronic Acid

Sayed Behnam Abdulahy[1,2], *Mona Esmaeili Bidhendi*[2], *Mohammad Reza Vaezi*[3] and *Mehrdad Moosazadeh Moghaddam*[4]*

[1]Biomaterial and Tissue Engineering Department, Breast Cancer Research Center, Motamed Cancer Institute, ACECR, Tehran, Iran, [2]Faculty of New Science and Technology, University of Tehran (UT), Tehran, Iran, [3]Department of Nanotechnology and Advanced Material, Materials and Energy Research Center (MERC), Karaj, Iran, [4]Applied Biotechnology Research Center, Baqiyatallah University of Medical Sciences, Tehran, Iran

OPEN ACCESS

Edited by:
Kyong Rhee,
Kyung Hee University, South Korea

Reviewed by:
Amir Rostami,
Persian Gulf University, Iran
Jafar Khademzadeh Yeganeh,
Qom University of Technology, Iran

***Correspondence:**
Mehrdad Moosazadeh Moghaddam
mm.genetics@gmail.com
rsr.moosazadeh@bmsu.ac.ir

Specialty section:
This article was submitted to Nanobiotechnology, a section of the journal Frontiers in Bioengineering and Biotechnology

Received: 06 March 2022
Accepted: 08 April 2022
Published: 25 April 2022

Citation:
Abdulahy SB, Esmaeili Bidhendi M, Vaezi MR and Moosazadeh Moghaddam M (2022) Osteogenesis Improvement of Gelatin-Based Nanocomposite Scaffold by Loading Zoledronic Acid. Front. Bioeng. Biotechnol. 10:890583. doi: 10.3389/fbioe.2022.890583

Bisphosphonates (BPs) such as Zoledronic acid (ZA) are a subset of synthetic small molecules, which are now marketed as the main drugs to stimulate the growth and differentiation of osteoblast cells, thereby increasing bone formation as well as preventing bone loss. Also, Halloysite Nanotubes (HNTs)-polymer composites have attracted a lot of attention due to their high surface-to-volume ratio, low density, and high hydrophilicity, and are easily dispersed in hydrophilic biopolymers. In addition, their ability to carry enough amounts of drugs and the ability to control release has been demonstrated. Based on studies, the Gelatin-based scaffold with Halloysite nanotube (HNT) has the capacity as a drug carrier and Zoledronic acid (ZA) sustains release. Previous studies show that using ZA intravenously has some severe side effects and limitations. But by attention to the advantages of its osteogenesis, the current study has been done in order to reduce the side effects of local delivery of it. The 3-dimensional scaffolds were prepared by the Freeze-drying method. Characterization methods such as FE-SEM, FTIR, XRD, and release behavior of the scaffold has been performed to evaluate the features of the scaffolds. In fact, as-prepared Gel-HNT/ZA release 49% ZA in Phosphate Buffered Saline (PBS) within 21 days. The mechanical properties have been increased after adding HNTs and ZA from 10.27 to 26.18 MPa. Also, the water absorption has been increased after adding HNTs and ZA from 1.67 to 5.02 (g/g). Seeded human Adipose stem cells (hASCs) on the prepared scaffolds showed that the ZA effectively elevated the proliferation of the hASCs and also the MTT results proved the non-toxicity of all prepared scaffolds by high cell viability (˃80%). The osteogenic differentiation has been accelerated as displayed by ALP and Ca assay. The results propose that the HNTs-loaded Gelatin scaffold could control the releasing of ZA and its localized delivery at the defect site, simultaneously promoting the mechanical and osteogenesis ability of gelatin-based scaffolds.

Keywords: zoledronic acid, halloysite, gelatin, nanocomposite, osteogenesis, scaffolds

1 INTRODUCTION

An important and big class of orthopedic problems is bone defects (Wiese and Pape, 2010; Guerado and Caso, 2017; Gage et al., 2018; Kim et al., 2020). Over the last few decades, many efforts have been made by researchers to find suitable bone replacements. Early efforts focused on the use of metal substitutes. However, corrosion of these implants in the patient's body, in addition to their mechanical properties and gradual loosening, led to the release of highly toxic metal ions and subsequent inflammatory reactions of these products with the surrounding tissue (Parks and Lakes, 1992). Another problem with metals is their very high modulus (Liu and Dixit, 1997). The elastic modulus of metals is higher than 100 GPa, which will be much higher than the density of dense bone (6–20 GPa). The result of this high stiffness is the occurrence of the phenomenon of stress protection on the growing bone, which will lead to thinning of the new bone tissue and will increase the probability of its re-failure (Flahiff et al., 1996). Problems such as this have drawn the attention of many researchers to newer materials; Materials that do not have the problems of previous implants and at the same time allow the formation of bone tissue in the defect position with higher speed and quality. Thus, a new chapter called "Bone Tissue Engineering" was opened and new biomaterials for this purpose were introduced to the medical community (Park and Bronzino, 2000; Burg et al., 2000; Lee et al., 2001). It has been reported that the production of novel scaffolds as the carrier for osteogenesis drugs could be an advantageous approach to eschew systemic problems of the drug while improving its therapeutic efficiency (Cartmell, 2009; Xu et al., 2020).

Small molecules are natural or synthetic molecules that have low molecular weight and have the ability to regulate cellular, tissue, and therapeutic functions. These molecules are organic in nature and have less than 1,000 Da in size (Carbone et al., 2014). Bisphosphonates (BPs) are a subset of small molecules, small synthetic compounds, and now marketed as the main drugs to stimulate the growth and differentiation of osteoblast cells, thereby increasing bone formation as well as preventing bone loss.

BPs have been shown to reduce the risk of vertebral and non-vertebral fractures (Lambrinoudaki et al., 2006). They are pyrophosphate analogues that have been modified to act as a specific stimulant of osteogenesis and anti-bone resorption, the mechanism of which is to have a strong inhibitory effect on osteoclasts and increase bone induction. BPs have a strong affinity for bone surfaces and accumulate there, and due to this selective action, they have systemic side effects. BPs are also potent bone resorption inhibitors that inhibit osteoclast differentiation (Coxon et al., 2000) and stimulate the programmatic death of osteoclast cells (Benford et al., 2001). The results show a high tendency of BPs to bone mineralization and especially the return of lost bone volume (Nancollas et al., 2006). Using of bisphosphonates is considered, as one of the applicable methods that can be increased the integration of scaffolds with the surrounding bone tissue by increasing bone growth, for example, Zoledronic acid (ZA), which is a member of this group. (Yang et al., 2020).

In recent decades, Halloysite Nanotubes (HNTs)-polymer composites have attracted a lot of attention due to their high surface-to-volume ratio, low density and high hydrophilicity, and are easily dispersed in hydrophilic biopolymers (Ji et al., 2017; Zare and Rhee, 2021c; Zare and Rhee, 2021b). In addition, HNTs have shown excellent mechanical properties and good biocompatibility (Abdollahi Boraei et al., 2020a; Abdollahi Boraei et al., 2021a; Zare and Rhee, 2022). HNT-containing polymer nanocomposite scaffolds have been shown to be capable of carrying sufficient amounts of drugs as well as their controlled release (Zare et al., 2021). Also, the opposite charge on the outer and inner surface of HNTs makes them attractive for electrostatic bonding with polymers and drugs (Lee Y. J. et al., 2019; Zare and Rhee, 2021a).

In the present study, a gelatin based-nanocomposite with HNTs containing of Zoledronic acid was used for bone regeneration, with the aim of targeting ZA release in a controlled manner. This new drug delivery system is designed as a novel nanocomposite system for use in bone tissue engineering. Also, HNT was also used as a carrier of ZA drug, which strengthened the specificity of the system. Moreover, improving the physical, mechanical and bone properties of gelatin scaffolds has been expected by using this composition. The application of BTE is evaluated by making a specific scaffold in combination with gelatin. Gelatin was selected as a matrix of scaffold due to its non-toxicity, low cost, availability, ease of processing, high cell adhesion and proliferation (Ji et al., 2017). Finally, the effects of both HNT and ZA loading on the biological properties of gelatin-based scaffolds were evaluated *in vitro* and *in vivo*.

2 MATERIALS AND METHODS

2.1 Loading of ZA on/into HNTs

At the first, HNTs (4 mg/ml; Sigma Co.) were added to ZA supersaturated solution (4 mg/ml; Sigma Co.) mixed in deionized water under vacuum situation. After 20 min, the suspension was removed, stirred vigorously overnight and then centrifuged for 20 min with 6,000 rpm. The obtained precipitates were washed thoroughly and then freeze dried.

2.2 Preparation and Characterization of Scaffolds

2.2.1 Preparation

Gelatin (2.4 g; sigma, Type A) was poured in 40 ml of deionized water to be dissolved at room temperature and HNTs (4 wt. % relative to gelatin) and ZA-loaded HNTs were added to the solution of gelatin. After stirring thoroughly, the prepared suspensions were dispensed in 24 well tissue culture plates, kept in the refrigerator at 4°C for 24 h and finally frozen at −80°C overnight before doing freeze-drying process (OPERON Company, Korea). Moreover, pure gelatin scaffold without HNTs was chosen as the control group. The prepared scaffolds were coded as 1) Gel (without HNTs), 2) Gel/HNTs (without ZA), and 3) Gel/HNT-ZA (with ZA). Then, the cross linking of scaffolds

was done in a sealed desiccator in the presence of glutaraldehyde (8 ml) at 37°C for 4 h. Afterward, the prepared scaffolds were washed with 1% (W/V) of *Glycine* solution to remove the unreacted glutaraldehyde.

2.2.2 Field Emission Scanning Electron Microscopy

The ross-section views of the composite scaffolds were investigated by FE-SEM (S-4700 model, HITACHI Company, Japan). The dispersion of the ZA into the nanocomposite samples was evaluated by energy dispersive spectroscopy (EDS). The ImageJ software was hired to examined pore size and the porosity percentage of each scaffold from the three SEM images by the following equation (Shahriarpanah et al., 2016):

$$Porosity\,(\%) = \frac{A_p}{A_T} \times 100$$

In this equation, A_p is total area of pores in each cross-section and A_T is total area of each cross-section from the SEM images.

2.2.3 Water Uptake

In order to examine the equilibrium water adsorption, the finalized scaffolds with the initial weight (W_o) were place into the deionized water for 24 h at 37°C. Then, the samples were pulled out and the excess water was wiped off by using a filter paper and weighed (Ws). The equilibrium water adsorption was gained by the following equation (Abdollahi Boraei et al., 2021a; Zadegan et al., 2019):

$$\text{Equilibrium water absorption}\,(g/g) = \frac{Ws - W0}{W0}$$

2.2.4 Fourier-Transform Infrared

FTIR spectroscopy (Spectrum 100, PerkinElmer Company, United Kingdom) was hired to investigate the changes in the structure of gelatin after HNTs and ZA-loaded HNTs addition. X-ray diffraction analysis (XRD; D8 ADVANCE diffractometer, BRUKER Company, United Kingdom) was done by using Cu-Kα radiation at 40 kV and speed of 2°/min to evaluate the crystallographic changes of (GEL) scaffolds after HNTs and ZA-loaded HNTs addition.

2.2.5 Mechanical Properties

The compressive behavior of the prepared scaffolds (GEL, GEL-HNT and GEL-HNT/ZA) were measured by the ZWICK/ROEL Z005 testing machine (ZWICK, Germany) with the cross-head speed of 1 mm/min.

2.3 Release Behavior of ZA

Drug release behavior of the scaffolds were measured by immersing and incubating the scaffolds in PBS at 37°C in a shaker incubator (90 rpm). The scaffold-released ZA level was examined by UV-Visible spectroscopy (NANODROP 2000c; Thermo Scientific Company, United States) at the wavelength of 210 nm at many times point (24, 48, 72 h and 7, 14 and 21 days).

2.4 Cellular Assays

2.4.1 Cell Culture Procedure

The hASCs (Shariati Hospital, Tehran, Iran) were cultured in Dulbecco's modified Eagle's medium (DMEM/F-12; Gibco, United States) with 12% fetal bovine serum and 1% Pen-strep (Gibco, United States), followed by incubation at humidified condition with 5% CO_2 at 37°C. Moreover, the osteogenic agents (10,000 μM Beta-Glycerophosphate, 50 μg/ml L-Ascorbic acid and 10^{-4} μM Dexamethasone) were added to the medium. The prepared medium must be changing every 3 days. All cellular assays were performed by the second-passage of cells. Before seeding the cells on the scaffolds, all scaffolds were sterilized by UV irradiation for 20 min on each side of them.

2.4.2 Cytotoxicity of Prepared Scaffolds

Cytotoxicity of the scaffolds were measured by the 3-(4,5-Dimethylthiazol-2-yl)-2,5- Diphenyl Tetrazolium Bromide assay kit (MTT, Bioidea, Iran). The hASCs were seeded on sterilized scaffolds (20,000 cells/cm^2). Then they were cultured in DMEM (15% FBS) at 5% CO_2 and 37°C in the incubator for 1, 4 and 7 days. After that, 30 μl MTT was poured into each well, and incubation proceeded for 3 h. Then 200 μl DMSO (Bioidea, Iran) was added to cells and keep them for 30 min in a dark place. Finally, the absorption amounts were examined by using an ELISA plate reader (Stat Fax-2100, United States) at a wavelength of 545 nm.

2.4.3 Osteogenesis Assays

Alkaline phosphatase (ALP) activity assay was performed by using 200 μl of RIPA buffer. The total protein was extracted from hASCs cultured on Tissue Culture polystyrene (TCPS) and different scaffolds after 7 and 14 days during the period of study. In order to sedimentation of cell debris, the lysate was centrifuged at 1,200 rpm at 4°C for 5 min. Then, the supernatant was collected and ALP activity was examined with an ALP assay kit (Parsazmun, Tehran, Iran).

2.4.4 Calcium Assay

Calcium deposition on the scaffolds was examined by using Alizarin red staining (ARS) method. The hASCs cells were seeded on the scaffolds which were placed in the 24 well tissue culture plate. After 7 and 14 days of incubation, the fixation of cell-sample constructs was performed by the following instruction: 1) rinsing samples with PBS, 2) dehydration of samples through graded concentrations of ethanol 50, 70, 80 (for 15 min), 96, and 100% (for 8–10 min), respectively, 3) the Alizarin red-40 mM was poured on the samples and keep for 20–30 min. The deposited calcium, which is red/purple colour, was then observed using an inverted optical microscope (Nikon Eclipse TE2000-U, Japan).

2.5 Statistical Analysis

All tested were performed in triplicates and the data were presented as the mean ± standard deviation (SD). One-way ANOVA was used to evaluate the differences between the samples. Statistically significant levels were considered to be $p < 0.05$.

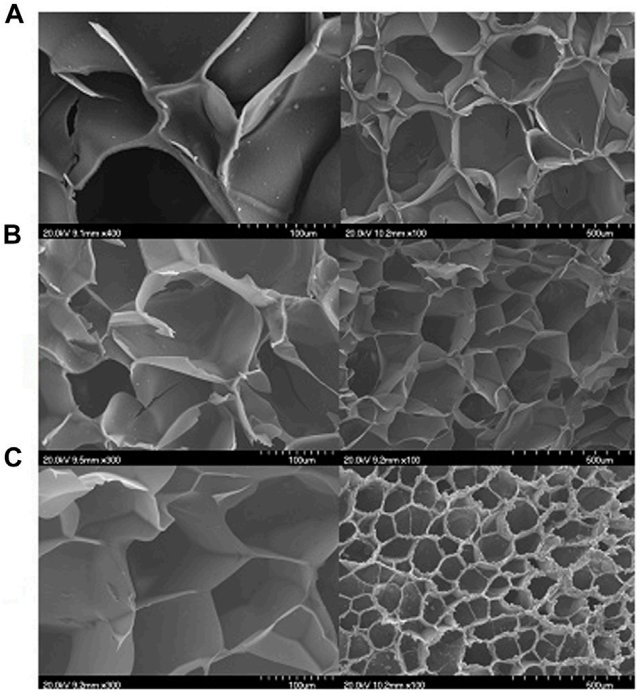

FIGURE 1 | The morphology of the **(A)** Gel, **(B)** Gel-HNT and **(C)** Gel-HNT/ZA scaffolds.

TABLE 1 | Pore size of the scaffolds.

Sample	Gel	Gel-HNT	Gel-HNT/ZA
Pore size (μm)	80.94 ± 43.80	175.57 ± 21.09	257.89 ± 16.11

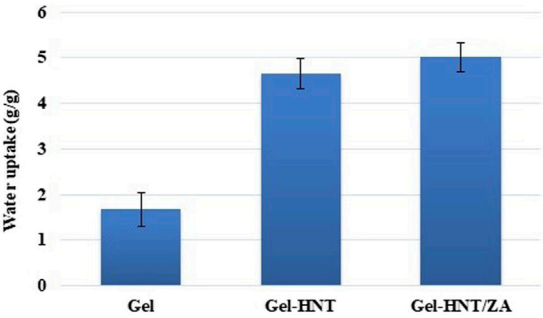

FIGURE 2 | Equilibrium water uptake values of the scaffolds.

3 RESULTS AND DISCUSSION

3.1 Characterization of the Nanocomposite Scaffolds

The morphology and pore size of the prepared scaffolds are shown in **Figure 1**. As expected, an interconnected network structure was observed in the scaffolds that is in line with the our previous study in which a gelatin-based scaffold containing HNTs and the hydrophilic drug strontium ranelate was synthesized, and the results showed a uniform structure with well-sized and interconnected cavities (Abdollahi Boraei et al., 2020b). Since the pore size distribution doesn't significantly change with the addition of ZA, the prepared scaffolds show almost similar surface morphologies which consisted of homogenous porosities.

The pore size results showed that the Gel scaffold has the minimum pore size with the mean value of 80.94 ± 43.80 μm, while the pore size elevated to 175.57 ± 21.09 μm in Gel-HNT and 257.89 ± 16.11 μm in Gel-HNT/ZA scaffolds. As expected, the augmentation of HNTs and HNT/ZA leads to create bigger pores, which is in a desire range for BTE applications. In the studies, different numbers have been reported for the appropriateness of the pore size of scaffolds in tissue engineering, for example, in the article of Li et al., The number of 300–400 microns has been selected as the appropriate range (Li et al., 2016; Rashedi et al., 2021). Lee et al. Also considered the number 500 microns to be suitable for adhesion, differentiation, and proliferation of cells inside the scaffold (Lee D. J. et al., 2019). In our studies reported that the scaffolds with larger pore size (>100 μm) provide better matrices for bone regeneration (Abdollahi Boraei et al., 2021b). In general, this number (porosity) should be suitable for delivering nutrients into the scaffold and removing waste from the scaffold (Tolba et al., 2010; Ghazalian et al., 2022).

Table 1 displays the porosity percentage of the prepared scaffolds. A similar upward trend is observed for porosity. Increasing pore size and porosity probably can effects on the electrostatic repulsion forces between carboxyl and hydroxyl groups in gelatin (Type A; pI = 7–9) and HNTs, since both HNTs and gelatin are negatively charged at pH 7 (Abdollahi Boraei et al., 2021a).

The equilibrium water uptake results of the scaffolds are brought in **Figure 2**. The water uptake for the Gel-HNT/ZA scaffold was the highest (5.02 ± 0.316 (g/g)), while this value for the Gel and Gel-HNT scaffolds decreased to 4.66 ± 0.33 and 1.67 ± 0.369 (g/g), respectively. This increase can be related to the larger pore nature in the Gel-HNT/ZA scaffold and proved by such studies that the microstructure can affect the swelling ratio (Mirahmadi et al., 2013). The more swelling ratio resulted in more water adsorption that is suitable for dipper diffusion of nutrition and better removing of waste from the matrix (Mirahmadi et al., 2013).

FTIR analysis examines the chemical interaction of scaffold components that can determine the three-dimensional structure, the drug release properties, and the biological properties of the scaffold. **Figure 3** shows the FTIR graphs of the scaffolds. As expected, in the gelatinous scaffold graph, characteristic gelatin peaks, including amide I, II, III, amide B, and amide A peaks, were observed at 1,698, 1,543, 1,236, 3,067, and 3,421 cm^{-1}, respectively. In the previous study, where the gelatin-based scaffold was made by the freeze-drying method, the peaks mentioned above were observed in the scaffold structure and examined (Abdollahi Boraei et al., 2020a). After the HNTs are added to the scaffold, most of its peaks are overlapped with

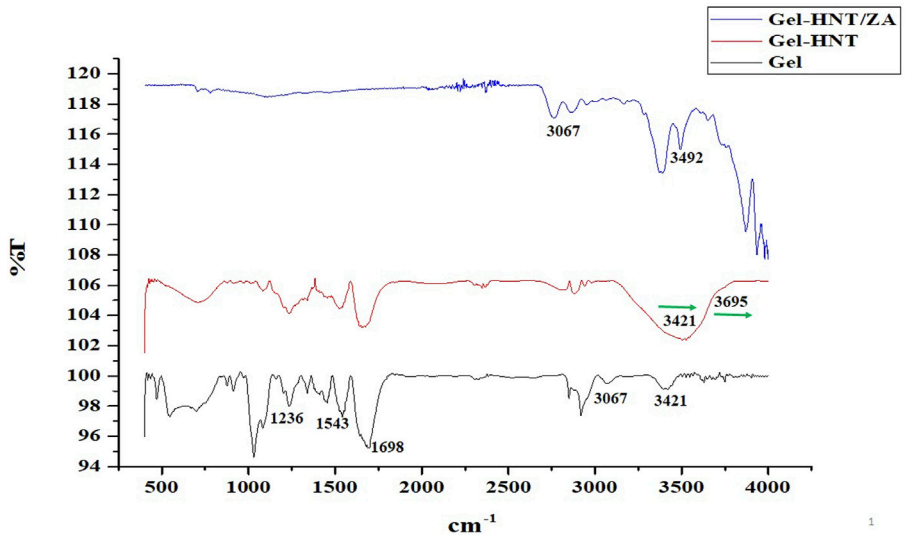

FIGURE 3 | The FTIR spectra of the Gel, Gel-HNT and Gel-HNT/ZA Scaffolds.

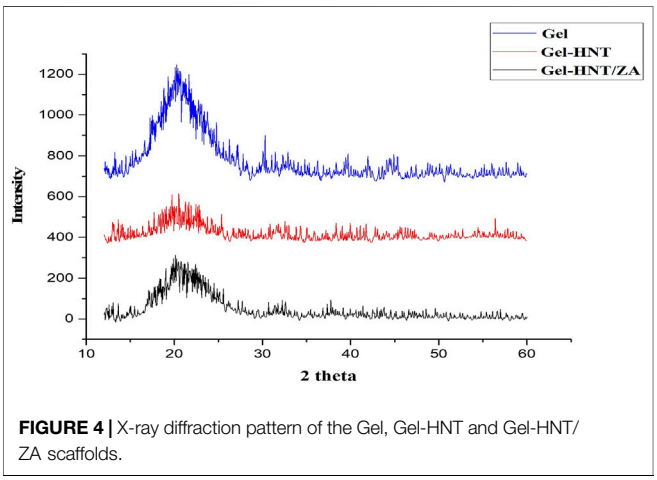

FIGURE 4 | X-ray diffraction pattern of the Gel, Gel-HNT and Gel-HNT/ZA scaffolds.

gelatin, a phenomenon that has been observed in the previous study (Abdollahi Boraei et al., 2021b). Only peaks of gelatin amide A (3,421 cm^{-1}) and O-H stretching of HNTs (3,695 cm^{-1}) shifted slightly, indicating successful incorporation of HNTs into the gelatin structure and even reinforcing the possibility of hydrogen bonding interactions between them. With the addition of ZA to the structure and synthesis of Gel-HNT/ZA nanocomposite scaffolds, new peaks appeared, these peaks include the following: P-O bond (1,300 and 1,322 cm^{-1}), free hydroxyl group (3,492 cm^{-1}), hydroxyl group (2,500–3,300 cm^{-1}) (Paris et al., 2015; Chen et al., 2020) that is the reason for the successful addition of ZA to the structure.

Figure 4 shows the diffraction pattern of a gelatinous scaffold with a wide peak at 20.25°, which is related to the crystalline structure of the gelatin triple helical, which has been reported in several studies (Jalaja et al., 2015). In general, the HNT pattern has many sharp peaks (Liao et al., 2016). A peak at 20.3° is observed which is one of the characteristic peaks of HNT that related to (020/110) plane (Liao et al., 2016). The location of this peak has not changed due to the scaffolding production process, which indicates that the HNT layers do not change and that the HNT and gelatin do not intercalate (White et al., 2012). As a result of the addition of ZA to the Gel-HNT scaffold, a small increase in the intensity of the Gel-HNT scaffold peaks occurred, which could be due to the penetration of ZA into the silicate layers of the HNTs. However, due to the absence of ZA characteristic peaks in the graph, it can be concluded that ZA is not completely crystalline in structure. This may be due to the very low concentration of ZA (˃10^{-4} mol/L) in the structure that is in line with the results of a previous study in which ZA was loaded into a composite structure and coated on a magnesium implant containing strontium (Li et al., 2019).

TABLE 2 | Compressive strength of the scaffolds.

Sample	Gel	Gel-HNT	Gel-HNT/ZA
Compressive strength (MPa)	10.27 ± 1.58	20.92 ± 2.16	26.18 ± 2.9

Table 2 shows the results of the mechanical compressive strength test of scaffolds. As can be seen, the Gel scaffold has the lowest mechanical strength (σ = 10.27 ± 1.58 MPa), followed by the Gel-HNT scaffold with (σ = 20.92 ± 2.16 MPa) and Gel-HNT/ZA scaffold with (σ = 26.18 ± 2.9 MPa). Despite the increase in pore size in Gel-HNT and Gel-HNT/ZA scaffolds, which should have led to a decrease in mechanical strength, the strength of these samples has increased. The reason for this can be related to the presence of HNTs, which is a ceramic with very high mechanical properties, and the presence of HNT in the structure may lead to the bearing and transfer of force throughout the structure and increase the mechanical properties of scaffolds containing HNTs. In several studies, the effect of adding HNT

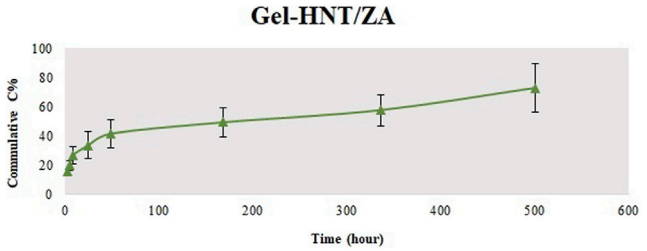

FIGURE 5 | ZA release behavior from the Gel-HNT/ZA.

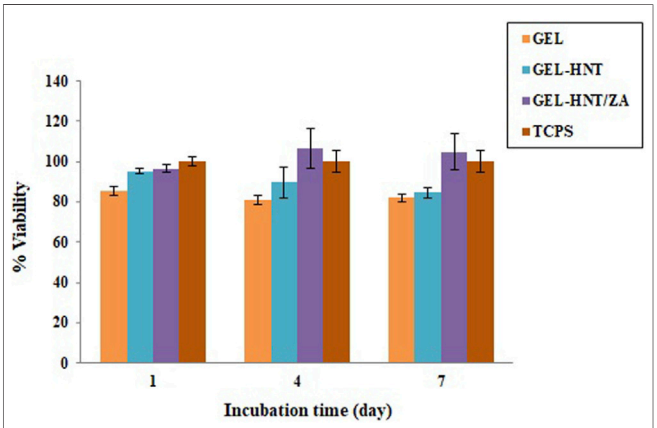

FIGURE 6 | MTT assay of hASCs cultured on the scaffolds ($p < 0.05$).

to biopolymers was investigated, all of which showed an increase in the mechanical properties of the resulting structure (Liu et al., 2013; Liu et al., 2015). Increasing the strength of synthesized tissue engineering scaffolds is considered as one of the practical advantages because scaffolds must act as temporary support against stresses and forces until the tissue is completely repaired (Liu et al., 2015).

3.2 *In vitro* Release Study

Recent studies have shown that local delivery of osteogenesis drugs with a controlled behavior can be used as a way to improve large and severe bone defects with low side effects (Boraei et al., 2020). The release behavior of ZA was initiated by a low burst mode and then continued via a stable release with a low rate. Also, the release profile successfully extended to 21 days, meaning proper time to complete *in vitro* osteogenic differentiation of stem cells (Bou Assaf et al., 2019) (**Figure 5**). Of course, the actual burst release is reduced through bonding between HNT and ZA. In addition, the low crystallinity of the scaffolds with more ZA facilitated the water diffusion into the scaffolds and consequently increased the ZA release from the samples. These results are in accordance with the previous study (Karavelidis et al., 2011), which proved that the ZA release rate is amplified by lowering the crystallinity of the polymer matrix.

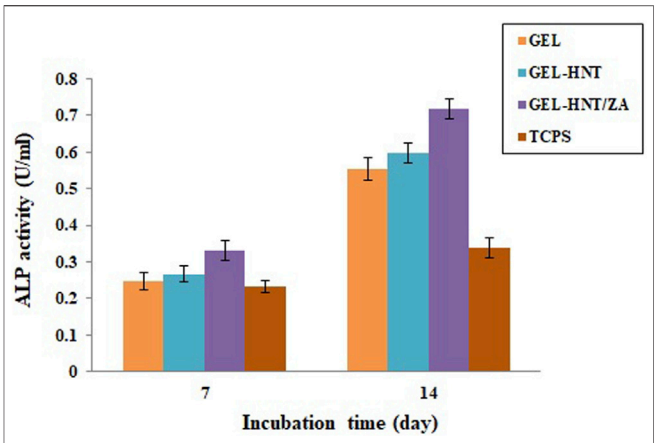

FIGURE 7 | Alkaline phosphatase (ALP) activity of (Gel, Gel-HNT and Gel-HNT/ZA) scaffolds and tissue culture polystyrene (TCPS) at 7 and 14 days, during osteogenic differentiation ($p < 0.05$).

3.3 hASCs Proliferation and Differentiation

Cell viability and cytocompatibility of the scaffolds are shown in **Figure 6**. Human Adipose Stem Cells (hASCs) were cultured onto the samples, and an MTT assay was done. Cell proliferation was investigated after 1, 4, and 7 days. In a study by Davydenko et al., OD in a sample with pure gelatin scaffold was higher than OD of TCPs, which can be considered due to the presence of more sites for cell-matrix interaction. These places are mostly due to the presence of interconnected micron porosity (Davidenko et al., 2016). These results were also observed in this study, which shows the importance of interconnected porous structures. According to the results, both Gel-HNT and Gel-HNT/ZA showed more proliferation than Gel sample during the days of culture, especially in ZA-containing scaffold. By adding HNTs nanorods to the structure, the surface-to-volume ratio increases dramatically, and consequently the cell-matrix interaction increase, which in turn increases cell proliferation and differentiation, which is consistent with previous studies (Ji et al., 2017).

Alkaline phosphatase (ALP) activity assay was used to investigate the osteogenic ability of hASCs. This enzyme is one of the most famous early markers of osteogenesis. There are some researches that demonstrated the role of ALP in osteogenic differentiation (Ardeshirylajimi et al., 2015). The ALP is the final marker for stem cell osteogenic differentiation that promotes the mineralization of calcium (Boraei et al., 2020). This test was performed on scaffolds for 7 and 14 days (**Figure 7**). The results showed a higher expression of the activity of samples containing ZA on day 14. There was also a slight increase in ALP on day 7. It is important to note that ALP values for all scaffolds were significantly higher than those calculated for TCPs. In addition, the ALP amount is considerably more in the samples including ZA, suggesting the speed up of osteogenic differentiation of seeded hASCs by the scaffold-released ZA. As reported previously,

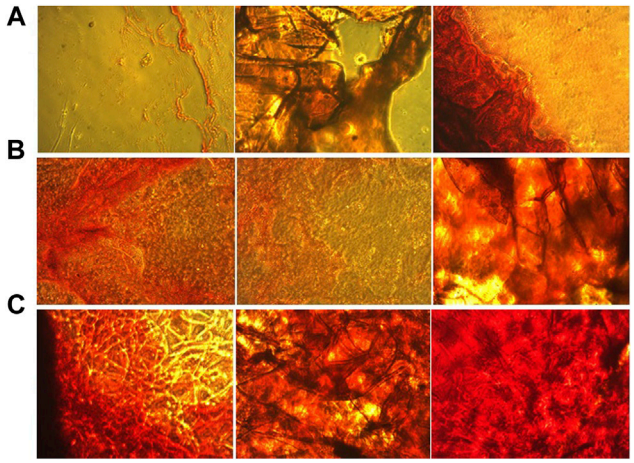

FIGURE 8 | Alizarin red staining of culture hASCs on the **(A)** Gel, **(B)** Gel-HNT and **(C)** Gel-HNT/ZA Scaffolds at 7, 14 and 21 days.

maximum ALP activity is caused by enhancement in the mineralization (Santo et al., 2012).

The state of mineralization, which is the formation of inorganic calcium, was also investigated for 7, 14 and 21 days (**Figure 8**). This state of mineralization (calcium deposition) acts as the late marker of osteogenesis were investigated by Alizarin Red Staining (ARS) (Veernala et al., 2019). In this analysis, the red dots after imaging indicate the amount of calcium deposition at specific times. The amount of deposited calcium was remarkably increased with increasing the incubation time and adding the ZA until 21st day. On day 14, ZA release from the scaffolds caused a large difference in the amount of calcium deposited. The Bone Mineral Density (BMD) and osteogenic ability of ZA have been widely investigated and different mechanisms have been discussed (Pavón de Paz et al., 2019; Jin et al., 2020). In previous studies on ZA, the rate of increase in calcium deposits was observed with increasing time, the amount of calcium islets on the 14th day was significantly higher than the 7th day, which is consistent with our present study that the deposits Calcium has increased over time and the amount of ZA in the scaffold has increased (Raina et al., 2020; Demir-Oğuz and Ege, 2021).

CONCLUSION

The present study aimed to inset a novel nanocomposite scaffold to accelerate osteogenesis and deliver enough amount of Zoledronic Acid (ZA) to the bone cells in a suitable and continues manner for osteogenesis. The size of the pores in the scaffold containing ZA reached about 257 microns, which is completely suitable for use in bone tissue engineering. The XRD results showed that the ZA was molecularly scattered in the scaffold structure and addition of ZA diminished the crystallinity of the nanocomposite scaffolds. FTIR and EDS results were proved the successful loading of ZA in the samples. The *in vitro* release assay showed that ZA has displayed a low primary burst release (15%) and then was stable and controlled release up to 21 days (about 49%). The results of Gel-HNT and Gel-HNT/ZA showed higher pore size, porosity, mechanical properties, degradation rate, and water adsorption in comparison with Gel scaffold. Cellular assays on hASCs during 7 and 14 days of culture, demonstrated growth cell viability on all Gel-based scaffolds with and without HNT and ZA. ALP activity assay significantly increased after ZA adding from 0.553 to 0.718. Also, calcium deposition assay completely increased after ZA adding. Hence, Gel-HNT/ZA could be proposed as a capable nanocomposite scaffold for enhancing cell proliferation, osteogenic differentiation, and improving bone regeneration.

DATA AVAILABILITY STATEMENT

The original contributions presented in the study are included in the article/supplementary material, further inquiries can be directed to the corresponding author.

AUTHOR CONTRIBUTIONS

SA and MM contributed to the design of the study and organized the database. SA wrote sections of the manuscript. ME performed the statistical analysis and wrote the first draft of the manuscript. MV performed the statistical analysis and wrote the first draft of the manuscript. All authors contributed to manuscript revision, read, and approved the submitted version.

REFERENCES

Abdollahi Boraei, S. B., Nourmohammadi, J., Bakhshandeh, B., Dehghan, M. M., Gholami, H., Calle Hernández, D., et al. (2021a). Enhanced Osteogenesis of Gelatin-Halloysite Nanocomposite Scaffold Mediated by Loading Strontium Ranelate. *Int. J. Polymeric Mater. Polymeric Biomater.* 70, 392–402. doi:10.1080/00914037.2020.1725754

Abdollahi Boraei, S. B., Nourmohammadi, J., Bakhshandeh, B., Dehghan, M. M., Gholami, H., Gonzalez, Z., et al. (2021b). Capability of Core-Sheath Polyvinyl Alcohol-Polycaprolactone Emulsion Electrospun Nanofibrous Scaffolds in Releasing Strontium Ranelate for Bone Regeneration. *Biomed. Mater.* 16, 025009. doi:10.1088/1748-605x/abdb07

Abdollahi Boraei, S. B., Nourmohammadi, J., Bakhshandeh, B., Dehghan, M. M., Gonzalez, Z., and Ferrari, B. (2020a). The Effect of Protelos Content on the Physicochemical, Mechanical and Biological Properties of Gelatin-Based Scaffolds. *J. Appl. Biotechnol. Rep.* 7, 41–47. doi:10.1080/00914037.2020.1725754

Abdollahi Boraei, S. B., Nourmohammadi, J., Sadat Mahdavi, F., Yus, J., Ferrandez-Montero, A., Sanchez-Herencia, A. J., et al. (2020b). Effect of SrR Delivery in the Biomarkers of Bone Regeneration during the *In Vitro* Degradation of HNT/GN Coatings Prepared by EPD. *Colloids Surf. B: Biointerfaces* 190, 110944. doi:10.1016/j.colsurfb.2020.110944

Ardeshirylajimi, A., Mossahebi-Mohammadi, M., Vakilian, S., Langroudi, L., Seyedjafari, E., Atashi, A., et al. (2015). Comparison of Osteogenic Differentiation Potential of Human Adult Stem Cells Loaded on Bioceramic-Coated Electrospun Poly (L-Lactide) Nanofibres. *Cell Prolif.* 48, 47–58. doi:10.1111/cpr.12156

Benford, H. L., Mcgowan, N. W. A., Helfrich, M. H., Nuttall, M. E., and Rogers, M. J. (2001). Visualization of Bisphosphonate-Induced Caspase-3 Activity in Apoptotic Osteoclasts *In Vitro*. *Bone* 28, 465–473. doi:10.1016/s8756-3282(01)00412-4

Bou Assaf, R., Fayyad-Kazan, M., Al-Nemer, F., Makki, R., Fayyad-Kazan, H., Badran, B., et al. (2019). Evaluation of the Osteogenic Potential of Different Scaffolds Embedded with Human Stem Cells Originated from Schneiderian Membrane: an *In Vitro* Study. *Biomed. Res. Int.* 2019, 1–10. doi:10.1155/2019/2868673

Burg, K. J. L., Porter, S., and Kellam, J. F. (2000). Biomaterial Developments for Bone Tissue Engineering. *Biomaterials* 21, 2347–2359. doi:10.1016/s0142-9612(00)00102-2

Carbone, E. J., Jiang, T., Nelson, C., Henry, N., and Lo, K. W.-H. (2014). Small Molecule Delivery through Nanofibrous Scaffolds for Musculoskeletal Regenerative Engineering. *Nanomedicine: Nanotechnology, Biol. Med.* 10, 1691–1699. doi:10.1016/j.nano.2014.05.013

Cartmell, S. (2009). Controlled Release Scaffolds for Bone Tissue Engineering. *J. Pharm. Sci.* 98, 430–441. doi:10.1002/jps.21431

Chen, S., Wan, P., Zhang, B., Yang, K., and Li, Y. (2020). Facile Fabrication of the Zoledronate-Incorporated Coating on Magnesium alloy for Orthopaedic Implants. *J. Orthopaedic Translation* 22, 2–6. doi:10.1016/j.jot.2019.09.007

Coxon, F. P., Helfrich, M. H., Van'T Hof, R., Sebti, S., Ralston, S. H., Hamilton, A., et al. (2000). Protein Geranylgeranylation Is Required for Osteoclast Formation, Function, and Survival: Inhibition by Bisphosphonates and GGTI-298. *J. Bone Miner Res.* 15, 1467–1476. doi:10.1359/jbmr.2000.15.8.1467

Davidenko, N., Schuster, C. F., Bax, D. V., Farndale, R. W., Hamaia, S., Best, S. M., et al. (2016). Evaluation of Cell Binding to Collagen and Gelatin: a Study of the Effect of 2D and 3D Architecture and Surface Chemistry. *J. Mater. Sci. Mater. Med.* 27, 148. doi:10.1007/s10856-016-5763-9

Demir-Oğuz, Ö., and Ege, D. (2021). Effect of Zoledronic Acid and Graphene Oxide on the Physical and *In Vitro* Properties of Injectable Bone Substitutes. *Mater. Sci. Eng. C* 120, 111758. doi:10.1016/j.msec.2020.111758

Flahiff, C. M., Blackwell, A. S., Hollis, J. M., and Feldman, D. S. (1996). Analysis of a Biodegradable Composite for Bone Healing. *J. Biomed. Mater. Res.* 32, 419–424. doi:10.1002/(sici)1097-4636(199611)32:3<419::aid-jbm15>3.0.co;2-b

Gage, M. J., Liporace, F. A., Egol, K. A., and Mclaurin, T. M. (2018). Management of Bone Defects in Orthopedic Trauma. *Bull. NYU Hosp. Jt. Dis.* 76, 4–8.

Ghazalian, M., Afshar, S., Rostami, A., Rashedi, S., and Bahrami, S. H. (2022). Fabrication and Characterization of Chitosan-Polycaprolactone Core-Shell Nanofibers Containing Tetracycline Hydrochloride. *Colloids Surf. A: Physicochemical Eng. Aspects* 636, 128163. doi:10.1016/j.colsurfa.2021.128163

Guerado, E., and Caso, E. (2017). Challenges of Bone Tissue Engineering in Orthopaedic Patients. *Wjo* 8, 87. doi:10.5312/wjo.v8.i2.87

Jalaja, K., Naskar, D., Kundu, S. C., and James, N. R. (2015). Fabrication of Cationized Gelatin Nanofibers by Electrospinning for Tissue Regeneration. *Rsc Adv.* 5, 89521–89530. doi:10.1039/C5RA10384C

Ji, L., Qiao, W., Zhang, Y., Wu, H., Miao, S., Cheng, Z., et al. (2017). A Gelatin Composite Scaffold Strengthened by Drug-Loaded Halloysite Nanotubes. *Mater. Sci. Eng. C* 78, 362–369. doi:10.1016/j.msec.2017.04.070

Jin, Z. H., Wang, S. F., and Liao, W. (2020). Zoledronic Acid Accelerates Osteogenesis of Bone Marrow Mesenchymal Stem Cells by Attenuating Oxidative Stress via the SIRT3/SOD2 Pathway and Thus Alleviates Osteoporosis. *Eur. Rev. Med. Pharmacol. Sci.* 24, 2095–2101. doi:10.26355/eurrev_202002_20389

Karavelidis, V., Karavas, E., Giliopoulos, D., Papadimitriou, S., and Bikiaris, D. (2011). Evaluating the Effects of Crystallinity in New Biocompatible Polyester Nanocarriers on Drug Release Behavior. *Int. J. Nanomedicine* 6, 3021–3032. doi:10.2147/IJN.S26016

Kim, T., See, C. W., Li, X., and Zhu, D. (2020). Orthopedic Implants and Devices for Bone Fractures and Defects: Past, Present and Perspective. *Engineered Regen.* 1, 6–18. doi:10.1016/j.engreg.2020.05.003

Lambrinoudaki, I., Christodoulakos, G., and Botsis, D. (2006). Bisphosphonates. *Ann. N.Y Acad. Sci.* 1092, 397–402. doi:10.1196/annals.1365.036

Lee, D. J., Kwon, J., Kim, Y. I., Wang, X., Wu, T. J., Lee, Y. T., et al. (2019). Effect of Pore Size in Bone Regeneration Using Polydopamine-laced Hydroxyapatite Collagen Calcium Silicate Scaffolds Fabricated by 3D Mould Printing Technology. *Orthod. Craniofac. Res.* 22, 127–133. doi:10.1111/ocr.12261

Lee, Y.-J., Lee, S.-C., Jee, S. C., Sung, J.-S., and Kadam, A. A. (2019). Surface Functionalization of Halloysite Nanotubes with Supermagnetic Iron Oxide, Chitosan and 2-D Calcium-Phosphate Nanoflakes for Synergistic Osteoconduction Enhancement of Human Adipose Tissue-Derived Mesenchymal Stem Cells. *Colloids Surf. B: Biointerfaces* 173, 18–26. doi:10.1016/j.colsurfb.2018.09.045

Lee, Y.-M., Seol, Y.-J., Lim, Y.-T., Kim, S., Han, S.-B., Rhyu, I.-C., et al. (2001). Tissue-engineered Growth of Bone by Marrow Cell Transplantation Using Porous Calcium Metaphosphate Matrices. *J. Biomed. Mater. Res.* 54, 216–223. doi:10.1002/1097-4636(200102)54:2<216::aid-jbm8>3.0.co;2-c

Li, G., Wang, L., Pan, W., Yang, F., Jiang, W., Wu, X., et al. (2016). *In Vitro* and *In Vivo* Study of Additive Manufactured Porous Ti6Al4V Scaffolds for Repairing Bone Defects. *Sci. Rep.* 6, 34072. doi:10.1038/srep34072

Li, M., Wan, P., Wang, W., Yang, K., Zhang, Y., and Han, Y. (2019). Regulation of Osteogenesis and Osteoclastogenesis by Zoledronic Acid Loaded on Biodegradable Magnesium-Strontium alloy. *Sci. Rep.* 9, 933. doi:10.1038/s41598-018-37091-8

Liao, L., Lv, G., Cai, D., and Wu, L. (2016). The Sequential Intercalation of Three Types of Surfactants into Sodium Montmorillonite. *Appl. Clay Sci.* 119, 82–86. doi:10.1016/j.clay.2015.08.003

Liu, D., and Dixit, V. (1997). *Porous Materials for Tissue Engineering*. Switzerland: Trans Tech Pub.

Liu, M., Dai, L., Shi, H., Xiong, S., and Zhou, C. (2015). *In Vitro* evaluation of Alginate/halloysite Nanotube Composite Scaffolds for Tissue Engineering. *Mater. Sci. Eng. C* 49, 700–712. doi:10.1016/j.msec.2015.01.037

Liu, M., Wu, C., Jiao, Y., Xiong, S., and Zhou, C. (2013). Chitosan-halloysite Nanotubes Nanocomposite Scaffolds for Tissue Engineering. *J. Mater. Chem. B* 1, 2078–2089. doi:10.1039/c3tb20084a

Mirahmadi, F., Tafazzoli-Shadpour, M., Shokrgozar, M. A., and Bonakdar, S. (2013). Enhanced Mechanical Properties of Thermosensitive Chitosan Hydrogel by Silk Fibers for Cartilage Tissue Engineering. *Mater. Sci. Eng. c* 33, 4786–4794. doi:10.1016/j.msec.2013.07.043

Nancollas, G. H., Tang, R., Phipps, R. J., Henneman, Z., Gulde, S., Wu, W., et al. (2006). Novel Insights into Actions of Bisphosphonates on Bone: Differences in Interactions with Hydroxyapatite. *Bone* 38, 617–627. doi:10.1016/j.bone.2005.05.003

Paris, J. L., Román, J., Manzano, M., Cabañas, M. V., and Vallet-Regí, M. (2015). Tuning Dual-Drug Release from Composite Scaffolds for Bone Regeneration. *Int. J. pharmaceutics* 486, 30–37. doi:10.1016/j.ijpharm.2015.03.048

Park, J. B., and Bronzino, J. (2000). *The Biomedical Engineering Handbook*, 4. Boca Raton, FL: CRC Press, 1–8.

Parks, J., and Lakes, R. (1992). *Metallic Implant materialsBiomaterials—An Introduction*. New York: Plenum Press, 75.

Pavón de Paz, I., Rosado Sierra, J. A., Pérez Blanco, C., Modroño Móstoles, N., Guijarro de Armas, G., and Navea Aguilera, C. (2019). Acute and Long-Term Effects of Zoledronate in Adult Patients with Osteogenesis Imperfecta. An Observational Spanish Study with Five Years of Follow-Up. *Endocrinología, Diabetes y Nutrición (English ed.)* 66, 108–116. doi:10.1016/j.endien.2019.02.001

Raina, D. B., Matuszewski, L. M., Vater, C., Bolte, J., Isaksson, H., Lidgren, L., et al. (2020). A Facile One-Stage Treatment of Critical Bone Defects Using a Calcium Sulfate/hydroxyapatite Biomaterial Providing Spatiotemporal Delivery of Bone Morphogenic Protein-2 and Zoledronic Acid. *Sci. Adv.* 6, eabc1779. doi:10.1126/sciadv.abc1779

Rashedi, S., Afshar, S., Rostami, A., Ghazalian, M., and Nazockdast, H. (2021). Co-electrospun Poly(lactic Acid)/gelatin Nanofibrous Scaffold Prepared by a New Solvent System: Morphological, Mechanical and *In Vitro* Degradability Properties. *Int. J. Polymeric Mater. Polymeric Biomater.* 70, 545–553. doi:10.1080/00914037.2020.1740987

Santo, V. E., Duarte, A. R. C., Popa, E. G., Gomes, M. E., Mano, J. F., and Reis, R. L. (2012). Enhancement of Osteogenic Differentiation of Human Adipose Derived Stem Cells by the Controlled Release of Platelet Lysates from Hybrid Scaffolds Produced by Supercritical Fluid Foaming. *J. controlled release* 162, 19–27. doi:10.1016/j.jconrel.2012.06.001

Shahriarpanah, S., Nourmohammadi, J., and Amoabediny, G. (2016). Fabrication and Characterization of Carboxylated Starch-Chitosan Bioactive Scaffold for Bone Regeneration. *Int. J. Biol. macromolecules* 93, 1069–1078. doi:10.1016/j.ijbiomac.2016.09.045

Tolba, E., Abd-Elhady, B., Elkholy, B., Elkady, H., and Eltonsi, M. (2010). Biomimetic Synthesis of Guided-Tissue Regeneration Hydroxyapatite/polyvinyl Alcohol Nanocomposite Scaffolds: Influence of Alginate on Mechanical and Biological Properties. *J. Am. Sci.* 6, 239–249.

Veernala, I., Giri, J., Pradhan, A., Polley, P., Singh, R., and Yadava, S. K. (2019). Effect of Fluoride Doping in Laponite Nanoplatelets on Osteogenic Differentiation of Human Dental Follicle Stem Cells (hDFSCs). *Sci. Rep.* 9, 915–15. doi:10.1038/s41598-018-37327-7

White, R. D., Bavykin, D. V., and Walsh, F. C. (2012). The Stability of Halloysite Nanotubes in Acidic and Alkaline Aqueous Suspensions. *Nanotechnology* 23, 065705. doi:10.1088/0957-4484/23/6/065705

Wiese, A., and Pape, H. C. (2010). Bone Defects Caused by High-Energy Injuries, Bone Loss, Infected Nonunions, and Nonunions. *Orthop. Clin. North America* 41, 1–4. doi:10.1016/j.ocl.2009.07.003

Xu, T., Sheng, L., He, L., Weng, J., and Duan, K. (2020). Enhanced Osteogenesis of Hydroxyapatite Scaffolds by Coating with BMP-2-Loaded Short Polylactide Nanofiber: a New Drug Loading Method for Porous Scaffolds. *Regen. Biomater.* 7, 91–98. doi:10.1093/rb/rbz040

Yang, X.-J., Wang, F.-Q., Lu, C.-B., Zou, J.-W., Hu, J.-B., Yang, Z., et al. (2020). Modulation of Bone Formation and Resorption Using a Novel Zoledronic Acid Loaded Gelatin Nanoparticles Integrated Porous Titanium Scaffold: An *In Vitro* and *In Vivo* Study. *Biomed. Mater.* 15, 055013. doi:10.1088/1748-605x/ab8720

Zadegan, S., Nourmohammadi, J., Vahidi, B., and Haghighipour, N. (2019). An Investigation into Osteogenic Differentiation Effects of Silk Fibroin-Nettle (Urtica Dioica L.) Nanofibers. *Int. J. Biol. macromolecules* 133, 795–803. doi:10.1016/j.ijbiomac.2019.04.165

Zare, Y., and Rhee, K. Y. (2021a). A Model for Tensile Modulus of Halloysite-Nanotube-Based Samples Assuming the Distribution and Networking of Both Nanoparticles and Interphase Zone after Mechanical Percolation. *Mech. Adv. Mater. Structures*, 1–10. doi:10.1080/15376494.2021.1962457

Zare, Y., and Rhee, K. Y. (2021b). A Simple Model for Determining the Strength of Polymer Halloysite Nanotube Systems. *Composites B: Eng.* 227, 109411. doi:10.1016/j.compositesb.2021.109411

Zare, Y., and Rhee, K. Y. (2022). Expansion of Takayanagi Model by Interphase Characteristics and Filler Size to Approximate the Tensile Modulus of Halloysite-Nanotube-Filled System. *J. Mater. Res. Technol.* 16, 1628–1636. doi:10.1016/j.jmrt.2021.12.082

Zare, Y., Rhee, K. Y., and Park, S.-J. (2021). An Applicable Model for the Modulus of Polymer Halloysite Nanotubes Samples by the Characteristics of Halloysite Nanotubes, Interphase Zone and Filler/interphase Network. *Colloids Surf. A: Physicochemical Eng. Aspects* 628, 127330. doi:10.1016/j.colsurfa.2021.127330

Zare, Y., and Rhee, K. Y. (2021c). The Strengthening Efficacy of Filler/interphase Network in Polymer Halloysite Nanotubes System after Mechanical Percolation. *J. Mater. Res. Technol.* 15, 5343–5352. doi:10.1016/j.jmrt.2021.10.116

Conflict of Interest: The authors declare that the research was conducted in the absence of any commercial or financial relationships that could be construed as a potential conflict of interest.

Publisher's Note: All claims expressed in this article are solely those of the authors and do not necessarily represent those of their affiliated organizations, or those of the publisher, the editors and the reviewers. Any product that may be evaluated in this article, or claim that may be made by its manufacturer, is not guaranteed or endorsed by the publisher.

frontiers | Frontiers in Bioengineering and Biotechnology

ORIGINAL RESEARCH
published: 18 July 2022
doi: 10.3389/fbioe.2022.939312

Nanoscale Porphyrin Metal-Organic Frameworks Deliver siRNA for Alleviating Early Pulmonary Fibrosis in Acute Lung Injury

Changmei Weng[1], *Guanhua Li*[1], *Dongdong Zhang*[1], *Zhaoxia Duan*[1], *Kuijun Chen*[1], *Jieyuan Zhang*[1], *Tao Li*[2,3]* *and Jianmin Wang*[1]*

[1]State Key Laboratory of Trauma, Burns and Combined Injury, Research Institute of Surgery, Daping Hospital, Third Military Medical University (Army Medical University), Chongqing, China, [2]Center for Joint Surgery, Southwest Hospital, Third Military Medical University (Army Medical University), Chongqing, China, [3]State Key Laboratory of Trauma, Burns and Combined Injury, Chongqing Engineering Research Center for Nanomedicine, Department of Preventive Medicine, Institute of Combined Injury, Third Military Medical University (Army Medical University), Chongqing, China

OPEN ACCESS

Edited by:
Seyed Morteza Naghib,
Iran University of Science and Technology, Iran

Reviewed by:
Mehdi Rahmanian,
Motamed Cancer Institute, Iran
Mohammadmahdi Akbari Edgahi,
Iran University of Science and Technology, Iran
Fatemeh Yaghoubi,
Shahid Sadoughi University of Medical Sciences and Health Services, Iran

***Correspondence:**
Tao Li
whutlit@tmmu.edu.cn
Jianmin Wang
jmwang@tmmu.edu.cn

Specialty section:
This article was submitted to Nanobiotechnology, a section of the journal Frontiers in Bioengineering and Biotechnology

Received: 09 May 2022
Accepted: 07 June 2022
Published: 18 July 2022

Citation:
Weng C, Li G, Zhang D, Duan Z, Chen K, Zhang J, Li T and Wang J (2022) Nanoscale Porphyrin Metal-Organic Frameworks Deliver siRNA for Alleviating Early Pulmonary Fibrosis in Acute Lung Injury. Front. Bioeng. Biotechnol. 10:939312. doi: 10.3389/fbioe.2022.939312

Acute lung injury (ALI) has high mortality and still lacks novel and efficient therapies. Zinc finger E-box binding homeobox 1 and 2 (ZEB1/2) are highly expressed in the early stage of ALI and are positively correlated with the progression of pulmonary fibrosis. Herein, we developed a nanoscale Zr(IV)-based porphyrin metal-organic (ZPM) framework to deliver small interfering ZEB1/2 (siZEB1/2) to alleviate early pulmonary fibrosis during ALI. This pH-responsive nano-ZPM system could effectively protect siRNAs during lung delivery until after internalization and rapidly trigger siRNA release under the mildly acidic environment of the endo/lysosome (pH 4.0–6.5) for transfection and gene silencing. Furthermore, the *in vivo* studies confirmed that this nano-ZPM system could anchor in inflamed lungs. Moreover, the ZEB1/2 silencing led to increased E-cadherin and decreased α-SMA levels. Overall, the nano-ZPM system was an excellent non-viral vector system to deliver siRNAs to alleviate early pulmonary fibrosis during ALI.

Keywords: porphyrin metal-organic framework, non-viral vector, siRNA, pulmonary fibrosis, endosomal escape

INTRODUCTION

Acute lung injury (ALI) is associated with acute hypoxic respiratory insufficiency or respiratory failure, resulting from pulmonary injury during non-cardiogenic diseases such as severe infections, shocks, traumas, and burns (Fan et al., 2018; Bian et al., 2021). Additionally, ALI can develop into acute respiratory distress syndrome (ARDS) in more serious injuries (Matthay et al., 2019; Kaku et al., 2020). For example, the widespread of COVID-19 can cause ARDS, which is the primary factor leading to death. Although fluid management, glucocorticoids, and other therapeutic modalities have been applied to control ALI/ARDS, the clinical efficacy is still far from satisfactory (Matthay et al., 2017), leading to mortality as high as 30–50% (Beitler et al., 2022). Mechanical ventilation is the most important supportive treatment for patients with ALI/ARDS, but related complications such as ventilator-associated lung injury (VILI) and ventilator-associated pneumonia (VAP) also significantly affect the prognosis of ALI/ARDS patients (Aranda-Valderrama and Kaynar 2018; Zoulikha et al., 2022). Pharmaceutical drugs such as corticosteroids, lung surfactants, nitric oxide, and keratinocyte growth factors have been widely investigated for ALI/ARDS treatment. Unfortunately, none of them have been proved to effectively reduce the mortality of patients

with ALI/ARDS in clinical trials (Qiao et al., 2021). In addition, many studies have demonstrated that the mesenchymal stem cell (MSC)-based therapy with anti-inflammatory, antifibrotic, anti-oxidative stress, and anti-apoptotic abilities is an alternative strategy to the treatment of ALI/ARDS (Fernandez-Francos et al., 2021). However, MSC treatment efficacy in ALI/ARDS is debated and controversial, so adequate mechanism research and functional test are needed before their clinical application. Consequently, the development of novel and efficient therapies for the prevention and treatment of ALI/ARDS is of great interest.

Pulmonary fibrosis can occur in the early stage of ALI, comprehending its crucial pathological process (Li et al., 2009; Burnham et al., 2014). The primary factors of ALI are the generation of reactive oxygen species (ROS) and the dysfunction of antioxidant systems. The epithelial-mesenchymal transition (EMT) in cells is also involved in those processes (Zhang et al., 2015; Kawami et al., 2022). The EMT is crucial for epithelial cells to acquire the mesenchymal phenotype and plays a critical role in the development of pulmonary fibrosis, mediated by different transcription factors (Zhou et al., 2016; Chen et al., 2017). The zinc finger E-box binding homeobox (ZEB) family is one of the important nuclear transcription factors, including Zinc-finger E-box binding homeobox 1/δ-crystallin E2-box factor 1 (ZEB1/δEF1) and Smad-interacting protein 1 (ZEB2/SIP1), important regulators of E-cadherin expression and the EMT (Chilosi et al., 2017). Silencing of both ZEB1 and ZEB2 can reverse the EMT and abolish the repression of epithelial splicing regulatory proteins (ESRP) induced by TGF-β in NMuMG cells (Horiguchi et al., 2012). Moreover, ZEB1/2 is positively correlated with the progression of early pulmonary fibrosis induced by lipopolysaccharide (LPS) (Cao et al., 2018). Therefore, ZEB1/2 can be considered novel target for the treatment of early-stage pulmonary fibrosis after ALI.

Small interference RNA (siRNA) technology has been widely used to explore gene function and gene therapy of malignant tumors, viral infections, autoimmune, and inflammatory diseases due to its high specificity (Kole et al., 2012; Weng et al., 2019; Hu et al., 2020). The clear anatomy, accessibility, and relatively low enzyme activity make the lung a good target for local siRNA therapy (Kandil and Merkel 2019; Zoulikha et al., 2022). For example, inhaled siRNAs can directly target and have long-term contact with pulmonary cells, which can be quickly effective and avoid first-pass elimination (Merckx et al., 2018; Zhu et al., 2022). However, large molecular weight (~14 kDa), abundant negative charge, and poor stability of naked siRNAs limit their permeation across cell membranes (Wittrup and Lieberman 2015; Saeed et al., 2021). Thus, the development of new carriers for siRNA delivery into pulmonary cells is urgent. Nanoscale metal-organic frameworks (NMOFs) are a class of porous materials that have become promising candidates for drug encapsulation and delivery (Carrillo-Carrion 2020; Zhao et al., 2022). Recently, NMOFs have emerged as non-viral vector systems for delivering siRNA due to their high porosity, biodegradable structures, and controllable surface functionalities (He et al., 2014; Feng et al., 2020; Liu et al., 2022a). For example, Huang's group developed a tumor-targeted, biomimetic manganese dioxide-shrouded metal-organic framework-based nanomedicine to deliver siRNA against the pyruvate kinase muscle isozyme M2 (siPKM2) to inhibit the reprogrammed glycolysis of triple-negative breast cancer cells (Huang et al., 2021). Herein, we reported the first use of NMOFs for siRNA delivery to treat ALI.

In the present study, we designed a nanoscale Zr(IV)-based porphyrin metal-organic framework (ZPM) release system to deliver siZEB1/2 for alleviating early pulmonary fibrosis during ALI (**Scheme 1**). To promote the endosomal escape and cytosolic release of siZEB1/2, branched polyethyleneimine (bPEI) was conjugated to poly (2-diethylamino) ethyl methacrylate (PDEA) (abbreviate as PDE). Moreover, bPEI has a strong siRNA binding affinity and PDEA is ultra-pH-sensitive (pKa ≈6.4) and can aggregate into a hydrophobic core at pH 7.4 and undergo a charge transition to positive in acidic environments (Dai et al., 2018). Additionally, the ZPM-coated can protect the siRNA from enzymatic degradation in stable physiological pH 7.4 and decrease the cytotoxicity of bPEI. After ZPM@PDE-siZEB1/2 enters the cell through endocytosis, PDEA is quickly protonated in endo/lysosomes (pH 4.5–6.0), resulting in endosomal escape and cytosolic release of siRNA (Dai et al., 2017). Finally, the released siZEB1/2 can inhibit the expression of ZEB1/2, leading to EMT attenuation and alleviating early pulmonary fibrosis in LPS-induced ALI mice. This strategy might comprehend the basis for the smart design of a pulmonary siRNA delivery system to treat ALI/ARDS.

MATERIALS AND METHODS

Materials

Branched polyethyleneimine (PEI, Mw 2 kDa), 2-(N,N-diethylamino)ethyl methacrylate (DEA), Cysteamine (95%), Azobisisobutyronitrile (AIBN), Succinic anhydride (SA), cis-Aconitic anhydride, dimethyl sulfoxide (DMSO), Triethylamine (TEA), pyridine, and acetone were purchased from J&K Scientific Ltd. (Beijing, China). ZrOCl2·8H2O, Tetrakis (4-carboxyphenyl)porphyrin (TCPP), N,N-Dimethylformamide (DMF), N-ethyl-N-(3-(dimethylamino)-propyl) carbodiimide hydrochloride (EDC), and N-hydroxysuccinimide (NHS) were supplied by Aladdin Industrial Co., Ltd. (Shanghai, China). The siZEB1 (GTTGTTCTGCCAACAGTTG) and siZEB2 (GGCCGAATG AGAAACAATA) target both human and mice's genes, and Cy5-labeled siZEB1/2 were designed and synthesized by RiboBio (Guangzhou, China). Lipofectamine 2000 was purchased from Invitrogen (Carlsbad, United States), and the LPS was obtained from Sigma-Aldrich (Missouri, United States). The Cell Counting Kit-8 (CCK-8) was bought from Boster Biological Technology (Wuhan, China). DAPI and total RNA Reagent Trizol were purchased from Life Technologies (New York, United States). The PrimeScript®RT Reagent Kit with gDNA Eraser was provided by TaKaRa (Beijing, China). Quantitative real-time qPCR kits (iTaq™ universal SYBR® Green Supermix) were purchased from Bio-Rad (California, United States).

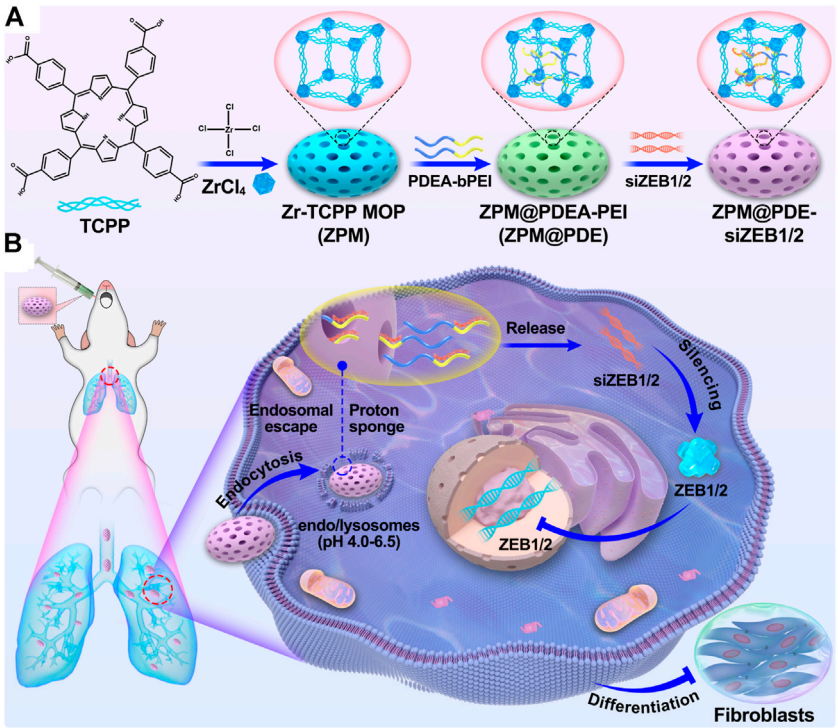

SCHEME 1 | (A) The scheme for ZPM@PDE-siZEB1/2 preparation and **(B)** intratracheal therapeutic mechanism of ZPM@PDE-siZEB1/2 in ALI model mice.

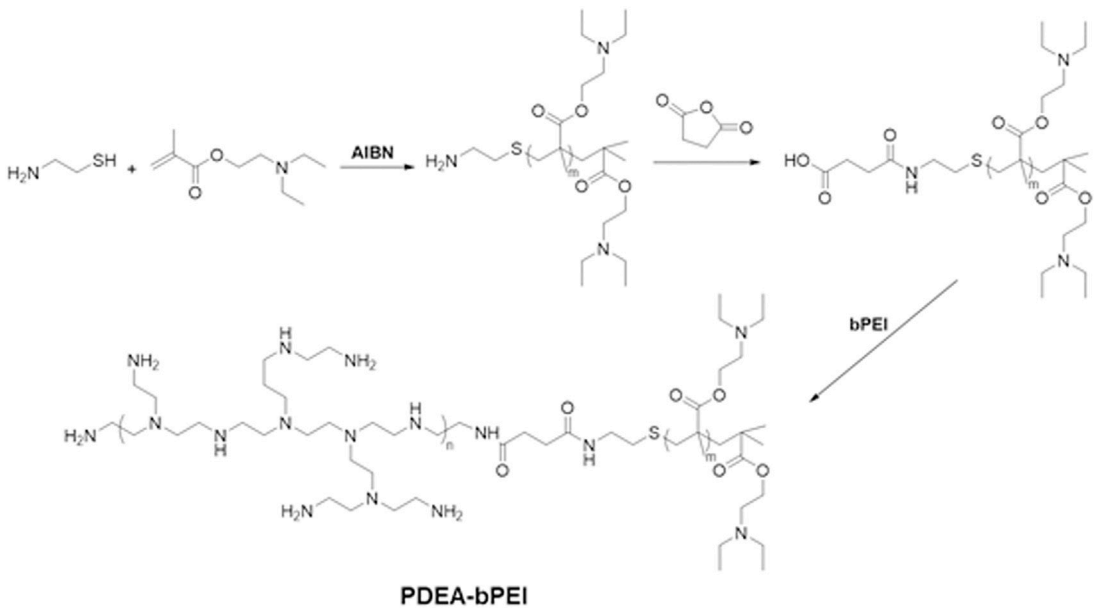

SCHEME 2 | The synthetic scheme of PDEA-bPEI (PDE).

Synthesis of PDEA-bPEI

The PDEA-bPEI was synthesized as shown in **Scheme 2**. DEA (5.6 g, 30 mmol), Cysteamine (154.3 mg, 2 mmol), AIBN (16.4 mg, 0.1 mmol), and anhydrous THF (20 ml) were added into a 50 ml Schlenk tube under a nitrogen atmosphere. Then, the Schlenk tube was sealed, and freeze-pump-thaw degassing was performed to remove oxygen from the reaction tube. The mixture was immersed in an oil bath at 50°C under stirring for 4 h,

followed by adding 8.0 ml of methanol to terminate the reaction. After cooling down, the crude product was repeatedly precipitated in cold n-hexane, filtered, and dried at 40 °C to generate oily PDEA (80% yield).

The linker SA-PDEA was synthesized as follows: in a three-port flask, PDEA (2.9 g, 1.0 mmol) and SA (150.1 mg, 1.5 mmol) were dissolved into DMSO/cis-Aconitic anhydride (1:5, 12 ml) under nitrogen atmosphere, then TEA (30 μL) and pyridine (30 μL) were added and continuously stirred for another 24 h at room temperature. The crude product was precipitated in cold n-hexane, filtered, and dried at 40°C under a vacuum to afford SA-PDEA. Next, SA-PDEA (2.4 g, 0.8 mmol), EDC (230.0 mg, 1.2 mmol) and NHS (138.1 mg, 1.2 mmol) were dissolved into DMSO (30 ml) under nitrogen atmosphere. After stirring at room temperature for 3 h, bPEI (0.8g, 0.4 mmol) was added and continuously stirred for another 24 h (overnight). First, the reaction solution was filtered, and the filtrate was added dropwise to water (150 ml), then purified by dialyzing (MWCO 3500) against Milli-Q water for another 3 days. The final product PDEA-bPEI (PDE) was obtained by freeze-drying.

Preparation of ZPM@PDE-siZEB1/2

The zirconium porphyrin NMOFs (ZPM) was synthesized as follows: ZPM was synthesized using the solvothermal method with the morphology control of benzoic acid. $ZrOCl_2{\cdot}8H_2O$ (64.5 mg, 0.2 mmol), 25 mg of tetrakis (4-carboxyphenyl) porphyrin (26.8 mg, 0.04 mmol), and benzoic acid (0.73 g, 6 mmol) were dissolved into dry DMF solution (10 ml). Then, the mixture was vigorously stirred at 90°C for 5 h. After cooling down, the crude product was repeatedly washed with DMF and ethanol. The product was dispersed in ethanol for further use.

PDEA-bPEI was incorporated with ZPM as follows: PDEA-bPEI was dissolved in 10 ml of DMF (2 mg/ml), then 10 ml of the ZPM solution (2 mg/ml) was added and stirred for 24 h. ZPM@PDEA-bPEI (ZPM@PDE) was obtained by repeatedly washing with DMF and ethanol, then dried at 80°C in an oven for further use.

The ZPM@PDE-siZEB1/2 was prepared as follows: 1 mg of ZPM@PDE was dissolved in 1 ml RNase-free water. The siZEB1 and siZEB2 (each with 20 μM) were added and shaken for 12 h at 4°C in the dark. The ZPM@PDE-siZEB1/2 was collected by centrifugation and freeze-dried. The obtained product was stored at 4°C for further use. The Cy5-labeled siZEB1/2 of NMOF were prepared similarly. The binding ability of ZPM@PDE with siZEB1/2 was evaluated by agarose gel electrophoresis retardation assay (2% agarose gel, 80 V, 40 min).

Material Characterization

The PDEA-bPEI was characterized by ^{1}H NMR (400 MHz Agilent) and Fourier transform infrared (FT-IR) spectrophotometer (PerkinElmer S100, United States). Transmission electron microscopy (TEM, LIBRA 200 CS, Carl Zeiss Co., Germany), X-ray powder diffraction (XRD, PANalytical, Netherlands), thermal gravimetric analysis (TGA, Mettler Toledo, Switzerland), and N_2 adsorption-desorption (ASAP 2460, Micromeritics, United States) were used to characterize the ZPM@PDE. The particle size and ζ-potential of ZPM@PDE were investigated by dynamic light scattering (DLS) (Nano ZS90 Zeta sizer, Malvern Instruments Co., Ltd., United Kingdom).

Release of siRNAs

To quantify the release rate of siZBE1/2, ZPM@PDE-siZBE1/2 was cultured in PBS at 37°C and pH 5.0 or pH 7.4. At predetermined time points, samples from each group were centrifuged, then the concentration of siZBE1/2 in the supernatant was measured using a spectrophotometer. All release experiments were conducted in triplicates.

Cytotoxicity *In Vitro*

The cytotoxicity of the ZPM@PDE-siZBE1/2 was determined by CCK-8 with the A549 cell line. Briefly, A549 cells were cultured in 96-well plates with an initial density of 8×10^3 cells per well and cultured for 24 h, then incubated with 10 μL of ZPM@PDE-siZBE1/2 and PDE-siZEB1/2 at different concentrations (0, 20, 50, 100, 200, and 500 μg/ml) in complete medium for 24 h. Finally, 10 μL of CCK-8 solution was added per well and incubated for 2 h. The absorbance was measured on a microplate reader (Varioskan LUX, Thermo Scientific, MA, United States) at 450 nm.

Cellular Uptake and Gene Silencing Efficiency *In Vitro*

First, A549 cells were inoculated in 6-well plates (2×10^5 cells per well) or 12-well plates (1×10^5 cells per well) and cultured for 24 h. Before the NMOF was added, the growth medium was replaced with fresh DMEM (pH 7.4 or 5.0). Then, ZPM@PDE-Cy5-siZEB1/2 (20 μg/ml) was added to each well and co-cultured for another 12 h. Cells were gently washed with PBS to remove redundant ZPM@PDE-Cy5-siZEB1/2. Cells seeded in 6-well plates were harvested for total RNA extraction. Cells seeded in 12-well plates were fixed with 4% paraformaldehyde for 15 min at room temperature. The nuclei were co-stained with 4′,6-diamidino-2-phenylindole (DAPI) and imaged using a fluorescence microscope (Olympus VS.200 ASW and Olympus BX48, Japan). The treatments were Lipofectamine 2000-Cy5-siZEB1/2 (Lip 2000-Cy5-siZEB1/2), naked Cy5-siZEB1/2, and fresh DMEM (control).

Animal Experiments

All animal experiments were performed following the regulations and guidelines of the Ethics Committee for Animal Experiments and were approved by the Ethics Committee of the Third Military Medical University. C57BL/6 mice (18–22 g, 6 weeks) were obtained from the animal center of the Daping Hospital (Chongqing, China). Mice were maintained in specific pathogen-free (SPF) conditions with free access to water and laboratory rodent food. The LPS-induced ALI mice model was established as follows: after being anesthetized with 0.1% pentobarbital (30 mg/kg of body weight), mice were fixed on cardboard with a 60° slope in the supine position and an intratracheal quantitative drug delivery device (YuYan

instruments, Shanghai, China) was applied. Mice were treated with LPS (5 mg/kg), naked siZEB1/2, and saline (control). After LPS instillation, mice tracheal inhaled ZPM@PDE-siZEB1/2 or ZPM@PDE-Cy5-siZEB1/2 at 0.5 h. Treated mice were observed for 3 days, then sacrificed. Lung tissues were obtained for imaging, histopathologic analysis, and total RNA and protein extraction.

Ex Vivo Lung Imaging Analysis

The lungs of C57BL/6 mice that tracheal inhaled LPS, then ZPM@PDE-Cy5-siZEB1/2 were collected and rinsed with PBS. Mice were treated with the same volume of saline as the control. Fluorescence images of the lungs were acquired using an *in vivo* imaging system (IVIS Spectrum, Perkin Elmer, United States).

Histological Examination

To observe the pathological changes in lung tissues, including inflammatory cell infiltration, pulmonary edema, hemorrhage, and pulmonary structural changes, lung tissue samples were fixed with 4% paraformaldehyde, embedded in paraffin, and sliced (5 μm thick). After representative organ sections were deparaffinized, hydrated, and stained with hematoxylin-eosin (H&E) or Masson's trichrome staining, they were observed under a microscope (Olympus VS.200 ASW and Olympus BX48, Japan). The semi-quantitative scoring on lung injury degree was determined using the Smith score (Smith et al., 1997): in each field, inflammation, hemorrhage, and edema, in both alveolar and interstitium, were graded on a 0–4 point scale (0: no injury, absent or appears normal, 0%; 1: light, < 25%; 2: moderate, 25–50%; 3: strong, 50–75%; 4: intense, > 75%). The pulmonary fibrotic grade of each field was assayed via the Aschoff score criteria as previously described (Chen et al., 2013). Five sections pictured from each lung were analyzed, and three independent observers marked the score.

Isolation of RNA and Quantitative Real-Time qPCR

Total RNA was extracted from A549 cells and lung tissues with Trizol, and reverse transcribed with PrimeScript®RT Reagent Kit according to the manufacturer's instructions. Then, cDNA was subjected to 10 μL real-time qPCRs and implemented in CFX96TM Real-Time System using SYBR Green Supermix (Bio-Rad Company, United States). GAPDH and β-actin were used as reference genes. Data are presented as the fold change relative to the control using the $2^{-\Delta\Delta Ct}$ method and the expression levels for the target gene were calculated by the comparative threshold cycle (CT) method. Primer sequences are shown in **Supplementary Table S1**.

Total Protein Extract for Western Blotting Analysis

Total protein was extracted from A549 cells and lung tissues using a total protein extraction kit. Protein samples were separated by 8% sodium dodecyl sulfate (SDS)-polyacrylamide gel and transferred to PVDF membrane by electrophoresis, then blocked with 5% non-fat milk at room temperature for 2 h. After membranes were incubated overnight with ZBE1, ZBE2, and β-actin antibodies at the appropriate dilution at 4°C, horseradish peroxidase (HRP)-linked secondary antibody was used for detection by Immobion™ Western Chemiluminescent (Millipore, United States). The band's density was quantified using Image-Pro Plus software (Version 6.0; Media Cybernetics, Silver Springs, MD, United States). β-actin was used as the internal control to normalize protein levels.

Immunofluorescence Staining and Immunohistochemistry Assay

For the immunofluorescence assay, the specific operation before incubation of the second antibody was the same as the immunohistochemistry staining. After incubating with E-cadherin and α-SMA primary antibodies under 4°C overnight, slides were washed with PBS buffer, then incubated with Cy3 or FITC fluorescent secondary antibody. Finally, nuclei were co-stained with DAPI. E-cadherin and α-SMA expression levels were observed under a fluorescence microscope.

Immunohistochemistry staining for detection of E-cadherin and α-SMA was performed as follows. Briefly, paraffin-embedded slices were cleared and antigen repair was performed. Then, endogenous peroxidase activity was quenched with an endogenous peroxidase blocker, and samples were incubated with E-cadherin or α-SMA primary antibodies at 4°C overnight. The target protein was recognized using horseradish peroxidase-conjugated and DAB chromogenic solution, then images were observed under a microscope.

Statistical Analysis

Data are presented as means ± SDs (standard deviations). Statistical analyses were conducted with SPSS 23 (IBM.United States) using one-way ANOVA or Student's *t*-test. A $p < 0.05$ was considered statistically significant.

RESULTS AND DISCUSSION

Fabrication and Characterization of ZPM@PDE

The PDEA-bPEI (PDE) was successfully synthesized as confirmed by ^{1}H NMR and FT-IR (Supplementary Text and **Supplementary Figures S1, S2**). In the ^{1}H-NMR spectrum (**Supplementary Figure S1**), the bPEI peak appeared at 2.46–2.81 ppm. In the PDE, the double peak at 2.40–2.81 ppm was attributed to the presence of methylene protons (-N-CH_2CH_2-N-) in the bPEI. Signals at δ = 0.72–1.21 ppm and δ = 3.99 ppm corresponded to the -CH_3 and (-O-CH_2-) protons of PDEA, respectively. In the FT-IR spectrum (**Supplementary Figure S2**), the strong absorption peak at 3,438 cm^{-1} was attributed to the–NH_2 on bPEI. The strong absorption peaks at 2,970 cm^{-1} and 1,150 cm^{-1} were attributed to the characteristic absorption peak of–CH_3 and O-C bonds stretching vibration on PDEA, respectively. These results confirmed that the PDE was successfully synthesized.

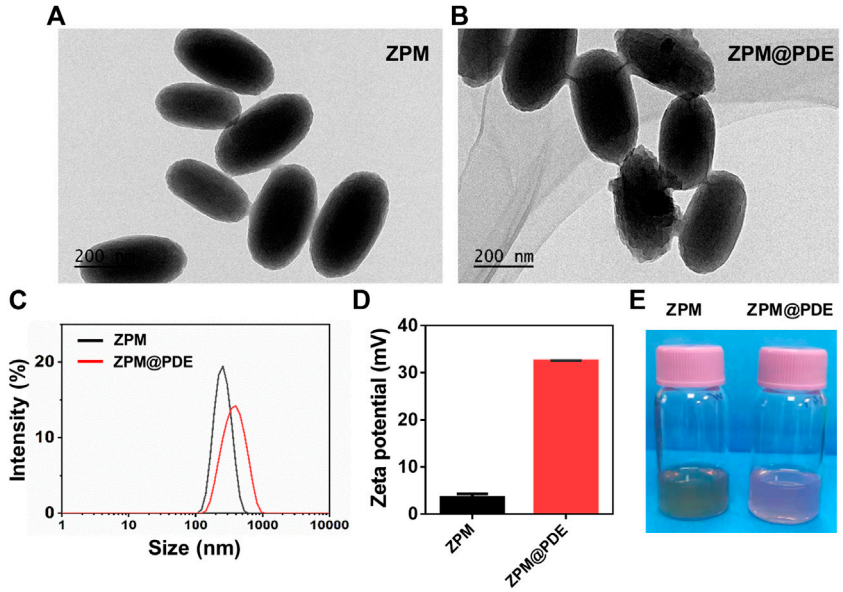

FIGURE 1 | (A,B) TEM of TZM and TZM@PDE, **(C)** Hydrodynamic size distribution, **(D)** Zeta potential, and **(E)** Photographs of TZM and TZM@PDE in aqueous solutions.

Further, the ZPM was successfully synthesized by solvothermal methods. The ZPM@PDE was obtained via ZPM adsorption with PDE by blending for 24 h. Based on the SEM, the morphology of ZPM and ZPM@PDE was of uniform monodispersed nanoshuttles (**Figures 1A,B**). The hydrodynamic size distribution increased from 240.6 to 330.4 nm and the zeta potential increased from 3.5 ± 0.4 to 32.5 ± 0.3 mV with PDE incorporation according to the dynamic light scattering (**Figures 1C,D**). Furthermore, the colors changed from green to pink (**Figure 1E**). These results showed that PDE was successfully wrapped in ZPM.

Then, FT-IR, powder X-ray diffraction (XRD), thermogravimetric analyzer (TGA), HR-TEM, and N_2 adsorption-desorption were used to validate the successful incorporation of PDE to ZPM. The FT-IR spectra of the ZPM@PDE had new characteristic peaks at 2,969, 1732, and 1,150 cm^{-1} assigned to the vibration of -NH2 in the PDE, which indicated the presence of PDE in ZPM@PDE (**Figure 2A**). Additionally, the TGA results showed that ZPM@PDE had lower heat flow intensity compared to ZPM due to the poor thermal stability of PDE (**Figure 2B**). Furthermore, the powder X-ray diffraction (XRD) pattern of ZPM and ZPM@PDE were consistent, which demonstrated that ZPM@PDE maintained the same crystal structure as ZPM during the incorporation process (**Figure 2C**). In addition, the HR-TEM images with elemental mapping showed that N was uniformly distributed in the particles (**Figure 2D**). Overall, these results further demonstrated that PDE was successfully wrapped in ZPM. In addition, the surface area and average pore diameter of ZPM were 775.8 m^2/g and 2.6 nm, respectively. (**Figure 2E**). Consistent with previous literature, our results exhibited the similar structure and pore size distribution with the acid-resistant mesoporous MOF (PCN-222) (Wang et al., 2019). DLS verified that ZPM had excellent colloidal stability in H_2O for at least 5 days (**Figure 2F**) verifying ZPM was suitable as a delivery carrier.

siRNA Loading Affinity of ZPM@PDE and Release Profile

The ZPM@PDE-siZBE1/2 was prepared by incubating ZPM@PDE with siZEB1/2. The siRNA binding ability of ZPM@PDE was detected by gel retardation assay. The bright band gradually disappeared with increasing ZPM@PDE/siZEB1/2 mass ratios (**Figure 3A**). When the mass ratio reached 14/1, the bright band completely disappeared, demonstrating that the siZBE1/2 was tightly bonded. The release profile of siZBE1/2 from ZPM@PDE/siZEB1/2 was measured in PBS at different pH values for 7 h (**Figure 3B**). Under physiological conditions (pH 7.4), the release of siZBE1/2 was less than 40% after 7 h. On the other hand, under the endo/lysosome mimic condition (pH 5.0), the release of siZEB1/2 reached more than 80% within 2 h, indicating that ZPM@PDE/siZEB1/2 had a pH-responsive feature. This phenomenon also indicated that PDEA segments can transform from hydrophobic to hydrophilic when the environmental pH is reduced (pH < 6.4) (Dai et al., 2017; Dai et al., 2018). Therefore, the NMOF could effectively protect the siRNA during lung delivery until after internalization, and rapidly trigger siRNA release under the mildly acidic environment of the endo/lysosome (pH 4.0–6.5), thereby allowing siRNA transfection and gene silencing (Zhuang et al., 2014; Zhuang et al., 2020).

Cytotoxicity, Cellular Uptake, and Gene Silence Ability of ZPM@PDE-siZEB1/2

Furthermore, we investigated the cytotoxicity of ZPM@PDE-siZEB1/2 on A549 cells using the CCK-8 assay (**Figure 3C**). The cell viability in ZPM@PDE-siZEB1/2-treated cells was higher than in PDE-

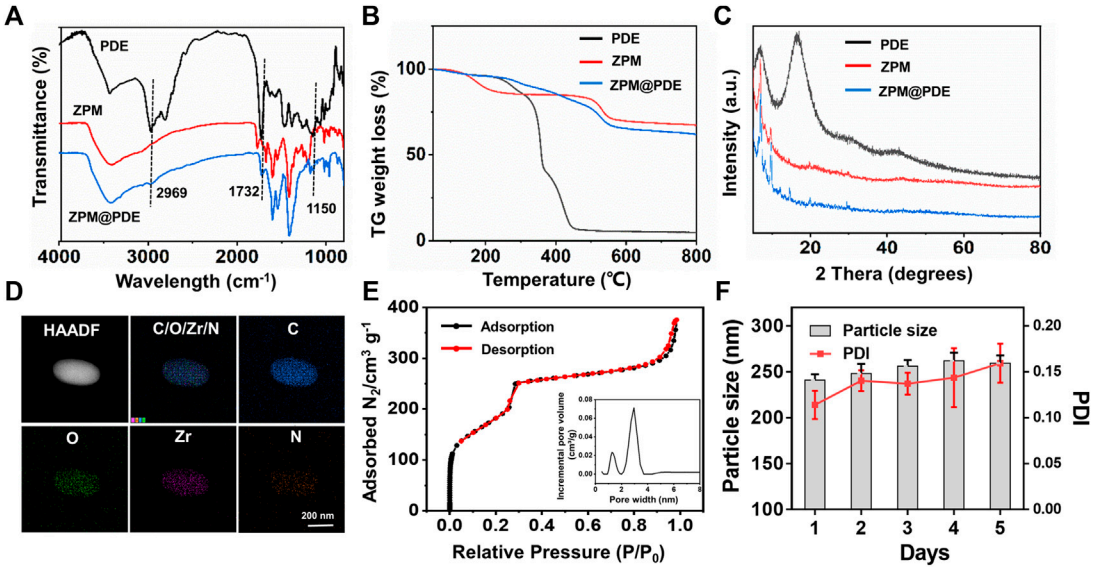

FIGURE 2 | (A) Fourier transform infrared (FT-IR) spectra, **(B)** TG weight loss profiles, **(C)** XRD patterns of PDE, ZPM, and ZPM@PDE, **(D)** HR-TEM and elemental mapping images of ZPM@PDE, **(E)** N_2 adsorption-desorption isotherms and DFT pore size distribution of ZPM, and **(F)** Hydrodynamic size distribution and PDI of ZPM in H_2O for 5 days.

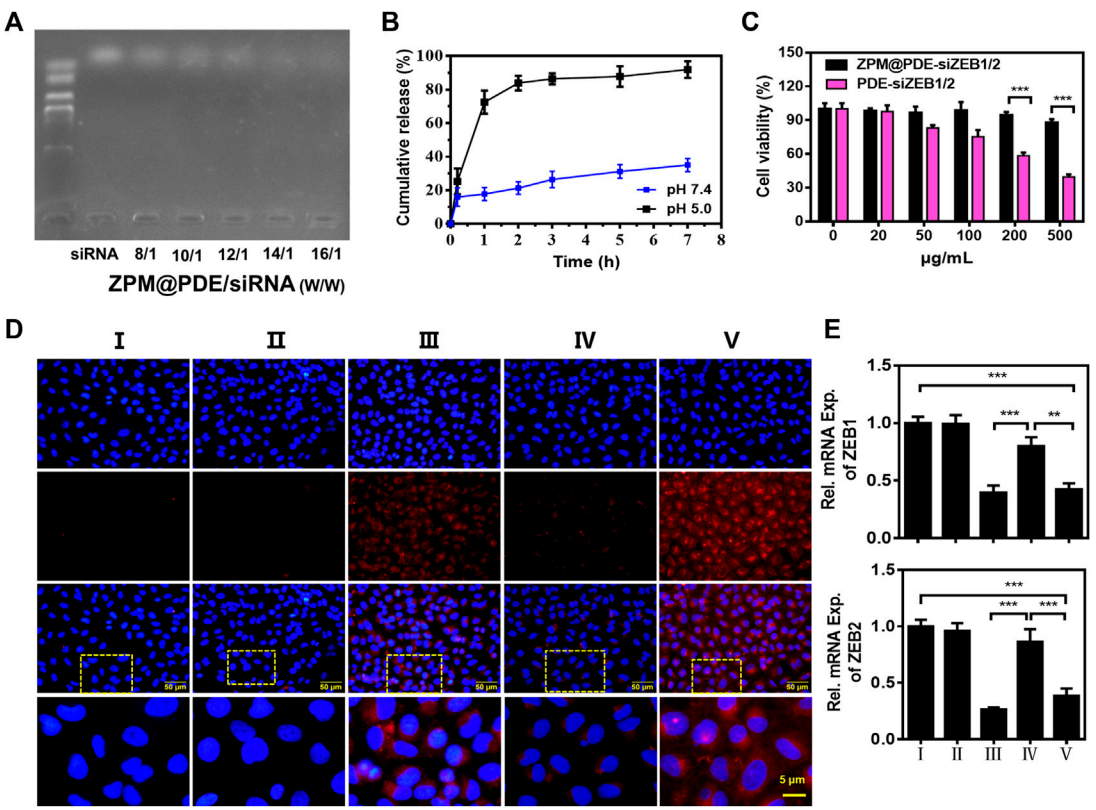

FIGURE 3 | (A) Gel retardation assay of ZPM@PDE/siZEB1/2 with different mass ratio, **(B)** siZEB1/2 release from ZPM@PDE-siZEB1/2 at pH 5.0 or pH 7.4 over time, **(C)** Cytotoxicity of PDE@siZEB1/2 and ZPM@PDE-siZEB1/2, **(D)** Uptake of ZPM@PDE-Cy5-siZEB1/2 (red) *in vitro*. Nuclei stained with DAPI nuclear dye (blue), and **(E)** Silencing efficacy of ZPM@PDE-siZEB1/2 *in vitro*. ($n = 3$, $^*p < 0.05$, $^{**}p < 0.01$, $^{***}p < 0.001$). For each group: **I**, Control; **II**, Naked CY5-siZEB1/2; **III**, Lip 2000-CY5-siZEB1/2; **IV**, ZPM@PDE-CY5-siZEB1/2 (pH 5.0); **V**, ZPM@PDE-CY5-siZEB1/2 (pH 7.4).

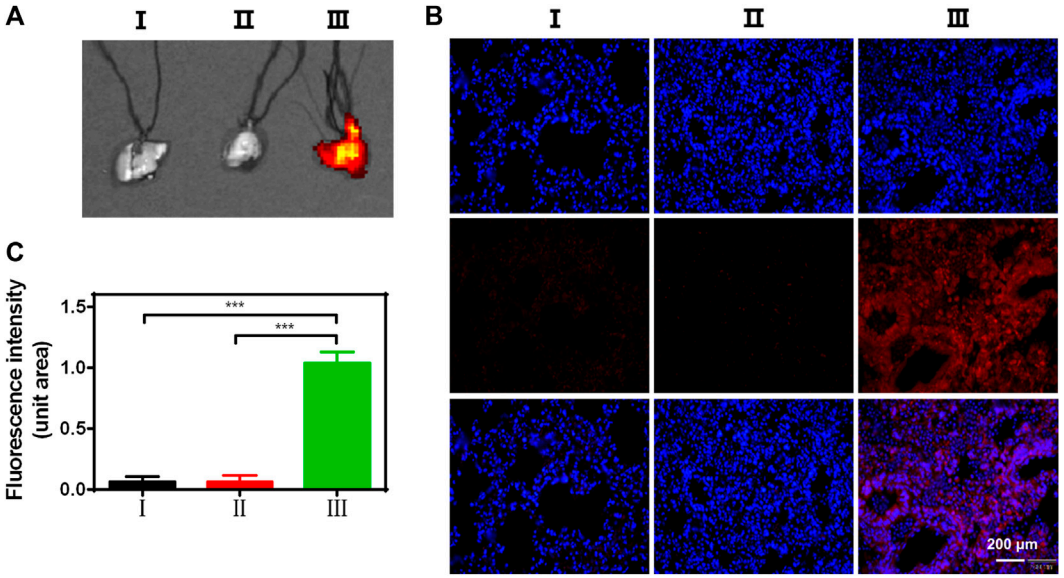

FIGURE 4 | (A) Fluorescent images of lungs, **(B)** Uptake of CY5-siZEB1/2 (red) in mice, and **(C)** The relative fluorescence intensity of CY5. Nuclei stained with DAPI nuclear dye (blue). For each group: I, Control; II, LPS + Naked CY5-siZEB1/2; III, LPS + ZPM@PDE-CY5-siZEB1/2.

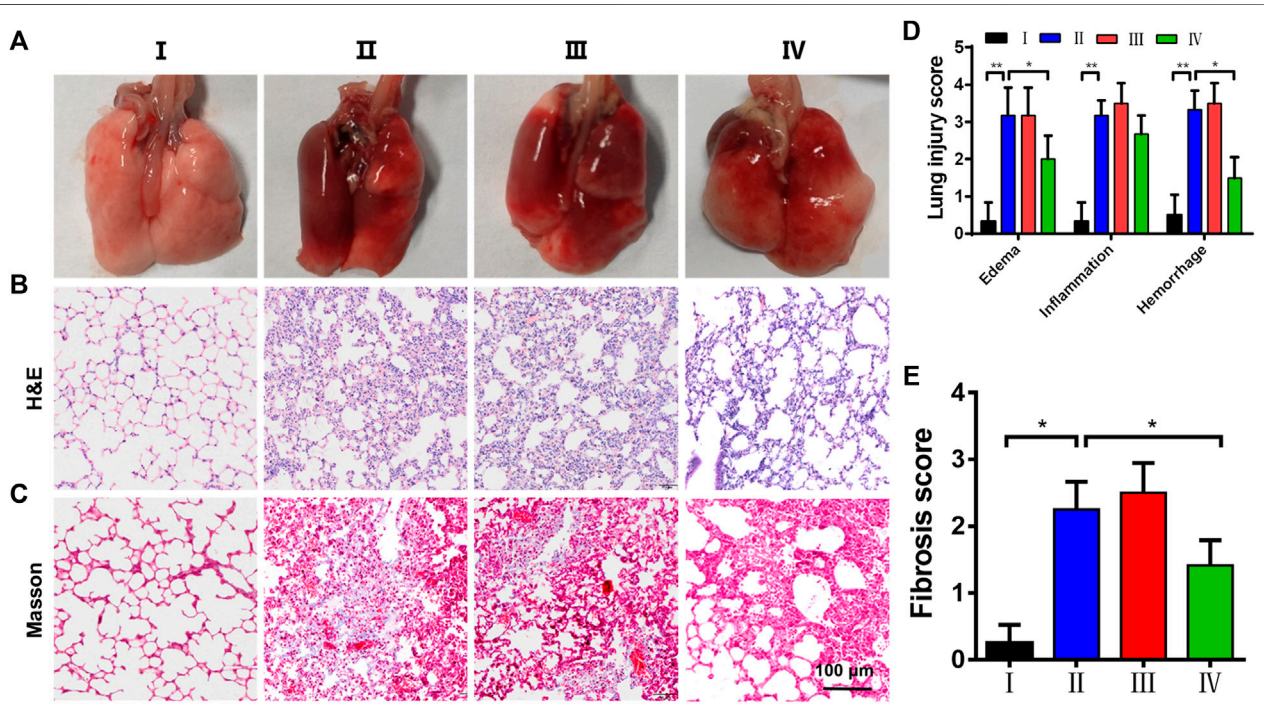

FIGURE 5 | The histopathological change of lung tissues. **(A)** Macroscopic appearance of lungs, **(B,C)** H&E and Masson's trichrome staining of lungs; **(D)** pulmonary injury score (Smith score); and **(E)** pulmonary fibrosis score (Aschoff score) from mice treated with saline (control), LPS, LPS + Naked siZEB1/2 and LPS + ZPM@PDE-siZEB1/2. (*$p < 0.05$, **$p < 0.01$, ***$p < 0.001$). For each group:I, Control; II, LPS; III, LPS + Naked siZEB1/2; IV, LPS + ZPM@PDE-siZEB1/2.

siZEB1/2-treated cells with the same concentration. This result verified that the ZPM outer layer improved the biocompatibility of the NMOF. Moreover, the ZPM@PDE-siZEB1/2 presented excellent biocompatibility with cell viability >87.9%, even when the concentration of ZPM@PDE-siZEB1/2 was up to 500 μg/ml. Similarly, the nanoscale ZMP exhibited enhanced cellular uptake and excellent biocompatibility for intracellular delivery of proteins in the research of Wang et al. (2019).

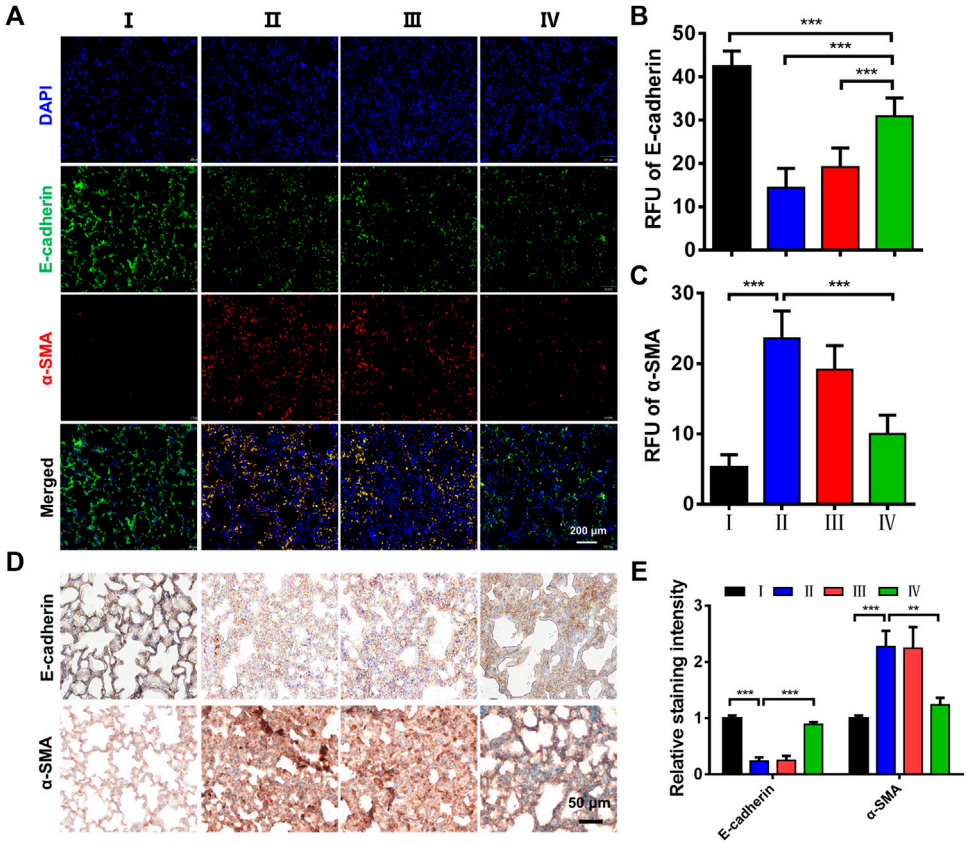

FIGURE 6 | Effects of ZPM@PDE-siZEB1/2 on the expression of E-cadherin and α-SMA in mice. **(A)** Immunofluorescence assays expression of E-cadherin (green) and α-SMA protein (red), nuclei stained with DAPI nuclear dye (blue), **(B,C)** The relative fluorescence unit (RFU) of E-cadherin and α-SMA, **(D)** Immunohistochemical analysis expression, and **(E)** The relative staining intensity of E-cadherin and α-SMA. (*$p < 0.05$, **$p < 0.01$, ***$p < 0.001$). For each group:I, Control; II, LPS; III, LPS + Naked siZEB1/2; IV, LPS + ZPM@PDE-siZEB1/2.

Next, the fluorophore Cy5-labeled siZEB1/2 was used to evaluate the cellular delivery of ZPM@PDE-siZEB1/2 at different pH levels (**Figure 3D**). ZPM@PDE-CY5-siZEB1/2-treated A549 cells exhibited higher cellular red fluorescence of Cy5-labeled siZEB1/2 at pH 7.4 than pH 5.0. When ZPM@PDE-siZEB1/2 are in the mild acidity condition (pH 5.0), PDEA segments can be quickly protonated resulting in siRNA release out of the cells, losing the ability to pass through cell membranes. The fluorescence signal of ZPM@PDE-CY5-siZEB1/2-treated A549 cells was similar to Lip2000-siZEB1/2-treated cells, which might ascribe indicate that the siRNA delivery system accelerated the endocytosis by interacting with anionic proteoglycans on the cell surface (Subhan and Torchilin 2020).

To investigate the gene silencing efficiency of siZEB1/2 deliver by ZPM@PDE-siZEB1/2, A549 cells were transfected with ZPM@PDE-siZEB1/2 at different pH levels and analyzed by real-time qPCR (**Figure 3E**). The ZPM@PDE-siZEB1/2 showed significantly lower ZEB1 and ZEB2 gene levels at pH 7.4 than pH 5.0. These data supported that ZPM@PDE-siZEB1/2 could efficiently deliver siZEB1/2 to cells and mediate gene silence, especially under physiological conditions.

ZPM@PDE-siZEB1/2 Delivers siZEB1/2 to the Lungs

In ALI/ARDS treatment, siRNAs have been previously confirmed as an effective nucleic acid-based therapy. However, siRNAs can be easily degraded by enzymes during transport progress (Jagrosse et al., 2019; Ge et al., 2020). Therefore, the delivery ability of siRNAs in the lungs is an important factor to evaluate an optimal siRNA delivery vector. To explore the lung delivery ability, ZPM@PDE-CY5-siZEB1/2 was inhaled by LPS-induced ALI mice and normal mice using the intratracheal quantitative drug delivery method. The lungs collected were imaged with an *in vivo* imaging system (**Figure 4A**). The LPS + ZPM@PDE-Cy5-siZEB1/2 group presented much stronger fluorescence in the lung compared to the LPS + Naked Cy5-siZEB1/2-treated group. The fluorescence of Cy5 was vividly observed in the LPS + ZPM@PDE-Cy5-siZEB1/2 group, indicating that siZEB1/2 was successfully delivered into the lungs. Meanwhile, the fluorophore Cy5-labeled siZEB1/2 was also identified in lung tissue sections (**Figures 4B,C**). Moreover, the tissue sections presented uniformly distributed high fluorescence intensity, demonstrating that the siZEB1/2 were also delivered to pulmonary local tissues including the depth part.

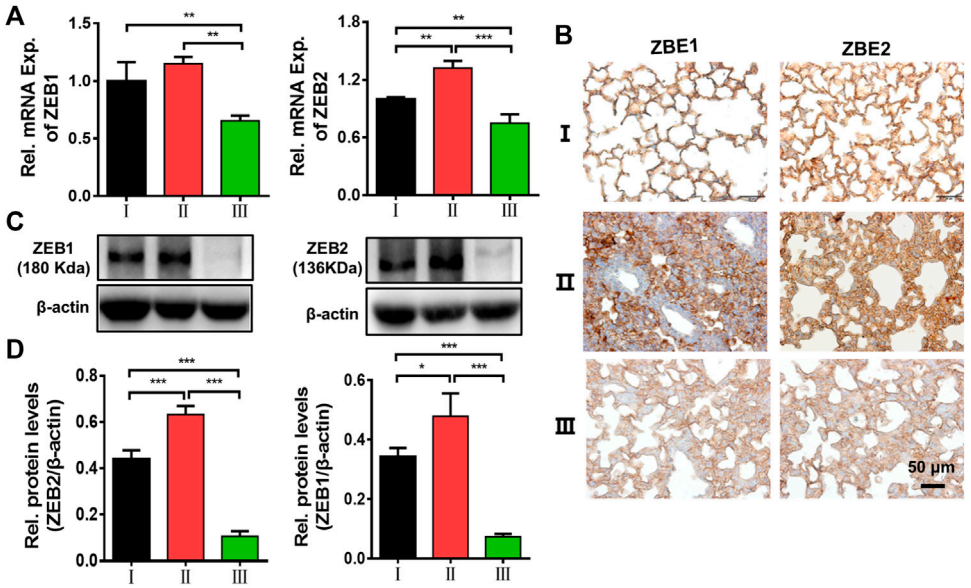

FIGURE 7 | Effects of ZEB1/2 silencing ability *in vivo*. **(A)** Immunohistochemical analysis expression of ZEB1/2 in mice lungs, **(B)** expression of ZEB1/2 were detected by quantitative RT-PCR, and **(C,D)** western blot analysis. (*$p < 0.05$, **$p < 0.01$, ***$p < 0.001$). For each group:**I**, Control; **II**, LPS + Naked siZEB1/2; **III**, LPS + ZPM@PDE-siZEB1/2.

ZPM@PDE-siZEB1/2 Alleviates Early Pulmonary Fibrosis in ALI Mice

Based on the siZEB1/2 could be effectively delivered to pulmonary local tissues, an ALI model was developed by intratracheal administration of LPS to evaluate the therapeutic function *in vivo*. The macroscopic observation of the lungs is shown in **Figure 5A**. In the control group, the lungs showed pink, soft, and clear texture, while the LPS and LPS + Naked siZEB1/2 groups showed dark red with obvious damage. While treated with ZPM@PDE-siZEB1/2, the symptoms were significantly alleviated. The histopathological change of lung tissues was examined using H&E and Masson staining (**Figures 5B,C**). H&E staining results showed that alveolar walls thickening, alveolar collapse, and inflammatory cell infiltration were obviously observed in LPS and LPS + Naked siZEB1/2 groups. In contrast, these pathological changes were significantly alleviated in LPS + ZPM@PDE-siZEB1/2 group. Consistently, the lung injury scores including edema, inflammation, and hemorrhage of LPS + ZPM@PDE-siZEB1/2 group were significantly lower than that of LPS and LPS + Naked siZEB1/2 groups, but there was no significant difference between LPS + ZPM@PDE-siZEB1/2 group and control group (**Figure 5D**). Moreover, Masson staining results revealed that a large number of collagen fibers appeared around the vessels and bronchi in LPS group, which indicated the typical pulmonary fibrosis formation. Treatment with ZPM@PDE-siZEB1/2 effectively rescued these changes. Similarly, the fibrosis score of LPS + ZPM@PDE-siZEB1/2 group was also lower than that of LPS group (**Figure 5E**). Collectively, These results revealed that simultaneous silencing of ZEB1 and ZEB2 in local lung tissue could alleviate LPS-induced early pulmonary fibrosis. For delivering siRNA to impede ZEB1 and ZEB2, PEI has been widely used to deliver siRNA in many fields due to its high gene condensation ability, quick endosome escape activity, and high transfection efficiency (Nimesh 2012; Sung and Kim 2020; Zoulikha et al., 2022). However, the positive charge of PEI with molecular weight-dependent cytotoxicity could led to apoptosis and necrosis of cells limiting its final use in the clinic (Nimesh et al., 2011; Cavallaro et al., 2017). RNA transfection reagent jetPEI could deliver paxillin siRNA AG975 by intratracheal administration to attenuate LPS-induced paxillin tyrosine phosphorylation and lung injury in mice (Fu et al., 2015). To improve the shortcomings of PEI in the use of ALI, we developed nanoscale MOFs with high porosity, high specific surface area, and good biocompatibility to cover PEI. MOFs have been proved to be an effective delivery carrier in the lungs (Zuo et al., 2020; Liu et al., 2022b).

Furthermore, the EMT plays a crucial role in the development of early pulmonary fibrosis, accompanied by the change of molecular biomarkers (Tellez et al., 2011; Nagaraja and Nagarajan 2018). The epithelial marker E-cadherin and mesenchymal marker α-SMA are well-accepted markers to evaluate the EMT. Herein, the immunofluorescence images showed that LPS treatment significantly decreased the levels of E-cadherin and increased the levels of α-SMA (**Figure 6A**). Meanwhile, the ZPM@PDE-siZEB1/2 treatment resulted in an E-cadherin increase and α-SMA decrease. The relative fluorescence unit (RFU) statistical analysis also showed an increase in E-cadherin and a decrease in α-SMA expression in the LPS + ZPM@PDE-siZEB1/2 group (**Figures 6B,C**). The immunohistochemical staining presented similar results

(**Figures 6D,E**). Overall, the abovementioned results together demonstrated that the ZPM@PDE-siZEB1/2 is effective and safe in treating the ALI by delaying EMT progress in the development of early pulmonary fibrosis.

Gene Silencing Ability of ZPM@PDE-siZEB1/2 in Lungs

In vitro and *in vivo* results have shown that our delivery system as a type of siRNA vector has a good anti-pulmonary fibrosis feature in ALI. Finally, the possible mechanism of action was examined. Real-time qPCR, immunohistochemical staining, and Western blotting for ZEB1/2 were performed on lung tissues. Firstly, we detected the mRNA levels of ZEB1 and ZEB2 to evaluate the gene regulation activity of ZPM@PDE-siZEB1/2 in the lungs (**Figure 7A**). The mRNA levels of ZEB1 and ZEB2 were significantly downregulated in the LPS + ZPM@PDE-siZEB1/2 group compared to the control and LPS + Naked siZEB1/2 groups. Then, the immunohistochemical staining results showed that the lung tissues were dark brown stained in LPS + Naked siZEB1/2 mice compared to controls (**Figure 7B**), indicating that both ZEB1 and ZEB2 were highly expressed in these lungs. Meanwhile, the LPS + ZPM@PDE-siZEB1/2 group presented lighter brown staining, indicating decreased expression of ZEB1 and ZEB2. At last, the protein levels of ZEB1/2 (**Figures 7C,D**) were consist with the results of real-time qPCR and immunohistochemical staining. Collectively, the ZEB1 and ZEB2 expression levels could be effectively inhibited after being treated with ZPM@PDE-siZEB1/2, which verified the superb ZEB1 and ZEB2 silencing capacity and efficiency of the ZPM@PDE-siZEB1/2 as a new strategy for promising ALI treatment. After cellular entry, the entrapped siRNA/siRNA-carrier vesicles can be transported to early endosomes that mature into late endosomes (pH 4.0–6.5), then enter into lysosomes (pH ~ 4.5) containing nucleases and other degradative enzymes (Zoulikha et al., 2022). Thus, ZPM@PDE-siZEB1/2 could enter cells via endocytosis and rapidly escape from endo/lysosomes via proton sponge effect of PDEA segments and osmolarity disruption effect of ZPM on the endosomal membrane. Then, the released siZEB1/2 could effectively knock down the level of ZEB1/2. ZEB1 and ZEB2 both are important regulators in the regulation of E-cadherin expression and EMT (Chilosi et al., 2017). When EMT occurs, the expression of E-cadherin was decreased, while the expression of ZEB1/2 was increased (Cao et al., 2018). EMT appeared in the early stage of pulmonary fibrosis caused by ALI, so silencing ZEB1/2 could alleviate early LPS-induced pulmonary fibrosis in ALI.

CONCLUSION

In summary, we developed a novel NMOFs-based non-viral vector system to deliver siRNA for ALI treatment, which could protect the siRNA from enzymatic degradation in stable physiological pH 7.4 and decrease the cytotoxicity of bPEI. This system could effectively deliver siZEB1/2 into A549 cells for siRNA transfection and gene silencing. Besides, in ALI model mice, intratracheal administration of ZPM@PDE-siZEB1/2 could simultaneously deliver siZEB1 and siZEB2 into the inflammatory lung and effectively silence ZEB1/2, thereby delaying the progression of LPS-induced early pulmonary fibrosis in ALI mice. We did not only demonstrate that ZEB1/2 is a therapy target for ALI but also developed a promising siRNA delivery system for inflamed lung delivery to attenuate the progression of early pulmonary fibrosis during ALI. Finally, our delivery system might also have great potential in the treatment of COVID-19 infection-induced ALI/ARDS, inflammatory-related diseases, and tumors.

DATA AVAILABILITY STATEMENT

The original contributions presented in the study are included in the article/**Supplementary Material**; further inquiries can be directed to the corresponding authors.

ETHICS STATEMENT

The animal study was reviewed and approved by the Ethics Committee of Third Military Medical University (Army Medical University).

AUTHOR CONTRIBUTIONS

CW: investigation, methodology, formal analysis, and writing—original draft. GL and DZ: methodology and investigation. ZD: methodology, investigation, and validation. KC and JZ: data curation and investigation. TL: conceptualization, methodology, writing—original draft, and writing—review and editing. JW: conceptualization, funding acquisition, supervision, and writing—review and editing.

FUNDING

This research was funded by the National Natural Science Foundation of China, grant number 81671945.

ACKNOWLEDGMENTS

The authors thank Knorigene Technologies (Chongqing, China) for providing gene analysis.

SUPPLEMENTARY MATERIAL

The Supplementary Material for this article can be found online at: https://www.frontiersin.org/articles/10.3389/fbioe.2022.939312/full#supplementary-material

REFERENCES

Aranda-Valderrama, P., and Kaynar, A. M. (2018). The Basic Science and Molecular Mechanisms of Lung Injury and Acute Respiratory Distress Syndrome. *Int. Anesthesiol. Clin. Winter* 56, 1–25. doi:10.1097/aia.0000000000000177

Beitler, J. R., Thompson, B. T., Baron, R. M., Bastarache, J. A., Denlinger, L. C., Esserman, L., et al. (2022). Advancing Precision Medicine for Acute Respiratory Distress Syndrome. *Lancet Respir. Med.* 10, 107–120. doi:10.1016/s2213-2600(21)00157-0

Bian, S., Cai, H., Cui, Y., Liu, W., and Xiao, C. (2021). Nanomedicine-Based Therapeutics to Combat Acute Lung Injury. *Ijn* Vol. 16, 2247–2269. doi:10.2147/ijn.s300594

Burnham, E. L., Janssen, W. J., Riches, D. W. H., Moss, M., and Downey, G. P. (2014). The Fibroproliferative Response in Acute Respiratory Distress Syndrome: Mechanisms and Clinical Significance. *Eur. Respir. J.* 43, 276–285. doi:10.1183/09031936.00196412

Cao, Y., Liu, Y., Ping, F., Yi, L., Zeng, Z., and Li, Y. (2018). miR-200b/c Attenuates Lipopolysaccharide-Induced Early Pulmonary Fibrosis by Targeting ZEB1/2 via P38 MAPK and TGF-B/smad3 Signaling Pathways. *Lab. Invest.* 98, 339–359. doi:10.1038/labinvest.2017.123

Carrillo-Carrión, C. (2020). Nanoscale Metal-Organic Frameworks as Key Players in the Context of Drug Delivery: Evolution toward Theranostic Platforms. *Anal. Bioanal. Chem.* 412, 37–54. doi:10.1007/s00216-019-02217-y

Cavallaro, G., Sardo, C., Craparo, E. F., Porsio, B., and Giammona, G. (2017). Polymeric Nanoparticles for siRNA Delivery: Production and Applications. *Int. J. Pharm.* 525, 313–333. doi:10.1016/j.ijpharm.2017.04.008

Chen, L., Liu, P., Feng, X., and Ma, C. (2017). Salidroside Suppressing LPS-Induced Myocardial Injury by Inhibiting ROS-Mediated PI3K/Akt/mTOR Pathway *In Vitro* and *In Vivo*. *J. Cell. Mol. Med.* 21, 3178–3189. doi:10.1111/jcmm.12871

Chen, Q., Yang, Y., Huang, Y., Pan, C., Liu, L., and Qiu, H. (2013). Angiotensin-(1-7) Attenuates Lung Fibrosis by Way of Mas Receptor in Acute Lung Injury. *J. Surg. Res.* 185, 740–747. doi:10.1016/j.jss.2013.06.052

Chilosi, M., Caliò, A., Rossi, A., Gilioli, E., Pedica, F., Montagna, L., et al. (2017). Epithelial to Mesenchymal Transition-Related Proteins ZEB1, β-catenin, and β-tubulin-III in Idiopathic Pulmonary Fibrosis. *Mod. Pathol.* 30, 26–38. doi:10.1038/modpathol.2016.147

Dai, L. L., Cai, R. S., Li, M. H., Luo, Z., Yu, Y. L., Chen, W. Z., et al. (2017). Dual-Targeted Cascade-Responsive Prodrug Micelle System for Tumor Therapy *In Vivo*. *Chem. Mater* 16, 6976–6992. doi:10.1021/acs.chemmater.7b02513

Dai, L. L., Li, K., Li, M. H., Zhao, X. J., Luo, Z., Lu, L., et al. (2018). Size/Charge Changeable Acidity-Responsive Micelleplex for Photodynamic-Improved PD-L1 Immunotherapy with Enhanced Tumor Penetration. *Adv. Funct. Mat. May* 4, 28. doi:10.1002/adfm.201707249

Fan, E., Brodie, D., and Slutsky, A. S. (2018). Acute Respiratory Distress Syndrome. *Jama* 319, 698–710. doi:10.1001/jama.2017.21907

Feng, J., Yu, W., Xu, Z., Hu, J., Liu, J., and Wang, F. (2020). Multifunctional siRNA-Laden Hybrid Nanoplatform for Noninvasive PA/IR Dual-Modal Imaging-Guided Enhanced Photogenetherapy. *ACS Appl. Mat. Interfaces* 12, 22613–22623. doi:10.1021/acsami.0c04533

Fernandez-Francos, S., Eiro, N., Gonzalez-Galiano, N., and Vizoso, F. J. (2021). Mesenchymal Stem Cell-Based Therapy as an Alternative to the Treatment of Acute Respiratory Distress Syndrome: Current Evidence and Future Perspectives. *Int. J. Mol. Sci. Jul* 22, 22. doi:10.3390/ijms22157850

Fu, P., Usatyuk, P. V., Lele, A., Harijith, A., Gregorio, C. C., Garcia, J. G. N., et al. (2015). c-Abl Mediated Tyrosine Phosphorylation of Paxillin Regulates LPS-Induced Endothelial Dysfunction and Lung Injury. *Am. J. Physiology-Lung Cell. Mol. Physiology* 308, L1025–L1038. doi:10.1152/ajplung.00306.2014

Ge, C., Yang, J., Duan, S., Liu, Y., Meng, F., and Yin, L. (2020). Fluorinated α-Helical Polypeptides Synchronize Mucus Permeation and Cell Penetration toward Highly Efficient Pulmonary siRNA Delivery against Acute Lung Injury. *Nano Lett.* 20 (20), 1738–1746. doi:10.1021/acs.nanolett.9b04957

He, C., Lu, K., Liu, D., and Lin, W. (2014). Nanoscale Metal-Organic Frameworks for the Co-delivery of Cisplatin and Pooled siRNAs to Enhance Therapeutic Efficacy in Drug-Resistant Ovarian Cancer Cells. *J. Am. Chem. Soc.* 136 (136), 5181–5184. doi:10.1021/ja4098862

Horiguchi, K., Sakamoto, K., Koinuma, D., Semba, K., Inoue, A., Inoue, S., et al. (2012). TGF-β Drives Epithelial-Mesenchymal Transition through δEF1-mediated Downregulation of ESRP. *Oncogene* 31, 3190–3201. doi:10.1038/onc.2011.493

Hu, B., Zhong, L., Weng, Y., Peng, L., Huang, Y., Zhao, Y., et al. (2020). Therapeutic siRNA: State of the Art. *Sig Transduct. Target Ther.* 5, 101. doi:10.1038/s41392-020-0207-x

Huang, S., Zhu, W., Zhang, F., Chen, G., Kou, X., Yang, X., et al. (2021). Silencing of Pyruvate Kinase M2 via a Metal-Organic Framework Based Theranostic Gene Nanomedicine for Triple-Negative Breast Cancer Therapy. *ACS Appl. Mat. Interfaces* 13, 56972–56987. doi:10.1021/acsami.1c18053

Hui Li, H., Shaohui Du, S., Lina Yang, L., Yangyan Chen, Y., Wei Huang, W., Rong Zhang, R., et al. (2009). Rapid Pulmonary Fibrosis Induced by Acute Lung Injury via a Lipopolysaccharide Three-Hit Regimen. *Innate Immun.* 15, 143–154. doi:10.1177/1753425908101509

Jagrosse, M. L., Dean, D. A., Rahman, A., and Nilsson, B. L. (2019). RNAi Therapeutic Strategies for Acute Respiratory Distress Syndrome. *Transl. Res.* 214, 30–49. doi:10.1016/j.trsl.2019.07.011

Kaku, S., Nguyen, C. D., Htet, N. N., Tutera, D., Barr, J., Paintal, H. S., et al. (2020). Acute Respiratory Distress Syndrome: Etiology, Pathogenesis, and Summary on Management. *J. Intensive Care Med.* 35, 723–737. doi:10.1177/0885066619855021

Kandil, R., and Merkel, O. M. (2019). Pulmonary Delivery of siRNA as a Novel Treatment for Lung Diseases. *Ther. Deliv.* 10, 203–206. doi:10.4155/tde-2019-0009

Kawami, M., Yumoto, R., and Takano, M. (2022). Preventive Approach against Drug-Induced Pulmonary Fibrosis through the Suppression of Epithelial-Mesenchymal Transition. *Biocell. Feb* 24. doi:10.32604/biocell.2022.019667

Kole, R., Krainer, A. R., and Altman, S. (2012). RNA Therapeutics: beyond RNA Interference and Antisense Oligonucleotides. *Nat. Rev. Drug Discov.* 11, 125–140. doi:10.1038/nrd3625

Liu, J., Cordova Wong, B. J., Liu, T., Yang, H., Yao Ye, L., and Lei, J. (2022a). Glutathione-Responsive Heterogeneous Metal-Organic Framework Hybrids for Photodynamic-Gene Synergetic Cell Apoptosis. *Chem. Mar.* 20, e202200305.

Liu, Y., Zhou, P., Cao, Z., Liang, W., Yan, J., Xu, H., et al. (2022b). Simultaneous Solubilization and Extended Release of Insoluble Drug as Payload in Highly Soluble Particles of γ-cyclodextrin Metal-Organic Frameworks. *Int. J. Pharm.* 619, 121685. doi:10.1016/j.ijpharm.2022.121685

Matthay, M. A., Zemans, R. L., Zimmerman, G. A., Arabi, Y. M., Beitler, J. R., Mercat, A., et al. (2019). Acute Respiratory Distress Syndrome. *Nat. Rev. Dis. Prim.* 5, 18. doi:10.1038/s41572-019-0069-0

Matthay, M. A., McAuley, D. F., and Ware, L. B. (2017). Clinical Trials in Acute Respiratory Distress Syndrome: Challenges and Opportunities. *Lancet Respir. Med.* 5, 524–534. doi:10.1016/s2213-2600(17)30188-1

Merckx, P., De Backer, L., Van Hoecke, L., Guagliardo, R., Echaide, M., Baatsen, P., et al. (2018). Surfactant Protein B (SP-B) Enhances the Cellular siRNA Delivery of Proteolipid Coated Nanogels for Inhalation Therapy. *Acta Biomater.* 78 (78), 236–246. doi:10.1016/j.actbio.2018.08.012

Nagaraja, S. S., and Nagarajan, D. (2018). Radiation-Induced Pulmonary Epithelial-Mesenchymal Transition: A Review on Targeting Molecular Pathways and Mediators. *Cdt* 19, 1191–1204. doi:10.2174/1389450119666180207092234

Nimesh, S., Gupta, N., and Chandra, R. (2011). Cationic Polymer Based Nanocarriers for Delivery of Therapeutic Nucleic Acids. *J. Biomed. Nanotechnol.* 7, 504–520. doi:10.1166/jbn.2011.1313

Nimesh, S. (2012). Polyethylenimine as a Promising Vector for Targeted siRNA Delivery. *Ccp* 7, 121–130. doi:10.2174/157488412800228857

Qiao, Q., Liu, X., Yang, T., Cui, K., Kong, L., Yang, C., et al. (2021). Nanomedicine for Acute Respiratory Distress Syndrome: The Latest Application, Targeting Strategy, and Rational Design. *Acta Pharm. Sin. B* 11, 3060–3091. doi:10.1016/j.apsb.2021.04.023

Saeed, R. M., Abdullah, M., Ahram, M., and Taha, M. O. (2021). Novel Ellipsoid Chitosan-Phthalate Lecithin Nanoparticles for siRNA Delivery. *Front. Bioeng. Biotechnol.* 9, 695371. doi:10.3389/fbioe.2021.695371

Smith, K. M., Mrozek, J. D., Simonton, S. C., Bing, D. R., Meyers, P. A., Connett, J. E., et al. (1997). Prolonged Partial Liquid Ventilation Using Conventional and

High-Frequency Ventilatory Techniques. *Crit. Care Med.* 25, 1888–1897. doi:10.1097/00003246-199711000-00030

Subhan, M. A., and Torchilin, V. (2020). siRNA Based Drug Design, Quality, Delivery and Clinical Translation. *Nanomedicine Nanotechnol. Biol. Med.* 29, 102239. doi:10.1016/j.nano.2020.102239

Sung, Y. K., and Kim, S. W. (2020). Recent Advances in Polymeric Drug Delivery Systems. *Biomater. Res.* 24, 12. doi:10.1186/s40824-020-00190-7

Tellez, C. S., Juri, D. E., Do, K., Bernauer, A. M., Thomas, C. L., Damiani, L. A., et al. (2011). EMT and Stem Cell-like Properties Associated with miR-205 and miR-200 Epigenetic Silencing Are Early Manifestations during Carcinogen-Induced Transformation of Human Lung Epithelial Cells. *Cancer Res.* 71 (71), 3087–3097. doi:10.1158/0008-5472.CAN-10-3035

Wang, S., Chen, Y., Wang, S., Li, P., Mirkin, C. A., and Farha, O. K. (2019). DNA-functionalized Metal-Organic Framework Nanoparticles for Intracellular Delivery of Proteins. *J. Am. Chem. Soc.* 13141, 2215–2219. doi:10.1021/jacs.8b12705

Weng, Y., Xiao, H., Zhang, J., Liang, X.-J., and Huang, Y. (2019). RNAi Therapeutic and its Innovative Biotechnological Evolution. *Biotechnol. Adv.* 37, 801–825. doi:10.1016/j.biotechadv.2019.04.012

Wittrup, A., and Lieberman, J. (2015). Knocking Down Disease: a Progress Report on siRNA Therapeutics. *Nat. Rev. Genet.* 16, 543–552. doi:10.1038/nrg3978

Zhang, Y.-Q., Liu, Y.-J., Mao, Y.-F., Dong, W.-W., Zhu, X.-Y., and Jiang, L. (2015). Resveratrol Ameliorates Lipopolysaccharide-Induced Epithelial Mesenchymal Transition and Pulmonary Fibrosis through Suppression of Oxidative Stress and Transforming Growth Factor-B1 Signaling. *Clin. Nutr.* 34, 752–760. doi:10.1016/j.clnu.2014.08.014

Zhao, D., Zhang, W., Wu, Z. H., and Xu, H. (2022). Nanoscale Metal-Organic Frameworks and Their Nanomedicine Applications. *Front. Chem. Jan.* 24, 9.

Zhou, W., Mo, X., Cui, W., Zhang, Z., Li, D., Li, L., et al. (2016). Nrf2 Inhibits Epithelial-Mesenchymal Transition by Suppressing Snail Expression during Pulmonary Fibrosis. *Sci. Rep.* 6 (6), 38646. doi:10.1038/srep38646

Zhu, J., Guo, M., Cui, Y., Meng, Y., Ding, J., Zeng, W., et al. (2022). Surface Coating of Pulmonary siRNA Delivery Vectors Enabling Mucus Penetration, Cell Targeting, and Intracellular Radical Scavenging for Enhanced Acute Lung Injury Therapy. *ACS Appl. Mat. Interfaces* 14, 5090–5100. doi:10.1021/acsami.1c23069

Zhuang, J., Gong, H., Zhou, J., Zhang, Q., Gao, W., Fang, R. H., et al. (2020). Targeted Gene Silencing *In Vivo* by Platelet Membrane-Coated Metal-Organic Framework Nanoparticles. *Sci. Adv.* 6, eaaz6108. doi:10.1126/sciadv.aaz6108

Zhuang, J., Kuo, C.-H., Chou, L.-Y., Liu, D.-Y., Weerapana, E., and Tsung, C.-K. (2014). Optimized Metal-Organic-Framework Nanospheres for Drug Delivery: Evaluation of Small-Molecule Encapsulation. *ACS Nano* 8, 2812–2819. doi:10.1021/nn406590q

Zoulikha, M., Xiao, Q., Boafo, G. F., Sallam, M. A., Chen, Z., and He, W. (2022). Pulmonary Delivery of siRNA against Acute Lung Injury/acute Respiratory Distress Syndrome. *Acta Pharm. Sin. B* 12, 600–620. doi:10.1016/j.apsb.2021.08.009

Zuo, J., Yuan, Y., Zhao, M., Wang, J., Chen, Y., Zhu, Q., et al. (2020). An Efficient Electrochemical Assay for miR-3675-3p in Human Serum Based on the Nanohybrid of Functionalized Fullerene and Metal-Organic Framework. *Anal. Chim. Acta* 1140, 78–88. doi:10.1016/j.aca.2020.10.017

Conflict of Interest: The authors declare that the research was conducted in the absence of any commercial or financial relationships that could be construed as a potential conflict of interest.

Publisher's Note: All claims expressed in this article are solely those of the authors and do not necessarily represent those of their affiliated organizations, or those of the publisher, the editors, and the reviewers. Any product that may be evaluated in this article, or claim that may be made by its manufacturer, is not guaranteed or endorsed by the publisher.

frontiers | Frontiers in Bioengineering and Biotechnology

ORIGINAL RESEARCH
published: 15 August 2022
doi: 10.3389/fbioe.2022.917368

Multifunctional PEGylated Niosomal Nanoparticle-Loaded Herbal Drugs as a Novel Nano-Radiosensitizer and Stimuli-Sensitive Nanocarrier for Synergistic Cancer Therapy

Saeid Afereydoon[1], Fateme Haghiralsadat[2,3], Nima Hamzian[1], Ali Shams[4]*, Mahdie Hemati[3,5], Seyed Morteza Naghib[6,7]*, Masoud Shabani[8], Behrouz Zandieh-doulabi[9] and Davood Tofighi[10]*

[1]Department of Medical Physics, School of Medicine, Shahid Sadoughi University of Medical Sciences, Yazd, Iran, [2]Department of Advanced Medical Sciences and Technologies, School of Paramedicine, Shahid Sadoughi University of Medical Sciences, Yazd, Iran, [3]Medical Nanotechnology and Tissue Engineering Research Center, Yazd Reproductive Sciences Institute, Shahid Sadoughi University of Medical Sciences, Yazd, Iran, [4]Department of Immunology, School of Medicine, Shahid Sadoughi University of Medical Sciences, Yazd, Iran, [5]Department of Clinical Biochemistry, Faculty of Medicine, Shahid Sadoughi University of Medical Sciences, Yazd, Iran, [6]Nanotechnology Department, School of Advanced Technologies, Iran University of Science and Technology (IUST), Tehran, Iran, [7]Biomaterials and Tissue Engineering Department, Breast Cancer Research Center, Motamed Cancer Institute, ACECR, Tehran, Iran, [8]Department of Radiation Oncology, School of Medicine, Shahid Sadoughi University of Medical Sciences, Yazd, Iran, [9]Department of Oral Cell Biology, Academic Centre for Dentistry Amsterdam (ACTA), University of Amsterdam and Vrije Universiteit Amsterdam, Amsterdam Movement Sciences, Amsterdam, Netherlands, [10]Epidemiology and Research Design Support (BERD), Clinical and Translational Science Center, Department of Psychology, University of New Mexico, Albuquerque, NM, United States

OPEN ACCESS

Edited by:
Chih-Chia Huang,
National Cheng Kung University,
Taiwan

Reviewed by:
Mehdi Dadashpour,
Semnan University of Medical Sciences, Iran
Cheng-I Lee,
National Chung Cheng University,
Taiwan

***Correspondence:**
Seyed Morteza Naghib
naghib@iust.ac.ir
Nima Hamzian
Hamzian.nima@gmail.com
Ali Shams
alis743@yahoo.com

Specialty section:
This article was submitted to Nanobiotechnology, a section of the journal Frontiers in Bioengineering and Biotechnology

Received: 11 April 2022
Accepted: 26 May 2022
Published: 15 August 2022

Citation:
Afereydoon S, Haghiralsadat F, Hamzian N, Shams A, Hemati M, Naghib SM, Shabani M, Zandieh-doulabi B and Tofighi D (2022) Multifunctional PEGylated Niosomal Nanoparticle-Loaded Herbal Drugs as a Novel Nano-Radiosensitizer and Stimuli-Sensitive Nanocarrier for Synergistic Cancer Therapy. Front. Bioeng. Biotechnol. 10:917368. doi: 10.3389/fbioe.2022.917368

Nowadays, radiotherapy is one of the most effective treatments for breast cancer. In order to overcome the radioresistance of cancer cells, radio-sensitizing agents can be used combined with irradiation to increase the therapeutic efficiency. Curcumin can enhance the radiosensitivity of cancer cells and decrease their viability by the accumulation of these cells in the G2 phase. The encapsulation of curcumin in a nanoniosomal delivery system increases aqueous solubility and bioavailability, resulting in increased radio sensitivity. The present study aimed to enhance the radio-sensitizing effect of the curcumin-containing nanoniosome (Cur-Nio) when combined with irradiation. Thus, curcumin (0.5 mg ml^{-1}) was loaded on a PEGylated nanoniosome containing Tween 60, cholesterol, DOTAP, and 1,2-distearoyl-sn-glycero-3-phosphoethanolamine-poly(ethylene glycol) (DSPE-PEG) (at ratios of 70:30:10:5, respectively) by the thin-film hydration method. The particle size, zeta potential, entrapment efficiency, and drug-release rate of formulated nanoniosomes were determined. In order to assess cytotoxicity and apoptosis, different doses of irradiation along with various concentrations of free curcumin and Cur-Nio (single or in combination with irradiation) were treated with breast cancer cells. The particle size and zeta potential of Cur-Nio were reported to be 117.5 nm and −15.1 mV, respectively. The entrapment efficiency (EE%) and loading capacities were 72.3% and 6.68%, respectively. The drug-release rate during 6 h was 65.9%. Cell survival in the presence of curcumin at doses of 1 and 3 Gy showed a significant reduction compared with cells irradiated at 48 h and 72 h ($p < 0.000$). Also, the rate of cytotoxicity and apoptosis was significantly higher in

cells treated with the combination of curcumin-containing nanoniosomes and irradiation in comparison with those treated with free curcumin. These findings indicate that the efficacy of pre-treatment with Cur-Nio as a radiosensitizer during radiotherapy enhances irradiation-induced breast cancer cell apoptosis and is a useful strategy to increase the effectiveness of breast cancer therapy.

Keywords: niosome nanoparticles, irradiation, curcumin, radiosensitizing, breast cancer

INTRODUCTION

Irradiation therapy (Yi et al., 2021; Zhao et al., 2021), chemotherapy (Jiang et al., 2021; Li et al., 2021), surgery (Cui et al., 2021), and hormone therapy (Im et al., 2019) are the most common therapies used for the treatment of breast cancer. Nowadays, radiotherapy is used as first-line therapy in patients with breast cancer depending on the grade of the tumor used alone or along with surgery or chemotherapy (Garg et al., 2005). The main goal of radiotherapy is established on reducing the side effects on normal tissues by minimizing the irradiation dose while providing the maximum efficiency to induce cell death in tumors (Crokart et al., 2005). The combination of chemotherapeutic agents with some chemical radio-sensitizers increases the rate of targeted therapies (Goel & Aggarwal, 2010). The use of synthetic radio-sensitizers can cause nausea, vomiting, hypotension, and allergic reactions due to their toxicity, even in daily prescribed doses. Therefore, it is still necessary to identify new, non-toxic, effective, and suitable compounds to increase radiation sensitivity. Plants, as non-toxic (or low-toxic) agents, are readily available and appear to be the ideal low-cost solution. Curcumin is a potent chemosensitizer known as a radio-sensitizing agent in various types of cancer. It seems that the radiosensitizing effects of curcumin are mediated *via* the inhibition of NF-κB activity in colon cancer (Kunnumakkara et al., 2008; Hamzian et al., 2017; Hamzian et al., 2019), reducing the signaling pathways of AP-1 and NF-κB in brain cancer (Dhandapani et al., 2007), downregulation of Bcl-2 and MDM2 proteins in prostate cancer (Li et al., 2007; Ghaffari et al., 2021), reduction of extracellular regulated kinases (ERK1 and 2), overexpression of the epidermal growth factor receptor (EGFR) in skin cancer (Park & Lee, 2007), and suppression of cells in the G2/M cell cycle phase in squamous cell carcinoma (Khafif et al., 2005). Overall, these investigations suggest that the combination of curcumin with irradiation is a potential treatment to increase the effectiveness of treatment regimens on breast cancers. On the other hand, curcumin is hydrophobic and insoluble in water and is poorly absorbed by the intestine, leading to the limited bioavailability and concentration of this compound in the serum after oral administration (Liu et al., 2016; Abtahi N. A. et al., 2021; Yaghoubi et al., 2021). In order to overcome these challenges, nanotechnology has provided a multifunctional nano-delivery system, which acts as a drug carrier, improving the *in vivo* stability, bioavailability, and biodistribution of curcumin (Sim & Wong, 2021). Nanoparticles may consist of silver, gold, and iron oxide nanoparticles (metallic nanoparticles) or could be made of liposome, noisome, and micelle (lipid nanoparticles). These nanoparticles are able to be loaded with different hydrophilic and hydrophobic compounds. Metallic nanoparticles play an important role in radiosensitization as a result of having a high atomic number (Z) of metals, photoelectric absorption, and the production of hydroxyl radicals (Butterworth et al., 2013; Siddique & Chow, 2020). Encapsulation of curcumin in the form of nanoparticles at the nanoscale size leads to increased biocompatibility, cellular internalization, and water solubility, whereas decreases the side effects of the loaded compound in the process of cancer treatment. Several studies have demonstrated the radiosensitivity potential of curcumin encapsulated in metallic and lipidic nanoparticles (Minafra et al., 2019; Gao et al., 2022); however, the impact of curcumin-containing nanoniosomes on the radiosensitivity of cancer cells has not been evaluated. Niosomes have considerable advantages, including acceptable stability, long-lasting stability in the bloodstream, small size, high encapsulation efficacy, no special condition for the storage process, and low cast. In this study, to boost pharmacological properties, curcumin was encapsulated in the form of nanoniosomes, which are bilayer non-ionic surfactant-based vehicles. These particles are stable, non-toxic, and biodegradable at the nanoscale size and could be employed as a novel drug delivery system (Kalantari et al., 2019). Tween 60, with hydrophilic-lipophilic balance (HLB) of 14.9, is not appropriate as the main surfactant for the formulation of curcumin-containing nanoniosomes. So the presence of cholesterol in niosomal compounds provides high physical stability for these nanoparticles (Abtahi N. A. et al., 2021).

The current study evaluated the radiosensitizing effect of nanoniosomes containing curcumin. For this purpose, we developed cationic PEGylated nanoniosome-containing curcumin with high entrapment efficiency (EE%), nanoscale size, and a controlled release profile. In our study, the breast cancer cell line (MCF-7) was irradiated with ionizing beams in the presence or absence of Cur-Nio. The MTT assay and flow cytometry were applied to evaluate cell viability and apoptosis between cells treated with free curcumin and cationic PEGylated nanoniosome-containing curcumin (**Figure 1**).

MATERIALS AND METHODS

The thin-film hydration method was used to synthesize nanoliposomes containing curcumin with desired vesicle size, high entrapment efficiency, and the controlled release rate. Cholesterol (Sigma-Aldrich, United States), DOTAP, Tween 60 (DaeJung Chemicals & Metals, South Korea), and DSPE-PEG2000 (Ludwigshafen, Germany) were dissolved in chloroform. Curcumin (Sigma-Aldrich, United States) at a

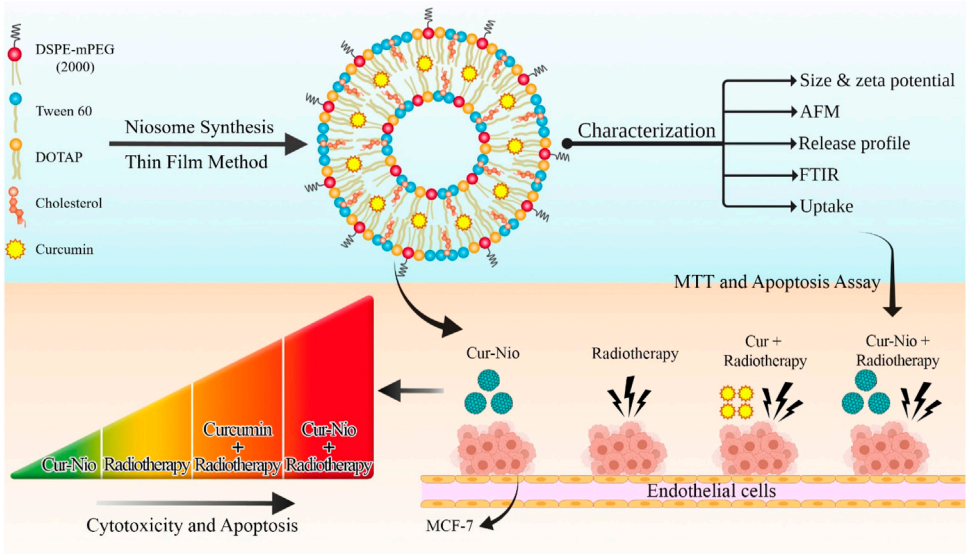

FIGURE 1 | Schematic view of synthesizing the PEGylated niosomal nanoformulation based on Tween 60, cholesterol, DOTAP, and DSPE-PEG at ratios of 70:30: 10:5, respectively. The process of curcumin encapsulation was performed by the thin-film hydration method and then used in combination with radiotherapy.

concentration of 0.5 mg/ml was dissolved in methanol and poured into a container. In order to evaluate cellular uptake, 0.1% M of the fluorescent label Dil (Sigma, United States) was added to the lipid phase. The organic solvent was eliminated by using a rotary evaporator (Heidolph, Germany) at 45°C to form a dried lipid thin film. After that, it was hydrated with a suitable volume of phosphate-buffered saline for 60 min at 60°C. Sonication was performed using a microtip probe sonicator (model UP200St, Hielscher Ultrasonics GmbH, Germany) on ice for 30 min to reduce the particle size. Finally, a dialysis membrane (M.W. = 12 kDa, Sigma-Aldrich, United States) was utilized to separate the free drug from niosomal vesicles.

Particle Size and Zeta-Potential Values

The range of particle size distribution, as well as the peak particle size, was assessed by the dynamic light scattering (DLS) technique (the Brookhaven Instruments Corp). Nanoniosomes were diluted in distilled water and measured at an angle of 90°, and the laser light was emitted at a wavelength of 657 nm at 25 ± 1°C. Zeta potential values (ζ-potential) were evaluated at 25 ± 1°C by using a zeta-sizer instrument (the Brookhaven Instruments Corp).

Drug-Loading Capacity and Entrapment Efficiency Determination

The standard concentrations of curcumin were prepared by dissolving a serial concentration of curcumin in isopropanol, and their absorption was detected by using a UV-VIS spectrophotometer (model T80+, P.G. Instruments, United Kingdom) at 429 nm. Also, nanoniosome-containing curcumin was dissolved in isopropanol with a certain dilution, and its absorption was obtained using a spectrophotometer at 429 nm. The entrapment efficiency of curcumin in nanoniosome was calculated based on the low formula using a standard curve:

EE % = drug concentration in nanocarrier ($mg.ml^{-1}$)/total drug ($mg.ml^{-1}$) ×100.

The loading capacity of curcumin was evaluated by using a UV-Vis spectrophotometer (Perkin Elmer Germany) at 429 nm as follows:

LC % = mass of drug in nanocarrier (mg)/mass of nanocarrier (mg)× 100.

In Vitro Drug Release Study

The *in vitro* release profile of nanoniosome-containing curcumin was measured using a dialysis bag with a molecular weight cut-off of 12,000–14,000 kDa against PBS while being stirred on a magnetic stirrer for 72 h at 37°C (pH = 7.4). In order to calculate the drug-released profile at different times, the dialysis medium was collected and immediately exchanged for an equal volume of the fresh PBS. The absorbance of specimens was measured at 429 nm using a UV–VIS spectrophotometer. Based on the total concentration of niosomal drugs, the release percentage at different time intervals was calculated.

Fourier Transform Infrared Spectroscopy

The characterization of functional groups and chemical interactions between curcumin and nanoniosome components was analyzed by Fourier transform infrared (FTIR) spectroscopy (Model 8300, Shimadzu Corporation, Tokyo, Japan). The FTIR spectrum was analyzed at the wavelength range of 400–4000 cm^{-1} in samples dispersed in KBr pellets.

Irradiation Procedures

The source-to-axis distance (SAD) irradiations were conducted in a 20 × 20 cm^2 field, with the gantry angle being 180 and 5 cm deep

TABLE 1 | Characterization of blank nanoniosomes and Cur-Nio.

Formula	Lipid (molar ratio%) cholestrol: Tween 60	DOTAP (%)	DSPE-PEG (%)	Size (nm)	PDI	Zeta potential (mV)	EE (%)	LC (%)	Release (6 h)%
Blank nanoniosome	30:70	10	5	108.7	0.305	-20.1	-	-	-
Cur-Nio	30:70	10	5	117.5	0.423	-15.1	72	6.68	65.9%

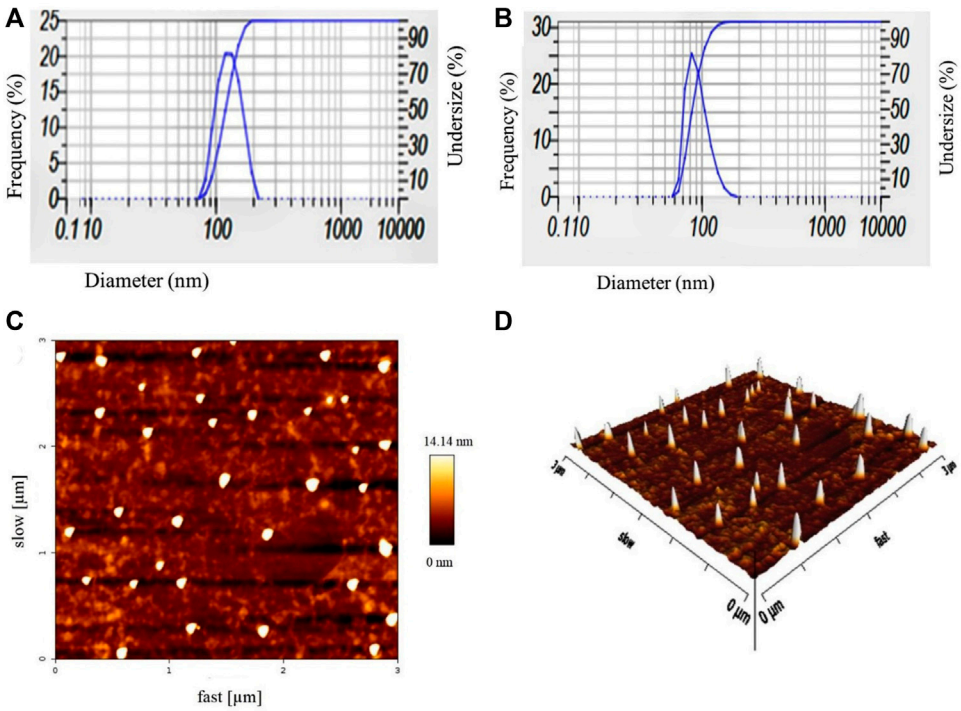

FIGURE 2 | Particle size distribution and zeta potential values of blank nanoniosomes **(A)** and Cur-Nio **(B)**. Two-dimensional **(C)** and three-dimensional **(D)** AFM images of Cur-Nio.

in solid phantom equivalent to tissue. The monitor unit was performed by Panther three-dimensional treatment design software version 5.2 (Prowess-USA). In order to optimize the dosimetry condition, central wells of the plate were used for cell culture as much as possible, and the culture medium was added to empty wells. Then, irradiation was performed using X-rays of a linear accelerator photon beam (Compact-Electa, England) to assess the irradiation efficacy, thereby creating a dose-dependent curve (1, 3, 5, and 7 Gy).

Cell Culture

Human breast cancer (MCF-7), lung cancer (A549), osteosarcoma (Saos2), and prostate cancer (PC3) cell lines were purchased from the Pasteur Institute, Tehran, Iran. They were grown in DMEM (Dulbecco's modified Eagle's medium, Gibco, Dublin, Ireland) supplemented with 10% fetal bovine serum (FBS Gibco) and 100 U/ml penicillin-streptomycin (Gibco) in a 5% CO_2 incubator at 37°C.

Cellular Uptake of Nanoniosome–Containing Curcumin

In order to determine and compare the cellular uptake behavior of Cur-Nio and free curcumin, MCF7, A549, Saos2, and PC3 cells were seeded on to 6-well plates at a density of 1.5×10^5 cells/well. Then, the cells were incubated with free curcumin, Cur-Nio (20 µg ml^{-1}), and blank nanoniosomes. After 3 h, cells were washed twice with fresh cold PBS (pH 7.4) and fixed with the 96% ethanol solution. The nuclei were counterstained with DAPI (0.15 µg ml^{-1}, Thermo Fisher Scientific, United States) and

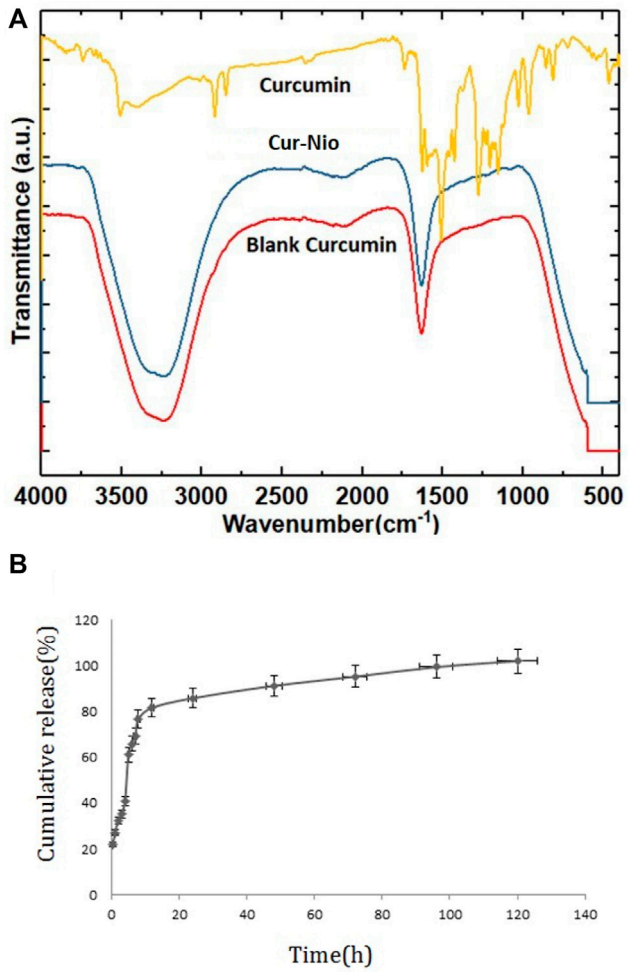

FIGURE 3 | FTIR spectra; a comparison of free curcumin, Cur-Nio, and blank nanoniosome **(A)**. The *in vitro* release profile of curcumin from the nanoniosome system **(B)**.

visualized under a fluorescence microscope (BX61, Olympus, Japan).

Cytotoxicity Assay

In order to examine whether curcumin could be considered a radio-sensitizing agent, the cytotoxicity effects of irradiation with or without curcumin and Cur-Nio on MCF7 cells were evaluated. The inhibitory concentration (IC10) of drugs, a concentration without obvious drug toxicity, and the lethal dose (LD50) of radiation, as a minimum dose with the highest efficacy and no toxicity, were determined. To this aim, 10^4 cells were seeded onto a 96-well plate with five replicates for each treatment. After 24 h, the different doses of irradiation (1, 3, 5, and 7 Gy) or Cur-Nio at different concentrations (2, 5, 10, 20, 40, 80, and 100 μg ml^{-1}) were treated with cancer cell lines. For combinational therapy, Cur-Nio at a dose of 20 μg ml^{-1} (IC10) or free curcumin was treated with cell lines for 24 h before being irradiated at doses of 1 and 3 Gy (LD50). Untreated cells were considered the control cells. Finally, after 48 and 72 h of incubation, the cell culture media were removed, and 100 μl of the MTT solution [10 μl of the MTT reagent (0.5 mg/ml) + 90 μl culture media] was added to each well and incubated for 4 h at room temperature. The formazan crystals were dissolved in 150 μl DMSO. The absorbance of each well was read by using a spectrophotometer (Synergy HTX, Bio-Tek, Winooski, VT) instrument at a wavelength of 570 nm. The cell viability rate of different treatments was calculated compared with the control group.

Apoptosis Analysis

In order to examine the effect of curcumin-loaded nanoniosome and irradiation, either alone or in combination, Annexin-V and propidium iodide assays were carried out. In brief, in each well, 4×10^4 MCF-7 cells were seeded onto a 24-well microplate. After 24 h, cells were divided into nine groups. In group 1, MCF-7 cells were left without being exposed to any treatments; MCF-7 cells in groups 2 and 3 were irradiated at doses of 1 and 3 Gy, respectively. In groups 4 and 5, MCF-7 cells were incubated with curcumin and Cur-Nio at a concentration of 20 μg/ml, respectively. In groups 6 and 7, MCF-7 cells were treated with curcumin and Cur-Nio at a concentration of 20 μg/ml and irradiated at a dose of 1 Gy. In groups 8 and 9, MCF-7 cells were treated with curcumin and Cur-Nio at a concentration of 20 μg/ml and irradiated at a dose of 3 Gy, following pretreatment. After 24 and 72 h, the total cells were isolated by 0.05% trypsin/EDTA, centrifuged, and rinsed in 100 μl binding buffer. Then, the cells were suspended with Annexin V-FITC and propidium iodide (P.I.) as fluorescent dyes and incubated in a dark place without light for 20 min. The samples were analyzed by using a flow cytometer (B.D. Biosciences, United States).

Statistical Analysis

The results were analyzed by GraphPad Prism version 8 software, and the obtained values were represented as the means and standard deviation (mean ± SD). The independent t-test was applied to compare two groups, while a one-way analysis of variance (ANOVA) was used to compare multiple groups. A *p*-value of less than 0.05 was considered a statistically significant difference.

RESULTS

Characterization of Synthesized Nanoparticles

The DLS analysis determined the mean hydrodynamic diameter, polydispersity index (PDI) of blank nanoniosomes, and Cur-Nio. As shown in **Table 1** and **Figures 2A,B**, blank nanoniosomes and Cur-Nio exhibit average diameters of 117.5 and 108.7 nm and PDI values of 0.403 and 0.305, respectively. The zeta potential values of the blank nanoniosomes and Cur-Nio are shown in **Figure 2**. The great extent of the negative zeta potential and anionic nanoparticles enhanced the potential stability of the nanosystem solution. The two-dimensional, three-dimensional, and surface morphology of Cur-Nio were characterized by atomic force microscopy (AFM) (**Figures 2C,D**). All results were in

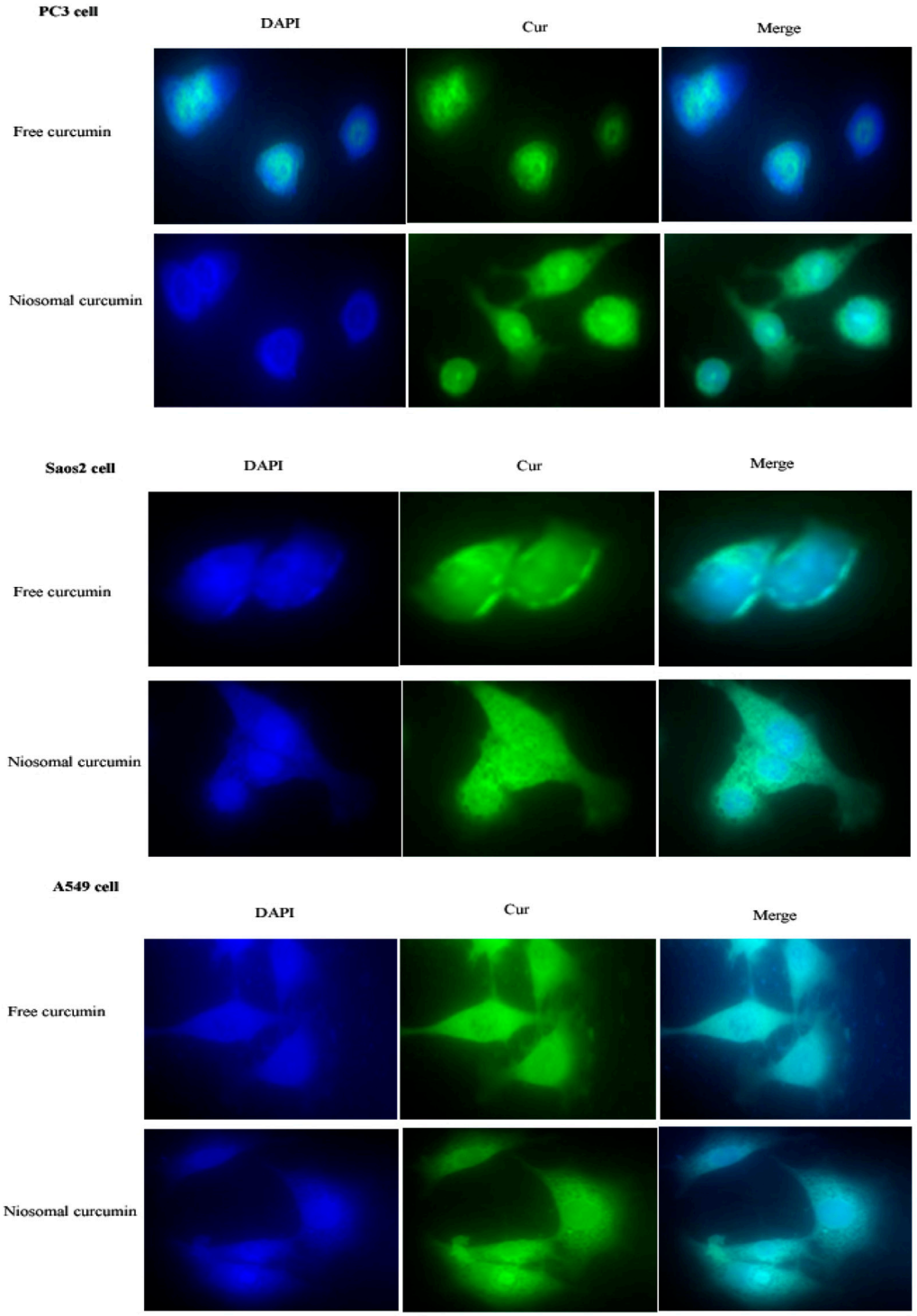

FIGURE 4 | (Continued).

accordance with the findings of the DLS analysis. The chemical structure of compounds in the synthesized nanoniosome and curcumin, as well as the molecular interaction of curcumin with a lipid membrane of nanoniosomes, was applied by FTIR spectroscopy. **Figure 3A** illustrates the FTIR spectra of the free curcumin. The absorption bands at 3510 cm^{-1} were assigned for the O–H stretching bond; the absorption peak at 1509 cm^{-1} corresponds to the aromatic ring, C=C stretching, and

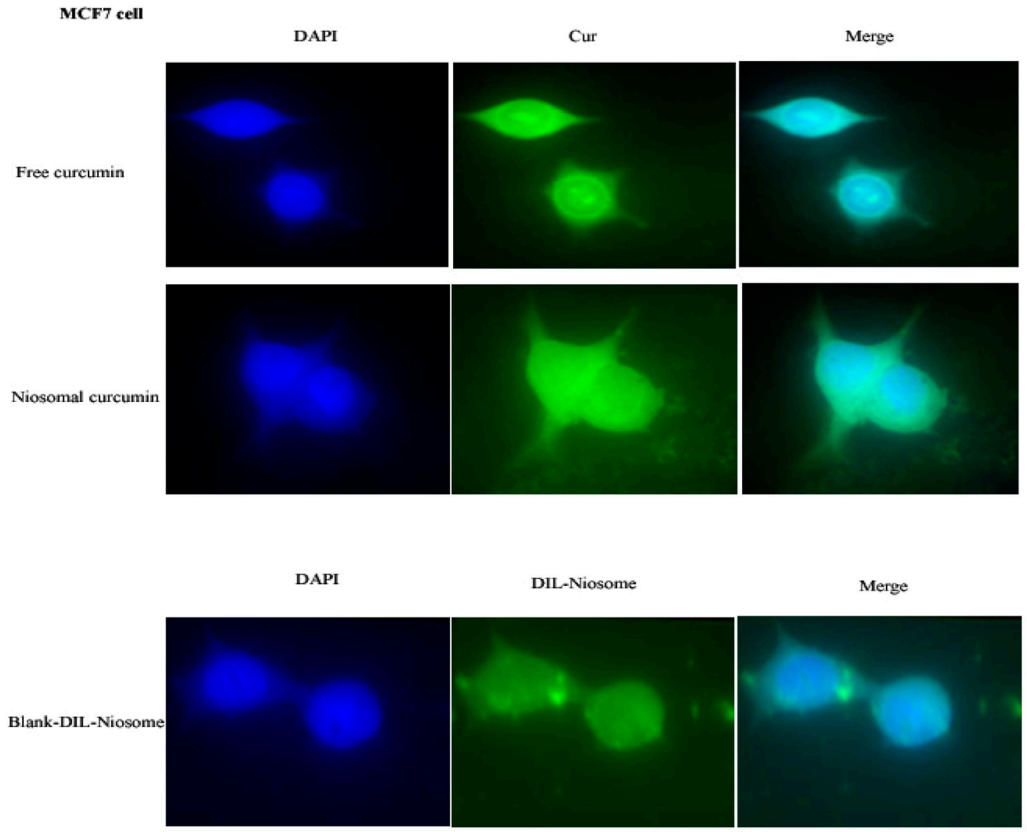

FIGURE 4 | (Continued). Cellular uptake of the free curcumin, Cur-Nio, and blank-DIL-niosomes on PC3, $SaOs_2$, A549, and MCF7 cell lines (×60 magnification).

C=O stretching bonds at 1155 cm^{-1}. The absorption peak at 1155cm^{-1} was assigned to the C–H stretching bond in the curcumin molecule. The blank nanoniosome exhibits various peaks of FTIR patterns for DOTAP, Tween-60, cholesterol, and DSPE-mPEG in a range of 4000–500 cm^{-1} (**Figure 3A**). The peak at 3243 cm^{-1} was assigned to the existence of the O–H stretching bond in phenols and N–H stretching in 2°-amines of cholesterol and Tween-60. The carbonyl group in Tween-60, DOTAP, and DSPE-mPEG demonstrated a strong peak at 1632 cm^{-1}, corresponding to the C=O stretching vibration.

Additional drug bands were not visible in the FTIR diagram of nanoniosomes. This phenomenon results from the complete encapsulation of curcumin in niosomal spherical nanocarriers, and therefore, the functional groups of these compounds are masked. On the other hand, long fatty acid chains with abundant hydrocarbon functional groups overlap and eliminate other functional groups. Curcumin encapsulated in nanocarrier membranes did not form any chemical interactions between curcumin and PEGylated niosomes. Also, the loading of curcumin on PEGylated niosomes did not affect its structural characterization. The *in vitro* curcumin release from nanoniosomes was evaluated using the dialysis bag method against the PBS buffer at 37°C. As exhibited in **Figure 3B**, the release of loaded drugs was 65.9% after 6 h. The cumulative release profile of curcumin showed a biphasic pattern, the first phase with an initial burst release period followed by a slower release rate in the second phase.

Nanoniosomal Curcumin Cellular Uptake Experiments

The cellular uptake of PEGylated nanoniosomes was assessed by fluorescence microscopy to evaluate and compare the penetration and localization of the free curcumin and Cur-Nio. The fluorescence images of niosome uptake were taken after 3 h of continuous exposure of niosomes to the cells. As depicted in **Figure 4**, the intensity of green and cyan colors of nanoniosomal curcumin in cancer cells was much higher than that of the free curcumin. These findings exhibit that the amounts of Cur-Nio formulations inside cancer cells were significantly higher than those of the free curcumin. These results were in accordance with cytotoxicity and radio-sensitization results. Also, **Figure 4** represents the successful internalization of DIL-labeled niosomes into cells.

Cytotoxicity of the Modified Curcumin-Loaded Nanoniosomes

In order to examine whether there was a radio-sensitive effect in the use of free curcumin or Cur-Nio along with irradiation, the

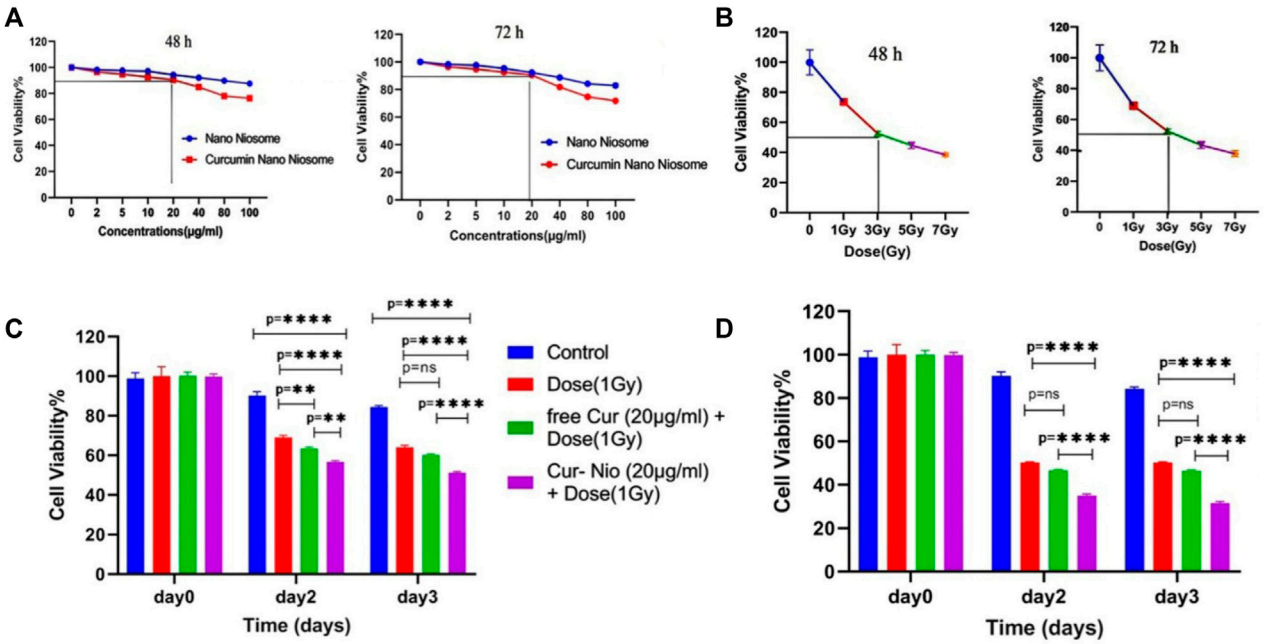

FIGURE 5 | Viability of MCF7 cells treated with blank nanoniosomes and Cur-Nio at 48 and 72 h **(A)**. Dose-response curves of MCF7 cells that were exposed to increasing irradiation doses at 48 and 72 h **(B)**. The viability of MCF7 cells treated with irradiation with or without 20 μg ml^{-1} of free-Cur **(C)** and Cur-Nio. **(D)** NS stands for "not statistically significant;" $^{**}p < 0.01$ and $^{****}p < 0.0001$.

TABLE 2 | Comparison of dose enhancement ratios (DER) between the free curcumin and Cur-Nio at a single dose of 3 Gy after 48 h.

Therapeutic group	Dose (3 Gy)	*p*-value	DER (3 Gy)
Control	52.53	-	-
Free curcumin	46.58	0.0003	1.12
Cur-Nio	34.96	≤0.0001	1.50

TABLE 3 | Comparison of dose enhancement ratios (DER) between the free curcumin and Cur-Nio at a single dose of 3 Gy after 72 h.

Therapeutic group	Dose (3 Gy)	*p*-value	DER (3 Gy)
Control	50.14	-	-
Free curcumin	46.37	0.0003	1.07
Cur-Nio	31.66	≤0.0001	1.57

MTT assay was conducted. The LD50 value was calculated from the ir radiation dose-response curves acquired by the increase in concentrations of irradiation, using a second-order polynomial fitting analysis. The MTT assay exhibited that blank nanoniosomes had no significant cytotoxic effects on MCF-7 cells at concentrations used (**Figure 5A**). In order to assay the IC10 value of Cur-Nio and LD50 of irradiation against MCF7 cells, a dose-response experiment was performed. The IC10 value of Cur-Nio and the LD50 value of irradiation were reported to be 20 μg ml^{-1} (**Figure 5A**) and 3 Gy (**Figure 5B**), respectively. As shown in **Figures 5C,d**, cell death and radio-sensitization effect were increased, following irradiation with Cur-Nio compared with exposure to 1 and 3 Gy ($p < 0.05$) alone. This result demonstrates that curcumin plays a major role in radio-sensitizing and irradiation-induced cell death. In the combined treatments, the level of cell viability is always significantly lower than that observed in samples exposed to irradiation alone, indicating the efficacy of the nano-delivery system in the potent induction of radio-sensitization. Also, a comparison of the dose enhancement ratios (DERs) of the free curcumin and Cur-Nio was calculated after 48 and 72 h at a dose of 3Gy irradiation. As illustrated in **Tables 2**, **3**, such a ratio was 1.5 folds higher in Cur-Nio than that of the free curcumin after 48 and 72 h.

Apoptosis Assay

Flow cytometry was used to evaluate the percentage of apoptosis and necrosis in MCF7 cells exposed to irradiation using a 6-MV linear accelerator at doses of 1 and 3 Gy alone or in combination with the free curcumin or Cur-Nio as radio-sensitizing agents after 24 and 48 h. The Annexin V-FITC marker was used for the assessment of apoptosis, while the P.I. dye was applied for the evaluation of necrosis. The percentages of necrotic and apoptotic cells, along with statistical analysis obtained from the application of different doses and incubation periods of 48 and 72 h, are shown in **Figures 6**, **7**. As shown in **Figures 8A,B**, irradiation caused apoptosis in 1.98 ± 0.06% and 2.56 ± 0.08% of cells when utilized at a dose of 1 Gy and 3 Gy for 24 h, respectively. Such percentages were 1.98 ± 0.06% and 2.11 ± 0.11% of cells irradiated with 1 Gy and 3 Gy for 48 and 72 h, respectively. The treatment of MCF-7 cells with the free curcumin (20 μg ml^{-1}) caused apoptosis

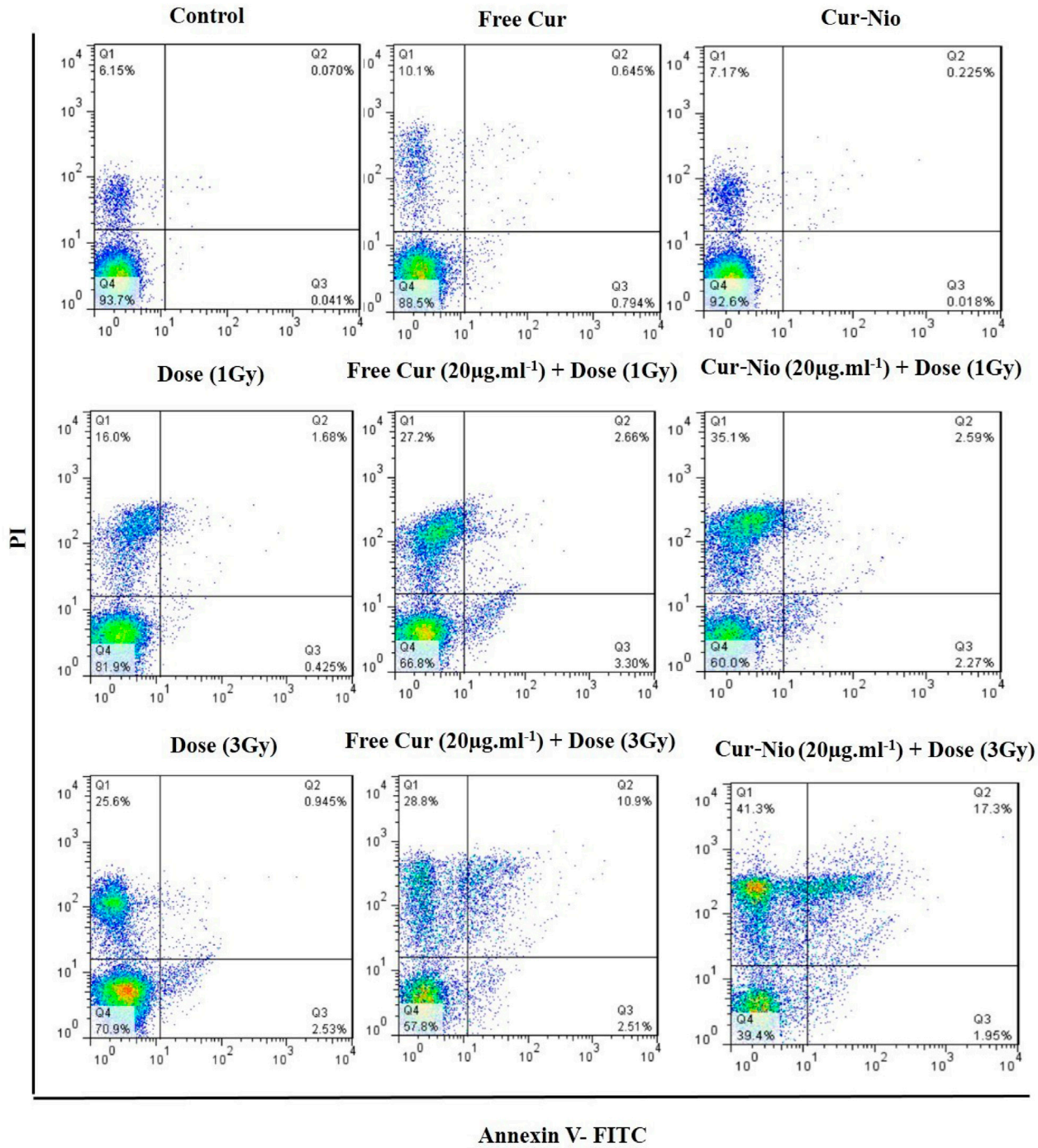

FIGURE 6 | Apoptosis assay using flow cytometry, following treatment of cells at 48 h.

in 1.37 ± 0.12% and 1.32 ± 0.12% of cells irradiated with 1 Gy and 3 Gy at 24 h. Such percentages were reported to be 1.31 ± 0.07% and 1.45 ± 0.10% when the cells were exposed to Cur-Nio at 48 and 72 h, respectively. The combination therapy of cells with 20 µg ml^{-1} free curcumin and irradiation at a dose of 1 Gy showed 2.58 ± 0.08% and 2.55 ± 0.09% apoptosis rates at 24 h. The apoptosis rates at a dose of 3 Gy were reported to be 3.25 ± 0.09% and 3.55 ± 0.11% at 48 and 72 h, respectively. The apoptosis percentages of the combined treatment of cancer cells with irradiation and Cur-Nio at a dose of 1 Gy were reported to be 3.25 ± 0.10% and 3.11 ± 0.08%, while at a dose of 3 Gy, such percentages were 4.03 ± 0.05% and 4.11 ± 0.08% at 48 and 72 h, respectively (**Figures 8A,B**). The results illustrated that the combination of irradiation with radio-sensitizing agents

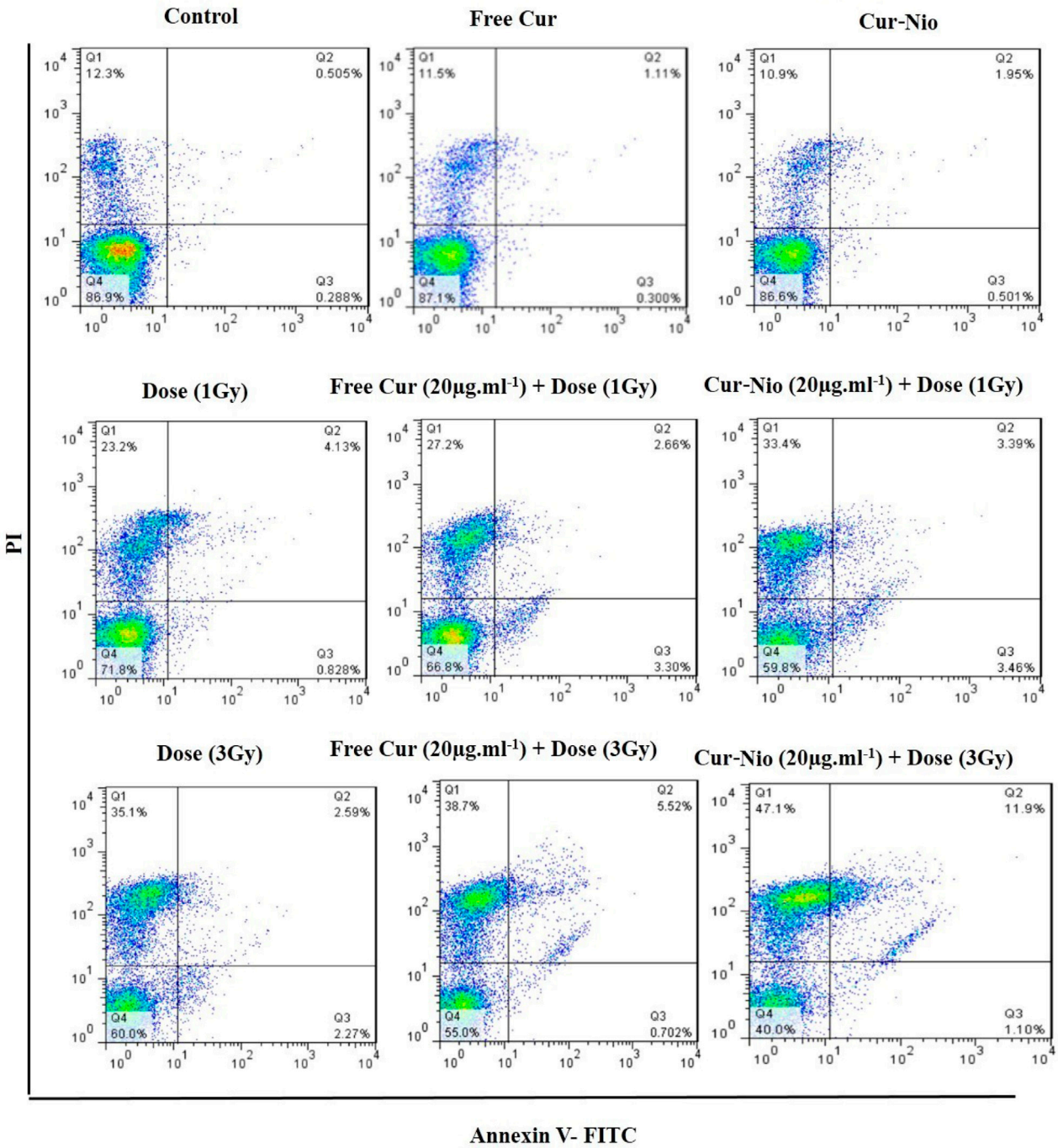

FIGURE 7 | Apoptosis assay using flow cytometry, following treatment of cells at 72 h.

significantly increased apoptosis in cancer cells compared with the single use of each treatment. In addition, the rate of apoptosis was significantly higher in cells exposed to the encapsulated form of curcumin than that in the free form. Moreover, as shown in **Figures 8C,D**, the necrosis ratios were almost 1.4 folds at 1 Gy and 1.2 fold at 3 Gy for 48 h. Such ratios were 1.3 fold at 1 Gy and 1.2 fold at 3 Gy for 72 h when the cells were treated by the combination of irradiation and nanoniosome-containing curcumin compared with cells exposed to irradiation alone. The necrosis ratios of cells exposed to irradiation and free curcumin were 1.2 folds at 1 Gy and 1.1 fold at 3 Gy for 48 h. Also, such ratios were 1.1 fold at 1 Gy and 1.0 fold at 3 Gy for 72 h. On the other hand, the necrosis ratios of cells treated with Cur-Nio and irradiation were almost 1.2 fold at 1 Gy and one fold at 3 Gy compared with those exposed to free curcumin for 48 h. These results displayed not only higher percentages of apoptosis

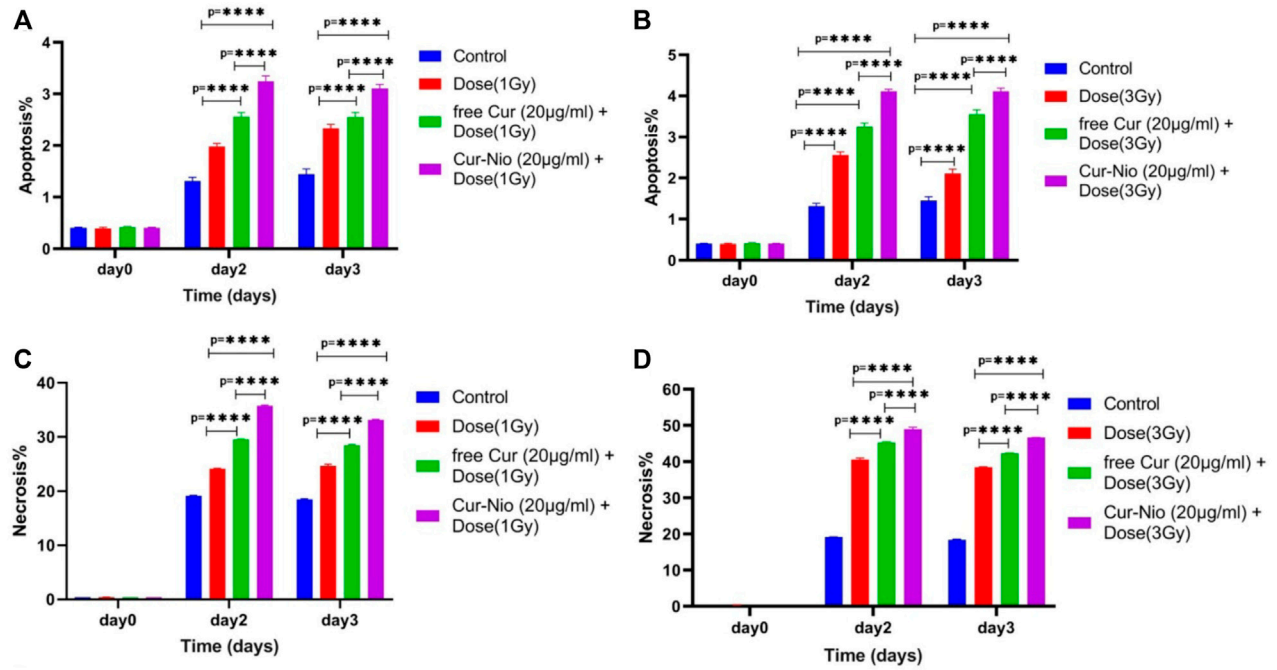

FIGURE 8 | Apoptosis rate of MCF7 cells treated with irradiation at doses of **(A)** 1 Gy and **(B)** 3 Gy with or without 20 μg ml^{-1} of the free curcumin and Cur-Nio (****$p < 0.0001$). The necrosis rate of MCF7 cells treated with irradiation doses of **(A)** 1 Gy and **(B)** 3 Gy with or without 20 μg ml^{-1} of the free curcumin and Cur-Nio (****$p < 0.0001$).

and necrosis in cells exposed to the combination of irradiation and irradiation-sensitizing agents but also showed higher efficacy of irradiation doses (1 Gy vs. 3 Gy) and encapsulated form of curcumin in the induction of cell death in cancer cells.

DISCUSSION

The radioresistance of breast cancer cells leads to the neutralization of irradiation therapy as an adjuvant treatment. Studies demonstrated that curcumin is a radio-protectant agent with antioxidant activity and is known as a radio-sensitizing agent that damages the mitochondrial membrane and induces apoptosis in cancer cells (Chendil et al., 2004; Khafif et al., 2005; Girdhani et al., 2009). The main purpose of our study was to examine the effects of pre-treatment of curcumin-loaded PEGylated nanoniosome as a radiosensitizing agent, followed by irradiation on the MCF-7 cell line in comparison to free curcumin. First, we characterized the curcumin-loaded PEGylated nanoniosome using various techniques. The mean diameter of nanoparticles was almost 100 nm at the nanoscale size, which facilitates their entry to the blood barrier and increases their concentrations in cancer cells (Hemati et al., 2019b). The zeta potential value was reported to be negative, and there was an electrostatic repulsion between vesicles resulting in the stability and homogeneity of nanoniosomes (Chen et al., 2012; Spirou et al., 2018). Also, the accordance of AFM images with DLS results showed rounded and smooth shapes with rigid boundary nanostructures in the synthesized nanoniosomes. Hydrophilic-lipophilic balance (HLB) and phase transfer temperature are two essential parameters that affect entrapment efficiency. The higher transition temperature (Tc) of Tween 60 (55°C) and a lower HLB value (14.9) led to the highest entrapment efficiency of curcumin as a lipophilic drug (Palozza et al., 2006; Bnyan et al., 2018). Tween 60 has a high transfer temperature and an impermeable bilayer that reduces the release rate of curcumin and leads to a continuous release. Moreover, PEGylation of nanoniosomes improves their stability, enhances drug loading, reduces nanoparticle size, and decreases the drug-release rate in niosomal formulations (Haghiralsadat et al., 2017; Hemati et al., 2019a). The endocytosis mechanism of Cur-Nio plays a crucial role in penetrating and increasing the accumulation of curcumin into cells, causing a higher intensity in green and turquoise blue fluorescence. In other words, the nanoniosomal curcumin delivery system was more efficient in the delivery and localization of curcumin compared with the free one that crosses through the cell membrane by a diffusion process. These findings are in agreement with a number of studies conducted in this regard (Huang et al., 2014; Deljoo et al., 2019). Our results demonstrate that cells treated with irradiation produce intracellular reactive oxygen species (ROS), leading to a decreased proliferation rate (~50% at 3 Gy) in cancer cells in a dose-dependent manner compared with control cells. We examined irradiation doses (1 Gy and 3 Gy) in combination with free curcumin and Cur-Nio based on the IC10 values. Our findings indicated that concomitant use of the free curcumin or niosome-containing curcumin with irradiation increased cell death by ~1 and ~1.5 folds in comparison to

cells exposed to irradiation alone, respectively. Accordingly, our results were in compliance with studies performed in this regard (Girdhani et al., 2009; Swati et al., 2009; Goel & Aggarwal, 2010; Yallapu et al., 2010; Shehzad et al., 2013b; Minafra et al., 2019). We found that the combined use of curcumin with irradiation increased the efficiency of radiotherapy against breast cancer cells. The radio-sensitivity of curcumin is attributed to its influences on various molecules involved in the cellular signaling pathway, including PI3-kinase, NF-κB, STAT3, COX2, Akt, MAPK, AMPK, p53, Nrf2, Notch-1, β-catenin, and the upregulation of genes responsible for cell death that induce apoptosis and inhibit proliferation of cancer cell (Shehzad & Lee, 2013a). We also showed that the presence of curcumin-containing PEGylated nanoniosomes increased the radiation efficiency (3Gy) compared to free curcumin in breast cancer cells, and cell death changed from 50% to% 68% at 72 h. This phenomenon might be due to the fact that nanoniosomes promote solubility, stability, and bioavailability of curcumin and enhance the cellular uptake and localization of curcumin in cancer cells (Kolter et al., 2019; Karimi et al., 2020). Minafra et al. (2019) evaluated the radio-sensitizing ability of curcumin-containing solid nanoparticles (Cur-SLN) in comparison to free curcumin at three concentrations with increasing irradiation doses. They demonstrated that Cur-SLN caused higher radio-sensitivity in MCF7 cells by increasing curcumin bioavailability in a synergistic manner (Minafra et al., 2019). Ahmed et al. assessed the impact of free curcumin as a radiosensitizer on breast cancer cells before gamma irradiation. They showed that the combination of curcumin and irradiation increased cancer cell death by 62% compared to the single-use of curcumin, causing 48% apoptosis in cancer cells (Girdhani et al., 2009). Xu et al. (2018)sensitized colorectal cancer cells to ionizing irradiation by developing curcumin-based supramolecular nanofibers (Cur-SNF) and found these structures caused higher radio-sensitivity in these cancer cells compared to those treated with the free curcumin. These structures reduced tumor volume *in vivo* by inhibiting irradiation-induced nuclear factor kappa B activation (Xu et al., 2018). Our results were consistent with these results. Also, Liang et al. determined the cell survival effect of combined and single curcumin and cisplatin with irradiation on non-small cell lung cancer (NSCLC) A549 cells. The viability of these cells was reduced following treatment with curcumin, cisplatin, or curcumin + cisplatin with irradiation compared to a single dose of irradiation. These findings exhibited that curcumin and cisplatin promote radio-sensitivity of lung cancer cells through the inhibition of the epidermal growth factor receptor (EGFR)-associated signaling pathway (Cai et al., 2019). Their results were in line with our findings.

CONCLUSION

In general, we have developed a new curcumin-containing PEGylated nanoniosome to enhance the radiosensitivity of breast cancer cells instead of using the free curcumin. The results demonstrated that PEGylated nanoniosomes have nanoscale size, spherical shape, high entrapment efficiency, and a controlled release pattern. Our study highlights the significance of the application of curcumin in sensitizing breast cancer cells to irradiation, and PEGylated nanoniosome is a very promising system for cancer therapy in combination with radiotherapy through boosting solubility, bioavailability, and cellular uptake of curcumin.

DATA AVAILABILITY STATEMENT

The raw data supporting the conclusions of this article will be made available by the authors, without undue reservation.

AUTHOR CONTRIBUTIONS

SA performed the experimental procedures. FH, NH, AS, and SN drafted the manuscript. MS and MH wrote the manuscript. SN, BZ-D, NH, and AS revised the manuscript. All authors contributed to the general discussion. All authors read and approved the final version of the manuscript.

REFERENCES

Abtahi, N. A., Naghib, S. M., Ghalekohneh, S. J., Mohammadpour, Z., Nazari, H., Mosavi, S. M., et al. (2021a). Multifunctional Stimuli-Responsive Niosomal Nanoparticles for Co-delivery and Co-administration of Gene and Bioactive Compound: *In Vitro* and *In Vivo* Studies. *Chem. Eng. J.* 429, 132090. doi:10.1016/j.cej.2021.132090

Abtahi, N. A., Naghib, S. M., Haghiralsadat, F., Reza, J. Z., Hakimian, F., Yazdian, F., et al. (2021b). Smart Stimuli-Responsive Biofunctionalized Niosomal Nanocarriers for Programmed Release of Bioactive Compounds into Cancer Cells *In Vitro* and *In Vivo*. *Nanotechnol. Rev.* 10, 1895–1911. doi:10.1515/ntrev-2021-0119

Bnyan, R., Khan, I., Ehtezazi, T., Saleem, I., Gordon, S., O'Neill, F., et al. (2018). Surfactant Effects on Lipid-Based Vesicles Properties. *J. Pharm. Sci.* 107, 1237–1246. doi:10.1016/j.xphs.2018.01.005

Butterworth, K., Mcmahon, S., Taggart, L., and Prise, K. (2013). Radiosensitization by Gold Nanoparticles: Effective at Megavoltage Energies and Potential Role of Oxidative Stress. *Transl. Cancer Res.* 2, 269–279.

Cai, Y., Sheng, Z., and Liang, S. (2019). Radiosensitization Effects of Curcumin Plus Cisplatin on Non-small Cell Lung Cancer A549 Cells. *Oncol. Lett.* 18, 529–534. doi:10.3892/ol.2019.10364

Chen, Y., Wu, Q., Zhang, Z., Yuan, L., Liu, X., and Zhou, L. (2012). Preparation of Curcumin-Loaded Liposomes and Evaluation of Their Skin Permeation and Pharmacodynamics. *Molecules* 17, 5972–5987. doi:10.3390/molecules17055972

Chendil, D., Ranga, R. S., Meigooni, D., Sathishkumar, S., and Ahmed, M. M. (2004). Curcumin Confers Radiosensitizing Effect in Prostate Cancer Cell Line PC-3. *Oncogene* 23, 1599–1607. doi:10.1038/sj.onc.1207284

Crokart, N., Radermacher, K., Jordan, B. F., Baudelet, C., Cron, G. O., Grégoire, V., et al. (2005). Tumor Radiosensitization by Antiinflammatory Drugs: Evidence for a New Mechanism Involving the Oxygen Effect. *Cancer Res.* 65, 7911–7916. doi:10.1158/0008-5472.can-05-1288

Cui, G., Wu, J., Lin, J., Liu, W., Chen, P., Yu, M., et al. (2021). Graphene-based Nanomaterials for Breast Cancer Treatment: Promising Therapeutic Strategies. *J. Nanobiotechnol* 19, 211. doi:10.1186/s12951-021-00902-8

Deljoo, S., Rabiee, N., and Rabiee, M. (2019). Curcumin-hybrid Nanoparticles in Drug Delivery System (Review). *Asian J. Nanosci. Mater.* 2, 66–91.

Dhandapani, K. M., Mahesh, V. B., and Brann, D. W. (2007). Curcumin Suppresses Growth and Chemoresistance of Human Glioblastoma Cells via AP-1 and NFκB Transcription Factors. *J. Neurochem.* 102, 522–538. doi:10.1111/j.1471-4159.2007.04633.x

Gao, R., Gu, Y., Yang, Y., He, Y., Huang, W., Sun, T., et al. (2022). Robust Radiosensitization of Hemoglobin-Curcumin Nanoparticles Suppresses Hypoxic Hepatocellular Carcinoma. *J. nanobiotechnology* 20, 1–15. doi:10.1186/s12951-022-01316-w

Garg, A. K., Buchholz, T. A., and Aggarwal, B. B. (2005). Chemosensitization and Radiosensitization of Tumors by Plant Polyphenols. *Antioxidants redox Signal.* 7, 1630–1647. doi:10.1089/ars.2005.7.1630

Ghaffari, M., Kalantar, S. M., Hemati, M., Dehghani Firoozabadi, A., Asri, A., Shams, A., et al. (2021). Co-delivery of miRNA-15a and miRNA-16-1 Using Cationic PEGylated Niosomes Downregulates Bcl-2 and Induces Apoptosis in Prostate Cancer Cells. *Biotechnol. Lett.* 43, 981–994. doi:10.1007/s10529-021-03085-2

Girdhani, S., Ahmed, M. M., and Mishra, K. P. (2009). Enhancement of Gamma Radiation-Induced Cytotoxicity of Breast Cancer Cells by Curcumin. *Mol. Cell. Pharmacol.* 1, 208–217.

Goel, A., and Aggarwal, B. B. (2010). Curcumin, the Golden Spice From Indian Saffron, Is a Chemosensitizer and Radiosensitizer for Tumors and Chemoprotector and Radioprotector for Normal Organs. *Nutr. cancer* 62, 919–930. doi:10.1080/01635581.2010.509835

Haghiralsadat, F., Amoabediny, G., Sheikhha, M. H., Zandieh-Doulabi, B., Naderinezhad, S., Helder, M. N., et al. (2017). New Liposomal Doxorubicin Nanoformulation for Osteosarcoma: Drug Release Kinetic Study Based on Thermo and pH Sensitivity. *Chem. Biol. Drug Des.* 90, 368–379. doi:10.1111/cbdd.12953

Hamzian, N., Hashemi, M., Ghorbani, M., Aledavood, S. A., Ramezani, M., and Bahreyni Toosi, M. H. (2019). *In-vitro* Study of Multifunctional PLGA-SPION Nanoparticles Loaded with Gemcitabine as Radiosensitizer Used in Radiotherapy. *Iran. J. Pharm. Res.* 18, 1694–1703. doi:10.22037/ijpr.2019.14050.12131

Hamzian, N., Hashemi, M., Ghorbani, M., Bahreyni Toosi, M. H., and Ramezani, M. (2017). Preparation, Optimization and Toxicity Evaluation of (SPION-PLGA) ±PEG Nanoparticles Loaded with Gemcitabine as a Multifunctional Nanoparticle for Therapeutic and Diagnostic Applications. *Iran. J. Pharm. Res.* 16, 8–21.

Hemati, M., Haghiralsadat, F., Jafary, F., Moosavizadeh, S., and Moradi, A. (2019a). Targeting Cell Cycle Protein in Gastric Cancer with CDC20siRNA and Anticancer Drugs (Doxorubicin and Quercetin) Co-loaded Cationic PEGylated Nanoniosomes. *Int. J. Nanomedicine* 14, 6575–6585. doi:10.2147/ijn.s211844

Hemati, M., Haghiralsadat, F., Yazdian, F., Jafari, F., Moradi, A., and Malekpour-Dehkordi, Z. (2019b). Development and Characterization of a Novel Cationic PEGylated Niosome-Encapsulated Forms of Doxorubicin, Quercetin and siRNA for the Treatment of Cancer by Using Combination Therapy. *Artif. Cells, Nanomedicine, Biotechnol.* 47, 1295–1311. doi:10.1080/21691401.2018.1489271

Huang, Q., Zhang, L., Sun, X., Zeng, K., Li, J., and Liu, Y.-N. (2014). Coating of Carboxymethyl Dextran on Liposomal Curcumin to Improve the Anticancer Activity. *RSC Adv.* 4, 59211–59217. doi:10.1039/c4ra11181h

Im, S.-A., Lu, Y.-S., Bardia, A., Harbeck, N., Colleoni, M., Franke, F., et al. (2019). Overall Survival with Ribociclib Plus Endocrine Therapy in Breast Cancer. *N. Engl. J. Med.* 381, 307–316. doi:10.1056/nejmoa1903765

Jiang, Q., Liu, L., Li, Q., Cao, Y., Chen, D., Du, Q., et al. (2021). NIR-laser-triggered Gadolinium-Doped Carbon Dots for Magnetic Resonance Imaging, Drug Delivery and Combined Photothermal Chemotherapy for Triple Negative Breast Cancer. *J. Nanobiotechnol* 19, 64. doi:10.1186/s12951-021-00811-w

Kalantari, E., Naghib, S. M., Iravani, N. J., Esmaeili, R., Naimi-Jamal, M. R., and Mozafari, M. (2019). Biocomposites Based on Hydroxyapatite Matrix Reinforced with Nanostructured Monticellite (CaMgSiO4) for Biomedical Application: Synthesis, Characterization, and Biological Studies. *Mater. Sci. Eng. C* 105, 109912. doi:10.1016/j.msec.2019.109912

Karimi, M., Gheybi, F., Zamani, P., Mashreghi, M., Golmohammadzadeh, S., Darban, S. A., et al. (2020). Preparation and Characterization of Stable Nanoliposomal Formulations of Curcumin with High Loading Efficacy: *In Vitro* and *In Vivo* Anti-tumor Study. *Int. J. Pharm.* 580, 119211. doi:10.1016/j.ijpharm.2020.119211

Khafif, A., Hurst, R., Kyker, K., Fliss, D. M., Gil, Z., and Medina, J. E. (2005). Curcumin: A New Radio-Sensitizer of Squamous Cell Carcinoma Cells. *Otolaryngol. Head. Neck Surg.* 132, 317–321. doi:10.1016/j.otohns.2004.09.006

Kolter, M., Wittmann, M., Köll-Weber, M., and Süss, R. (2019). The Suitability of Liposomes for the Delivery of Hydrophobic Drugs - A Case Study with Curcumin. *Eur. J. Pharm. Biopharm.* 140, 20–28. doi:10.1016/j.ejpb.2019.04.013

Kunnumakkara, A. B., Diagaradjane, P., Guha, S., Deorukhkar, A., Shentu, S., Aggarwal, B. B., et al. (2008). Curcumin Sensitizes Human Colorectal Cancer Xenografts in Nude Mice to γ-Radiation by Targeting Nuclear Factor-κB-Regulated Gene Products. *Clin. Cancer Res.* 14, 2128–2136. doi:10.1158/1078-0432.ccr-07-4722

Li, M., Zhang, Z., Hill, D. L., Wang, H., and Zhang, R. (2007). Curcumin, a Dietary Component, Has Anticancer, Chemosensitization, and Radiosensitization Effects by Down-Regulating the MDM2 Oncogene through the PI3K/mTOR/ETS2 Pathway. *Cancer Res.* 67, 1988–1996. doi:10.1158/0008-5472.can-06-3066

Li, W., Cao, Z., Yu, L., Huang, Q., Zhu, D., Lu, C., et al. (2021). Hierarchical Drug Release Designed Au @PDA-PEG-MTX NPs for Targeted Delivery to Breast Cancer with Combined Photothermal-Chemotherapy. *J. Nanobiotechnol* 19, 143. doi:10.1186/s12951-021-00883-8

Liu, W., Zhai, Y., Heng, X., Che, F. Y., Chen, W., Sun, D., et al. (2016). Oral Bioavailability of Curcumin: Problems and Advancements. *J. Drug Target* 24, 694–702. doi:10.3109/1061186X.2016.1157883

Minafra, L., Porcino, N., Bravatà, V., Gaglio, D., Bonanomi, M., Amore, E., et al. (2019). Radiosensitizing Effect of Curcumin-Loaded Lipid Nanoparticles in Breast Cancer Cells. *Sci. Rep.* 9, 11134–11216. doi:10.1038/s41598-019-47553-2

Palozza, P., Muzzalupo, R., Trombino, S., Valdannini, A., and Picci, N. (2006). Solubilization and Stabilization of β-carotene in Niosomes: Delivery to Cultured Cells. *Chem. Phys. lipids* 139, 32–42. doi:10.1016/j.chemphyslip.2005.09.004

Park, K., and Lee, J.-H. (2007). Photosensitizer Effect of Curcumin on UVB-Irradiated HaCaT Cells through Activation of Caspase Pathways. *Oncol. Rep.* 17, 537–540. doi:10.3892/or.17.3.537

Shehzad, A., and Lee, Y.-S. (2013a). Molecular Mechanisms of Curcumin Action: Signal Transduction. *BioFactors* 39, 27–36. doi:10.1002/biof.1065

Shehzad, A., Park, J.-W., Lee, J., and Lee, Y.-S. (2013b). Curcumin Induces Radiosensitivity of *In Vitro* and *In Vivo* Cancer Models by Modulating Pre-mRNA Processing Factor 4 (Prp4). *Chemico-biological Interact.* 206, 394–402. doi:10.1016/j.cbi.2013.10.007

Siddique, S., and Chow, J. C. L. (2020). Gold Nanoparticles for Drug Delivery and Cancer Therapy. *Appl. Sci.* 10, 3824. doi:10.3390/app10113824

Sim, S., and Wong, N. K. (2021). Nanotechnology and its Use in Imaging and Drug Delivery. *Biomed. Rep.* 14, 1–9. doi:10.3892/br.2021.1418

Spirou, S., Basini, M., Lascialfari, A., Sangregorio, C., and Innocenti, C. (2018). Magnetic Hyperthermia and Radiation Therapy: Radiobiological Principles and Current Practice †. *Nanomaterials* 8, 401. doi:10.3390/nano8060401

Swati, G., Ahmed, M., and Mishra, K. (2009). Enhancement of Gamma Radiation-Induced Cytotoxicity of Breast Cancer Cells by Curcumin. *Mol. Cell. Pharmacol.* 1. doi:10.4255/mcpharmacol.09.25

Xu, H., Wang, T., Yang, C., Li, X., Liu, G., Yang, Z., et al. (2018). Supramolecular Nanofibers of Curcumin for Highly Amplified Radiosensitization of Colorectal Cancers to Ionizing Radiation. *Adv. Funct. Mater.* 28, 1707140. doi:10.1002/adfm.201707140

Yaghoubi, F., Naghib, S. M., Motlagh, N. S. H., Haghiralsadat, F., Jaliani, H. Z., Tofighi, D., et al. (2021). Multiresponsive Carboxylated Graphene Oxide-Grafted Aptamer as a Multifunctional Nanocarrier for Targeted Delivery of Chemotherapeutics and Bioactive Compounds in Cancer Therapy. *Nanotechnol. Rev.* 10, 1838–1852. doi:10.1515/ntrev-2021-0110

Yallapu, M. M., Maher, D. M., Sundram, V., Bell, M. C., Jaggi, M., and Chauhan, S. C. (2010). Curcumin Induces Chemo/radio-Sensitization in Ovarian Cancer Cells and Curcumin Nanoparticles Inhibit Ovarian Cancer Cell Growth. *J. Ovarian Res.* 3, 11. doi:10.1186/1757-2215-3-11

Yi, H., Lu, W., Liu, F., Zhang, G., Xie, F., Liu, W., et al. (2021). ROS-responsive Liposomes with NIR Light-Triggered Doxorubicin Release for Combinatorial Therapy of Breast Cancer. *J. Nanobiotechnol* 19, 134. doi:10.1186/s12951-021-00877-6

Zhao, P., Xu, Y., Ji, W., Zhou, S., Li, L., Qiu, L., et al. (2021). Biomimetic Black Phosphorus Quantum Dots-Based Photothermal Therapy Combined with Anti-PD-L1 Treatment Inhibits Recurrence and Metastasis in Triple-Negative Breast Cancer. *J. Nanobiotechnol* 19, 181. doi:10.1186/s12951-021-00932-2

Conflict of Interest: The authors declare that the research was conducted in the absence of any commercial or financial relationships that could be construed as a potential conflict of interest.

Publisher's Note: All claims expressed in this article are solely those of the authors and do not necessarily represent those of their affiliated organizations, or those of the publisher, the editors, and the reviewers. Any product that may be evaluated in this article, or claim that may be made by its manufacturer, is not guaranteed or endorsed by the publisher.

frontiers | Frontiers in Bioengineering and Biotechnology

TYPE Original Research
PUBLISHED 23 September 2022
DOI 10.3389/fbioe.2022.1027351

OPEN ACCESS

EDITED BY
Yasser Zare,
Motamed Cancer Institute, Iran

REVIEWED BY
Sayed Behnam Abdulahi,
University of Tehran, Iran
Jafar Khademzadeh Yeganeh,
Qom University of Technology, Iran

*CORRESPONDENCE
Hossein Nazockdast,
nazdast@aut.ac.ir

SPECIALTY SECTION
This article was submitted to Nanobiotechnology, a section of the journal Frontiers in Bioengineering and Biotechnology

RECEIVED 24 August 2022
ACCEPTED 09 September 2022
PUBLISHED 23 September 2022

CITATION
Mosallanezhad P, Nazockdast H, Ahmadi Z and Rostami A (2022), Fabrication and characterization of polycaprolactone/chitosan nanofibers containing antibacterial agents of curcumin and ZnO nanoparticles for use as wound dressing.
Front. Bioeng. Biotechnol. 10:1027351.
doi: 10.3389/fbioe.2022.1027351

Fabrication and characterization of polycaprolactone/chitosan nanofibers containing antibacterial agents of curcumin and ZnO nanoparticles for use as wound dressing

Pezhman Mosallanezhad[1], Hossein Nazockdast[2]*, Zahed Ahmadi[3] and Amir Rostami[4]

[1]Department of Polymer Engineering, Amirkabir University of Technology, Mahshahr, Iran, [2]Department of Polymer Engineering and Color Technology, Amirkabir University of Technology, Tehran, Iran, [3]Department of Chemistry, Amirkabir University of Technology, Tehran, Iran, [4]Department of Chemical Engineering, Faculty of Petroleum, Gas, and Petrochemical Engineering, Persian Gulf University, Bushehr, Iran

The potential of the nanoscale structure is utilized by electrospun nanofibers, which are promising materials for wound dressings. Here, we prepared wound dressings constituting polycaprolactone (PCL) and chitosan (CS). Curcumin (Cur) and zinc oxide nanoparticles (ZnO) as antibacterial agents were embedded in PCL/CS electrospun nanofibers and different properties including morphology, physicomechanical, interaction with water, antibacterial efficiency, and *in vitro* studies were investigated. SEM images confirmed the nanofibrous structure of samples with 100 ± 5 to 212 ± 25 nm in average diameter. Elemental analysis of nanofibers showed a good distribution of ZnO along nanofibers which not only caused decreasing in nanofiber diameter but also increased tensile strength of nanofibers up to 2.9 ± 0.5 MPa and with good elongation at break of 39 ± 2.9. ZnO nanoparticles also facilitated the interaction of nanofibers with water, and this led to the highest water vapor transition rate, which was equal to 0.28 ± 0.02 g cm^{-2} day^{-1}. The sample containing 3 wt% Cur had the highest water uptake value (367 ± 15%) and the lowest water contact angle (78 ± 3.7°), although Cur has a hydrophobic nature. The release profile of Cur showed a two-stage release and the Peppas model predicted a non-fickian diffusion. Simultaneous incorporation of CS, ZnO, and Cur effectively inhibited bacterial growth. In addition, *in vitro* studies represented that high content of Cur decreases cell viability and cell attachment. The outcomes from the fabricated nanofibrous scaffolds demonstrated appropriate properties for application as a wound dressing.

KEYWORDS

polycaprolactone (PCL), chitosan, zinc oxide, curcumin, wound dressing, drug release, antibacterial activity

Introduction

In light of the advancements made in tissue engineering, the topic of electrospinning is gaining popularity in the biomedical world. The high available surface area and high porosity of electrospun nanofibers, being affordable and easy to handle, make electrospun nanofibers an ideal option for wound dressing (Kakoria and Sinha-Ray, 2018; Huang et al., 2022). Electrospun nanofibers can be formed by a range of natural polymers such as cellulose, chitosan (CS), collagen, gelatin, and silk, as well as synthetic biodegradable polymers such as polylactic acid (PLA), polyglycolic acid (PGA), and polycaprolactone (PCL) (Mendes et al., 2017; Zhang et al., 2022).

Electrospinning of pure CS is accompanied by several challenges associated with the limited solubility of pure CS in most organic solvents, its typically large molecular weights, and strong physical networks from hydrogen bonds (Pillai and Sharma, 2009; Qasim et al., 2018). To address this issue, the blending of CS with other natural and synthetic polymers such as polyethylene oxide (PEO), polyvinyl alcohol (PVA), PLA, and collagen have been reported so far. In fact, these polymers, which are well-known for their fiber-forming ability, were used to facilitate the electrospinning of CS (Jia et al., 2007; Chen et al., 2008; Lou et al., 2008; Xu et al., 2009). PCL is an aliphatic semi-crystalline biodegradable polyester known for its good mechanical properties. Being non-toxic and tissue compatible, it has been used in different biomedical applications such as tissue engineering scaffolds, resorbable sutures, and drug delivery (Janmohammadi and Nourbakhsh, 2019; Dwivedi et al., 2020). Nanofibers from pure PCL and its blends with other biopolymers like PLA, gelatin, and polyethylene glycol (PEG) were also produced by many researchers through the electrospinning method (De Prá et al., 2017; Radisavljevic et al., 2018; Janmohammadi and Nourbakhsh, 2019; Semitela et al., 2020).

In recent years, electrospun PCL/CS has received a great deal of attention for the preparation of nanofiber scaffolds (Saatcioglu et al., 2021). PCL/CS nanofibers loaded with tetracycline hydrochloride (TCH) (Ghazalian et al., 2022), azithromycin (Alimohammadi et al., 2022), and metformin (Zhu et al., 2020) and its wound dressing containing aloe vera (Yin and Xu, 2020), Melilotus officinalis (Shahrousvand et al., 2021), and Jaft (Hashemi et al., 2021) have been recently reported in the literature. For instance, Ghazalian et al. (2020) prepared TCH-loaded PCL/CS core-shell nanofibrous structure. The prepared samples demonstrated a two-stage behavior of drug release, with an initial burst release stage followed by a sustained release stage. In another study by Alimohammadi et al. (2020), PCL/CS nanofibers containing azithromycin were prepared *via* electrospinning which showed a sustained release of the drug with minimized burst release. Zhu et al. (2020) also prepared crosslinked PCL/CS nanofibrous scaffolds as a carrier for the metformin drug. They showed that crosslinked samples were more suitable for drug release, osteogenic differentiation, cell adhesion, and bone mesenchymal stem cells.

In addition, with the development of electrospun nanocomposite scaffolds containing nickel nanoparticles (Karakas et al., 2017), graphene oxide (Aidun et al., 2019), hydroxyapatite (Shirzaei Sani et al., 2021), and multi-walled carbon nanotubes (Mirmusavi et al., 2022) enhanced functional performances of complex nanostructures have been demonstrated. For example, Aidun et al. (2019) investigated the biological activity and physicochemical properties of the PCL/CS scaffolds incorporated with graphene oxide. They found that an increase in nanoparticles corresponded to an increase in the hydrophilicity, bioactivity, cell adhesion, and proliferation of the scaffolds. Sani et al. (Shirzaei Sani et al., 2021) incorporated hydroxyapatite nanoparticles onto PCL/CS nanofibers to enhance their mechanical properties, proliferation, cell viability, and bioactivity of them. In another work, the structural, mechanical, and biological properties of PCL/CS electrospun nanocomposite scaffolds containing multi-walled carbon nanotubes were studied by Mirmusavi et al. (2022). The samples containing nanoparticles showed more cell viability and bioactivity compared to the neat samples. Among these investigations, no research on the Cur drug and ZnO nanoparticles has been seen. Cur is a natural polyphenol with antioxidant, anti-tumor, and anti-inflammatory properties (Afshar et al., 2019; Al-Bishari et al., 2022). The US Food and Drug Administration (FDA) has designated Cur as Generally Recognized As Safe (GRAS) and clinical trials have demonstrated good tolerability and safety profiles even at doses up to 12,000 mg/day of a 95% concentration (Hewlings and Kalman, 2017). Furthermore, ZnO is a multifunctional nanoparticle with effective antimicrobial and photocatalytic properties, biocompatibility as well as being nontoxic and inexpensive. ZnO can also promote the scaffold surface's hydrophilicity resulting in cell attachment and proliferation (Karthikeyan et al., 2020). It is well known that curcumin can chelate zinc metal ions strongly by acting as a ligand and forming stable complexes. The use of this substance may represent a novel strategy for the early detection and treatment of chronic illnesses (Prasad et al., 2021).

In this study, we electrospun a homogeneous mixture of CS and PCL and evaluated the success of creating nanofibrous scaffolds with the desired morphology. For the first time, Cur and ZnO were simultaneously added to the PCL/CS nanofibrous scaffolds because the antibacterial activity of CS-containing nanofibers is limited by the NH2 groups of the CS backbone (Korniienko et al., 2022). The findings of the investigation into the structural, physicomechanical, and biological characteristics of the prepared scaffolds demonstrated their appropriate properties as wound dressings.

TABLE 1 Sample codes and their corresponding compositions.

Concentration (wt%)				Sample code
PCL	CS	ZnO	Cur	
15	0	0	0	PCL15
15	3	0	0	PCL15CS3
15	3	1	0	PCL15CS3ZnO1
15	3	1	1	PCL15CS3ZnO1Cur1
15	3	1	3	PCL15CS3ZnO1Cur3

Experimental

Materials

PCL granules with average molecular weight (Mn) of 80,000 g mol^{-1}, and density of 1.145 g cm^3, CS with medium molecular weight and degree of deacetylation of 80%–85% (CAS Number: 9012-76-4), Cur drug, Hexafluoroisopropanol (HFIP), 3- [4,5- dimethylthiazol-2-yl]-2,5 diphenyltetrazolium bromide (MTT), Phosphate-buffered saline (PBS), methanol, and ethanol were purchased from Sigma-Aldrich (Germany). ZnO with particles size of 10–30 nm, specific surface area of 20–60 m^2 g^{-1} and purity of 99+% was purchased from US Research Nanomaterials, Inc (United States). The *Staphylococcus aureus* (*S. aureus*, ATCC 25,923), *Escherichia coli* (*E. coli*, ATCC 25,922), and Fibroblast cells (L929) were purchased from the Pasteur Institute of Tehran (Iran).

Scaffolds fabrication method

To determine the optimum condition of electrospinning a full factorial design experiment was conducted. Additional information is provided in the Supplementary Material (Supplementary Table S1). In brief, it was found that the optimal PCL concentration, CS concentration, flow rate, and voltage were 15 wt%, 3 wt%, 15 kV, and 1 ml h^{-1}, respectively. The needle-to-collector distance and collector speed were fixed at 15 cm and 300 rpm, respectively. To prepare the electrospinning solution, a 15 wt% PCL solution in HFIP was first prepared by stirring (500 rpm) at ambient temperature for 120 min. Then CS was gradually added to the previous solution to reach a total concentration of 3 wt% and stirred (500 rpm) for 90 min. In the case of samples containing Cur and ZnO, they were added to the PCL/CS solution and sonicated for 30 min before electrospinning. A transition from yellow to orange was seen after the sonication process was finished. Finally, the prepared solutions were loaded in a 5 ml syringe with a standard blunt end needle (20 G) in the electrospinning setup. The electrospun nanofibers were placed in an oven for 24 h to dry completely. The sample codes and concentrations are listed in Table 1.

Characterization method

The chemical structure of samples was investigated by attenuated total reflectance Fourier transform spectroscopy (ATR-FTIR). The spectrum was recorded through 64 scans at a resolution of 4 cm^{-1} and in the range of 600–4000 cm^{-1} by FTIR spectrometer of Thermo Nicolet Nexus 670 (Madison, WI, United States).

The morphology of scaffold surfaces was evaluated with a scanning electron microscope (SEM, AIS 2100, Seron Technology, South Korea) with an acceleration voltage of 20 kV. The distribution of ZnO nanoparticles incorporated into samples was investigated by using a scanning electron microscope with energy dispersive X-ray spectroscopy (TESCAN. MIRA II, France) with an accelerating voltage of 10 kV.

The physical state of ZnO incorporated in samples was analyzed with X-ray diffraction (XRD, EQuniox 3000, Inel, France) in the 2θ range of 5–80°. Applied radiation was Cu Kα with 40 kV, λ = 0.15418 nm, and 30 mA at room temperature.

To investigate the mechanical properties, 5 replicates of each sample (50 mm × 10 mm × 2 mm) were stretched at a rate of 5 mm min^{-1} until the fracture point according to ASTM D882 on a universal material testing machine (Instron 5566, United States).

Thermogravimetric analysis was used to assess the thermal behavior of the materials (TGA, Q-500, TA Instruments, United States). Under a nitrogen atmosphere, the pre-weighed samples (15 mg) were heated at a rate of 10°C.min^{-1} from 25 to 550°C.

The hydrophilicity of the samples was evaluated using the sessile drop method by contact angle goniometer (OCA20, Data Physics Instruments, Germany). To this end, a drop of distilled water was placed on the surface of samples (10 × 10 mm^2) using a 0.3 ml syringe. The contact angle of water drop on the surface of the samples was recorded after a few seconds from both sides of the drop. The reported contact angle was the mean of 5 replicates at 5 different sites of a sample.

To evaluate the water uptake behavior of the scaffolds, the samples were accurately weighed and then immersed in distilled water at 37°C. After immersion, the samples were weighed at regular intervals. The percent of water uptake in the samples was calculated based on the Eq. 1 (Ghaee et al., 2019):

$$Water\,Uptake\ (\%) = \frac{W_w - W_d}{W_d} \times 100 \qquad (1)$$

Where W_d and W_w represent the weight of dry and submerged samples, respectively.

To investigate the ability to control water loss, the water vapor transmission rate (WVTR) of samples was analyzed according to ASTM E96/E96M-10. The samples covered the opening of the 5 ml glass vial containing 1 ml distilled water. The container was placed in the humidity chamber with a constant temperature of 37°C and humidity of 25% for 48 h. A similar container without any sample was also placed in the humidity chamber as a control. WVTR was calculated using the Eq. 2 (Fahimirad et al., 2021):

$$WVTR\ (\mathrm{g.cm^{-2}.day^{-1}}) = -\frac{\Delta W}{A \times \Delta t} \quad (2)$$

Where ΔW is the variation of weight (g) of water before and after the test, A is the exposure area of the samples (cm^2), and Δt is the test time (day).

To investigate the *in vitro* degradation behavior of samples under physiological conditions, the samples (20 × 20 mm^2) were immersed in PBS (pH = 7.4) and incubated at 37°C. The PBS solution was refreshed every 48 h. At each time point, the sample was removed from the solution and dried at 50°C. the weight loss of samples was calculated based on the Eq. 3 (Varshosaz et al., 2021):

$$Weight\ loss\,(\%) = \frac{W_i - W_t}{W_i} \times 100 \quad (3)$$

Where W_i and W_t are the initial dry weight and the final dry weight of the samples (n = 3).

To investigate the release profile of Cur drug, samples (1 × 1 cm^2) were immersed in 5 ml of PBS (pH = 7.4) and incubated at 37°C. At specific time points, 1 ml of the media was extracted and replaced with 1 ml of fresh media. To determine the concentration of the sample, 5 solutions of Cur were prepared with different concentrations, and their maximum absorbance at 425 nm was measured by UV-Vis (Secomam, France).

The Eq. 4 was used to fit Peppas' model to the experimental data to study the kinetics of Cur release from electrospun nanofibers (Lao et al., 2008):

$$\frac{M_t}{M_\infty} = Kt^n \quad (4)$$

Where *K* and *t* are the kinetic constant and release exponent, and M_t and M_∞ are the amount of drug released at time *t* and the total amount of drug, respectively.

The antibacterial activity of samples was investigated using two types of bacteria, a Gram-positive (*S. aureus*) and a Gram-negative (*E. coli*) according to agar diffusion method at 37°C. The strip-shaped samples (20×20 mm^2) were immersed in methanol (90%) and PBS (pH = 7.4) for 15 min to neutralize and then sterilized by Gama radiation with a dose of 15 kGy. The samples were then suspended in bacterium solution and incubated in at 37°C in a shaking incubator

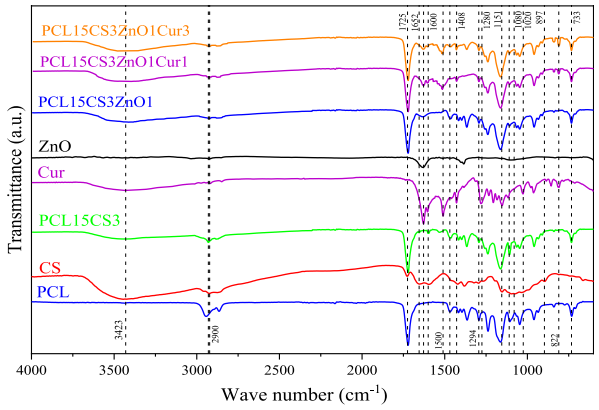

FIGURE 1
FTIR spectrum of PCL, CS, ZnO, Cur, and the electrospun samples.

for 24 h. The control was a suspension culture without any samples. The optical density of the samples was read by spectrophotometer at wavelength of 600 nm. The antibacterial efficiency was calculated based on the Eq. 5 (Chen et al., 2017):

$$Antibacterial\ efficiency\ (\%) = \left(1 - \frac{OD_1}{OD_2}\right) \times 100 \quad (5)$$

Where OD_1 and OD_2 are the optical densities of the control medium and the bacteria in the solution-containing sample, respectively.

Cell viability of samples was investigated by MTT assay in direct mode. First, samples were sterilized using Gama radiation with a dose of 15 kGy. Suspensions of L929 cell line were seeded on the sterilized samples with a density of 5×10^4 cells per well and stored in an incubator (at 37°C, 5% CO_2, and 90% humidity). After 24 h, the medium of each well was replaced with 200 μL of 0.5% MTT solution and incubated for 4 h. The MTT solution of each well was replaced with 150 μL isopropanol and the absorbance was read by ELISA at wavelengths of 490 and 630 nm as reference. Cell viability of samples was calculated by the Eq. 6 (Ghaee et al., 2019):

$$Cell\ viability\ (\%) = \frac{OD_s}{OD_c} \times 100 \quad (6)$$

Where OD_s and OD_c are absorption of sample and control, respectively.

To investigate cell adhesion of samples, after 7 days of seeding cells on them, the media was extracted. The cells were fixed with glutaraldehyde (2.5% v/v) for 24 h. Then samples were dried with a series of ethanol solutions from 10 to 100% v/v and coated with gold to prepare for SEM analysis.

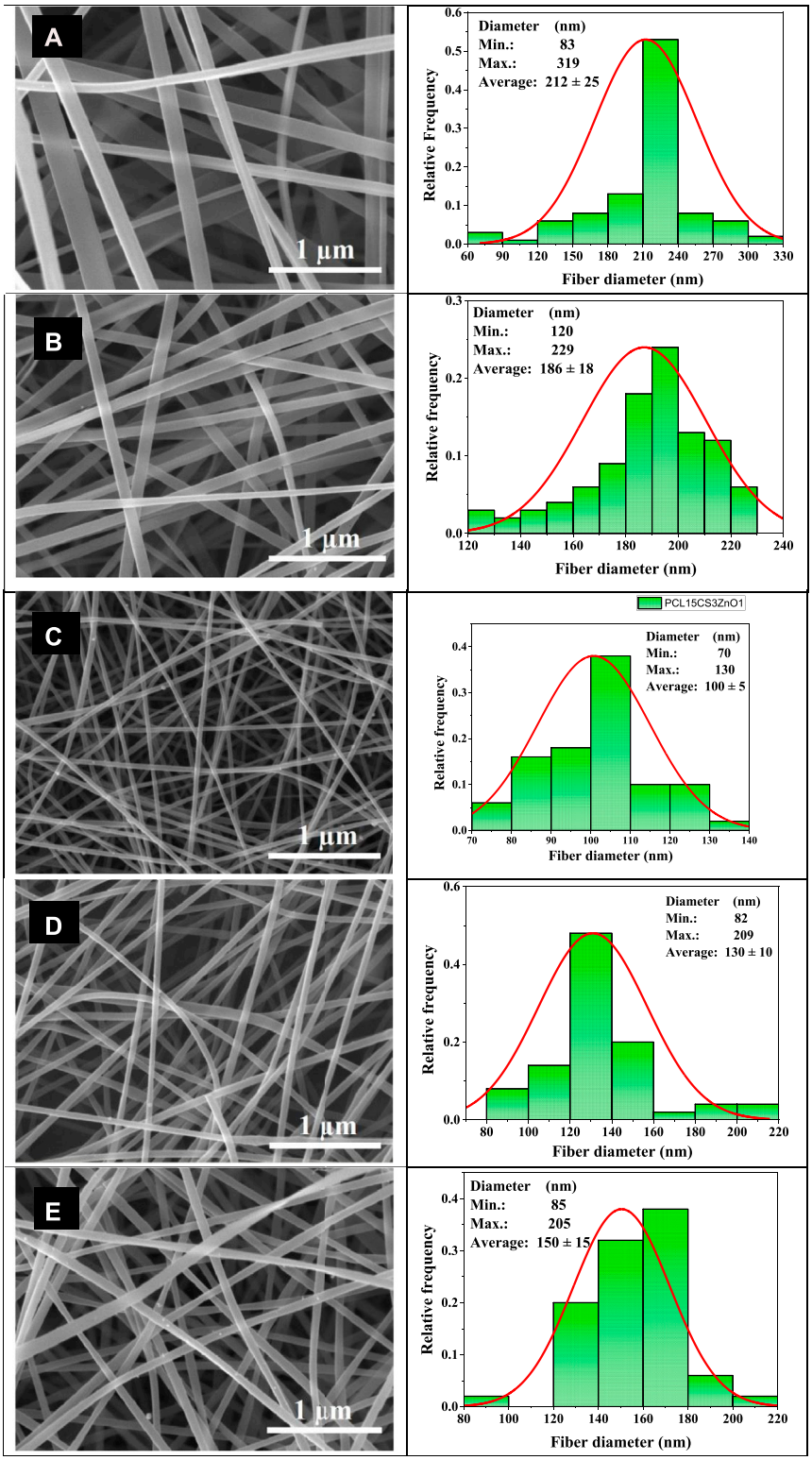

FIGURE 2
SEM images of the electrospun nanofibers and their diameter distribution histograms, **(A)** PCL15, **(B)** PCL15CS3, **(C)** PCL15CS3ZnO1, **(D)** PCL15CS3ZnO1Cur1, and **(E)** PCL15CS3ZnO1Cur3.

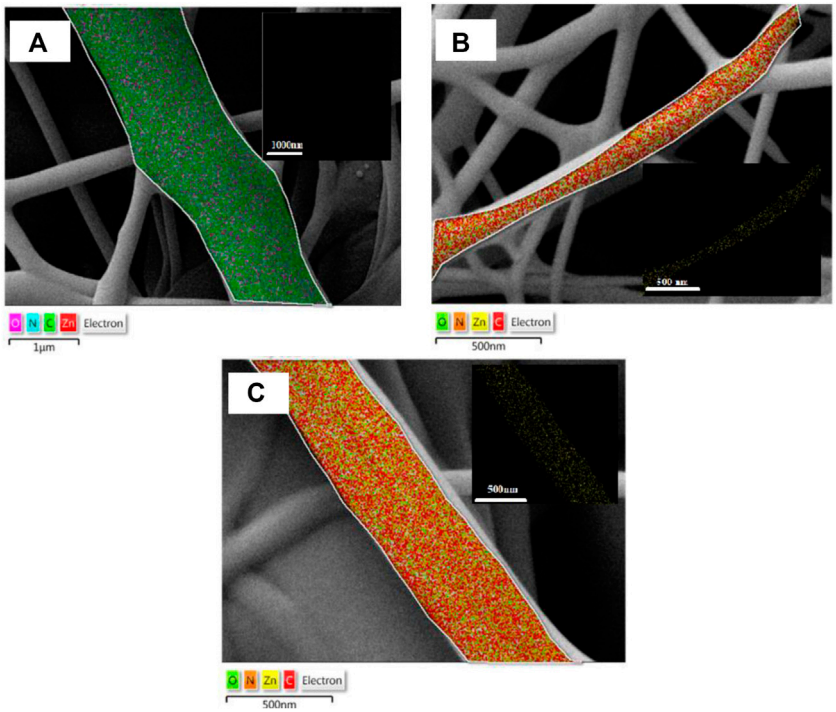

FIGURE 3
Elemental map of **(A)** PCL15CS3, **(B)** PCL15CS3ZnO1Cur1, and **(C)** PCL15CS3ZnO1Cur3.

TABLE 2 Data of the elemental analysis of the electrospun samples.

Sample	Carbon (C) atomic ratio (%)	Nitrogen (N) atomic ratio (%)	Oxygen (O) atomic ratio (%)	Zinc (Zn) atomic ratio (%)
PCL15CS3	69.8 ± 2.1	1.9 ± 0.8	28.3 ± 1.8	—
PCL15CS3ZnO1Cur1	69.3 ± 3.4	0.9 ± 0.6	29.1 ± 1.9	0.7 ± 0.4
PCL15CS3ZnO1Cur3	68.9 ± 3.1	0.8 ± 0.5	29.7 ± 1.6	0.6 ± 0.2

Results and discussion

Fourier transform spectroscopy analysis

The result of ATR-FTIR is shown in Figure 1 for pure PCL, CS, ZnO, Cur, and the electrospun nanofibers. Characteristic peaks of PCL include peaks at 733, 1294, 1469, and 1725 cm^{-1} which are attributed to C-O stretching, asymmetric stretching of C-O-C bridge, CH_2 deformation, and carbonyl ester bonds (C=O), respectively (Ghaee et al., 2019). CS also showed its main characteristic peaks at 897, 1080, 1151, 1652 cm^{-1}, 2922 cm^{-1}, and 3423 cm^{-1}, which belong to the CH_3OH groups, C-O stretching, asymmetric stretching of C-O-C bridge, N-H bending, C-H stretching, and O-H stretching, respectively (Ghazalian et al., 2022). The characteristic peaks of PCL and CS exist in the FTIR of electrospun nanofiber of PCL15CS3. However, they shifted slightly due to the electrostatic interaction of PCL with CS. Also, the peaks at 2900 cm^{-1} and 1600 cm^{-1} belong to the stretching of C-H and bending of N-H, respectively. The peak at 1110 cm^{-1} is attributed to the C-O-C bridge.

The main characteristic peak of ZnO is located in the range of 500–700 cm^{-1} indicates the stretching of the Zn–O bond. The peak around 800 cm^{-1} can be attributed to the stretching vibration mode of Zn-O-Zn (Babaei et al., 2022). The main characteristic peaks of Cur are attributed to the aromatic peaks. Cur exhibits peaks at 822 cm^{-1} and 1020 cm^{-1} that are related to C-H aromatic in-plane bending modes and out-of-plane bending, respectively. The peaks at 1280, 1408,1510, and 1626 cm^{-1} belong to C–O–C stretching, aromatic C–O

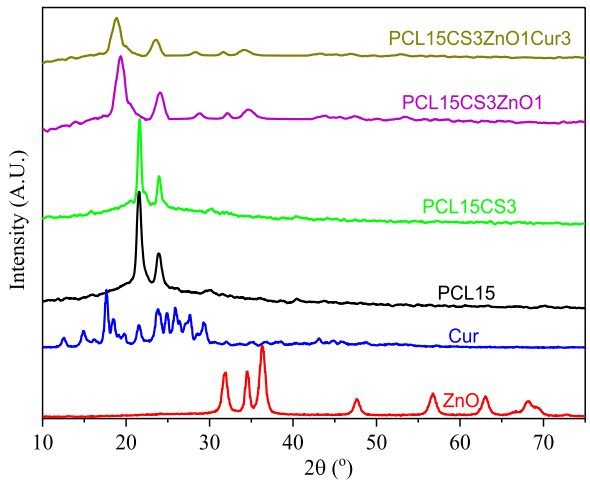

FIGURE 4
XRD pattern of Cur, ZnO, and the electrospun samples.

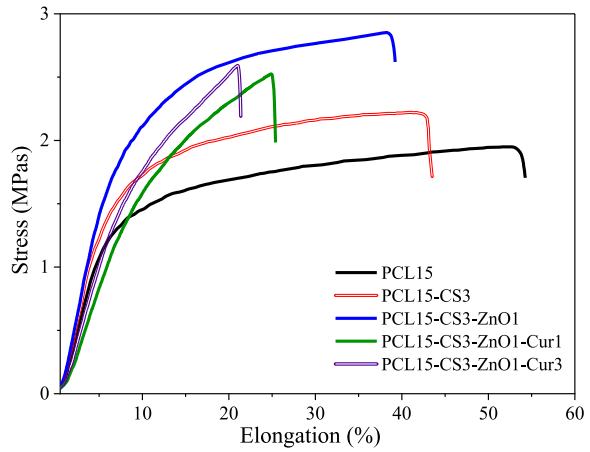

FIGURE 5
Stress-strain diagram of the electrospun nanofibers.

stretching, C=O stretching and C–C symmetric aromatic ring stretching, respectively (Ghaee et al., 2019). Characteristic peaks of ZnO and Cur are present with a shifted position in the spectrum of electrospun nanofibers containing them, confirming their presence.

Scanning electron microscope images of samples

Figure 2 shows the SEM images of electrospun nanofibers and their diameter distribution histograms. All samples had uniform bead-free morphology. The pure PCL nanofibers showed smooth morphology with an average diameter of

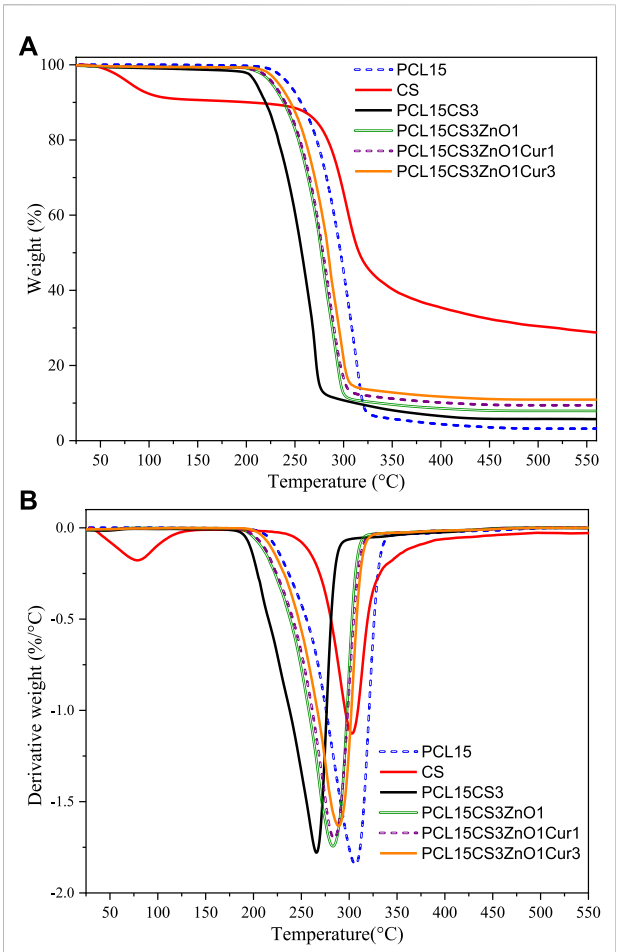

FIGURE 6
(A) TGA and **(B)** DTG curves of CS and electrospun samples.

212 ± 25 nm. The addition of CS decreased the diameter of nanofibers by about 186 ± 18 nm. The CS increases the polarity of electrospinning solution due to its charged functional groups that cause the stretching of fibers under an electrical field (Van der Schueren et al., 2012; Bolaina-Lorenzo et al., 2016). Moreover, ZnO nanoparticles increase conductivity of solution and cause more drawn. It can be seen that the PCL15CS3ZnO1 sample had the lowest average fiber diameter (100 ± 5 nm). The ZnO nanoparticles are also shown by the yellow arrow that have a good distribution state. The Cur drug affects viscosity more than conductivity. This increased solution viscosity led to increased average fiber diameters by 130 ± 10 and 150 ± 15 nm for nanofibers with 1 and 3 wt% Cur, respectively (Mitra et al., 2022).

Elemental analysis of samples

The elemental maps of pure PCL15CS3 electrospun nanofibers and its composites containing ZnO and Cur are

TABLE 3 Mechanical properties of the electrospun nanofibers.

Sample code	Tensile strength (MPa)	Tensile modulus (MPa)	Elongation at break (%)
PCL15	1.9 ± 0.2	0.25 ± 0.01	54 ± 3.2
PCL15CS3	2.2 ± 0.3	0.29 ± 0.02	43 ± 3.6
PCL15CS3ZnO1	2.9 ± 0.5	0.32 ± 0.04	39 ± 2.9
PCL15CS3ZnO1Cur1	2.5 ± 0.4	0.18 ± 0.03	25 ± 2.2
PCL15CS3ZnO1Cur3	2.6 ± 0.3	0.22 ± 0.02	22 ± 1.6

demonstrated in Figure 3. In these maps, zinc as the characteristic element of ZnO, and O, C, and N elements were detected. Based on this elemental map, ZnO nanoparticles (yellow points show Zn element) distributed homogeneously in samples of PCL15CS3ZnO1-Cur1 and PCL15CS3ZnO1Cur3. The obtained data from this analysis are also shown in Table 2.

X-ray diffraction analysis of samples

The XRD pattern of ZnO, Cur, and the electrospun nanofibers is shown in Figure 4. The X-ray diffractogram of ZnO showed several strong and sharp peaks at 2θ of 31.84°, 34.52°, 36.33°, 47.63°, 56.71°, and 68.13° which are related to planes of 100, 002, 101, 102, 110, and 112 and confirm the hexagonal structure of ZnO nanoparticles. The peak occurred at 34.52° is responsible the antibacterial capability of ZnO (Tajdari et al., 2021; Babaei et al., 2022). The exhibition of sharp peaks at 2θ of 17.3°, 21.3°, 23.4°, and 24.7° indicates high crystallinity of Cur (Rahimi et al., 2017).

The PCL15 nanofibers show two characteristic peaks at 2θ of 21.4° and 23.8° (Pekdemir et al., 2021). Although these two peaks appear in all electrospun nanofibers, they are slightly shifted to lower 2θ, which means PCL retained its crystallinity. By adding ZnO and Cur, the crystallinity of electrospun nanofibers was decreased due to the interaction of ZnO and Cur with the polymeric phase, which decreased the intensity of crystalline peaks in the PCL15CS3ZnO1Cur3 scaffold. The reduced mobility of polymer segments by CS and the blending of the elements in the amorphous phase can both contribute to the reduction of PCL crystallinity (Karthikeyan et al., 2020).

Mechanical behavior of samples

Electrospun nanofibers must possess appropriate mechanical properties especially elongation at break for wound dressing applications. It implies that a wound dressing must meet certain criteria to cover the wound without rupturing during the healing process. Figure 5 illustrates tensile stress-strain curves for electrospun nanofibers. The obtained results from the tensile test are summarized in Table 3. The tensile strength of electrospun nanofibers was between 1.9 ± 0.2 and 2.9 ± 0.5 MPa, which is in a good range for wound dressing application. Pure PCL15 nanofibers showed the lowest tensile strength and highest elongation at break (1.9 ± 0.2 MPa and 54 ± 3.2%, respectively). By blending PCL with CS, although the tensile strength increased to some extent (2.2 ± 0.3 MPa) compared to pure PCL15, but caused a decrease in elongation at break (43 ± 3.6%).

The high mechanical strength of ZnO as an inorganic phase and forming hydrogen bonds with the polymeric phase caused the highest tensile strength and modulus for PCL15CS3ZnO1 (2.9 ± 0.5 MPa and 0.32 ± 0.04 MPa) compared to other samples. The results also revealed that Cur weakened the mechanical properties of electrospun nanofibers in a dose-dependent manner. The tensile strength, tensile modulus, and elongation at break of the nanofibrous scaffold containing 1 and 3 wt% Cur were 2.5 ± 0.4 and 2.6 ± 0.3 MPa, 0.18 ± 0.03 and 0.22 ± 0.02 MPa and 25 ± 2.2 and 22 ± 1.6%, respectively.

Thermogravimetric analysis analysis of samples

The TGA curve of samples up to 550°C is shown in Figure 6. As can be seen, the thermogram of CS shows two-stage weight loss. The first decay happened at about 90°C due to the evaporation of intercalated or crystal moisture in the CS network, which was about 10% of the sample's initial weight. In the second stage, about 60% of the weight of CS is lost, which is related to the breakdown of glycosidic bonds and the breakdown of CS chains consequently (Wanjun et al., 2005; Afshar et al., 2019). In addition, pure PCL15 has good thermal stability with the starting point of degradation about 230°C due to aliphatic polyester groups and its semi-crystalline structure (Pekdemir et al., 2021). By blending CS with PCL, the thermal stability of electrospun nanofibers decreased in comparison with pure CS and PCL15. The PCL15CS3 showed the lowest thermal

TABLE 4 WCA values of the electrospun nanofibers.

Sample code	Contact angle (°)
PCL15	118 ± 6.7
PCL15CS3	97 ± 5.1
PCL15CS3ZnO1	95 ± 4.5
PCL15CS3ZnO1Cur1	89 ± 4.6
PCL15CS3ZnO1Cur3	78 ± 3.7

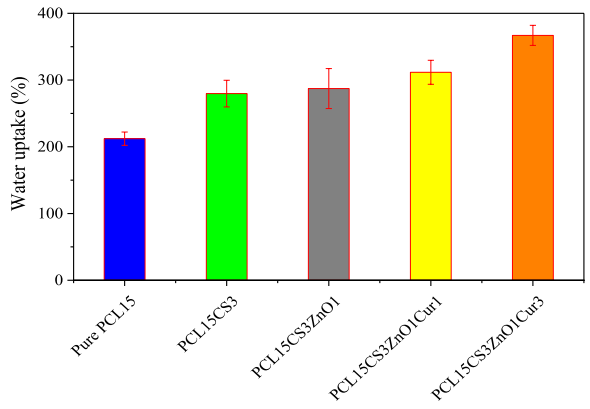

FIGURE 7
Water uptake of the electrospun samples.

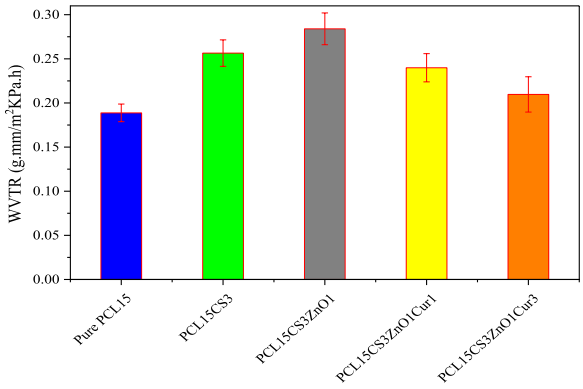

FIGURE 8
WVTR of the electrospun samples.

stability and decomposition temperature (about 160–275°C) compared to other electrospun nanofibers.

The addition of ZnO shifted starting point of degradation to higher temperatures (from 160°C to about 200°C). The ZnO nanoparticles are inorganic compounds with high thermal conductivity that accelerates heat transfer to other parts of the electrospun nanofibers and delays degradation. The effect of 1 wt % Cur on the thermal degradation of electrospun nanofibers is negligible, but for 3 wt% Cur an enhancement is shown. Notably, thermogravimetric analysis of the nanofibers verified the lack of HFIP solvent in them (boiling point = 58.2°C), which guarantees the biocompatibility of electrospun nanofibers.

Water contact angle

The contact angle between the water and the wound dressing provides useful information about the *in vivo* interaction between the surface of the damaged tissue and the wound dress. In general, increasing the hydrophilicity of the wound dressing surface leads to facilitated and improved cell adhesion and proliferation. The water contact angle (WCA) values of electrospun nanofibers are summarized in Table 4. The contact angle of PCL with water was about 118 ± 6.7° which is expected due to the hydrophobicity nature of PCL (Bolaina-Lorenzo et al., 2016). The addition of CS significantly increased the surface hydrophilicity of PCL nanofibers, which is thanks to the amino ester and hydroxyl groups in the CS chains (97 ± 5.1°). The ZnO also helped WCA decreases to 95 ± 4.5° because of increasing roughness and forming hydrogen bonds with water molecules. Although Cur does not dissolve in water, its oxygen can interact with water and serve as a proton donor. Therefore, the addition of Cur caused the nanofibers to become more hydrophilic and reduced the contact angle (Pulla Reddy et al., 1999; Nandhini et al., 2020).

Water uptake

The results of water uptake are summarized in Figure 7. To manage wound dryness and transfer nutrients and waste, optimum water uptake is necessary for wound dressing nanofibers. Water uptake of samples was about 210–370% which is appropriate for wound dressing. The pure PCL15 nanofibers had the lowest water uptake (212 ± 11%) compared to other samples, which is due to the hydrophobicity of t (Pekdemir et al., 2021). Notably, the water uptake capacity of a scaffold is influenced by several parameters such as including the polymer's crystallinity, porosity, and hydrophilicity. The water uptake rises with increased amorphous area and porosity as a result of facilitated water penetration in micro and macro states. As can be seen, PCL15CS3 nanofibers had a greater water uptake compared to pure PCL15. This was caused by the hydrophilicity and amorphousness of the CS chains in comparison to PCL. This increases their affinity for water molecules and the porous structure of the CS-containing

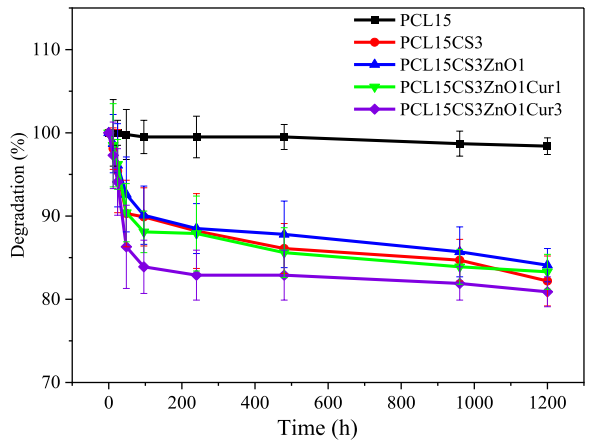

FIGURE 9
Degradation behavior of the electrospun samples.

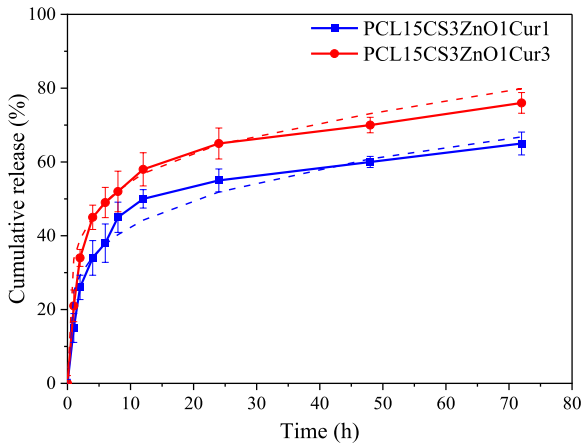

FIGURE 10
Release profile with their fitted Peppas model of the Cur-containing electrospun samples.

electrospun nanofibers, which allows water to be absorbed through the capillary effect. (Bolaina-Lorenzo et al., 2016; Fahimirad et al., 2021). ZnO nanoparticles increased water uptake of electrospun nanofibers by creating hydrogen bonds with water molecules. Although Cur has a hydrophobic nature, its hydrogen interactions with CS increase water uptake. The highest water uptake value (367 ± 15%) was achieved for PCL15CS3ZnO1Cur3.

Water vapor transmission rate results

A dry wound or a wound infection can result from an imbalance of moisture and secretions between the wound dressing and the wound. To determine the gas exchange to the wound site, the WVTR of electrospun samples was investigated and summarized in Figure 8. According to the results, the presence of CS in the PCL15CS3 led to an increase in WVTR compared to pure PCL15 due to more hydrophilicity, amorphousness, and porosity. In WVTR, the porosity plays a more impressive role compared to hydrophilicity and amorphousness. Due to the increased scaffold porosity that resulted from a decrease in the nanofiber diameter (see Figure 2), WVTR has increased in the case of PCL15CS3ZnO1. Additionally, water vapor molecules and ZnO nanoparticles interact electrostatically, increasing water vapor permeability in contrast, in the case of nanofibers containing Cur, an increase in the nanofiber diameter results in a decrease in the scaffold porosity, which in turn causes a decrease in WVTR (Fahimirad et al., 2021). Besides, the WVTR was further reduced as Cur content was increased. Altogether, the results obtained from the fabricated nanofiber scaffolds proved appropriate water uptake and WVTR properties for application as a wound dressing.

In vitro degradation

Figure 9 shows the degradation behavior of electrospun nanofibers during 50 days. Based on the literature, the long linear aliphatic polyester structure of PCL slows down its degradation rate which is consistent with the results of the pure PCL15 sample (Sun et al., 2006). Due to the NH_2 and OH groups that are found along the CS chains, which improve its hydrophilicity, CS can significantly contribute to boosting the degradation of electrospun nanofibers. In the other words, CS chains leak out of the scaffolds by dissolving in water over time (Sun et al., 2006). The effect of ZnO and 1 wt % Cur on the degradation of PCL15CS3 can be ignored, but PCL15CS3ZnO1Cur3 had the highest degradation.

In vitro release of Cur

Figure 10 illustrates the cumulative release profile of Cur drug in electrospun nanofibers with 1 and 3 wt% Cur. According to the results, both nanofibers present a two-stage Cur release, a burst release followed by a steady one. The burst release of PCL15CS3ZnO1Cur3 (34 ± 2.3 and 52 ± 5.5% of Cur in the first 2 and 6 h) is more than PCL15CS3ZnO1Cur1 (26 ± 3.3 and 45 ± 5.2% of Cur in the first 2 and 6 h) due to higher Cur content. The release of Cur at the beginning of the steady release stage (during 24 h) was 65 ± 4.2 and 55 ± 3.1% for PCL15CS3ZnO1Cur3 and PCL15CS3ZnO1Cur1, respectively. After 72 h, electrospun nanofibers of PCL15CS3ZnO1Cur3 and PCL15CS3ZnO1Cur1 released 76 ± 2.8 and 65 ± 3.1% of Cur, respectively.

Finally, six models were used to analyze the kinetics of drug release, which are listed in the Supplementary Material (Supplementary Table S2). The results of fitting for each model are summarized in Table 5. Among the presented models, the

TABLE 5 Parameters of different kinetic models for the release profile of Cur-containing electrospun samples.

Kinetic models	PCL15CS3ZnO1Cur1	PCL15CS3ZnO1Cur3
Zero order	$K_0^{''}$ = 0.005, R^2 = 0.669	$K_0^{''}$ = 0.006, R^2 = 0.672
First order	K_1 = 0.013, R^2 = 0.490	K_1 = 0.011, R^2 = 0.499
Higuchi	K'_H = 0.058, R^2 = 0.836	K'_H = 0.062, R^2 = 0.835
Hixson-Crowell	K_{HC} = 0.003, R^2 = 0.743	K_{HC} = 0.003, R^2 = 0.777
Baker-Lonsdale	K_{BL} = 0.001, R^2 = 0.859	K_{BL} = 0.002, R^2 = 0.881
Peppas	K = 24.97, R^2 = 0.952, n = 0.23	K = 32.75, R^2 = 0.934, n = 0.21

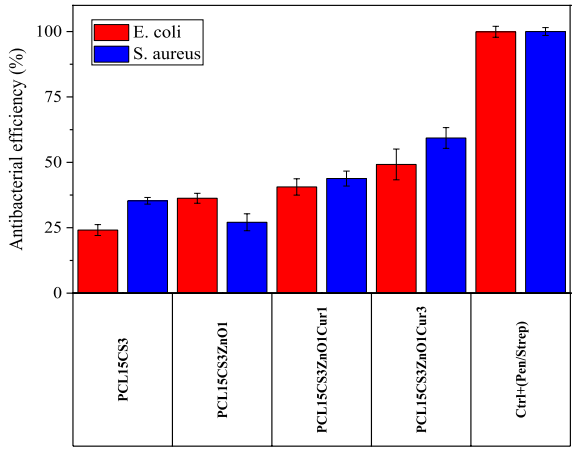

FIGURE 11
Antibacterial efficiency of the electrospun samples against *E. coli* and *S. aureus* bacteria after 24 h.

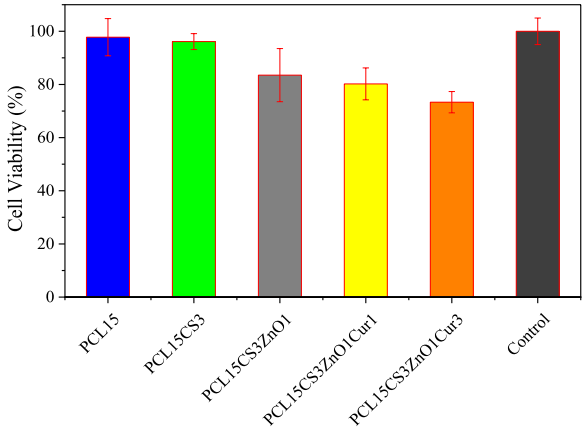

FIGURE 12
Cell viability of the electrospun samples after 24 h.

Peppas one had the highest correlation coefficient (R^2) and the best fitting (See Figure 10). The plots for other curve-fitting analysis are displayed in the Supplementary Material (Supplementary Figures S1–S5). Based on the Peppas model, the exponent (n) is used for describing the release mechanisms. n = 0.5 characterizes typical Fickian diffusion, whereas n = 1 describes case II diffusion. A non-Fickian is indicated by n values between 0.5 and 1. Predicted n exponents for both samples are below 0.5 which reveals the mechanism of drug release from electrospun nanofibers is non-Fickian diffusion (Shahrousvand et al., 2022). The correlation coefficients of the model for two Cur-containing samples was 0.93 and 0.95, indicating that the model fits the experimental data reasonably well.

Antibacterial efficiency of samples

The antibacterial activity of electrospun nanofibers against two types of bacteria, *Escherichia coli* (*E. coli*) and *Staphylococcus aureus* (*S. aureus*), was investigated (Figure 11). As expected, pure PCL15 did not show any inhibition. The results showed that the incorporation of CS into the PCL scaffold was effective in increasing the antibacterial efficiency against both bacteria. The PCL15CS3 scaffold had an antibacterial efficiency of 24.1 ± 2.1 and 35.3 ± 1.3 against *E. coli* and *S. aureus*, respectively. This is due to the interaction of NH_2 groups of CS with PCL chains. Moreover, CS is an effective natural antibacterial agent against both bacteria and chitosan's positive charge interacts with the negatively charged cell membranes to kill bacteria (Ono et al., 2000; Zou et al., 2020).

ZnO nanoparticles had different effects on the antibacterial activity of the scaffolds against bacteria, increasing antibacterial activity against *E. coli* while decreasing antibacterial effectiveness against *S. aureus*. It means that ZnO had a better performance against *E. coli* bacteria, which is due to their thin-walled nature (Bakhsheshi-Rad et al., 2021; Keyvani et al., 2021). Incorporation of Cur to PCL15CS3ZnO1 produced greater antibacterial activity against both bacteria. For example, PCL15CS3ZnO1Cur3 provided an antibacterial efficiency of 49.2 ± 5.8 and 59.3 ± 3.9% against *E. coli* and *S. aureus*

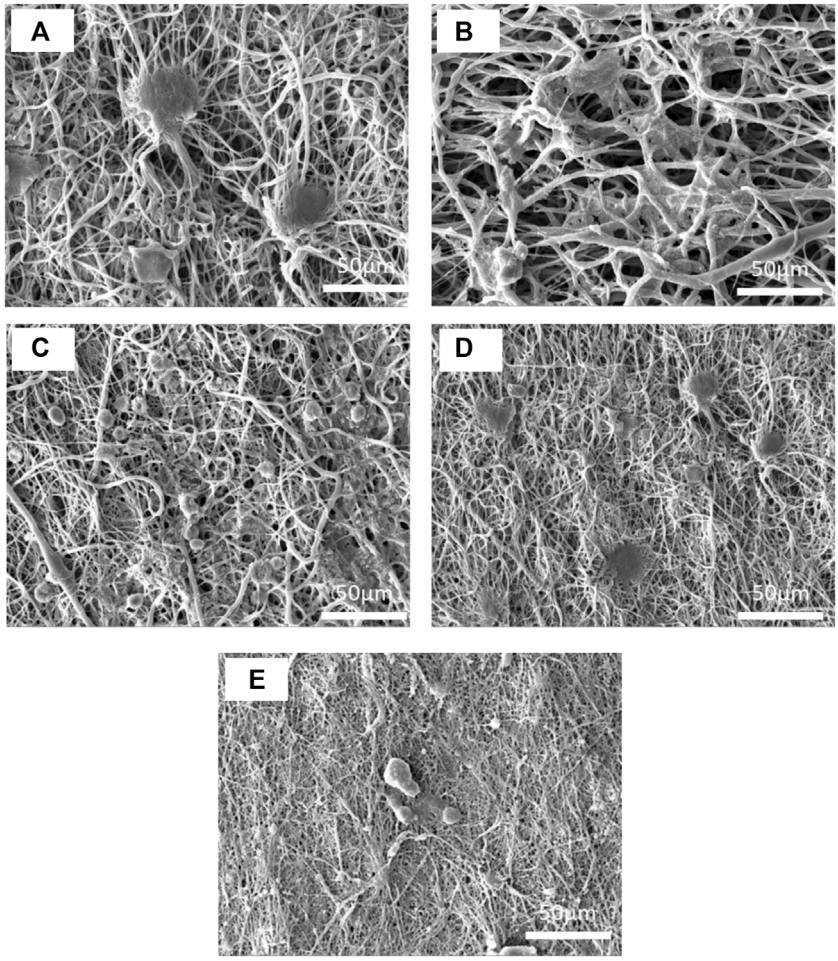

FIGURE 13
SEM images of L 929 fibroblast cells on the electrospun nanofibers of **(A)** PCL15, **(B)** PCL15CS3, **(C)** PCL15CS3ZnO1, **(D)** PCL15CS3ZnO1Cur1, and **(E)** PCL15CS3ZnO1Cur3 after 7 days cell seeding.

bacteria, respectively. These findings demonstrated that all nanofibers had appropriate antibacterial activity, making them viable scaffolds for use in wound dressings.

MMT and cell adhesion assay

In order to study the cell viability of electrospun scaffolds, L929 cells were cultured directly on the nanofibers for 24 h. The cell viability of electrospun nanofibers is shown in Figure 12. In the case of Cur-free samples, cell viability was greater than 80%, demonstrating that there was no cytotoxicity. However, cell viability is decreased by the addition of ZnO and Cur. In other words, Cur inhibited the proliferation and survival of L929 cells in a dose-dependent manner.

The cell morphology on the electrospun nanofibers is illustrated in Figure 13. Despite the pure PCL15 sample having high cell adhesion, there were undesirable cell distributions on the electrospun mat. The increase in cell adhesion on PCL15CS3 nanofibers is due to the polysaccharide structure of CS and its higher hydrophilicity compared to PCL. Cell shrinking and the spherical phenotype of cells are early signs of apoptosis. According to this phenomenon, ZnO nanoparticles and Cur decreased cell adhesion and cell distribution which is in agreement with MTT results.

Conclusion

In this study, the PCL and CS mixture was successfully electrospun using a 15 wt% PCL and a 3 wt% CS in HFIP solvent to improve the hydrophilicity of PCL nanofibers for use in wound dressing applications. Afterward, Cur and ZnO were incorporated into the electrospun nanofibers, and their

structural, physicomechanical, antibacterial activity, and *in vitro* properties were investigated. SEM analysis showed smooth nanofibers with a bead-free morphology. The elemental analysis also proved a good distribution of ZnO in scaffolds. By adding ZnO, WVTR and nanofibers' tensile characteristics were significantly improved, while the highest water uptake value was achieved for the sample containing 3 wt% Cur. The Cur drug released rapidly and reached a steady state about 24 h. The Peppas model provided the best fitting results on experimental data. Simultaneous incorporation of Cs, ZnO, and Cur effectively inhibited bacterial growth. The outcomes showed that electrospun nanofibers made of PCL, CS, ZnO, and Cur had a high potential for use as wound dressings.

Data availability statement

The original contributions presented in the study are included in the article/Supplementary Material, further inquiries can be directed to the corresponding author.

Author contributions

PM: Investigation, data curation, formal analysis, writing-original draft, HN: Methodology, conceptualization, supervision, project administration, ZA: Methodology, conceptualization, supervision, AR: Conceptualization, validation, formal analysis, Writing—review and editing.

Conflict of interest

The authors declare that the research was conducted in the absence of any commercial or financial relationships that could be construed as a potential conflict of interest.

Publisher's note

All claims expressed in this article are solely those of the authors and do not necessarily represent those of their affiliated organizations, or those of the publisher, the editors and the reviewers. Any product that may be evaluated in this article, or claim that may be made by its manufacturer, is not guaranteed or endorsed by the publisher.

Supplementary material

The Supplementary Material for this article can be found online at: https://www.frontiersin.org/articles/10.3389/fbioe.2022.1027351/full#supplementary-material

References

Afshar, S., Rashedi, S., Nazockdast, H., and Ghazalian, M. (2019). Preparation and characterization of electrospun poly (lactic acid)-chitosan core-shell nanofibers with a new solvent system. *Int. J. Biol. Macromol.* 138, 1130–1137. doi:10.1016/j.ijbiomac.2019.07.053

Aidun, A., Safaei Firoozabady, A., Moharrami, M., Ahmadi, A., Haghighipour, N., Bonakdar, S., et al. (2019). Graphene oxide incorporated polycaprolactone/chitosan/collagen electrospun scaffold: Enhanced osteogenic properties for bone tissue engineering. *Artif. Organs* 43 (10), E264–E81. doi:10.1111/aor.13474

Al-Bishari, A. M., Al-Shaaobi, B. A., Al-Bishari, A. A., Al-Baadani, M., Yu, L., Shen, J., et al. (2022). Vitamin D and curcumin-loaded PCL nanofibrous for engineering osteogenesis and immunomodulatory scaffold. *Front. Bioeng. Biotechnol.* 10, 975431. doi:10.3389/fbioe.2022.975431

Alimohammadi, M., Fakhraei, O., Moradi, A., Kabiri, M., Moradi, A., Passandideh-Fard, M., et al. (2022). Controlled release of azithromycin from polycaprolactone/chitosan nanofibrous membranes. *J. Drug Deliv. Sci. Technol.* 71, 103246. doi:10.1016/j.jddst.2022.103246

Babaei, A., Haji Abdolrasouli, M., and AjjoTCM, R. (2022). Polylactic acid/polycaprolactone bionanocomposites containing zinc oxide nanoparticles: Structure, characterization and cytotoxicity assay. *J. Thermoplast. Compos. Material* 2022, 08927057221118823. doi:10.1177/08927057221118823

Bakhsheshi-Rad, H. R., Hamzah, E., Ying, W. S., Razzaghi, M., Sharif, S., Ismail, A. F., et al. (2021). Improved bacteriostatic and anticorrosion effects of polycaprolactone/chitosan coated magnesium via incorporation of zinc oxide. *Materials* 14 (8), 1930. doi:10.3390/ma14081930

Bolaina-Lorenzo, E., Martínez-Ramos, C., Monleón-Pradas, M., Herrera-Kao, W., Cauich-Rodríguez, J. V., and Cervantes-Uc, J. M. J. B. M. (2016). Electrospun polycaprolactone/chitosan scaffolds for nerve tissue engineering: Physicochemical characterization and schwann cell biocompatibility. *Biomed. Mat.* 12 (1), 015008. doi:10.1088/1748-605x/12/1/015008

Chen, Z., Mo, X., He, C., and Wang, H. (2008). Intermolecular interactions in electrospun collagen–chitosan complex nanofibers. *Carbohydr. Polym.* 72 (3), 410–418. doi:10.1016/j.carbpol.2007.09.018

Chen, H., Xing, X., Tan, H., Jia, Y., Zhou, T., Chen, Y., et al. (2017). Covalently antibacterial alginate-chitosan hydrogel dressing integrated gelatin microspheres containing tetracycline hydrochloride for wound healing. *Mater. Sci. Eng. C* 70, 287–295. doi:10.1016/j.msec.2016.08.086

De Prá, M. A. A., Ribeiro-do-Valle, R. M., Maraschin, M., and Veleirinho, B. (2017). Effect of collector design on the morphological properties of polycaprolactone electrospun fibers. *Mater. Lett.* 193, 154–157. doi:10.1016/j.matlet.2017.01.102

Dwivedi, R., Kumar, S., Pandey, R., Mahajan, A., Nandana, D., Katti, D. S., et al. (2020). Polycaprolactone as biomaterial for bone scaffolds: Review of literature. *J. Oral Biol. Craniofacial Res.* 10 (1), 381–388. doi:10.1016/j.jobcr.2019.10.003

Fahimirad, S., Abtahi, H., Satei, P., Ghaznavi-Rad, E., Moslehi, M., and Ajcp, G. (2021). Wound healing performance of PCL/chitosan based electrospun nanofiber electrosprayed with curcumin loaded chitosan nanoparticles. *Carbohydr. Polym.* 259, 117640. doi:10.1016/j.carbpol.2021.117640

Ghaee, A., Bagheri-Khoulenjani, S., Afshar, H. A., and Bogheiri, H. (2019). Biomimetic nanocomposite scaffolds based on surface modified PCL-nanofibers containing curcumin embedded in chitosan/gelatin for skin regeneration. *Compos. Part B Eng.* 177, 107339. doi:10.1016/j.compositesb.2019.107339

Ghazalian, M., Afshar, S., Rostami, A., Rashedi, S., and Bahrami, S. H. (2022). Fabrication and characterization of chitosan-polycaprolactone core-shell nanofibers containing tetracycline hydrochloride. *Colloids Surfaces A Physicochem. Eng. Aspects* 636, 128163. doi:10.1016/j.colsurfa.2021.128163

Hashemi, S-S., Saadatjo, Z., Mahmoudi, R., Delaviz, H., Bardania, H., Rajabi, S-S., et al. (2021). Preparation and evaluation of polycaprolactone/chitosan/Jaft

biocompatible nanofibers as a burn wound dressing. *Burns* 4179, 00362–00364. doi:10.1016/j.burns.2021.12.009

Hewlings, S. J., and Kalman, D. S. J. F. (2017). Curcumin: A review of its effects on human health. *Foods* 6 (10), 92. doi:10.3390/foods6100092

Huang, C., Xu, X., Fu, J., Yu, D-G., and Liu, Y. J. P. (2022). Recent progress in electrospun polyacrylonitrile nanofiber-based wound dressing. *Polym. (Basel).* 14 (16), 3266. doi:10.3390/polym14163266

Janmohammadi, M., and Nourbakhsh, M. (2019). Electrospun polycaprolactone scaffolds for tissue engineering: A review. *Int. J. Polym. Mater. Polym. Biomaterials* 68 (9), 527–539. doi:10.1080/00914037.2018.1466139

Jia, Y-T., Gong, J., Gu, X-H., Kim, H-Y., Dong, J., and Shen, X-Y. (2007). Fabrication and characterization of poly (vinyl alcohol)/chitosan blend nanofibers produced by electrospinning method. *Carbohydr. Polym.* 67 (3), 403–409. doi:10.1016/j.carbpol.2006.06.010

Kakoria, A., and Sinha-Ray, S. (2018). A review on biopolymer-based fibers via electrospinning and solution blowing and their applications. *Fibers* 6 (3), 45. doi:10.3390/fib6030045

Karakas, K., Celebioglu, A., Celebi, M., Uyar, T., and Zahmakiran, M. (2017). Nickel nanoparticles decorated on electrospun polycaprolactone/chitosan nanofibers as flexible, highly active and reusable nanocatalyst in the reduction of nitrophenols under mild conditions. *Appl. Catal. B Environ.* 203, 549–562. doi:10.1016/j.apcatb.2016.10.020

Karthikeyan, C., Varaprasad, K., Akbari-Fakhrabadi, A., Hameed, A. S. H., and Rjcp, S. (2020). Biomolecule chitosan, curcumin and ZnO-based antibacterial nanomaterial, via a one-pot process. *Carbohydr. Polym.* 249, 116825. doi:10.1016/j.carbpol.2020.116825

Keyvani, A., Zamani, M., Bahamirian, M., Nikoomanzari, E., Fattah-alhosseini, A., and Sina, H. (2021). Role of incorporation of ZnO nanoparticles on corrosion behavior of ceramic coatings developed on AZ31 magnesium alloy by plasma electrolytic oxidation technique. *Surfaces Interfaces* 22, 100728. doi:10.1016/j.surfin.2020.100728

Korniienko, V., Husak, Y., Radwan-Pragłowska, J., Holubnycha, V., Samokhin, Y., Yanovska, A., et al. (2022). Impact of electrospinning parameters and post-treatment method on antibacterial and antibiofilm activity of chitosan nanofibers. *Molecules* 27 (10), 3343. doi:10.3390/molecules27103343

Lao, L. L., Venkatraman, S. S., and Peppas, N. A. (2008). Modeling of drug release from biodegradable polymer blends. *Eur. J. Pharm. Biopharm.* 70 (3), 796–803. doi:10.1016/j.ejpb.2008.05.024

Lou, C-W., Lin, J-H., Yen, K-C., Lu, C-T., and Lee, C-Y. (2008). Preparation of polyethylene oxide/chitosan fiber membranes by electrospinning and the evaluation of biocompatibility. *Text. Res. J.* 78 (3), 254–257. doi:10.1177/0040517507089752

Mendes, A. C., Stephansen, K., and Chronakis, I. S. J. F. H. (2017). Electrospinning of food proteins and polysaccharides. *Food Hydrocoll.* 68, 53–68. doi:10.1016/j.foodhyd.2016.10.022

Mirmusavi, M. H., Ahmadian, M., and Karbasi, S. (2022). Polycaprolactone-chitosan/multi-walled carbon nanotube: A highly strengthened electrospun nanocomposite scaffold for cartilage tissue engineering. *Int. J. Biol. Macromol.* 209, 1801–1814. doi:10.1016/j.ijbiomac.2022.04.152

Mitra, S., Mateti, T., Ramakrishna, S., and Laha, A. J. J. (2022). A review on curcumin-loaded electrospun nanofibers and their application in modern medicine. *JOM (1989)* 74 (9), 3392–3407. doi:10.1007/s11837-022-05180-9

Nandhini, G., Nivedha, B., Pranesh, M., and Karthega, M. (2020). Study of polycaprolactone/curcumin loaded electrospun nanofibers on AZ91 magnesium alloy. *Mater. Today Proc.* 33, 2170–2173. doi:10.1016/j.matpr.2020.03.327

Ono, K., Saito, Y., Yura, H., Ishikawa, K., Kurita, A., Akaike, T., et al. (2000). Photocrosslinkable chitosan as a biological adhesive. *J. Biomed. Mat. Res.* 49 (2), 289–295. doi:10.1002/(sici)1097-4636(200002)49:2<289:aid-jbm18>3.0.co;2-m

Pekdemir, M. E., Öner, E., Kök, M., and Qader, I. (2021). Thermal behavior and shape memory properties of PCL blends film with PVC and PMMA polymers. *Iran. Polym. J.* 30 (6), 633–641. doi:10.1007/s13726-021-00919-8

Pillai, C., and Sharma, C. P. (2009). Electrospinning of chitin and chitosan nanofibres. *Trends Biomater. Artif. Organs* 22 (3), 179–201.

Prasad, S., DuBourdieu, D., Srivastava, A., Kumar, P., and Lall, R. (2021). Metal–curcumin complexes in therapeutics: An approach to enhance pharmacological effects of curcumin. *Int. J. Mol. Sci.* 22 (13), 7094. doi:10.3390/ijms22137094

Pulla Reddy, A. C., Sudharshan, E., Appu Rao, A., and Lokesh, B. J. L. (1999). Interaction of curcumin with human serum albumin—A spectroscopic study. *Lipids* 34 (10), 1025–1029. doi:10.1007/s11745-999-0453-x

Qasim, S., Zafar, M., Najeeb, S., Khurshid, Z., Shah, A., Husain, S., et al. (2018). Electrospinning of chitosan-based solutions for tissue engineering and regenerative medicine. *Int. J. Mol. Sci.* 19 (2), 407. doi:10.3390/ijms19020407

Radisavljevic, A., Stojanovic, D. B., Perisic, S., Djokic, V., Radojevic, V., Rajilic-Stojanovic, M., et al. (2018). Cefazolin-loaded polycaprolactone fibers produced via different electrospinning methods: Characterization, drug release and antibacterial effect. *Eur. J. Pharm. Sci.* 124, 26–36. doi:10.1016/j.ejps.2018.08.023

Rahimi, M., Valeh-e-Sheyda, P., and Rashidi, H. (2017). Statistical optimization of curcumin nanosuspension through liquid anti-solvent precipitation (LASP) process in a microfluidic platform: Box-Behnken design approach. *Korean J. Chem. Eng.* 34 (11), 3017–3027. doi:10.1007/s11814-017-0201-3

Saatcioglu, E., Ulag, S., Sahin, A., Yilmaz, B. K., Ekren, N., Inan, A. T., et al. (2021). Design and fabrication of electrospun polycaprolactone/chitosan scaffolds for ligament regeneration. *Eur. Polym. J.* 148, 110357. doi:10.1016/j.eurpolymj.2021.110357

Semitela, Â., Girão, A. F., Fernandes, C., Ramalho, G., Bdikin, I., Completo, A., et al. (2020). Electrospinning of bioactive polycaprolactone-gelatin nanofibres with increased pore size for cartilage tissue engineering applications. *J. Biomater. Appl.* 35, 471–484. doi:10.1177/0885328220940194

Shahrousvand, M., Haddadi-Asl, V., and Shahrousvand, M. (2021). Step-by-step design of poly (ε-caprolactone) /chitosan/Melilotus officinalis extract electrospun nanofibers for wound dressing applications. *Int. J. Biol. Macromol.* 180, 36–50. doi:10.1016/j.ijbiomac.2021.03.046

Shahrousvand, M., Hajikhani, M., Nazari, L., Aghelinejad, A., Shahrousvand, M., Irani, M., et al. (2022). Preparation of colloidal nanoparticles PVA-PHEMA from hydrolysis of copolymers of PVAc-PHEMA as anticancer drug carriers. *Nanotechnology* 33, 275603. doi:10.1088/1361-6528/ac6089

Shirzaei Sani, I., Rezaei, M., Baradar Khoshfetrat, A., and Razzaghi, D. (2021). Preparation and characterization of polycaprolactone/chitosan-g-polycaprolactone/hydroxyapatite electrospun nanocomposite scaffolds for bone tissue engineering. *Int. J. Biol. Macromol.* 182, 1638–1649. doi:10.1016/j.ijbiomac.2021.05.163

Sun, H., Mei, L., Song, C., Cui, X., and Wang, P. J. B. (2006). The *in vivo* degradation, absorption and excretion of PCL-based implant. *Biomaterials* 27 (9), 1735–1740. doi:10.1016/j.biomaterials.2005.09.019

Tajdari, A., Babaei, A., Goudarzi, A., Partovi, R., and Rostami, A. J. P. C. (2021). Hybridization as an efficient strategy for enhancing the performance of polymer nanocomposites. *Polym. Compos.* 42 (12), 6801–6815. doi:10.1002/pc.26341

Van der Schueren, L., Steyaert, I., De Schoenmaker, B., and De Clerck Kjcp (2012). Polycaprolactone/chitosan blend nanofibres electrospun from an acetic acid/formic acid solvent system. *Carbohydr. Polym.* 88 (4), 1221–1226. doi:10.1016/j.carbpol.2012.01.085

Varshosaz, J., Sajadi-Javan, Z. S., Kouhi, M., and Mirian, M. (2021). Effect of bassorin (derived from gum tragacanth) and halloysite nanotubes on physicochemical properties and the osteoconductivity of methylcellulose-based injectable hydrogels. *Int. J. Biol. Macromol.* 192, 869–882. doi:10.1016/j.ijbiomac.2021.10.009

Wanjun, T., Cunxin, W., and Donghua, C. (2005). Kinetic studies on the pyrolysis of chitin and chitosan. *Polym. Degrad. Stab.* 87 (3), 389–394. doi:10.1016/j.polymdegradstab.2004.08.006

Xu, J., Zhang, J., Gao, W., Liang, H., Wang, H., and Li, J. (2009). Preparation of chitosan/PLA blend micro/nanofibers by electrospinning. *Mater. Lett.* 63 (8), 658–660. doi:10.1016/j.matlet.2008.12.014

Yin, J., and Xu, L. (2020). Batch preparation of electrospun polycaprolactone/chitosan/aloe vera blended nanofiber membranes for novel wound dressing. *Int. J. Biol. Macromol.* 160, 352–363. doi:10.1016/j.ijbiomac.2020.05.211

Zhang, T., Nie, M., and Li, Y. (2022). Biotechnology. Current advances and future perspectives of advanced polymer processing for bone and tissue engineering. *Morphol. Control Appl.* 10, 895766. doi:10.3389/fbioe.2022.895766

Zhu, J., Ye, H., Deng, D., Li, J., and Wu, Y. (2020). Electrospun metformin-loaded polycaprolactone/chitosan nanofibrous membranes as promoting guided bone regeneration membranes: Preparation and characterization of fibers, drug release, and osteogenic activity *in vitro*. *J. Biomater. Appl.* 34 (9), 1282–1293. doi:10.1177/0885328220901807

Zou, Y., Zhang, C., Wang, P., Zhang, Y., and Zhang, H. (2020). Electrospun chitosan/polycaprolactone nanofibers containing chlorogenic acid-loaded halloysite nanotube for active food packaging. *Carbohydr. Polym.* 247, 116711. doi:10.1016/j.carbpol.2020.116711

frontiers | Frontiers in Molecular Biosciences

TYPE Original Research
PUBLISHED 17 October 2022
DOI 10.3389/fmolb.2022.1043277

OPEN ACCESS

EDITED BY
Mahmood Barani,
Kerman University of Medical Sciences, Iran

REVIEWED BY
Maryam Roostaee,
Shahid Bahonar University of Kerman, Iran
Narendra Pal Singh Chauhan,
Bhupal Nobles University, India
Mohsen Chiani,
Pasteur Institute of Iran (PII), Iran

*CORRESPONDENCE
Seyed Morteza Naghib,
Naghib@iust.ac.ir
Fateme Haghiralsadat,
fhaghirosadat@gmail.com

SPECIALTY SECTION
This article was submitted to Nanobiotechnology, a section of the journal Frontiers in Molecular Biosciences

RECEIVED 13 September 2022
ACCEPTED 04 October 2022
PUBLISHED 17 October 2022

CITATION
Abtahi NA, Naghib SM, Haghiralsadat F, Akbari Edgahi M and Askari E (2022), A comparative study on biopharmaceutical function of curcumin and miR-34a by multistimuli-responsive nanoniosome carrier: In-vitro and in-vivo.
Front. Mol. Biosci. 9:1043277.
doi: 10.3389/fmolb.2022.1043277

A comparative study on biopharmaceutical function of curcumin and miR-34a by multistimuli-responsive nanoniosome carrier: *In-vitro* and *in-vivo*

Najmeh Alsadat Abtahi[1], Seyed Morteza Naghib[1]*, Fateme Haghiralsadat[2]*, Mohammadmahdi Akbari Edgahi[1] and Esfandyar Askari[3]

[1]Nanotechnology Department, School of Advanced Technologies, Iran University of Science and Technology, Tehran, Iran, [2]Medical Nanotechnology and Tissue Engineering Research Center, Yazd Reproductive Sciences Institute, Shahid Sadoughi University of Medical Sciences, Yazd, Iran, [3]Biomaterials and Tissue Engineering Research Group, Department of Interdisciplinary Technologies, Breast Cancer Research Center, Motamed Cancer Institute, ACECR, Tehran, Iran

This research conducted a comparative study on nanoscaled niosomal structures consisting of Tween-80, Tween-60, cholesterol, and dioleoyl-3-trimethylammonium propane (DOTAP). Thin-film hydration technique was used for the preparation and entrapment of curcumin and miRNA in niosomal formulations for enhancing the stability and delivery rate of the agents. Herein, the influence of Tween-80, Tween-60, cholesterol, and DOTAP on the entrapment efficiency (EE%) of curcumin and the physicochemical properties of the carrier are fully discussed. The optimum engineered formulation resulted in a positive charge of +11.23 mV, high EE (100%), smooth surface, spherical shape, small diameter (90 nm), and good stability in physiological buffers. Also, an accelerated cellular uptake, as well as drug release in PBS (pH 7.4, 37°C) after 72 h, were observed. The cytotoxic activity of curcumin (Cur)/miR-34a-loaded nanoparticles was determined by the MTT assay. The results displayed an improved cytotoxic activity of Cur-niosome towards cancer cells compared to free-dispersed Cur. The uptake of Cur-loaded niosome by A280s and A280cp-1 cancer cell lines faced 2.5 folds drop in the concentration compared to its free form. Generally, Cur-niosome exhibits a significant accumulation of superior anti-cancer properties. Likewise, the cytotoxicity of miR-34a-niosome against tumor cells was higher in comparison with its free form. The anti-cancer effects of the gene/drug delivery were investigated in the 4T1 xenografted Balb/C mouse tumor model. According to the *in vitro* and *in vivo* results, gene delivery from the modified niosome nanoparticles was distinctly greater than Cur delivery. Therefore, it was concluded that encapsulation of genes in the nano-niosomal delivery system is a promising procedure for the treatment of cancer cells.

KEYWORDS

curcumin, gene expression, coadminstration, nanopartcicles, chemotherapy, niosome

1 Introduction

While an alternation occurs in biological systems, there is a tendency for cells to lose their normal function and begin to do abnormal activities. Herein, p53 is a tumor suppressor protein that is highly critical in cell response to stresses such as DNA injury and oncogenes activation. Many tumor malignancies arise when their functionality is faced with problems (Boutelle and Attardi, 2021). P53 can modify specific gene expression captured *via* apoptosis, improve DNA repair, and prevent angiogenesis (Merlin et al., 2021).

As stated by many studies, the most frequent miRNA which is induced *via* this tumor suppressor protein is the miR-34 group (Sargolzaei et al., 2020). The anti-cancer mechanism of this category of miRNAs is based on the suppression of tumors which approves their potential for anti-tumoral purposes (Najminejad et al., 2019). Generally, microRNAs or miRNAs are small-sized RNAs with non-coding ability that strongly influence tumorigenesis, apoptosis, cell proliferation, and differentiation. They can alter gene expression in the post-transcriptional stage (Tricoli and Jacobson, 2007). Several pieces of research displayed a significant reduction in the level of specific miRNAs which operate as tumor suppressors within cancerous areas. From experimental findings, miRNAs with such properties are categorized in 15a, 16-1, 143, let-7, 145, and 34 (Pidíkova et al., 2020). The miR-34 family involves important mediators with tumor-suppressing ability. Various documents indicate that through ectopic expression of miR-34s, many factors, including proliferation, invasion, metastasis, and epithelial-to-mesenchymal transition, are eliminated. Besides, an initial viral vector in miR-34 delivery is critical (Flood et al., 2019). Two commonly used materials are niosomes and liposomes to deliver miRNA to the cancer site. In recent years, the use of these vesicular carriers in systemic delivery applications has received a lot of interest because of their acceptable entrapment efficacy, reduced side effects, increased drug solubility, long-term blood circulation, and capability to target a specific spot (Abtahi et al., 2022).

Curcumin (Cur) has also attracted scientific research in terms of delivery applications. Cur is a yellowish natural diphenolic compound derived from the rhizome of Curcuma Longa, turmeric, which has been widely used as a spice or as a medicine in Asian countries (India, China, and Indonesia) for the treatment of a variety of illnesses, including stomach disorders, skin diseases, bile formation problems, anorexia, rhinitis, sinusitis, cough, diabetic lesions, liver function problems, and rheumatism.

Polyphenol was revealed to have numerous pharmacological effects in 1970, including antibacterial, anti-inflammatory, antioxidant, and anti-tumor capabilities (Chauhan et al., 2019; He et al., 2021; Hassan et al., 2022; Moghadam et al., 2022). Cur's anti-cancer mechanism on malignant cells is based on complicated molecular signaling pathways, including estrogen receptor, proliferative pathways, and human epidermal growth factor 2 receptor, and eventually, induces apoptosis, according to recent reviews in this field (Wang Y et al., 2016; Kunnumakkara et al., 2017; Talib et al., 2018; Farhadihosseinabadi et al., 2019; Song et al., 2019). Moreover, Cur is a regulator of the p53 protein in breast cancer (Talib et al., 2018). Cur has been shown to regulate several cell signaling pathways, including cell survival (c-IAP1, cFLIP, Bcl-xL, Bcl-2, XIAP), cell multiplication (cyclin D1, c-myc), caspase stimulation (caspase-3, 8, 9), protein kinase (JNK, Akt, and AMPK), mitochondrial, death receptor (DR4, DR5), and tumor inhibitor (Yen et al., 2019).

Despite its positive characteristics, Cur free use in clinical cancer therapy is limited because of its low water solubility, poor oral absorption, and rapid metabolism. As a result, scientists have been looking for novel ways to address the aforementioned shortcomings (Chendil et al., 2004; Mozafari et al., 2015; Wong et al., 2019). Nanotechnology helps to solve these issues by establishing cancer diagnostics and treatment (Meng et al., 2020; Khan et al., 2021; Yi et al., 2021). The creation of drug delivery systems (DDSs) aids in the distribution of low-affinity medications to tissues and cells, improving treatment effectiveness and reducing systemic adverse effects at the target location (Meng et al., 2020; Eftekhari et al., 2021). The excellent efficacy of encapsulating, managing drug release, improving drug solvability, conveying hydrophilic and hydrophobic pharmaceuticals, and longer blood circulation given by these carriers have made vesicular medication administration popular in recent decades (Wu et al., 2021; Almansob et al., 2022). Due to its ability to capture both hydrophobic and hydrophilic medicines within its bilayer *via* non-polar and core cavity regions, niosomes have attracted increasing scientific interest as valuable DDSs in recent years. Niosome vesicles are non-ionic multilamellar or unilamellar surfactants ranging from 10 to 1,000 nm and are non-immunogenic, biodegradable, and biocompatible. Since the non-ionic surfactants used for the preparation of niosome are cheaper than phospholipids, they also have taken a larger part in nanotechnology. Niosomes are being studied for the delivery of drugs like Roxithromycin, Bovine Serum Albumin, and Doxorubicin, as well as siRNA/miRNA delivery. As a result, various nanocarrier formulations for Cur have been introduced, including liposomes and niosomes. Similarly, manifold documents on the nano-potential carriers for transporting other therapeutic medicines, such as miRNA, have been published.

Curcumin and miR-34a were therefore incorporated into novel niosomal nanoformulations in the current work to boost

cancer cell targeting while lowering harmful effects on healthy cells. To do this, we created and improved multiple nano-drug formulations, described them chemically and physically, and then tested their biological effects on normal and cancer cell lines. Co-delivery refers to the use of curcumin and miR-34a in the same carrier for medication delivery. Curcumin and miR-34a packaged in niosomes were delivered together, and the impact was studied *in vitro* and *in vivo* (Nikniaz et al., 2021).

2 Materials and methods

2.1 Materials

Herein, Tween-80 (T-80) and Tween-60 (T-60) (DaeJung Chemicals & Metals, Seoul, South Korea), DMSO (3-[4,5-dimethylthiazol-2-yl]-2), curcumin, cholesterol, and MTT (3-[4,5-dimethylthiazol-2-yl]-2,5 diphenyl tetrazolium bromide) (Sigma-Aldrich, Missouri, United States), and DOTAP (1,2-dioleoyl-3-trimethylammonium-propane), were acquired for this study. Human ovary cancer cells (Pasteur Institute, Tehran, Iran), FBS, antibiotics, PBS, cell culture medium (RPMI 1640), trypsin, and sodium pyruvate were also provided for the experiment (Gibco, New York, United States). All the chemicals were of analytical grade and no extra purification process was applied for salts, chemicals, and solvents, except in particular cases. The order synthesis of miR-34a primer was forward, CTTGAACTCCTGGGGCCTGAAG; reverse, GCCAAAGAAACACTCACAGCT, and Eurofins Genomics Ebersberg were utilized for this reason.

2.2 Preparation of niosomal delivery system

In the preparation of niosomes, thin-film hydration technique was employed. Cholesterol and T-80 were first computed precisely and then dissolved in 100 ml of chloroform. Then, a rotating flash evaporator (Ultrasonics GmbH, Heidolph, Germany) was conducted to form a thin lipid at low pressures. Afterward, the obtained film underwent 3 ml of PBS for the hydration process at pH 7.4 and 60°C. To decrease the mean size of vesicles, a microtip probe sonicator was utilized to operate the sonication process of hydrated lipids for 30 min. Then, the niosome formula was monitored to detect the physical properties. In the next step, for achieving enhanced stability of niosome formula cationic lipid, DOTAP, was added. Besides, forming a thin layer on a rotating evaporator resulted in eliminating organic solvent at 45°C. For obtaining niosome suspension, the hydration of the thin layers was achieved by adding PBS at pH 7.4 and 60°C for 45 min. Finally, the niosomal solution was sonicated using (Ultrasonics GmbH, Hielscher, Germany) for 15 min to reduce the average particle size.

2.3 Characterization of nanoparticles

To assess the overall characteristics of niosomes, including particle size, zeta potential, and poly-dispersity index (PDI), dynamic light scattering (DLS) analysis was conducted by Brookhaven Corp Instrument (Brookhaven Instruments; Holtsville; NY: United States). Likewise, Atomic force microscopy (AFM), Scanning electron microscopy (SEM), and Transmission electron microscopy TEM (AFM5100N, HITACHI) were conducted to assess the morphology of the gene and drug-loaded niosome. The resulting data and mean values were used for triplicate measurement.

2.4 Encapsulation efficiency of curcumin

To measure the encapsulation efficiency, first, the unencapsulated drugs were subtracted from the loaded niosomes by immersing them into the dialysis cellulose membrane tubing (12 kDa MWCO) against 4°C PBS solution. Afterward, the niosomes were lysed using isopropanol and a UV-Vis spectrophotometer, (T80+, PG Instruments, United Kingdom) 429 nm wavelength, was utilized to determine the encapsulation efficiency according to the following equation:

$$\text{Encapsulation Efficiency } (\%) = \frac{\text{The quantity of Cur capsulized inside niosomes}}{\text{The total quantity of Cur added}} \times 100$$

2.5 Drug release

To assess the released quantity of Cur from niosomes, a 12 kDa MWCO dialysis tube was employed (Shaker et al., 2015). For this purpose, 10 mM PBS was used as the buffer solution, and samples were held at 25, 37, and 42°C for 72 h, at pH values of 5.5, 6.5, and 7.4. Afterward, all samples were individually suspended into the dialysis bag and stirred constantly. At each interval, aliquots of PBS were taken and the same volume of PBS was inserted. Ultimately, UV-Vis spectrophotometry was employed to determine the release rate (Shaker et al., 2015).

2.6 Leakage stability

To assess the effect of long-lasting storage on the leakage behavior of miRNA from nanocomplexes, samples were held at 4°C for 2 months. Afterward, nanometer the stability of all samples was recorded using spectrophotometric at 260 nm.

2.7 Physical stability

The physical characteristic of Cur-loaded niosome, parameters such as the size of particles, PDI, residual

quantity, and zeta potential were obtained using DLS analysis through Zeta PALS zeta potential and particle size analyzer (Br particle size distribution, Brookhaven Instruments, New York, United States) at intervals of 15, 30, and 60 days.

2.8 Particle morphology

The morphology of nanoparticles was examined by subjecting a drop of the nanoparticle solution to negative staining with 1% (w/v) phosphor tungstic sodium solution and AFM, SEM, and TEM were performed.

2.9 Cell culture

To culture cells, first, human ovarian cancer A2780s and A2780cp-1 cells (Iranian Biological Resource Center, Tehran, Iran) were preserved as monolayer cultures in a mixture of Ham and RPMI-1640 medium (Ino Clon, Tehran, Iran) augmented with 2 mM of GlutaMAX™-I (100X), 10% FBS, and 1 mg/ml penicillin/streptomycin (Gibco, Massachusetts, United States). The MCF-10A cell line (Iranian Biological Resource Center, Tehran, Iran), a non-tumorigenic human breast epithelial cell line, was cultured in DMEM/F12 Ham's mixture enriched with 1 mg/ml of penicillin/streptomycin, 5% horse serum, 2 mM of Gluta MAX™-I (Gibco, Massachusetts, US), 100 ng/ml cholera toxin, 10 µg/ml insulin, EGF 20 ng/ml, and hydrocortisone 0.5 µg/ml (Sigma-Aldrich, Missouri, United States). The MCF-10A cells were utilized as the control group in all tests.

2.10 Cytotoxicity and cell growth

The cytotoxic activity of Cur-loaded nanoparticles was clarified by MTT assay (Sigma-Aldrich, Missouri, US) (Wang J et al., 2016; Xu et al., 2016). Briefly, cells were seeded in 96-well plates at 10,000 cells per well. After a day, 200 µL of a new media containing sequential dilutions of several formulations, including niosomal Cur, free Cur solution, and free niosome, was inserted into the cells. Then, all of the prepared samples were incubated for 1, 2, and 3 days (s). Next, in each 96-well plate, 20 ml of MTT (5 mg/ml in PBS) was added and followed by incubation at 37°C for 3 h for further verification. Next, the medium was carefully separated, instead, to suspend the produced formazan crystals, each well received 180 ml of dimethyl sulfoxide. Records of optical density in each well were conducted using EPOCH Microplate Spectrophotometer (synergy HTX, BioTek, Vermont, US) at the wavelengths of 570 and 630 nm.

The cytotoxic activity of samples was shown as the value of the Inhibitory Concentration (IC_{50}), which represents the least concentration of drug to inhibit 50% of cell growth compared to the control. The Cur IC_{50} levels as single drugs were estimated by Graph Pad Prism 6. The test was performed in triplicate.

2.11 Assessment of cellular uptake

A2780s and A2780cp-1 cells were seeded in 6-well plates at a concentration of 50,000 cells/well and kept in an incubator for 1 day to enable cell attachment. Next, different concentrations of Cur were added to wells. Then, cells were incubated for another 3 h followed by washing thrice with cold PBS and fixed with a mixed solution of methanol and citric acid (3:1) (Sigma-Aldrich, Missouri, United States). After staining with 4′,6-diamidino-2-phenylindole (DAPI, 0.125 µg/ml, Thermo Fisher Scientific, Massachusetts, US), cell images were obtained using fluorescent microscopy (BX61, Olympus, Japan) (Balakrishnan et al., 2009). The test was done only once.

2.12 Apoptosis assay

In apoptosis of cells, they were subjected to different samples as free Cur, free miRNA, niosomal Cur, and niosomal miRNA at IC_{50} concentration for all of them, and annexin V-FITC/PI double staining (Sigma-Aldrich, Missouri, United States) was performed to determine the dead cells. First, MCF-7 cells were seeded into 6-well plates at a concentration of 100,000 cells/well and incubated for 24 h. Afterward, for detaching the cells, 0.25% trypsin/EDTA was added to the wells and then they were centrifuged at 1,500 rpm for 3 min. Next, the pellet was dissolved in the ice-cold PBS at pH 7.4 and then 3 µl of Annexin V-FITC was inserted into the suspension. Ultimately, 3 µl of propidium iodide (PI) stock solution was inserted into the cells, followed by incubating for 30 min on ice. BD FACSCalibur instrument was used to analyze the flow cytometry and detect the stained cells.

2.13 *In vivo* experiments

To perform *in-vivo* examination according to NIH and IACUC guidelines, 35 six- to 8-week female BALB/c mice (Pasteur Institute, Tehran, Iran) with 20–25 g bodyweight were purchased and kept in a sterilized condition. First, each mouse was treated with 5×10^6 4T1 cells subcutaneously into the right flank. Next, they were randomly divided into 4 groups of 5 mice when the tumor reaches 100 mm^3. Free Cur and miRNA with 2.5 mg/kg and niosomal Cur and miRNA with 10 µg per mouse were injected within the tail vein of each group of mice. For the control group, normal saline was injected. The injections were repeated every 3 days up until 12 days and at each interval, the tumor size and bodyweight of each mouse were measured. All

mice were sacrificed on the 21st day. The tumor size was measured according to the equation (Abtahi et al., 2022):

$$V\ (mm^3) = \frac{LW^2}{2}$$

Where V represents the volume of the tumor, L and W are the lengths of the tumors, respectively. Also, the equation below was utilized to measure the inhibition rate (Abtahi et al., 2022):

$$\text{Tumor inhibition rate (TIR, \%)} = \frac{W_c - W_t}{W_c} \times 100$$

Where W_c and W_t represent the average weight of tumors in the control and treated groups, respectively.

2.14 Statistical analysis

Data were analyzed statistically using the GraphPad Prism6 software and reported as mean ± standard deviation. Student t-test was utilized to compare 2 independent groups, and multiple samples were compared by the ANOVA test. *p* values with less than 0.05, were considered as significant.

3 Results

Because of the widespread use of chemical pharmaceuticals and their negative side effects, interest in alternative therapies such as herbal medicines and gene therapy has grown. Herbal anticancer therapies have been pushed, including the isolation and identification of active plant components. New treatment tactics have recently switched to hybrid active agents, which are thought to be far more successful than separate forms. As a result of the reduced doses for each medicine, the treatment's efficacy improves while adverse effects diminish. Curcumin, a yellow pigment extracted from the rhizome of the turmeric plant, has a wide range of medicinal benefits. Curcumin has also been demonstrated to have anticancer properties. It was recently incorporated as a chemical prophylactic factor in the first phase of clinical research. Curcumin may make cancer cells more responsive to several therapies, including chemotherapy and gene therapy, as a new anticancer agent. Curcumin's therapeutic effectiveness, on the other hand, is hampered by its poor water solubility and, as a result, reduced therapeutic index. Nanotechnology is one of the powerful tools for increasing stability in aqueous solutions.

The therapeutic application of miRNAs has been documented in numerous research. However, their effectiveness is contingent on the carrier's ability to transport them to cancer cells. MiRNA should be protected from nuclease degradation in an optimal transport carrier under systematic circulation. All requirements are endosomal escape, biocompatibility, renal and hepatic clearance resistance, and reversible physical binding to miRNAs. As previously said, niosomes are better than phospholipid vesicles because of their high drug loading efficiency, biocompatibility, biodegradability, low cost of manufacture, lack of organic solvents, easy storage, and superior stability. Herein, curcumin and miR-34a were separately loaded in DOTAP-containing cationic niosomal formulations. Tween-80, a safe and healthful surfactant, and Tween-60, a commonly used surfactant in niosome synthesis, were used to make the niosome vesicles. The curcumin and gene entrapment efficiency, particle charge, and size of each formulation were all evaluated. Release profiles were obtained by releasing the curcumin in different buffers. The optimal formulation was tested in cytotoxicity, cellular uptake, gene expression, apoptosis, and *in vivo* tests to assess their significance in cancer therapy.

3.1 Characterization of nanocarriers

3.1.1 Curcumin entrapped niosomes: The effects of cholesterol on Curcumin's EE%

Curcumin delivery systems are optimized based on several parameters, including the nanocarrier size, zeta potential, and entrapment efficiency (EE%, Table 1). Cholesterol is a key element of niosomes that impact their physicochemical properties and stability. The EE of nanocarriers increased from 35.78 to 48.45% when cholesterol content was increased from 10 to 20% (F1 and F2), the zeta potential was modified from - 24.88 to -22.43 mv, and the size of nanocarriers dropped from 134.12 to 129.34 nm. The type of nonionic surfactant appears to be a critical factor in the influence of cholesterol percentage on niosome size. It has been reported that the rate of average size reduction by adding cholesterol depends on the surfactant type (Alemi et al., 2018).

3.1.2 The effects of T-60 and dioleoyl-3-trimethylammonium propane on Curcumin's EE%

For investigating the effect of T-60 on the EE%, zeta potential, and size of nanocarrier, the cholesterol concentration was kept constant, and T-60 was (30%) added to the formulation (F3). The entrapment of curcumin within the niosomes raised to 79% and reduced the nanocarrier average diameter. Interestingly, EE% of curcumin exceeded 90% when DOTAP was introduced into the formulation (F4 and 5). DOTAP also enhanced the zeta potential, positively charged, and reduced the size of the particles. Therefore, it was concluded that the Cur-niosome preparations comprising Tween-80: Tween-60:cholesterol:DOTAP with the molar ratio of 63:20: 10:7 (F5) owned the desirable properties based on the particle

TABLE 1 The effect(s) of T-80:T-60:cholesterol ratio on the EE%, PDI, zeta potential (mV), and particle size (nm) in Cur-niosome particles.

Code	Cur (μg)	T-80 (%)	T-60 (%)	Cholesterol (%)	DOTAP (%)	EE (%)	PDI	Zeta potential (mv)	Particle size (nm)
F1	500	90	—	10	—	35.87	0.20 ± 0.45	−24 ± 0.88	134 ± 0.12
F2	500	80	—	20	—	48.45	0.19 ± 0.56	−22 ± 0.43	129 ± 0.34
F3	500	60	30	10	—	79.44	0.18 ± 0.23	−19.6 ± 0.67	114.1 ± 0.023
F4	500	60	25	10	5	93.45	0.16 ± 0.76	+4.44 ± 0.49	98.23 ± 0.03
F5	500	63	20	10	7	99.91	0.15 ± 017	+11.23 ± 0.02	87.23 ± 0.03

TABLE 2 The effect(s) of T-80:T-60:cholesterol ratio on the PDI, zeta potential (mV), and particle size (nm) in miRNA-niosome particles.

Code	T-80 (%)	T-60 (%)	Cholesterol (%)	DOTAP (%)	PDI	Zeta potential (mv)	Particle size (nm)
F1	90	—	10	—	0.20 ± 0.45	−24 ± 0.88	134 ± 0.12
F2	80	—	20	—	0.19 ± 0.56	−22 ± 0.43	129 ± 0.34
F3	60	30	10	—	0.18 ± 0.23	−19.6 ± 0.67	114.1 ± 0.023
F4	60	20	10	10	0.168 ± 0.44	+13.04 ± 0.76	88.55 ± 0.44
F5	58	17	10	15	0.156 ± 0.23	+22.56 ± 0.11	81.45 ± 0.14
F6	F5 + miR-34a				0.173 ± 0.12	+8.23 ± 0.12	93.21 ± 0.34

size and EE%. The DLS assay indicated that the average diameter of F5 was 87.23 ± 234 nm at a homogenized pressure of 800 bar. Moreover, including DOTAP in the formulation made the size reduction and helped the vesicles to maintain the drugs and displayed no remarkable alterations in 2 months of storing compared to other formulations with respect to vesicle size zeta potential and EE%.

3.1.3 miR-34a entrapped niosomes

For preparing the miR-34a-niosome, almost the same material ratio used in F4, and F5 formulations of Cur-niosome, were employed. Because of their positive surface charge, positively charged lipids are frequently used to carry nucleic acids since these materials allow the spontaneous interconnection of negatively charged nucleic acids. The result is known as lipoplex. It has been shown that cationic lipids, such as 1,2-dioleoyl-3-trimethylammonium-propane (DOTAP), enhance positive loading on vesicles, making vesicles easier to connect with negative cell membranes *in vitro*. Due to their versatility, they are the most suitable gene carriers. In general, DOTAP-containing lipid vesicles have lower toxicities compared to those containing other kinds of lipids due to the inclusion of two ester linkages within the structure, says Balazs *et al.* (Balazs and Godbey, 2011). Likewise, with the addition of 10 and 15% DOTAP, particle size, charge, and zeta potential have changed. Therefore, it was concluded that the miRNA-niosome preparations comprising Tween-80:Tween-60:cholesterol:DOTAP with the molar ratio of 58:17:10:15 (F5) had the desirable property based on the zeta potential and particle size (Table 2).

3.2 Morphology of nanoparticles

The inner structure of drug-loaded niosomes was assessed by the AFM and shown in Figures 1A–F. The images were obtained from the optimal formula of niosomes in a sphere shape. SEM and TEM images were obtained in a similar way and shown in Figures 2A,B. In the images, niosome vesicles seemed to be spherical with smooth surfaces. The smooth surface provides the desired property for interaction with cells.

3.3 The *in-vitro* releasing pattern of cur-nanoparticles

The niosomes' *in vitro* drug release patterns in plasma and PBS were studied at 25°C, 37°C, and 42°C at pH values of 5.5, 7.4, and 9 (Figures 2C–H). Plasma was utilized to explore the release experiment in a nearly human-like environment. By modifying the solubility of the delivery system or cleaving pH-sensitive bonds upon a pH gradient, pH-sensitive delivery systems can lead to a site-specific release of medicinal payloads. This pH gradient, which may be found in a variety of bodily locations (including the tumor environment, the gastrointestinal tract, the vaginal area, and blood arteries), can be exploited as an endogenous stimulus for developing smart delivery systems and regulating medication release. The extracellular pH of cancer cells is lower than that of normal cells, whereas the intracellular pH of cancer cells is greater. As a result, the drug's

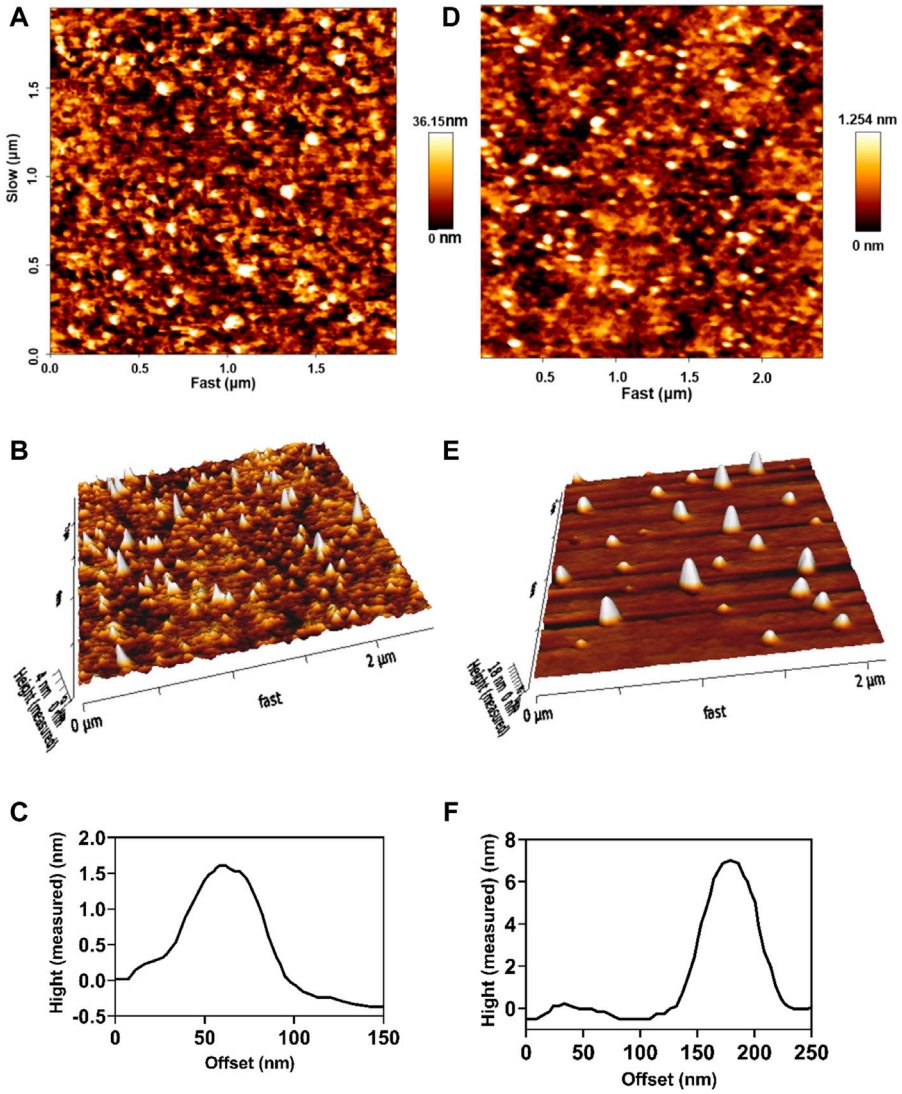

FIGURE 1
2D, 3D, and line analysis of Cur-niosomes as **(A–C)**, respectively. 2D, 3D, and line analysis of miRNA-niosomes as **(D–F)**, respectively.

release profile was studied under neutral, acidic, and alkaline pH environments. Every release profile is biphasic, with varying gradients. Cancer cells/tissues have a greater temperature than normal cells, which might be exploited to administer stimuli-responsive tumor-targeted drugs. At all of the pHs studied, the temperature influenced the release of curcumin from F5. For example, at pH 7.4, the release was 15.87, 19.84, and 23.76% at 25, 37, and 42°C in plasma, respectively. Furthermore, the data demonstrate that medication release is greater at acidic pH levels, which are typical of the tumor microenvironment than in neutral settings. Curcumin release from niosomal nanoformulation follows a two-phase pattern, according to *in vitro* release experiments. In the first phase, the medication is released quickly, followed by a slower release in the second phase. The dialysis bag or the medication size has no effect on the release. The initial rapid release is likely controlled by a diffusion mechanism caused by a curcumin gradient of concentration between the niosome and the buffer surrounding the dialysis bag, whereas the slow release in the second phase is caused by controlled release from the bilayer membrane of the niosomal formulation.

3.4 Physical stability assay

Curcumin is a flammable, water-insoluble chemical. Curcumin was integrated into cationic niosomes to improve

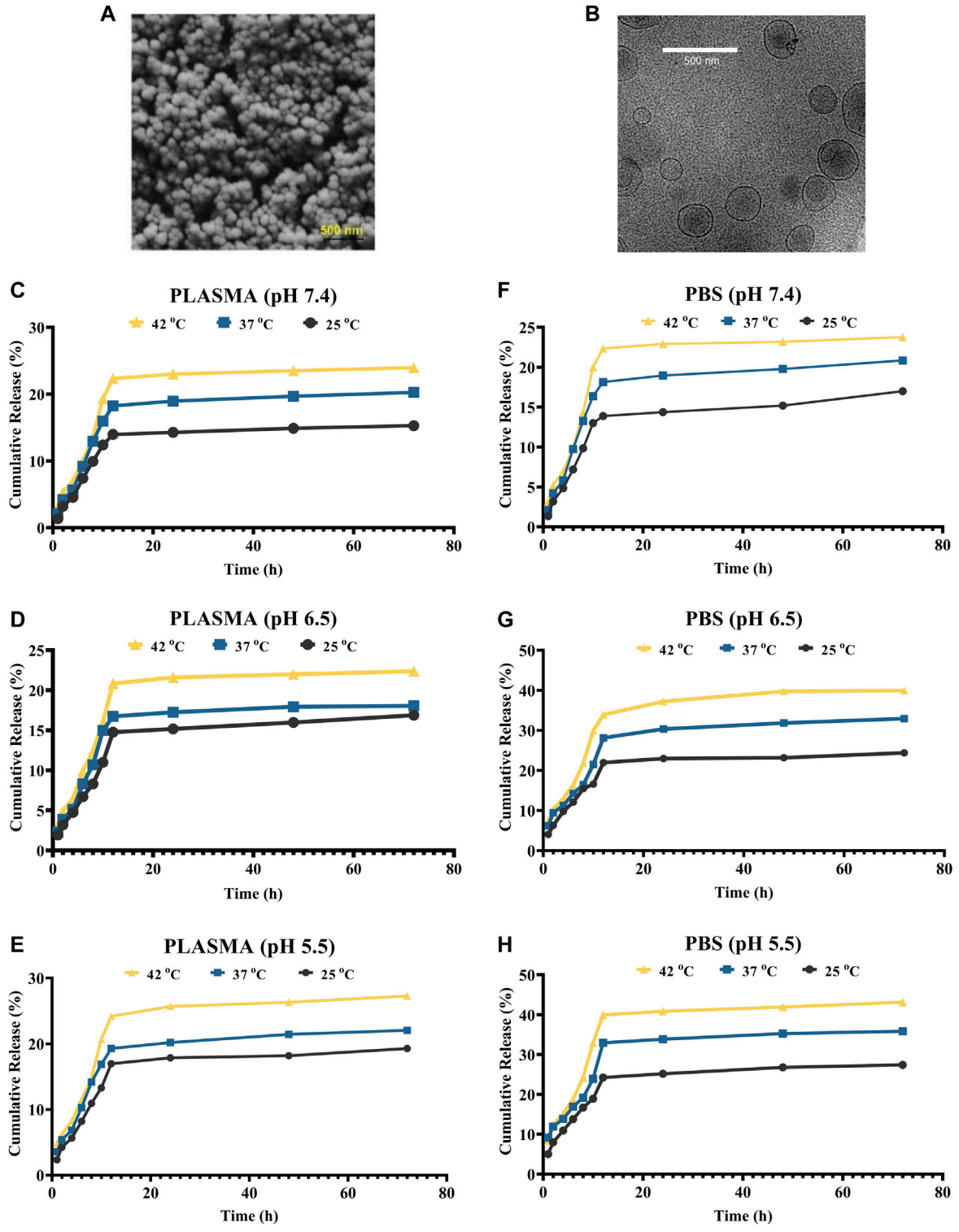

FIGURE 2
(A,B) SEM and cryo-TEM of the loaded niosomes, respectively. **(C–E)** Release of Cur in plasma solution at the pH of 7.4, 6.5, and 5.5, respectively. **(F–H)** Release of Cur in PBS solution at the pH of 7.4, 6.5, and 5.5, respectively.

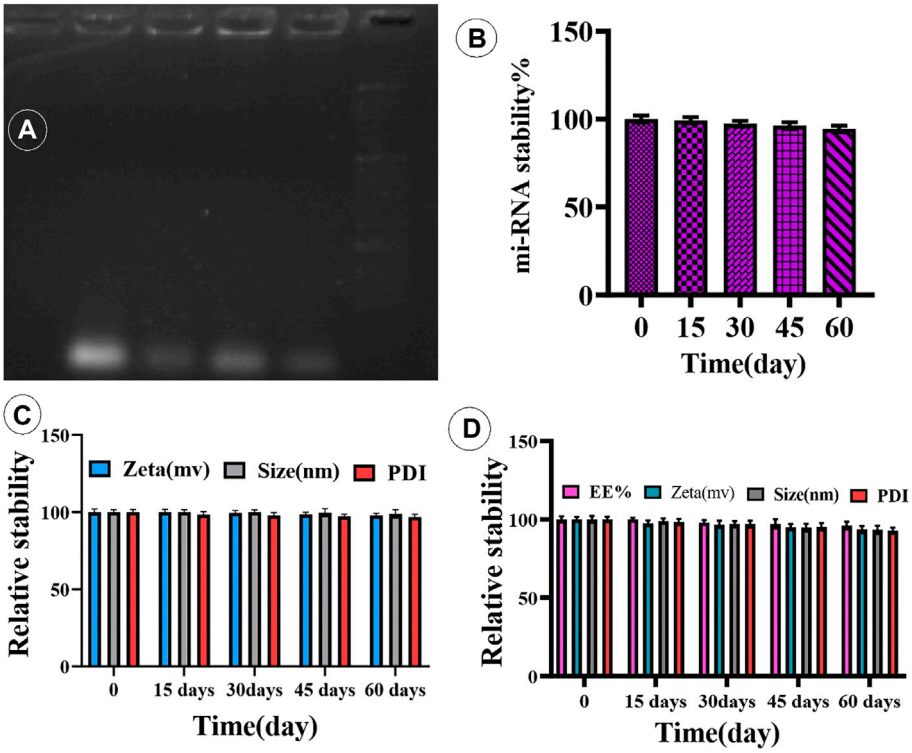

FIGURE 3
(A) Complex of miR-34a-loaded niosome. **(B)** Time-dependent stability of miR-34a-niosome. **(C,D)** Physical stability of Cur- and miRNA-niosome after 15, 30, 45, and 60 days, respectively.

the drug's stability and absorption. The drug-loaded nanocarrier's great stability after protracted storage is critical for the drug's effectiveness. The influence of particle size and zeta potential on vesicular system stability is well understood. As a result, barriers between vesicular particles are built to avoid accumulation. A charged molecule, for example, can be put on the system's surface. The zeta potential is a charge indicator, and if the particles have the right zeta potential, they repel each other and do not combine. NCur (F5) was therefore kept at 4°C for 15, 30, 45, and 60 days. The zeta potential, vesicle size, PDI, and EE% were measured after each time interval. From the results in Figure 3, the size/PDI of the vesicles and the EE% of the optimal niosomal formulation (F5) showed no significant changes after 60 days of storage when compared to pristinely synthesized samples (p-value 0.05), indicating that NCur is physically stable for at least 60 days. Therefore, the inclusion of DOTAP in the niosomal formulations only affected the zeta potential and either vesicle with a positively or negatively charged surface (with or without DOTAP), did not show alternation in their stability after 15, 30, 45 and 60 days in storage.

3.5 Complex formation of niosome with miRNA

To confirm that cationic niosomes and miR-34a formed a compound, a gel retardation experiment was employed. Cationic niosomes bind miR-34a in a dosage-dependent manner, as seen in Figure 3B. As can be observed, the best condition was a ratio of 20: 0.15 (cationic niosomes:mi-RNA34a). The loading of mi-RNAs onto cationic niosomes was ensured by zeta potential examination of the cationic niosomes before and after loading with miR-34a, as shown in Table 2. Furthermore, the size of the two parties grows due to electrostatic bonding and complex development. By forming a spatial barrier, the long chains of miR-34a that connect to the surface of niosomes directly enhance the hydrodynamic diameter. The final formulation (F5) has a size of 100 nm, which is satisfactory. The niosomes were stored at 4°C for 4 months to investigate the effect of long-term storage on miR-34a leaking from the surface. The complexes were stable with the lowest leakage after 4 months, according to the data (Figures 3C,D). The formulation is stable, according to the results of the stability test (electrophoresis), and the mi-RNA loaded in the niosome with a volume ratio of 20:0.15 (Niosome:mi-RNA) forms a complex.

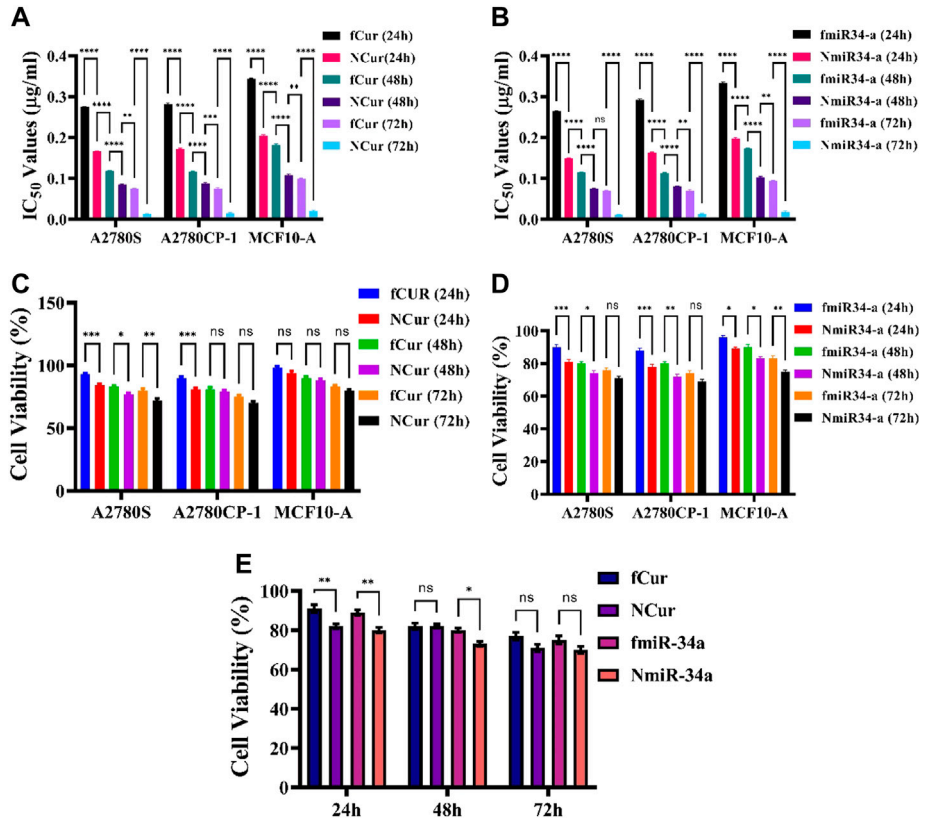

FIGURE 4
(A,B) IC_{50} values of free and niosomal Cur and miRNA on healthy and cancerous cells in 24, 48, and 72 h, respectively. **(C,D)** Cytotoxicity of free and niosomal Cur and miRNA on c healthy and cancerous cells in 24, 48, and 72 h, respectively. **(E)** A comparison between free and niosomal Cur and miRNA in 24, 48, and 72 h.

3.6 Cytotoxicity assays

Initially, we looked at the effects of free and niosomal curcumin on the viability of normal (MCF10-a) and cancer cell lines (A2780S, A2780CP1). We did this by calculating the IC_{50} values after 24, 48, and 72 h. According to the findings, normal cells required higher concentrations of either fCur or NCur to achieve IC_{50} than malignant cells. Furthermore, the drug encapsulated in niosomes was observed to improve cytotoxicity as compared to fCur. In comparison with free Cur, the IC_{50} values for A2780CP-1 and A2780S cells treated with NCur decreased by 45.6, 34.8, and 34.1%, respectively when incubated for 24 h. After 72 h, the disparity in the IC_{50} values of cancer cells cultured with free and encapsulated medications grew significantly. To evaluate the cytotoxic activities of free and niosomal Cur and miRNA on the human ovarian cancer A2780s, A2780cp, and MCF10-A cell lines were measured using the MTT test after incubation of cells for 24, 48, and 72 h. First, the inhibitory effects of free and niosomal Cur on A2780s, A2780cp, and MCF10-A cells were determined by dose-response tests. Next, the IC_{50} levels of these substances were evaluated (Figures 4A,B). Results displayed higher concentrations of drugs for MCF-10A than A2780s and A2780cp cells to achieve IC_{50} value. In comparison with the free state, the utilization of niosomes demonstrated remarkably lower IC_{50} values for all the cell lines.

The observations showed that free Cur and Cur-niosome had less effect on the MCF10-A cell line. At an equal dosage, drugs with niosomal carriers showed higher cytotoxicity than free drugs (Figures 4C,D). A total comparison in the average of the mean values of all cell lines after 24, 48, and 72 h showed that there are significant differences in the first day between the free and niosomal forms. Although the differences reduce after 72 h, still the niosomal forms demonstrated higher toxicity than their free forms (Figure 4E).

3.7 Cellular uptake of niosomal systems

In the cellular uptake tests, cancer cell models A2780S and A270cp-1 were utilized (Figures 5, 6, 7, 8). The cellular uptake

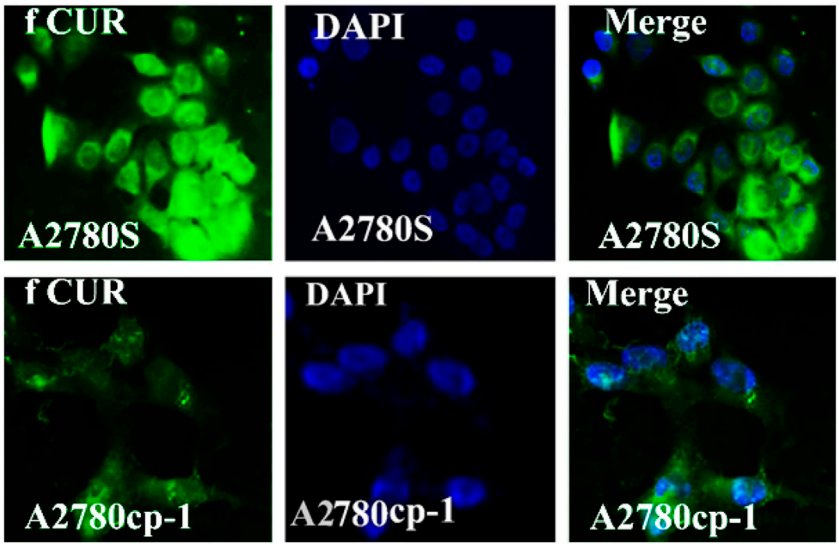

FIGURE 5
The uptake images of free Cur by A2780s and A270cp-1 cells after incubating for 4 h.

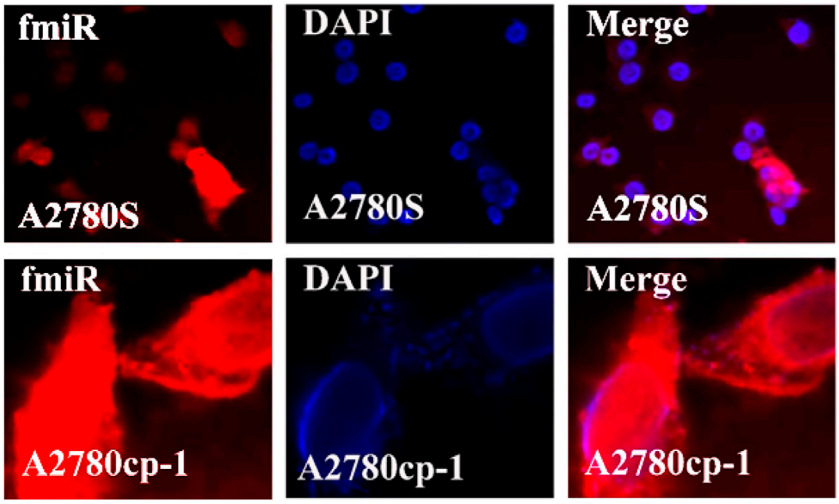

FIGURE 6
The uptake images of free miRNA by A2780s and A270cp-1 cells after incubating for 4 h.

behavior of two niosomal formulations was examined. Fluorescence microscopy was used to capture pictures of cancer cell lines treated with unloaded niosome, fCur, fmiR, NCur, and NmiR (Figures 5, 6, 7, 8). Cells treated with fCur or NCur glow red, whereas cells treated with fmiR or NmiR fluoresce green. The fluorescence intensity of cells incubated with niosomal nanoformulations was higher than that of cells treated with free versions of the medication or gene. Furthermore, although miR-34a accumulated in the cytoplasm, curcumin accumulated in both the nucleus area and the cytoplasm. Cancer cells are found to effectively absorb cationic niosomes. Endocytosis plays a significant role in the penetration of drug-loaded niosomes into cells as well as the transport of curcumin and miRNA into them as compared to free medicines transferred through the cell membranes *via* a diffusion process. Niosomes enhanced the solubility of curcumin, which has been considered as a hydrophobic medicine.

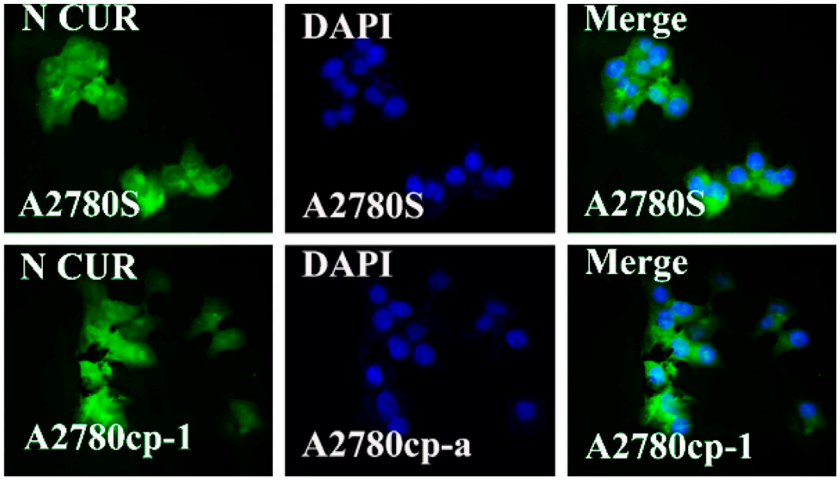

FIGURE 7
The uptake images of niosomal Cur by A2780s and A270cp-1 cells after incubating for 4 h.

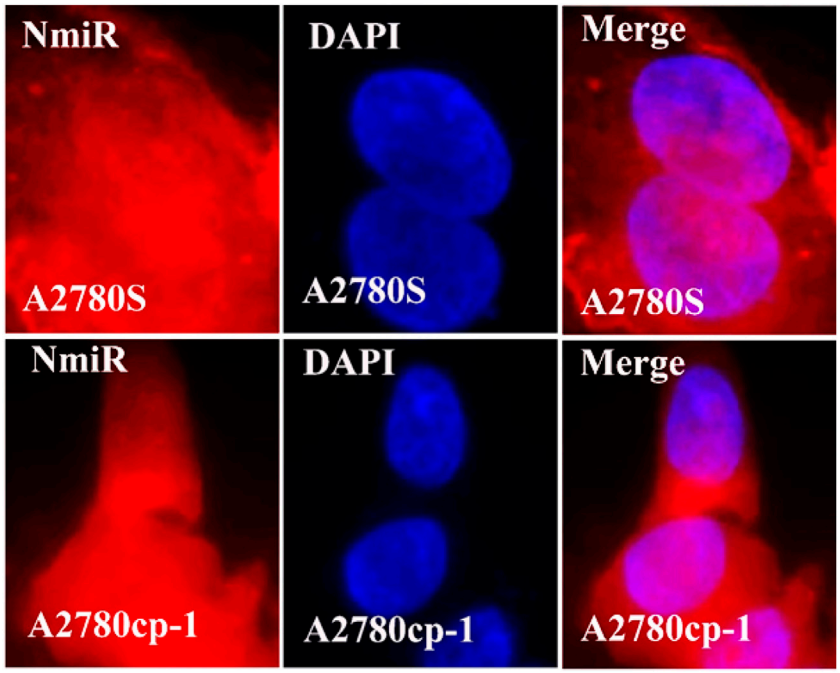

FIGURE 8
The uptake images of niosomal miRNA by A2780s and A270cp-1 cells after incubating for 4 h.

3.8 Gene expression

To measure the gene silencing efficiency of Cur and miR-34a, the expression of Nf-κB and P53 was evaluated to confirm their downstream impact. Generally, the anti-cancer mechanism of Nf-κB is based on the mitochondrial apoptosis pathways. Herein, qRT-PCR techniques were employed to detect the expression of Nf-κB and P53. For this purpose, first, cells were subjected to free Cur and miRNA, as well as niosomal Cur and miRNA, then, the

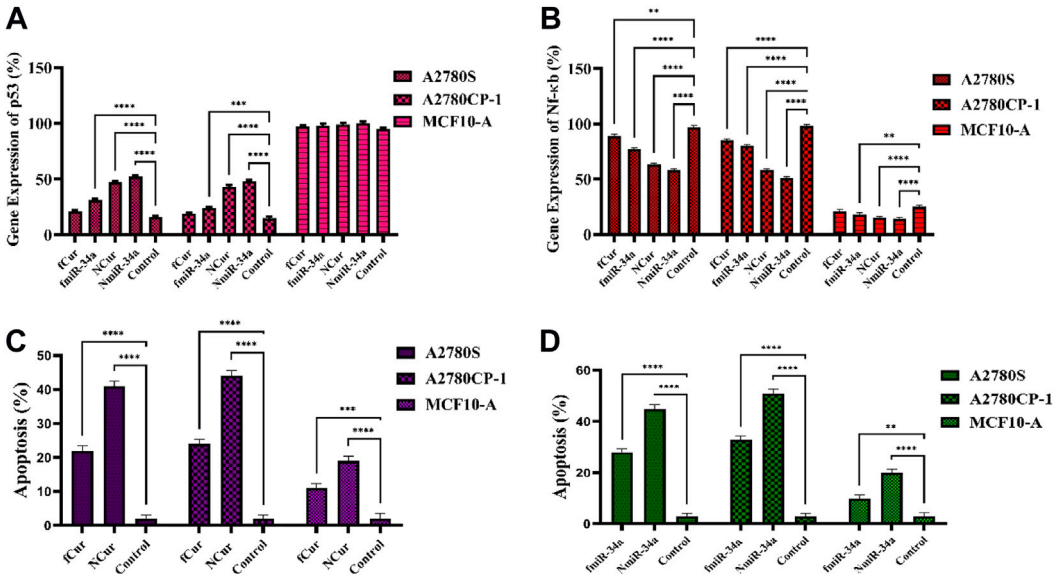

FIGURE 9
(A,B) The real-time PCR analysis of the expression of p53 and Nf-κB genes subjected to the samples for 48 h **(C,D)** Apoptosis assay of cells subjected to the samples using flow cytometry after 24 h.

expression of the genes was measured. The results showed a minor reduction in NF-κB and major improvement in P53 gene expression compared to the control group. Moreover, using the niosomal carrier remarkably enhanced the expression compared to their free forms. Specifically, it was observed that the gene expression using miRNA was higher than Cur. Ultimately, the gene expression of P53 and Nf-κB can be effectively improved by the utilization of nanocarriers by facilitating the intracellular delivery of medicines. The same results were achieved by both cytotoxicity and apoptosis assays.

3.9 Apoptosis analysis

To perform the apoptosis test on the cells, Annexin V-FITC/PI double staining assay was utilized on free Cur, free miRNA, niosomal Cur, and niosomal miRNA for 24 h and the result was obtained using a flow cytometer. Generally, in this assay, the phospholipid phosphatidylserine (PS) of the cell membrane of apoptotic cells translocates from the inward to the outward surface of the plasma membrane and subjects the PS to the exterior cellular environment. Annexin V is a Ca^{2+}-dependent phospholipid-binding protein with 35–36 kDa which has a high affinity to bind with PS of apoptotic cells. To improve the detection while maintaining the high affinity to PS, it is possible to conjugate annexin V to the fluorescent molecule like fluorescein isothiocyanate (FITC) and synthesis of Annexin V-FITC. Thus, to conduct the flow cytometric analyses, Annexin V-FITC was utilized which is a highly reactive probe for measuring the cells apoptosis. Moreover, to stain DNA, propidium iodide can be utilized not only is it a fluorescent DNA intercalating agent, but it also cannot penetrate inside the live or early apoptotic cells. Ultimately, the results were recorded after treatment for 48 h and displayed in Figure 9. It was observed that the utilization of niosomal carriers could effectively increase the apoptosis rate compared to their free forms. Moreover, the impact of miR-34a on cells in both forms was relatively higher than Cur.

3.10 *In-vivo* tumor prohibition

To assess the antitumor activity of the formulations, 4T1 xenografted Balb/C mouse tumor models were conducted. The mice from each group were subjected to one medicine including free Cur, free miRNA, niosomal Cur, and niosomal miRNA, as well as normal saline, every 3 days until 12 days. Medicins were injected into the tail vein of the mice. After 21 days, to evaluate the tumor volumes after the sacrifice and removal, a digital vernier caliper was employed. The results demonstrated that free Cur and miRNA groups displayed a reduction in the tumor size compared to the saline group. Likewise, niosomal Cur and miRNA groups had even smaller tumors than the previous groups (Figure 10E). It can be concluded that the decrease in cell growth was the result of the constant inhibition by the samples. The data concluded that niosomal miRNA could enhance the tumor prohibition activities and also, it presented an augmented therapeutic impact on cells

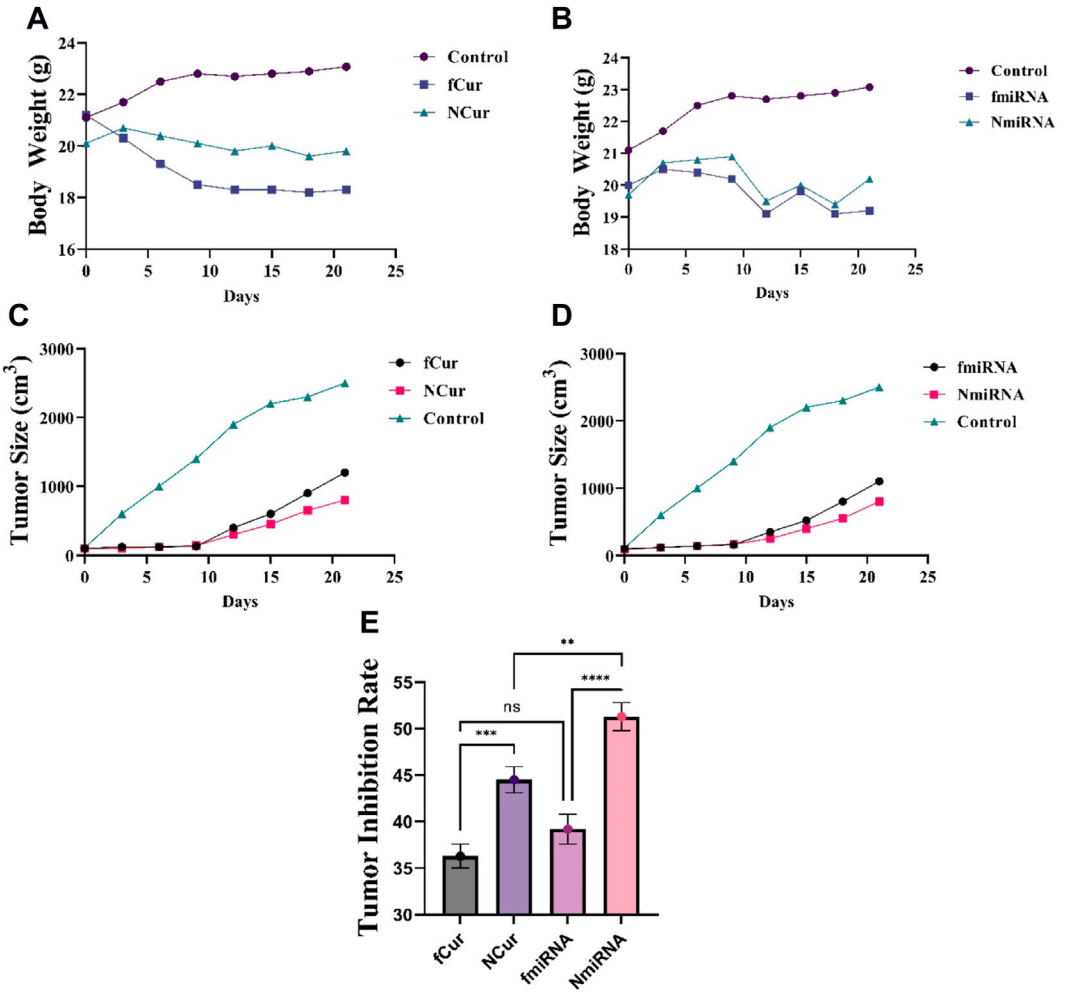

FIGURE 10
(A,B) Effect of Cur and miRNA formulations on the bodyweight at every 3-day-intervals, respectively. **(C,D)** The tumor size (cm^3) of different mice groups after 21 days of receiving the medicine. All groups displayed a major decrease ($p < 0.05$) in the tumor volumes than the control group after 14 and 21 days. **(E)** Tumor inhibition rate.

TABLE 3 The measured bodyweight (g) of the mice after receiving different medicine.

Duration (day)	Control group	Free Cur	Free miRNA	Niosomal Cur	Niosomal miRNA
0	22.1	22	22	22.1	22
3	22.7	21.1 ± 0.1	21.2	21.7	21.8
6	23.5 ± 0.1	20	20.7 ± 0.1	21.1	21.4 ± 0.01
9	23.8	19.3	20.1	20.6	21.2
12	23.7	19.1 ± 0.1	20 ± 0.1	20.1 ± 0.1	20.8
15	23.8 ± 0.1	19.2	20	20	20.8 ± 0.01
18	23.9	19.3 ± 0.1	19.8 ± 0.1	20.1 ± 0.1	20.6
21	24 ± 0.2	19.4	19.8	19.8 ± 0.1	20.2 ± 0.1

more than that of free miRNA or free forms of Cur and miR-34a (Figures 10C,D). The cytotoxicity of all medicine was assessed by weighing the mice at each interval (Figures 10A,B; Table 3). The body weight of treated mice encountered a minor reduction after 21 days, whereas the saline group gained weight. Meanwhile, on the 6th day, Cur groups faced the highest and the niosomal miRNA the lowest reduction in the bodyweight compared to the other groups.

4 Discussion

Chemotherapy is rapidly becoming the primary mode of treatment for a wide range of malignancies. The key issues in this context are the level of safety and the clinical efficacy of drugs. However, the use of chemical compounds has side effects such as toxicity, weight loss, and limited therapeutic efficiency.

Further research on herbal medication, either alone or in combination with chemotherapies, has recently shown its promise for cancer therapy. Curcumin, a yellowish spice obtained naturally from the rhizome of Curcuma longa, has been utilized for millennia in Asian nations and has been shown to have a wide variety of pharmacologic effects. This powder has antitumoral properties by inhibiting cell cycle signaling pathways, resulting in cell death. Cur has been shown in several studies to be effective against various cancer cell lines, including cervical, oral epithelial, brain, breast, hepatic, leukemia, colon, ovarian, pancreatic, melanoma, gastric, and prostate (Syng-Ai et al., 2004; Yallapu et al., 2013; Ag Seleci et al., 2016). Despite its impressive footprints, Cur's wide therapeutic benefits are restricted due to its weak water solubility and fast metabolism. To address this issue, nanotechnology developed nano DDSs including vesicular nanocarriers and niosomes. Surfactant and cholesterol are combined to generate unilamellar or multilamellar vesicles that contain both hydrophobic and hydrophilic drugs. As a result, the use of DDSs boosted medication efficacy, chemical stability, lowered economic preparation costs, and simplified long-term storage (Feng, 2004; Sezgin-Bayindir and Yuksel, 2012; Yallapu et al., 2012).

To encapsulate Cur, a new cationic niosomal preparation was designed in the present research. The vesicular system was made using T-80 and T-60 as the most frequently used surfactants in the new formulation of niosomes and industrial surfactants, respectively. The introduced formulations were analyzed by their entrapment effectiveness, zeta, drug release, and vesicle size. The size of nanoparticles has significant effects on the physical stability, cellular intake, and drug release from nanoparticles (Mukerjee and Vishwanatha, 2009). The sizes of nanoparticles in this study were between 87 and 135 nm compared to the other study which they were ranged from 50 to 500 nm, with different Cur formulations indeed (Ravindran et al., 2009). The zeta potential of the Cur preparation was +11.23 mV, which guaranteed physical stability and prevented aggregation during long-term storage (Garces et al., 2015). The investigation of the nano-vesicle morphology images (AFM and SEM) displayed spherical and circular particles with flat faces. After prolonged storage of 60 days, the result did not show any significant changes in the physiochemical features of the encapsulated drug inside the nanoparticles compared to the original samples. *In-vitro* treatment with Cur in both niosomal and free forms was exerted on A2780s and A2780cp cell lines, as the cancer cells and MCF10A cells, as control cells by a standard MTT assay. The results showed that Cur-contained nanoparticles had lower IC_{50} values on cancer cells than free Cur. Furthermore, cancer cells have reduced vitality than normal cells when treated with niosomal Cur. By activating growth inhibitory pathways in tumor cells, Cur-loaded nanoparticles might downregulate growth factors and their receptors, including NF-B activity, signaling channels for PI3K-AKT activity, and therefore block cancer cell development (Wang J et al., 2016). As a consequence of the gene expression data, free Cur had a similar impact on A2780s and A2780cp cells as cancer cells, but its adverse effects on normal cells were significantly lower. Furthermore, fluorescence microscopy on intracellular accumulation was explored, and it revealed that cancer cell absorption of Cur was simpler than free Cur. Finally, it was determined that the absorption of niosomal Cur by cancer cells *in vitro* may boost therapeutic optimism as a potential cancer therapy approach (Ravindran et al., 2009).

MicroRNA-34a (miR-34a) is a miRNA that is transcriptionally controlled by the p53 network and has been found to be significantly downregulated in a number of malignancies. In triple-negative and mesenchymal-type breast cancer cell lines, miR-34a expression has been found to be lower. Through targeting Bcl-2, CD44, and SIRT1 (silent information regulator 1), Rac1, Fra-1, Notch-1, and different cyclins, exogenous expression of miR-34a in breast cancer cells caused cell death and decreased cell proliferation and migration. For miRNA delivery, a number of viral carriers have been developed, with good transfection effectiveness across a wide range of cell types. However, safety problems are now seen as a barrier to viral vector-based therapy's practical implementation. Many kinds of nanoparticles have been utilized in gene delivery and transfection because of their small size, surface charge, and high surface area. In this study, DOTAP prepared the positive surface charge to link the miR-34a gene electrostatically on the surface of nanoformulation. Utilizing electrostatic interactions for loading the genes are the facile and conventional methods in nanoformulation when the controlled release is matter. Deng *et al.* fabricated a miR-34a containing nanoformulation using chitosan, hyaluronic acid, and doxorubicin for codelivery of doxorubicin and miR-34a against triple-negative breast cancer (Deng et al., 2014). They found that molecular weight and electrostatic

interaction density of miR-34a strongly influenced the release profile of genes and drugs. The employment of suitable materials such as DOTAP, Tween-60, Tween-80, and cholesterol a, which have already been used in drug delivery applications, is a point of strength in our inquiry regarding the production of nanomaterials for the effective distribution of miR-34a. These nanomaterials produced an efficient anticancer impact against ovarian carcinoma *in vitro* and 4T1 breast cancer model *in vivo* by way of intracellular localization of miR-34a, as established *in vitro*. The finding of the present study was in line with our previous reports and other research on niosome-based systemic drug delivery.

5 Conclusion

Ovary cancer is a primary cause of mortality in gynecological malignancies, which can be treated with surgery, chemotherapy, and radiation therapy. The majority of ovary cancers have acceptable initial responses to the existing therapeutics. One of the suitable approaches for the treatment of present ovary cancer is the use of chemo/radio-sensitizer accompanied by chemo/radiation methods. Hence, curcumin has earned the attention of researchers in the treatment of malignancies with unique properties such as anti-apoptosis, anti-inflammation, anti-angiogenesis, and chemo-sensitivity. Nevertheless, the weak aqueous solubility and fast metabolism of curcumin significantly restricted its clinical application. Using a vesicular nanocarrier, e.g., niosomes, which are a substitute for phospholipid vesicles for encapsulating hydrophobic drugs, helped to treat cancers due to the provision of high encapsulation efficiency, biocompatibility, biodegradability, low formulation costs, and adequate stability. Also, such nanocarriers are devoid of organic solvents and can be stored easily. Herein, we synthesized a curcumin-contained niosomal system, specifically designed for the effective delivery of curcumin to treat ovary cancer. According to the results, niosomal protection improved biochemical stability and elevated the entrapment efficiency of curcumin. Besides, it demonstrated improved cellular intake and cytotoxicity against the ovarian cancer cells, A280s, and A280cp-1. Altogether, curcumin-niosomes have the potential to be a suitable delivery system for curcumin to combat ovary cancer. The cellular toxicity of miR-34a-niosome was enhanced in cancer cells, compared to free miR-34a. Likewise, the antitumor influence of gene delivery was studied *in vivo*. According to the *in vitro* and *in vivo* results, gene delivery from the developed nanoscaled niosomes was more successful than curcumin delivery. Therefore, gene therapy using niosomal particles was a favorable strategy for advanced cancer therapy.

Data availability statement

The raw data supporting the conclusion of this article will be made available by the authors, without undue reservation.

Ethics statement

The animal study was reviewed and approved by the Animal Ethics Committee of Shahid Sadoughi University of Medical Sciences and were conducted in accordance with the policies of the Iran National Committee for Ethics in Biomedical Research (IR.SSU.MEDICINE.REC.1400.358).

Author contributions

NA performed the experimental procedure. SN and FH supervised the student, supported the research and edited the manuscript. MA and EA wrote the manuscript and helped data analysis.

Conflict of interest

The authors declare that the research was conducted in the absence of any commercial or financial relationships that could be construed as a potential conflict of interest.

Publisher's note

All claims expressed in this article are solely those of the authors and do not necessarily represent those of their affiliated organizations, or those of the publisher, the editors and the reviewers. Any product that may be evaluated in this article, or claim that may be made by its manufacturer, is not guaranteed or endorsed by the publisher.

References

Abtahi, N. A., Naghib, S. M., Ghalekohneh, S. J., Mohammadpour, Z., Nazari, H., Mosavi, S. M., et al. (2022). Multifunctional stimuli-responsive niosomal nanoparticles for co-delivery and co-administration of gene and bioactive compound: *in vitro* and *in vivo* studies. *Chem. Eng. J.* 429, 132090. doi:10.1016/j.cej.2021.132090

Ag Seleci, D., Seleci, M., Walter, J. G., Stahl, F., and Scheper, T. (2016). Niosomes as nanoparticular drug carriers: Fundamentals and recent applications. *J. Nanomater.* 2016, 1–13. doi:10.1155/2016/7372306

Alemi, A., Zavar Reza, J., Haghiralsadat, F., Zarei Jaliani, H., Haghi Karamallah, M., Hosseini, S. A., et al. (2018). Paclitaxel and curcumin coadministration in novel cationic PEGylated niosomal formulations exhibit enhanced synergistic antitumor efficacy. *J. Nanobiotechnology* 16 (1), 28–20. doi:10.1186/s12951-018-0351-4

Almansob, A., Ali, H. B., Ahmed, A., Mohammad, A., Abdulwahab, B., Waleed, A. H., et al. (2022). Effective treatment of resistant opportunistic fungi associated with immuno-compromised individuals using silver biosynthesized nanoparticles. *Appl. Nanosci.*, 1. doi:10.1007/s13204-022-02539-x

Balakrishnan, P., Shanmugam, S., Lee, W. S., Lee, W. M., Kim, J. O., Oh, D. H., et al. (2009). Formulation and *in vitro* assessment of minoxidil niosomes for enhanced skin delivery. *Int. J. Pharm.* 377 (1-2), 1–8. doi:10.1016/j.ijpharm.2009.04.020

Balazs, D. A., and Godbey, W. (2011). Liposomes for use in gene delivery. *J. Drug Deliv.* 2011, 326497. doi:10.1155/2011/326497

Boutelle, A. M., and Attardi, L. D. (2021). p53 and tumor suppression: it takes a network. *Trends Cell Biol.* 31, 298–310. doi:10.1016/j.tcb.2020.12.011

Chauhan, N., Jangid, N. K., Kaur, N., Rathore, B. S., Gholipourmalekabadi, M., and Mozafari, M. (2019). Medicines: Polymers for. M. Mishra (Editor), *Encyclopedia of Polymer Applications*, 1 st edn, Oxfordshire United Kingdom: Taylor & Francis, 1679–1691.

Chendil, D., Ranga, R. S., Meigooni, D., Sathishkumar, S., and Ahmed, M. M. (2004). Curcumin confers radiosensitizing effect in prostate cancer cell line PC-3. *Oncogene* 23 (8), 1599–1607. doi:10.1038/sj.onc.1207284

Deng, X., Cao, M., Zhang, J., Hu, K., Yin, Z., Zhou, Z., et al. (2014). Hyaluronic acid-chitosan nanoparticles for co-delivery of MiR-34a and doxorubicin in therapy against triple negative breast cancer. *Biomaterials* 35 (14), 4333–4344. doi:10.1016/j.biomaterials.2014.02.006

Eftekhari, B. S., Eskandari, M., Janmey, P. A., Samadikuchaksaraei, A., and Gholipourmalekabadi, M. (2021). Conductive chitosan/polyaniline hydrogel with cell-imprinted topography as a potential substrate for neural priming of adipose derived stem cells. *RSC Adv.* 11 (26), 15795–15807. doi:10.1039/d1ra00413a

Farhadihosseinabadi, B., Zarebkohan, A., Eftekhary, M., Heiat, M., Moosazadeh Moghaddam, M., and Gholipourmalekabadi, M. (2019). Crosstalk between chitosan and cell signaling pathways. *Cell. Mol. Life Sci.* 76 (14), 2697–2718. doi:10.1007/s00018-019-03107-3

Feng, S.-S. (2004). Nanoparticles of biodegradable polymers for new-concept chemotherapy. *Expert Rev. Med. Devices* 1 (1), 115–125. doi:10.1586/17434440.1.1.115

Flood, K. S., Houston, N. A., Savage, K. T., and Kimball, A. B. (2019). Genetic basis for skin youthfulness. *Clin. Dermatol.* 37 (4), 312–319. doi:10.1016/j.clindermatol.2019.04.007

Garces, Á. H. I., Dias, M. S. F., Paulino, E., Ferreira, C. G. M., and Melo, A. C. D. (2015). Treatment of ovarian cancer beyond chemotherapy: are we hitting the target? *Cancer Chemother. Pharmacol.* 75 (2), 221–234. doi:10.1007/s00280-014-2581-y

Hassan, S., Sabreena, S., Khurshid, Z., Bhat, S. A., Kumar, V., Ameen, F., et al. (2022). Marine bacteria and omic approaches: A novel and potential repository for bioremediation assessment. *J. Appl. Microbiol.* 133, 2299–2313. doi:10.1111/jam.15711

He, X., Zhu, Y., Yang, L., Wang, Z., Wang, Z., Feng, J., et al. (2021). MgFe-LDH nanoparticles: A promising leukemia inhibitory factor replacement for self-renewal and pluripotency maintenance in cultured mouse embryonic stem cells. *Adv. Sci.* 8 (9), 2003535. doi:10.1002/advs.202003535

Khan, S., Babadaei, M. M. N., Hasan, A., Edis, Z., Attar, F., Siddique, R., et al. (2021). Enzyme–polymeric/inorganic metal oxide/hybrid nanoparticle bio-conjugates in the development of therapeutic and biosensing platforms. *J. Adv. Res.* 33, 227–239. doi:10.1016/j.jare.2021.01.012

Kunnumakkara, A. B., Bordoloi, D., Harsha, C., Banik, K., Gupta, S. C., and Aggarwal, B. B. (2017). Curcumin mediates anticancer effects by modulating multiple cell signaling pathways. *Clin. Sci.* 131 (15), 1781–1799. doi:10.1042/CS20160935

Meng, F., Hasan, A., Mahdi Nejadi Babadaei, M., Hashemi Kani, P., Jouya Talaei, A., Sharifi, M., et al. (2020). Polymeric-based microneedle arrays as potential platforms in the development of drugs delivery systems. *J. Adv. Res.* 26, 137–147. doi:10.1016/j.jare.2020.07.017

Merlin, J. P., Rupasinghe, H. P. V., Dellaire, G., and Murphy, K. (2021). Role of dietary antioxidants in p53-mediated cancer chemoprevention and tumor suppression. *Oxid. Med. Cell. Longev.* 2021, 9924328. doi:10.1155/2021/9924328

Moghadam, N. C. Z., Jasim, S. A., Ameen, F., Alotaibi, D. H., Nobre, M. A. L., Sellami, H., et al. (2022). Nickel oxide nanoparticles synthesis using plant extract and evaluation of their antibacterial effects on Streptococcus mutans. *Bioprocess Biosyst. Eng.* 45 (7), 1201–1210. doi:10.1007/s00449-022-02736-6

Mozafari, M., GholipourMalekabadi, M., Chauhan, N. P. S., JalaliN.Asgari, S., Caicedoa, J. C., et al. (2015). Synthesis and characterization of nanocrystalline forsterite coated poly (l-lactide-co-β-malic acid) scaffolds for bone tissue engineering applications. *Mat. Sci. Eng. C Mat. Biol. Appl.* 50, 117–123. doi:10.1016/j.msec.2015.01.005

Mukerjee, A., and Vishwanatha, J. K. (2009). Formulation, characterization and evaluation of curcumin-loaded PLGA nanospheres for cancer therapy. *Anticancer Res.* 29 (10), 3867–3875.

Najminejad, H., Kalantar, S. M., Abdollahpour-Alitappeh, M., Karimi, M. H., Seifalian, A. M., Gholipourmalekabadi, M., et al. (2019). Emerging roles of exosomal miRNAs in breast cancer drug resistance. *IUBMB life* 71 (11), 1672–1684. doi:10.1002/iub.2116

Nikniaz, H., Zandieh, Z., Nouri, M., Daei-Farshbaf, N., Aflatoonian, R., Gholipourmalekabadi, M., et al. (2021). Comparing various protocols of human and bovine ovarian tissue decellularization to prepare extracellular matrix-alginate scaffold for better follicle development *in vitro*. *BMC Biotechnol.* 21 (1), 8. doi:10.1186/s12896-020-00658-3

Pidíkova, P., Reis, R., and Herichova, I. (2020). miRNA clusters with down-regulated expression in human colorectal cancer and their regulation. *Int. J. Mol. Sci.* 21 (13), 4633. doi:10.3390/ijms21134633

Ravindran, J., Prasad, S., and Aggarwal, B. B. (2009). Curcumin and cancer cells: How many ways can curry kill tumor cells selectively? *AAPS J.* 11 (3), 495–510. doi:10.1208/s12248-009-9128-x

Sargolzaei, J., Etemadi, T., and Alyasin, A. (2020). The P53/microRNA network: A potential tumor suppressor with a role in anticancer therapy. *Pharmacol. Res.* 160, 105179. doi:10.1016/j.phrs.2020.105179

Sezgin-Bayindir, Z., and Yuksel, N. (2012). Investigation of formulation variables and excipient interaction on the production of niosomes. *Aaps Pharmscitech* 13 (3), 826–835. doi:10.1208/s12249-012-9805-4

Shaker, D. S., Shaker, M. A., and Hanafy, M. S. (2015). Cellular uptake, cytotoxicity and *in-vivo* evaluation of Tamoxifen citrate loaded niosomes. *Int. J. Pharm.* 493 (1-2), 285–294. doi:10.1016/j.ijpharm.2015.07.041

Song, X., Zhang, M., Dai, E., and Luo, Y. (2019). Molecular targets of curcumin in breast cancer (Review). *Mol. Med. Rep.* 19 (1), 23–29. doi:10.3892/mmr.2018.9665

Syng-Ai, C., Kumari, A. L., and Khar, A. (2004). Effect of curcumin on normal and tumor cells: Role of glutathione and bcl-2. *Mol. Cancer Ther.* 3 (9), 1101–1108. doi:10.1158/1535-7163.1101.3.9

Talib, W. H., Al-Hadid, S. A., Ali, M. B. W., Al-Yasari, I. H., and Ali, M. R. A. (2018). Role of curcumin in regulating p53 in breast cancer: An overview of the mechanism of action. *Breast Cancer* 10, 207–217. doi:10.2147/BCTT.S167812

Tricoli, J. V., and Jacobson, J. W. (2007). MicroRNA: Potential for cancer detection, diagnosis, and prognosis. *Cancer Res.* 67 (10), 4553–4555. doi:10.1158/0008-5472.CAN-07-0563

Wang, J., Wang, F., Li, F., Zhang, W., Shen, Y., Zhou, D., et al. (2016). A multifunctional poly (curcumin) nanomedicine for dual-modal targeted delivery, intracellular responsive release, dual-drug treatment and imaging of multidrug resistant cancer cells. *J. Mat. Chem. B* 4 (17), 2954–2962. doi:10.1039/c5tb02450a

Wang, Y., Yu, J., Cui, R., Lin, J., and Ding, X. (2016). Curcumin in treating breast cancer: a review. *J. Lab. Autom.* 21 (6), 723–731. doi:10.1177/2211068216655524

Wong, K. E., Ngai, S. C., Chan, K. G., Lee, L. H., Goh, B. H., and Chuah, L. H. (2019). Curcumin nanoformulations for colorectal cancer: A review. *Front. Pharmacol.* 10, 152. doi:10.3389/fphar.2019.00152

Wu, S.-H., Hsieh, C. C., Hsu, S. C., Yao, M., Hsiao, J. K., Wang, S. W., et al. (2021). RBC-derived vesicles as a systemic delivery system of doxorubicin for lysosomal-mitochondrial axis-improved cancer therapy. *J. Adv. Res.* 30, 185–196. doi:10.1016/j.jare.2020.11.009

Xu, Y.-Q., Chen, W. R., Tsosie, J. K., Xie, X., Li, P., Wan, J. B., et al. (2016). Niosome encapsulation of curcumin: Characterization and cytotoxic effect on ovarian cancer cells. *J. Nanomater.* 2016, 1–9. doi:10.1155/2016/6365295

Yallapu, M. M., Othman, S. F., Curtis, E. T., Bauer, N. A., Chauhan, N., Kumar, D., et al. (2012). Curcumin-loaded magnetic nanoparticles for breast cancer therapeutics and imaging applications. *Int. J. Nanomedicine* 7, 1761–1779. doi:10.2147/IJN.S29290

Yallapu, M. M., Ebeling, M. C., Khan, S., Sundram, V., Chauhan, N., Gupta, B. K., et al. (2013). Novel curcumin-loaded magnetic nanoparticles for pancreatic cancer treatment. *Mol. Cancer Ther.* 12 (8), 1471–1480. doi:10.1158/1535-7163.MCT-12-1227

Yen, H.-Y., Tsao, C. W., Lin, Y. W., Kuo, C. C., Tsao, C. H., and Liu, C. Y. (2019). Regulation of carcinogenesis and modulation through Wnt/β-catenin signaling by curcumin in an ovarian cancer cell line. *Sci. Rep.* 9 (1), 17267–17314. doi:10.1038/s41598-019-53509-3

Yi, H., Lu, W., Liu, F., Zhang, G., Xie, F., Liu, W., et al. (2021). ROS-responsive liposomes with NIR light-triggered doxorubicin release for combinatorial therapy of breast cancer. *J. Nanobiotechnology* 19 (1), 134. doi:10.1186/s12951-021-00877-6

frontiers | Frontiers in Bioengineering and Biotechnology

TYPE Mini Review
PUBLISHED 16 December 2022
DOI 10.3389/fbioe.2022.1075670

OPEN ACCESS

EDITED BY
Yasser Zare,
Motamed Cancer Institute, Iran

REVIEWED BY
Amir Rostami,
Persian Gulf University, Iran

*CORRESPONDENCE
Yanghui Xing,
yhxing@stu.edu.cn

SPECIALTY SECTION
This article was submitted to Nanobiotechnology, a section of the journal Frontiers in Bioengineering and Biotechnology

RECEIVED 20 October 2022
ACCEPTED 05 December 2022
PUBLISHED 16 December 2022

CITATION
Xing Y, Zeng B and Yang W (2022), Light responsive hydrogels for controlled drug delivery.
Front. Bioeng. Biotechnol. 10:1075670.
doi: 10.3389/fbioe.2022.1075670

Light responsive hydrogels for controlled drug delivery

Yanghui Xing*, Buhui Zeng and Wang Yang

Department of Biomedical Engineering, Shantou University, Shantou, China

Light is an easy acquired, effective and non-invasive external stimulus with great flexibility and focusability. Thus, light responsive hydrogels are of particular interests to researchers in developing accurate and controlled drug delivery systems. Light responsive hydrogels are obtained by incorporating photosensitive moieties into their polymeric structures. Drug release can be realized through three major mechanisms: photoisomerization, photochemical reaction and photothermal reaction. Recent advances in material science have resulted in great development of photosensitizers, such as rare metal nanostructures and black phosphorus nanoparticles, in order to respond to a variety of light sources. Hydrogels incorporated with photosensitizers are crucial for clinical applications, and the use of ultraviolet and near-infrared light as well as up-conversion nanoparticles has greatly increased the therapeutic effects. Existing light responsive drug delivery systems have been utilized in delivering drugs, proteins and genes for chemotherapy, immunotherapy, photodynamic therapy, gene therapy, wound healing and other applications. Principles associated with site-specific targeting, metabolism, and toxicity are used to optimize efficacy and safety, and to improve patient compliance and convenience. In view of the importance of this field, we review current development, challenges and future perspectives of light responsive hydrogels for controlled drug delivery.

KEYWORDS

hydrogel, light responsive, drug delivery, photosensitizer, programmed release

1 Introduction

Hydrogels are three-dimensional crosslinked polymeric networks that can absorb large amounts of water or biological fluids. Their structures are formed through chemical or physical crosslinking of different polymer chains, between which either covalent bonds or physical interactions exist to maintain their structural stability (Ebara et al., 2014). Hydrogels are usually characterized with pH-neutral, colorless, odorless, non-toxic, high absorption ability, and excellent stability and constancy in storage with controllable biodegradability (Ullah et al., 2015). Given their technical features, hydrogels have been utilized in designing drug delivery systems for years. Hydrogels can protect the drug from surrounding environments, and their tunable properties plus the ability to retain large fraction of solvents make them ideal carriers for drug delivery systems. By changing hydrogel properties, drug release rate can be accurately controlled. Additionally, hydrogels usually have low affinity with drugs, thus achieve a high fraction of drug release.

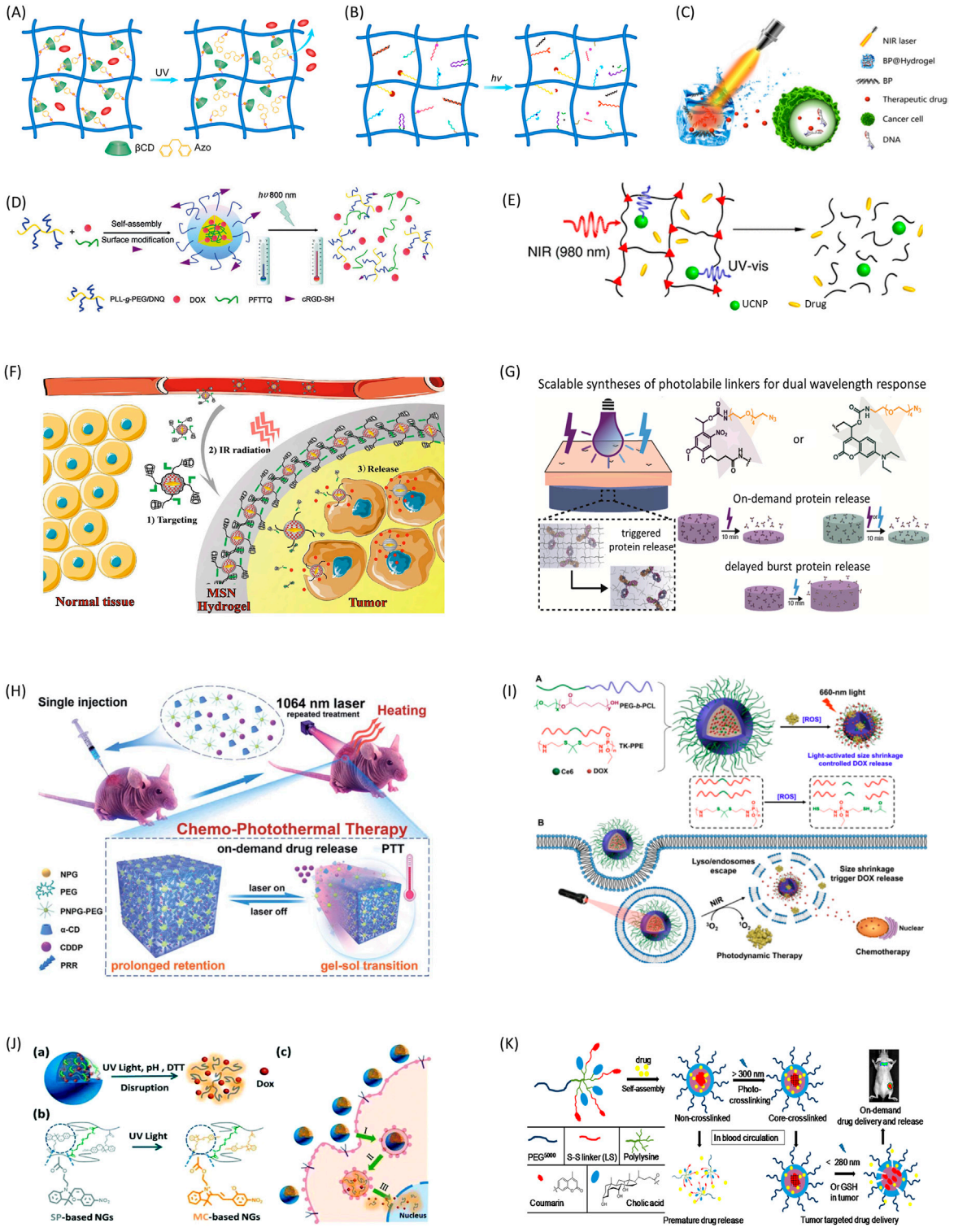

FIGURE 1
Representative mechanisms and applications of light-controlled drug delivery systems. **(A)** Photoisomerization induced drug release through guest-host interactions. **(B)** Photocleavage induced drug release through multi mechanisms. **(C)** Photothermal effect-induced drug release to break DNA chains. Copyright Qiu et al. (2018) NAS. **(D)** Two-photon light regulated chemo-photothermal therapy with fast drug release. Used with permission of RSC from Yuan et al. (2015). **(E)** NIR-triggered hydrogel degradation using the UV light generated by UCNPs. Adapted with permission from Yan et al. Copyright 2012 American Chemical Society. **(F)** Light-induced targeted drug delivery to tumor tissue through

(*Continued*)

FIGURE 1 (Continued)
photoisomerization. Adapted with permission from Chen et al. Copyright 2016 American Chemical Society. **(G)** On-demand protein release by dual wavelength lights. Adapted with permission from LeValley et al. Copyright 2020 American Chemical Society. **(H)** NIR induced repetitive on-demand drug release for chemo-photothermal therapy. Ruan et al. (2019). **(I)** Combination of photodynamic therapy and chemotherapy through light-induced drug release. Adapted with permission from Cao et al. Copyright 2018 American Chemical Society. **(J)** DOX release process from light-induced multi stimuli responsive system. Used with permission of RSC from Chen et al., 2017. **(K)** Light and redox dual responsive coumarin containing micelles as drug nanocarrier for cancer therapy. Shao et al. (2014).

Hydrogels can be classified into two groups according to their responses to external stimuli: one is conventional hydrogels, which have no particular sensation to changes of their environment, and the other is stimuli-responsive hydrogels, also known as smart hydrogels that are capable of responding to physical, chemical or biochemical stimuli (Ji et al.eng, 2020). In response to external stimuli, these hydrogels undergo a series of changes in their growth actions, network structure, mechanical strength and permeability (Zhang et al., 2021; Gil and Hudson, 2004/12). Stimuli-responsive hydrogels contain specific components as "on-off" sensors able to detect stimulation signals and subsequently control their changes. For example, ultrasound amplitude and time duration are associated FITC-BSA release rate in chitosan hydrogels with reversible Diels-Alder linkers (Arrizabalaga et al.eng, 2022); and thermosensitive mPEG-PA-PLL hydrogel was used for controlled oral delivery of calcitonin (Cheng et al., 2022). Combining two or more stimuli responsive mechanisms in one hydrogel system, multi-responsive hydrogels can be formed to respond to more than two external stimuli. PF127/TMC/PEG-HA can react to both pH and temperature, and is an example of a dual responsive hydrogel used for in textile-based transdermal therapy (Chatterjee et al., 2019).

2 Fundamentals of light responsive drug delivery system

Light responsive hydrogels are able to respond to light irradiation and subsequently give rise to structural and conformational changes (Jiang and Wen, 2015; Bustamante-Torres et al., 2021). Light is an easy acquired, effective and non-invasive external stimulus that can be highly focused and regulated by manipulating its parameters, including intensity, wavelength, exposure time and beam diameter. Consequently, light offers accurate and spatiotemporal control of drug delivery, and thus received great attention in the past decade (Li et al., 2018a; Rizzo et al., 2021). Light responsive hydrogels are obtained by incorporating photosensitive moieties into the polymer structure. Based on the photosensitizer (PS) used, the response can be reversible or irreversible (Bustamante-Torres et al., 2021). Light can cause cleavage, isomerization, or dimerization of photosensitive groups in hydrogels, and leads to partial or complete decrosslinking, degradation, swelling and/or shrinkage of the hydrogel structure.

The light-controlled drug delivery systems can be classified into three broad categories: photoisomerization-based, photochemical-based, and photothermal-based drug release platforms. Photoisomerization typically involves conformational changes of the hydrogels from *trans* to *cis* under light irradiation. During this process, hydrogels open pore sizes and allow drugs to diffuse out of their matrixes (Figure 1A). It does not break chemical bonds of hydrogels, and the process is usually reversible and repeatable (Tomatsu et al., 2011). Photochemical reactions can lead to network structure and configuration changes of the hydrogel, and subsequently induce drug release (Iwaso et al., 2016). Among all photochemical reactions, photocleavage is the one of most commonly used ones for controlled drug delivery. This method is realized by incorporating photocleavable linkers into the hydrogel structure to create nanoparticles that can be cut off by light (Figure 1B) (Miranda and Lovell, 2016; Liese and Hampp, 2011/04). In this case, drugs are tethered to the hydrogel network at designed or selected sites covalently through photocleavable linkers, and can maintain their efficacy and avoid unwanted release to a large extent (Shadish and DeForest, 2020; Wang et al., 2020). The photothermal reaction is utilizing materials able to convert light energy into the heat energy, which in turn induces a disruption of a thermally sensitive drug carrier (Figure 1C) (Qiu et al., 2018; Bordbar-Khiabani and Gasik, 2022). The reaction requires two components - a photosensitizer to convert light into heat, and a material sensitive to temperature changes for drug release.

The commonly used light sources include ultraviolet (UV), visible light and near-infrared (NIR). UV once was the most popular light sources because of the availability of a wide range of UV photosensitizers. But it is mainly for *in vitro* experiments due to its cytotoxicity and low tissue penetration. On the side, NIR is safer for *in vivo* studies and able to trigger drug release within deep tissues. Thus, NIR is very attractable for clinical applications. Due to recent advance of material science, many new photosensitizers responsive to NIR were developed. Additionally, the use of two-photon excitation (Figure 1D) and up-conversion nanoparticles (UCNPs) (Figure 1E) also greatly expanded situations that NIR can be used (Pokharel and Park, 2022; Yuan et al., 2015; Yan et al., 2012/10). Based on above mechanisms, a variety of drug delivery applications were presented in Table 1 (Tao et al., 2019; Liang et al.eng, 2020; Pourjavadi et al., 2020; Wei et al., 2020; Yu et al., 2020).

TABLE 1 Representative light-controlled drug delivery systems.

Delivery systems	Stimuli and drug release mechanisms	Applications	Highlights	Reference
PEG-Azo2 with alginate-βCD	UV/photoisomerization with guest-host chemistry	Release of small molecules for tissue engineering and wound healing	Light induced rapid and controlled release of small molecules, suitable for wound healing	Chiang and Chu, (2015)
HA with Azo and βCD	UV/photoisomerization with guest-host chemistry	BSA release in cell culture environments	Reversible guest-host interactions and accurate control of dug release	Rosales et al. (2018)
PAA with mAzo and βCD	Red light/photoisomerization with guest-host chemistry	*in vivo* protein release	Controlled deep tissue drug delivery	Wang et al. (2015)
SPMA with spiropyran–merocyanine	UV/photoisomerization induced volumetric change	*in vitro* DOX release	On-demand reversible drug release with hydrophobicity switch	(Ghani et al., 2021/01)
PAA, spiropyran, disulfide-containing cystamine	UV/photoisomerization resulted multi stimuli response	*in vitro* DOX release	Light, pH, and redox triple-responsive nanogel	Chen et al. (2017)
PEGMA with tethered exosomes	Blue light/photocleavage	BMP loaded exosome release in cells to deliver small molecules	Controlled release through hydrogel structure, efficient cell uptake	Yerneni et al.eng, (2022)
Injectable glycol chitosan with IR783-mHNK	NIR/photocleavage	*in vivo* mHNK release in mice	Accurate control, good biocompatibility and stability, minimum leakage and efficient light responsibility	Yang et al. (2022)
PEG-SH, S,S-Tetrazine	Green light/photocleavage - light induced gel degradation	*in vivo* DOX release in mice for cancer therapy	Drug release with hyperoxide-accelerated behaviors and antitumor effects	Wang et al. (2020)
PEG, polylysine, coumarin	UV/photocleavage induced light and redox responses	*in vivo* drug release for cancer therapy	Good drug loading capacity and stability, preferred tumor accumulation and the prolonged tumor residency	Shao et al. (2014)
PVA pBP composite	NIR/photothermal effects	*in vitro* congo red release	Robust mechanical properties, excellent biocompatibility, highly controllable drug release	Yang et al. (2018)
Oxidized dextran and platinum nanoparticles	NIR/photothermal effects	*in vitro* and *in vivo* drug release for cancer therapy	Long-term repeated PTT with excellent photothermal effects and good biocompatibility	Li et al. (2018b)
Agarose, HK ink, dihydroartemisinin	NIR-II/photothermal effects and reversible gel degradation	*in vivo* release of drug targeting tissues with pre-injected DHA	Injectable, deep tissue penetration, accurate tissue targeting	Chen et al. (2020)
GelPV-DOX-DBNP	NIR and red light/hydrogel degradation and photothermal effects	*in vivo* DOX release for cancer therapy	Combined chemo-photothermal therapy with two-step accurate control of drug release	Sun et al.eng, (2020)
Chitosan/PLA/PNIPAM Hydrogels coated Gold Nano Rods	NIR/hydrogel volumetric shrinkage due to photothermal effects	*In vitro* study of paclitaxel (PTX) delivery to cells	Multi-stimuli sensitive systems able to respond to light, heat, and pH	Pourjavadi et al. (2020)
PLGA nanoparticles with Graphene Quantum Dots or Methylene Blue	NIR/hydrogel degradation due to photothermal effects	Chemo-photothermal or chemo-photodynamic therapy for cancer	Combined chemotherapy with PTT and PDT, as well as accurate release control	Liang et al.eng, (2020)
NIPAm, MPCD with gold nanorods (GNRs)	NIR/photothermal and pH responsive effects	Chemophotothermal synergistic cancer therapy	Good mechanical and swelling properties, gelation characteristics, and excellent NIR-responsive property	Xu et al.eng, (2017)
PNPG-PEG-aCD	NIR-II/photothermal effects	Cisplatin release for *in vivo* chemo-photothermal therapy	Repeatable and accurate controlled drug release, deep tissue penetration	Ruan et al. (2019)
Gelatin, PDA and alginate	NIR/photothermal effects	Localized therapy of breast cancer	3D printed scaffolds for accurate structure control and drug release	Wei et al. (2020)
PLGA coated Au-TiO2	NIR/photothermal effects	Human papillary thyroid carcinoma therapy	High efficiency, good biocompatibility, accurate control	Yu et al. (2020)
Gel-MA, BACA with Cu NPs	NIR/photothermal effects and ROS production	Skin tissue regeneration	Multifunctional hydrogel for killing bacteria and accelerating wound healing	Tao et al. (2019)

3 Photoisomerization-based drug delivery systems

Photoisomerization takes advantage of the conformational changes of certain molecules when stimulated by light irradiation (Pan et al., 2021/10). Azobenzene is the most used molecules in this category. Modifying hydrogels with azobenzene and cyclodextrin (CD) can create light responsive crosslinking between the two components. When in the *trans* isomer form, azobenzene can have "host-guest" interaction with CD, forming strong crosslinks. Under UV light irradiation, the azobenzene changes to *cis* isomer form which leads to breaking of crosslinks and drug release.

Light responsive azobenzene-CD guest-host chemistry has been widely used for controlled release of drugs from hydrogels under light exposure (Rosales et al., 2018). In one study, the authors developed a light responsive hydrogel by permeating diazobenzene-modified poly(ethylene glycol) (PEG) into βCD grafted alginate. Exposure of UV light leads to controlled cargo release from the hydrogel which was used in wound healing and other applications (Chiang and Chu, 2015). In another study, a model drug was released from a light responsive hydrogel made from azobenzene and PEG. The system showed reversible photoisomerization between its *cis* and *trans* isomers under UV-light irradiation allowing model drug release from the hydrogel network. The authors observed clear volume changes during the photoisomerization process and characterized the peak effects at 330 nm and 435 nm respectively. Thus, the drug release can be controlled by the wavelength and intensity of light irradiation (Rastogi et al.eng, 2018). Additionally, Nehls et al. showed similar results with more accurately controlled release rate of an entrapped model drug based on azobenzene-CD chemistry in PEG hydrogels (Nehls et al., 2016). Furthermore, PAA-based hydrogel modified with methoxy-substituted azobenzene and βCD supramolecular complexes showed a gel to sol transition in response to red light irradiation, and subsequently resulted in a dose dependent manner of loaded BSA release. With higher wavelength than UV, red light can be used for deep tissue drug delivery with less energy-induced damage (Wang et al., 2015). Chen et al. designed a DOX-loaded delivery system targeted tumor tissues using muli-responsive formation and degradation of the hydrogel (Figure 1F) (Chen et al.eng, 2016).

Spiropyran is another well-known photosensitizer that can be incorporated into hydrogel networks. It was used to deliver a variety of drugs such as doxorubicin and paclitaxel based on photoisomerization of hydrophobic spiropyran to hydrophilic merocyanine after UV irradiation. During this process, the swelling of hydrogels cause water soluble drugs to diffuse out of the hydrogel networks (Li et al., 2020/05). Tong et al. reported a nanoparticulate drug delivery system comprising spiropyran and PEGylated lipid that allows repetitive drug delivery at given time and location. The light-sensitive switch enables particles to fluoresce and release drugs inside cells when illuminated with UV light providing a spatiotemporal control of drug delivery with and enhanced tissue penetration (Tong et al., 2012). Spiropyrans within hydrogels have also been used as on and off switch triggers for controlled drug release in a number of other studies due to its reversible properties (Ghani et al., 2021/01; Xiao et al.eng, 2016).

4 Photochemical reaction-based drug delivery systems

Photochemical reactions include photooxidation, photocleavage and photopolymerization. For photocleavage induced drug release, o-nitrobenzyl is the most popular photocleavable linkers. It can be incorporated into many hydrogels to give them light responsive properties. The cleavage of o-nitrobenzyls happens at C-O bond in its ester group after exposure to UV light or high energy visual light. In one study, o-nitrobenzyl moieties were added into gelatin methacryloyl(-acetyl) hydrogels with a biotin-functionalized photocleavable macromer, and then controlled release under UV-irradiation is studied. The authors found that liquid chromatography coupled to mass spectrometry analysis of aqueous linker solutions allows the identification of the main cleavage products and the cleavage kinetics (Claaßen et al., 2018). O-nitrobenzyls were also used to cause a macro physical change in the overall structure for drug delivery (Linsley et al., 2017). In o-nitrobenzyl linked PEG and PAM hydrogels, cleavage of o-nitrobenzyls with UV resulted volume shrinking of their polymeric structure, and caused controlled release of drugs entrapped within its matrix (Yan et al., 2012/10). In a similar study for PEG and dextran hydrogel with o-nitrobenzyl linkers, 60 min exposure to UV leads to fifty percent of model drug release due to hydrogel structure dissociation (Peng et al., 2011). In another study, authors showed a novel strategy enabling the use of upconversion luminescence converting NIR light into UV light, which are received by o-nitrobenzyl groups in PEG hydrogels. Subsequently, the photocleavage reaction leads to tethered drugs (Yan et al., 2011/12).

A ruthenium-based photocleavable linker was developed to form hydrogel with entrapped model drugs, which cannot be released until exposure to light. By varying the coordinated ligands, Ru-cross-linkers have 1-photon absorption maxima that are tunable across the visible spectrum and into the near-infrared, which enables photoactivation at multiple, different wavelengths (Rapp and Dmochowski, 2019). In a more recent study, Yerneni et al. tethered exosomes to poly(ethylene oxide)-based hydrogels using atom transfer radical polymerization. The method allowed controlled release over a period of 1 month and the release profile can be programmed through crosslinking density and light stimuli conditions (Yerneni et al.eng, 2022). Yang et al. developed a photocleavable prodrug loaded injectable glycol chitosan (GC) hydrogel for NIR-triggered repetitive drug

release. The hydrogel shows good stability, minimum leakage and efficient light responsibility both *in vitro* and *in vivo* (Yang et al., 2022).

When photocleavable linkers attach model drugs to polymer matrix covalently, it may cause great reduction to drug activities as well as unspecified tethers. To overcome these disadvantages, some researchers used recombinant protein techniques to modify proteins with a handle in order to attach a protein of interest to the hydrogel matrix. In one study, a PEG-based hydrogel was developed *via* a click reaction without impact on entrapped enzyme activity under 60°C thermal stress for weeks. The study showed a general method to preserve drug activities at certain conditions and enable controlled drug release when needed (Sridhar et al., 2018/03). In another study, the authors developed a technique to use light-sensing proteins as light-activated reversible binding sites within synthetic poly(ethylene glycol) (PEG) hydrogels. It has reversible changes between "light" and "dark" conformations in response to different lights to control a recombinant protein release from PEG hydrogels spatiotemporally (Hammer et al., 2020/07). In a recent study, both nitrobenzyl and coumarin were used for photolabile crosslinks, and subsequently, on-demand and tunable dual wavelength release of antibody was achieved (Figure 1G) (LeValley et al.eng, 2020).

5 Photothermal reaction-based drug delivery systems

Photothermal therapy-based drug delivery system includes a photothermal agent, which is able to generate heat through light irradiation. The heat energy is then used to trigger reversible structure changes of thermal-responsive hydrogels, subsequently cause drug release from the system (Pan et al., 2021/10). Some commonly used photothermal agents include both inorganic nanoparticles and organic compounds, such as rare metal nanostructures and black phosphorus (BP) nanoparticles, which have little phototoxicity. These photothermal agents have minimized damage to cells and good penetration for high efficiency, and thus can provide safe thermal effects for controlled drug release (Zhang et al., 2015; Zhu et al., 2015; Wang et al., 2016; Yang et al., 2018). Commonly used thermal-responsive hydrogels include poly(N-isopropylacrylamide) (PNIPAAm), thermosensitive PEG analogs and thermosensitive elastin peptides (ELPs) (Ward and Georgiou, 2011). Because high temperature can lead to cell necrosis, the parameters of applied light irradiation should be carefully selected to avoid thermal damage to surrounding areas of targeted cells or tissues (Yang et al.eng, 2017). For this reason, NIR light is widely used to initiate photothermal effects because of its low energy and deep penetration properties. The drug release parameters can be accurately controlled by light duration and intensity, concentration of photothermal agents, and hydrogel composition (Merino et al., 2015).

BP nanoparticles are one of the most popular photothermal agents. Qiu et al. developed a low–melting-point agarose drug delivery nanostructure containing BP. After injected into cancer tissue, the hydrogel experiences a phase transition to gel states at body temperature. Under NIR irradiation, the hydrogel entered in a melting state which caused drug release from its matrix. Additionally, the release rate is able to be accurately controlled (Qiu et al., 2018). The system demonstrated a high therapeutic efficacy for cancers, and it is harmless and degradable *in vivo*. In another study, an injectable, NIR-II light-modulated and thermosensitive hydrogel is synthesized through supramolecular self-assembly of a conjugated polymer and alpha-cyclodextrin. This hydrogel intrinsically features NIR responsive characteristics and thermo-responsive properties (Figure 1H) (Ruan et al., 2019).

Rare metals are also widely used as photothermal agents. In one study, platinum nanoparticles were integrated into a NIR light-responsive hydrogel consisting of αCD and PEG-modified dendrimer. Under NIR irradiation, this hydrogel underwent a disruption to release the encapsulated drugs in a controlled manner *via* the irradiation time (Wang et al., 2016). Platinum nanoparticle has a very good photothermal conversion efficiency and biocompatibility; thus, it is frequently used with hydrogels for drug delivery. In another similar study, aldehyde-modified dextran hydrogel containing dendrimer-encapsulated platinum nanoparticles were developed *via* imine bond formation. The hydrogel exhibited excellent biocompatibility, photothermal effect and biodegradable properties. It can stay in tumors for days to allow repeated drug release, resulting in tumor regression (Li et al., 2018b).

For a study using organic compounds as the photothermal agent, one type of PNIPAM hydrogel has been synthesized with protoporphyrin IX or pheophorbide as photothermal agents, which are covalently conjugated to the polymer chains. The hydrogels showed great biocompatibility with more than 90% cell viability even at very high photosensitizer concentration suggesting the hydrogels can be applied for photothermal therapy (Belali et al.eng, 2018). In another study, the authors designed a novel type of dynamic-covalent hydrogel (GelPV-DOX-DBNP) for combined chemical and photothermal therapy of cancers. Anticancer drug DOX and photosensitizer perylene diimide zwitterionic polymer (PDS) as well as reductant ascorbic acid (Vc) were encapsulated. Under 600 nm light irradiation, PDS and VC can turn oxygen to hydrogen and cause degradation of hydrogel, subsequently lead to DOX and DBNP release from hydrogel. DBNPs are able to generate heat under NIR irradiation, making the system a useful drug delivery platform (Sun et al.eng, 2020). Cao et al. developed a chemo-photodynamic therapy system using ROS sensitive structure and successfully used for cancer treatment (Figure 1I) (Cao et al., 2018).

6 Light-induced multi-stimuli responsive drug delivery systems

Multi-stimuli responsive hydrogels have been used in a variety of physiological or pathological conditions. Besides responding to light, hydrogels can also be designed to respond to pH, magnetic field and reductant etc (Sharifzadeh and Hosseinkhani, 2017; Pham et al., 2020). In one study, hydrogels that can respond to both pH and NIR is designed to release adamantane-modified doxorubicin (DOX) prodrug using N-isopropylacrylamide (NIPAm) and βCD-based hydrogel. The pH-responsive release of DOX from the nanocomposite hydrogel was observed owing to the cleavage of acid-labile hydrazone bond between DOX and the adamantyl group in acidic environment. NIR irradiation led to accelerated release of DOX from hydrogels because of photothermal effects. The hydrogel can respond to both pH and NIR light and speed up drug release rate in a controlled manner (Xu et al.eng, 2017). In another study combining light and magnetic field, the authors designed a temperature-responsive PNIPAm hydrogel microfibers with controlled shapes and sizes. Then they fabricated light-responsive materials by incorporating photothermal magnetic nanoparticles within the PNIPAm microfibers. The magnetic nanoparticles were incorporated into the PNIPAm microfibers and created heat when subjected to visible light exposure. Volume changes of the PNIPAm hydrogel can be induced by both light irradiation and temperature, suggesting its potential use for drug delivery (Lim et al., 2015). Shao et al. developed a PEG based nanocarrier with light and redox dual responsive properties for cancer therapy. The system possesses good drug loading capacity and stability, and showed preferred tumor accumulation and the prolonged tumor residency by *in vivo* and *ex vivo* experiments (Shao et al., 2014). In another study, photo, pH and redox multi-responsive nanogels were developed for drug delivery and fluorescence cell imaging (Chen et al., 2017) (Figures 1J, K). Multi-stimuli responsive hydrogels are multi-functional, and suitable for multi-step drug delivery systems especially for complicated *in vivo* studies.

7 Discussion

Light is a powerful trigger for controlled drug delivery systems. Intensity, spatial and temporal control of light allows excellent manipulation of therapeutic agents in comparison with other physical, chemical, and biological stimuli (Chen et al., 2020). So far, much progress has been made in developing of innovative light responsive hydrogel drug delivery systems with both breadth and depth. But translating these studies into clinical applications still poses a significant challenge. Major issues need to be addressed includes: 1) most tumors are deep within the body, and it is difficult to deliver drugs to these locations. 2) the *in vivo* biological conditions of human are complex, therapeutic effects of drugs are low comparing *in vitro* or animal studies. 3) biomaterials of the drug delivery system, including hydrogel, photosensitizer, drug carrier and other components, may accumulate within human body after long-term administration. 4) most light induced drug delivery systems are irreversible, which made drug release inconsistent during the process. 5) non-specific photoreactions in normal tissues need to be considered. 6) photosensitizers are still active in dark conditions, and thus stability of loaded drugs cannot be maintained especially for long-term use.

Considering above issues, potential future developments may include: 1) designing photosensitizers responsive to low energy light source with fast response, high efficacy and deep tissue penetration (Li et al., 2019). Low energy lights, such as NIR, also cause less non-specific phototoxicity in normal tissues. 2) characterizing *in vivo* biological conditions, such as pH, temperature, redox and enzymatic reactions. These stimuli should be used together with light for drug release. 3) developing highly biocompatible materials for drug delivery systems. Natural biomaterials that mimic human tissues may be promising. 4) combing photoisomerization with other reactions to design reversible systems. Light-responsive proteins may have wider applications for this purpose (Tao et al., 2020). 5) besides using low energy light, monitoring real time drug distribution within tissue is another way minimize non-specific photoreactions. 6) developing stable photosensitizers for long-term stable drug release. Additionally, combining two or more independent photo-induced reactions into one drug delivery system is appealing for clinical use (LeValley et al.eng, 2020).

Author contributions

YX wrote the manuscript. BZ and WY provided supports.

Funding

The research was supported grant #11672078 from the National Natural Science Foundation of China (NSFC) and grant #NTF21014 from Shantou University to YX.

Conflict of interest

The authors declare that the research was conducted in the absence of any commercial or financial relationships that could be construed as a potential conflict of interest.

Publisher's note

References

Arrizabalaga, J. H., Smallcomb, M., Abu-Laban, M., Liu, Y., Yeingst, T. J., Dhawan, A., et al. (2022). "Ultrasound-responsive hydrogels for on-demand protein release,". Editor eng, 5, 3212–3218.*ACS Appl. bio Mater.* 7. doi:10.1021/acsabm.2c00192

Belali, S., Savoie, H., O'Brien, J. M., Cafolla, A. A., O'Connell, B., Karimi, A. R., et al. (2018). "Synthesis and characterization of temperature-sensitive and chemically cross-linked poly(N-isopropylacrylamide)/Photosensitizer hydrogels for applications in photodynamic therapy,". Editor eng, 19, 1592–1601.*Biomacromolecules*5. doi:10.1021/acs.biomac.8b00293

Bordbar-Khiabani, A., and Gasik, M. (2022). Smart hydrogels for advanced drug delivery systems. *Int. J. Mol. Sci.* 23 (7), 3665. in eng. doi:10.3390/ijms23073665

Bustamante-Torres, M., Romero-Fierro, D., Arcentales-Vera, B., Palomino, K., Magaña, H., Bucio, E., et al. (2021). Hydrogels classification according to the physical or chemical interactions and as stimuli-sensitive materials. *Gels* 7 (4), 182. doi:10.3390/gels7040182

Cao, Z. Y., Sun, C., Lu, Z., Yao, Z., Wang, J., et al. (2018). ROS-sensitive polymeric nanocarriers with red light-activated size shrinkage for remotely controlled drug release. *Chem. Mat.* 30 (2), 517–525. doi:10.1021/acs.chemmater.7b04751

Chatterjee, S., Hui, P. C., Kan, C. W., and Wang, W. (2019). Dual-responsive (pH/temperature) Pluronic F-127 hydrogel drug delivery system for textile-based transdermal therapy. *Sci. Rep.* 9 (1), 11658. (in eng). doi:10.1038/s41598-019-48254-6

Chen, D., Chen, C., Huang, C., Chen, T., and Liu, Z. (2020). Injectable hydrogel for NIR-II photo-thermal tumor therapy and dihydroartemisinin-mediated chemodynamic therapy. *Front. Chem.* 8, 251. eng. doi:10.3389/fchem.2020.00251

Chen, S., Bian, Q., Wang, P., Zheng, X., Lv, L., Dang, Z., et al. (2017). Photo, pH and redox multi-responsive nanogels for drug delivery and fluorescence cell imaging. *Polym. Chem.* 8 (39), 6150–6157. doi:10.1039/c7py01424d

Chen, X., et al. (2016). "Light-induced hydrogel based on tumor-targeting mesoporous silica nanoparticles as a theranostic platform for sustained cancer treatment,". Editor eng, 8, 15857–15863.*ACS Appl. Mater. interfaces*25

Cheng, Y. E., Wu, I. E., Chen, Y. C., and Chu, I. M. (2022). Thermo-sensitive mPEG-PA-PLL hydrogel for drug release of calcitonin. *Gels* 8 (5), 282. (in eng). doi:10.3390/gels8050282

Chiang, C. Y., and Chu, C. C. (2015). Synthesis of photoresponsive hybrid alginate hydrogel with photo-controlled release behavior. *Carbohydr. Polym.* 119, 18–25. (in eng). doi:10.1016/j.carbpol.2014.11.043

Claaßen, C., Claaßen, M. H., Gohl, F., Tovar, G. E. M., Borchers, K., and Southan, A. (2018). "Photoinduced cleavage and hydrolysis of o-nitrobenzyl linker and covalent linker immobilization in gelatin methacryloyl hydrogels,". Editor eng, 18, e1800104.*Macromol. Biosci.* 9

Ebara, M., Kotsuchibashi, Y., Uto, K., Aoyagi, T., Kim, Y. J., Narain, R., et al. (2014). "Smart hydrogels," in *Smart biomaterials* (Tokyo, Japan: Springer Japan), 9–65.

Ghani, M., Heiskanen, A., Kajtez, J., Rezaei, B., Larsen, N. B., Thomsen, P., et al. (2021/01/27 2021). On-demand reversible UV-triggered interpenetrating polymer network-based drug delivery system using the spiropyran–merocyanine hydrophobicity switch. *ACS Appl. Mat. Interfaces* 13 (3), 3591–3604. doi:10.1021/acsami.0c19081

Gil, E. S., and Hudson, S. M. (2004). Stimuli-reponsive polymers and their bioconjugates. *Prog. Polym. Sci.* 29 (12), 1173–1222. doi:10.1016/j.progpolymsci.2004.08.003

Hammer, J. A., Ruta, A., and West, J. L. (2020). Using tools from optogenetics to create light-responsive biomaterials: LOVTRAP-PEG hydrogels for dynamic peptide immobilization. *Ann. Biomed. Eng.* 48 (7), 1885–1894. doi:10.1007/s10439-019-02407-w

Iwaso, K., Takashima, Y., and Harada, A. (2016). Fast response dry-type artificial molecular muscles with [c2]daisy chains. *Nat. Chem.* 8 (6), 625–632. in eng. doi:10.1038/nchem.2513

Ji, W., Wu, Q., Han, X., Zhang, W., Wei, W., Chen, L., et al. (2020). "Photosensitive hydrogels: From structure, mechanisms, design to bioapplications,". Editor eng, 63, 1813–1828.*Sci. China. Life Sci.* 12 doi:10.1007/s11427-019-1710-8

Jiang, L., and Wen, L. (2015). "2 - photonic sensitive switchable materials," in *Biophotonics for medical applications*, I. Meglinski (Sawston, UK: Woodhead Publishing), 25–51. doi:10.1016/B978-0-85709-662-3.00002-6

LeValley, P. J., Sutherland, B. P., Jaje, J., Gibbs, S., Jones, R. M., Gala, R. P., et al. (2020). "On-demand and tunable dual wavelength release of antibody using light-responsive hydrogels,". Editor eng, 3, 6944–6958.*ACS Appl. bio Mater.* 10. doi:10.1021/acsabm.0c00823

Li, C., Iscen, A., Palmer, L. C., Schatz, G. C., and Stupp, S. I. (2020). Light-driven expansion of spiropyran hydrogels. *J. Am. Chem. Soc.* 142 (18), 8447–8453. doi:10.1021/jacs.0c02201

Li, L., Scheiger, J. M., and Levkin, P. A. (2019). Design and applications of photoresponsive hydrogels. *Adv. Mat.* 31 (26), 1807333. doi:10.1002/adma.201807333

Li, L., Wang, C., Huang, Q., Xiao, J., Zhang, Q., and Cheng, Y. (2018). A degradable hydrogel formed by dendrimer-encapsulated platinum nanoparticles and oxidized dextran for repeated photothermal cancer therapy. *J. Mat. Chem. B* 6 (16), 2474–2480. doi:10.1039/c8tb00091c

Li, X., and Su, X. (2018). "Multifunctional smart hydrogels: Potential in tissue engineering and cancer therapy,". Editor eng, 6, 4714–4730.*J. Mater. Chem. B* 29, doi:10.1039/C8TB01078A

Liang, J., Liu, J., Jin, X., Yao, S., Chen, B., Huang, Q., et al. (2020). "Versatile nanoplatform loaded with doxorubicin and graphene quantum dots/methylene blue for drug delivery and chemophotothermal/photodynamic synergetic cancer therapy,". Editor eng, 3, 7122–7132.*ACS Appl. bio Mater.*10. doi:10.1021/acsabm.0c00942

Liese, J., and Hampp, N. A. (2011). Synthesis and photocleavage of a new polymerizable [2+2] hetero dimer for phototriggered drug delivery. *J. Photochem. Photobiol. A Chem.* 219 (2), 228–234. doi:10.1016/j.jphotochem.2011.02.021

Lim, D., Lee, E., Kim, H., Park, S., Baek, S., and Yoon, J. (2015). Multi stimuli-responsive hydrogel microfibers containing magnetite nanoparticles prepared using microcapillary devices. *Soft matter* 11 (8), 1606–1613. doi:10.1039/C4SM02564D

Linsley, C. S., and Wu, B. M. (2017). "Recent advances in light-responsive on-demand drug-delivery systems,". Editor eng, 8, 89–107.*Ther. Deliv.* 2, doi:10.4155/tde-2016-0060

Merino, S., Martín, C., Kostarelos, K., Prato, M., and Vázquez, E. (2015). Nanocomposite hydrogels: 3D polymer-nanoparticle synergies for on-demand drug delivery. *ACS Nano* 9 (5), 4686–4697. eng. doi:10.1021/acsnano.5b01433

Miranda, D., and Lovell, J. F. (2016). Mechanisms of light-induced liposome permeabilization. *Bioeng. Transl. Med.* 1 (3), 267–276. (in eng). doi:10.1002/btm2.10032

Nehls, E. M., Rosales, A. M., and Anseth, K. S. (2016). Enhanced user-control of small molecule drug release from a poly(ethylene glycol) hydrogel via azobenzene/cyclodextrin complex tethers. *J. Mat. Chem. B* 4 (6), 1035–1039. eng. doi:10.1039/c5tb02004b)

Pan, P., Svirskis, D., Rees, S. W. P., Barker, D., Waterhouse, G. I. N., and Wu, Z. (2021). Photosensitive drug delivery systems for cancer therapy: Mechanisms and applications. *J. Control. Release* 338, 446–461. doi:10.1016/j.jconrel.2021.08.053

Peng, K., Tomatsu, I., van den Broek, B., Cui, C., Korobko, A. V., van Noort, J., et al. (2011). Dextran based photodegradable hydrogels formed via a Michael addition. *Soft matter* 7 (10), 4881–4887. doi:10.1039/c1sm05291h

Pham, S. H., Choi, Y., and Choi, J. (2020). Stimuli-responsive nanomaterials for application in antitumor therapy and drug delivery. *Pharmaceutics* 12 (7), 630. doi:10.3390/pharmaceutics12070630

Pokharel, M., and Park, K. (2022). Light mediated drug delivery systems: A review. *J. drug Target.* 30 (4), 368–380. in eng. doi:10.1080/1061186x.2021.2005610

Pourjavadi, A., Bagherifard, M., and Doroudian, M. (2020). Synthesis of micelles based on chitosan functionalized with gold nanorods as a light sensitive drug

delivery vehicle. *Int. J. Biol. Macromol.* 149, 809–818. in eng. doi:10.1016/j.ijbiomac.2020.01.162

Qiu, M., Wang, D., Liang, W., Liu, L., Zhang, Y., Chen, X., et al. (2018). Novel concept of the smart NIR-light–controlled drug release of black phosphorus nanostructure for cancer therapy. *Proc. Natl. Acad. Sci. U. S. A.* 115 (3), 501–506. doi:10.1073/pnas.1714421115

Rapp, T. L., and Dmochowski, I. J. (2019). Ruthenium-cross-linked hydrogels for rapid, visible-light protein release. *Methods Enzymol.* 624, 151–166. (in eng). doi:10.1016/bs.mie.2019.04.017

Rastogi, S. K., Anderson, H. E., Lamas, J., Barret, S., Cantu, T., Zauscher, S., et al. (2018). "Enhanced release of molecules upon ultraviolet (UV) light irradiation from photoresponsive hydrogels prepared from bifunctional azobenzene and four-arm poly(ethylene glycol),". Editor eng, 10, 30071–30080.*ACS Appl. Mater. interfaces*36. doi:10.1016/bs.mie.2019.04.017

Rizzo, F., and Kehr, N. S. (2021). "Recent advances in injectable hydrogels for controlled and local drug delivery,". Editor eng, 10, e2001341.*Adv. Healthc. Mater.* 1, doi:10.1021/acsami.6b16183

Rosales, A. M., Rodell, C. B., Chen, M. H., Morrow, M. G., Anseth, K. S., and Burdick, J. A. (2018). "Reversible control of network properties in azobenzene-containing hyaluronic acid-based hydrogels,". Editor eng, 29, 905–913.*Bioconjugate Chem.*4, doi:10.1021/acs.bioconjchem.7b00802

Ruan, C. P., Liu, C., Hu, H., Guo, X. L., Jiang, B. P., Liang, H., et al. (2019). NIR-II light-modulated thermosensitive hydrogel for light-triggered cisplatin release and repeatable chemo-photothermal therapy. *Chem. Sci.* 10 (17), 4699–4706. doi:10.1039/c9sc00375d

Shadish, J. A., and DeForest, C. A. (2020). Site-selective protein modification: From functionalized proteins to functional biomaterials. *Matter* 2 (1), 50–77. doi:10.1016/j.matt.2019.11.011

Shao, Y., Shi, C., Xu, G., Guo, D., and Luo, J. (2014). "Photo and redox dual responsive reversibly cross-linked nanocarrier for efficient tumor-targeted drug delivery,". Editor eng, 6, 10381–10392.*ACS Appl. Mater. interfaces* 13. doi:10.1021/am501913m

Sharifzadeh, G., and Hosseinkhani, H. (2017). Biomolecule-responsive hydrogels in medicine. *Adv. Healthc. Mat.* 6 (24), 1700801. doi:10.1002/adhm.201700801

Sridhar, B. V., Janczy, J. R., Hatlevik, Ø., Wolfson, G., Anseth, K. S., and Tibbitt, M. W. (2018/03/12 2018). Thermal stabilization of biologics with photoresponsive hydrogels. *Biomacromolecules* 19 (3), 740–747. doi:10.1021/acs.biomac.7b01507

Sun, P., Huang, T., Wang, X., Wang, G., Liu, Z., Chen, G., et al. (2020). "Dynamic-covalent hydrogel with NIR-triggered drug delivery for localized chemo-photothermal combination therapy,". Editor eng, 21, 556–565.*Biomacromolecules* 2. doi:10.1021/acs.biomac.9b01290

Tao, B., Lin, C., Deng, Y., Yuan, Z., Shen, X., Chen, M., et al. (2019). Copper-nanoparticle-embedded hydrogel for killing bacteria and promoting wound healing with photothermal therapy. *J. Mat. Chem. B* 7 (15), 2534–2548. in eng. doi:10.1039/c8tb03272f

Tao, Y., Chan, H. F., Shi, B., Li, M., and Leong, K. W. (2020). "Light: A magical tool for controlled drug delivery,". Editor eng, 30.*Adv. Funct. Mater.* 49. doi:10.1002/adfm.202005029

Tomatsu, I., Peng, K., and Kros, A. (2011). Photoresponsive hydrogels for biomedical applications. *Adv. drug Deliv. Rev.* 63 (14-15), 1257–1266. (in eng). doi:10.1016/j.addr.2011.06.009

Tong, R., Hemmati, H. D., Langer, R., and Kohane, D. S. (2012). "Photoswitchable nanoparticles for triggered tissue penetration and drug delivery,". Editor eng, 134, 8848–8855.)*J. Am. Chem. Soc.*21

Ullah, F., Othman, M. B., Javed, F., Ahmad, Z., and Md Akil, H. (2015). Classification, processing and application of hydrogels: A review. *Mater. Sci. Eng. C* 57, 414–433. (in eng). doi:10.1016/j.msec.2015.07.053

Wang, C., Yang, P., Li, Y., Liu, C., Wei, Q., Yang, L., et al. (2020). S, S-Tetrazine-Based hydrogels with visible light cleavable properties for on-demand anticancer drug delivery. *Research* 2020, 6563091–6563111. doi:10.34133/2020/6563091

Wang, D., Wagner, M., Butt, H. J., and Wu, S. (2015). Supramolecular hydrogels constructed by red-light-responsive host-guest interactions for photo-controlled protein release in deep tissue. *Soft matter* 11 (38), 7656–7662. (in eng). doi:10.1039/c5sm01888a

Wang, X., Wang, C., Zhang, Q., and Cheng, Y. (2016). "Near infrared light-responsive and injectable supramolecular hydrogels for on-demand drug delivery,". Editor eng, 52, 978–981.*Chem. Commun. Camb. Engl.*5. doi:10.1039/c5cc08391e

Ward, M. A., and Georgiou, T. K. (2011). Thermoresponsive polymers for biomedical applications. *Polymers* 3 (3), 1215–1242. doi:10.3390/polym3031215

Wei, X., Liu, C., Wang, Z., and Luo, Y. (2020). 3D printed core-shell hydrogel fiber scaffolds with NIR-triggered drug release for localized therapy of breast cancer. *Int. J. Pharm.* 580, 119219. in eng. doi:10.1016/j.ijpharm.2020.119219

Xiao, X., Hu, J., Wang, X., Huang, L., Chen, Y., Wang, W., et al. (2016). "A dual-functional supramolecular hydrogel based on a spiropyran-galactose conjugate for target-mediated and light-controlled delivery of microRNA into cells,". Editor eng, 52, 12517–12520.*Chem. Commun. Camb. Engl.*84. doi:10.1039/c6cc07386g

Xu, X., Huang, Z., Huang, Z., Zhang, X., He, S., Sun, X., et al. (2017). "Injectable, NIR/pH-Responsive nanocomposite hydrogel as long-acting implant for chemophotothermal synergistic cancer therapy,". Editor eng, 9, 20361–20375.*ACS Appl. Mater. interfaces* 24. doi:10.1039/c6cc07386g

Yan, B., Boyer, J.-C., Branda, N. R., and Zhao, Y. (2011/12/14 2011). Near-infrared light-triggered dissociation of block copolymer micelles using upconverting nanoparticles. *J. Am. Chem. Soc.* 133 (49), 19714–19717. doi:10.1021/ja209793b

Yan, B., Boyer, J.-C., Habault, D., Branda, N. R., and Zhao, Y. (2012/10/10 2012). Near infrared light triggered release of biomacromolecules from hydrogels loaded with upconversion nanoparticles. *J. Am. Chem. Soc.* 134 (40), 16558–16561. doi:10.1021/ja308876j

Yang, G., Wan, X., Gu, Z., Zeng, X., and Tang, J. (2018). Near infrared photothermal-responsive poly(vinyl alcohol)/black phosphorus composite hydrogels with excellent on-demand drug release capacity. *J. Mat. Chem. B* 106 (11), 1622–1632. doi:10.1039/c7tb03090h

Yang, Y., Zhu, W., Dong, Z., Chao, Y., Xu, L, Chen, M., et al. (2017). "1D coordination polymer nanofibers for low-temperature photothermal therapy,". Editor eng, 29.*Adv. Mater. Deerf. Beach, Fla.)*40. doi:10.1002/adma.201703588

Yang, Y., Long, K., Wang, Y., Li, L., Shi, J., Liu, J., et al. (2022). NIR light-triggered quantitative pulsed drug release. *Adv. Healthc. Mat.* 11 (8), e2102362. (in eng). doi:10.1002/adhm.202102362

Yerneni, S. S., Lathwal, S., Cuthbert, J., Kapil, K., Szczepaniak, G., Jeong, J., et al. (2022). "Controlled release of exosomes using atom transfer radical polymerization-based hydrogels,". Editor eng, 23, 1713–1722.*Biomacromolecules*4. doi:10.1021/acs.biomac.1c01636

Yu, T., Tong, L., Ao, Y., Zhang, G., Liu, Y., and Zhang, H. (2020). "NIR triggered PLGA coated Au-TiO(2) core loaded CPT-11 nanoparticles for human papillary thyroid carcinoma therapy,". Editor eng, 27, 855–863.*Drug Deliv.*1. doi:10.1080/10717544.2020.1775723

Yuan, Y., Wang, Z., Cai, P., Liu, J., Liao, L. D., Hong, M., et al. (2015). Conjugated polymer and drug co-encapsulated nanoparticles for chemo- and photo-thermal combination therapy with two-photon regulated fast drug release. *Nanoscale* 7 (7), 3067–3076. in eng. doi:10.1039/c4nr06420h

Zhang, H., Zhu, X., Ji, Y., Jiao, X., Chen, Q., Hou, L., et al. (2015). Near-infrared-triggered *in situ* hybrid hydrogel system for synergistic cancer therapy. *J. Mat. Chem. B* 3 (30), 6310–6326. doi:10.1039/C5TB00904A

Zhang, P., Li, M., Xiao, C., and Chen, X. (2021). "Stimuli-responsive polypeptides for controlled drug delivery,". Editor eng, 57, 9489–9503.*Chem. Commun. Camb. Engl.*75. doi:10.1039/d1cc04053g

Zhu, X., Zhang, H., Huang, H., Zhang, Y., Hou, L., and Zhang, Z. (2015). Functionalized graphene oxide-based thermosensitive hydrogel for magnetic hyperthermia therapy on tumors. *Nanotechnology* 26 (36), 365103. (in eng). doi:10.1088/0957-4484/26/36/365103

frontiers | Frontiers in Bioengineering and Biotechnology

TYPE Original Research
PUBLISHED 06 January 2023
DOI 10.3389/fbioe.2022.1075166

OPEN ACCESS

EDITED BY
Yasser Zare,
Motamed Cancer Institute, Iran

REVIEWED BY
Nader Nezafati,
Materials and Energy Research Center, Iran
Fatemeh Yaghoubi,
Shahid Sadoughi University of Medical Sciences and Health Services, Iran
Hamideh Barghamadi,
Islamic Azad University South Tehran Branch, Iran

*CORRESPONDENCE
Maryam Tajabadi,
mtajabadi@iust.ac.ir

†These authors have contributed equally to this work and share first authorship

SPECIALTY SECTION
This article was submitted to Nanobiotechnology, a section of the journal Frontiersin Bioengineering andBiotechnology

RECEIVED 20 October 2022
ACCEPTED 19 December 2022
PUBLISHED 06 January 2023

CITATION
Gholami M, Tajabadi M, Khavandi A and Azarpira N (2023), Synthesis, optimization, and cell response investigations of natural-based, thermoresponsive, injectable hydrogel: An attitude for 3D hepatocyte encapsulation and cell therapy. *Front. Bioeng. Biotechnol.* 10:1075166. doi: 10.3389/fbioe.2022.1075166

Synthesis, optimization, and cell response investigations of natural-based, thermoresponsive, injectable hydrogel: An attitude for 3D hepatocyte encapsulation and cell therapy

Mahnaz Gholami[1†], Maryam Tajabadi[1*†], Alireza Khavandi[1] and Negar Azarpira[2]

[1]School of Metallurgy and Materials Engineering, Iran University of Science and Technology (IUST), Tehran, Iran, [2]Transplant Research Center, Shiraz University of Medical Science, Shiraz, Iran

For the purpose of developing a 3D vehicle for the delivery of hepatocytes in cell therapy, the improved system of crosslinker and new gelling agent combinations consisting of glycerophosphate and sodium hydrogen carbonate have been employed to produce injectable, thermoresponsive hydrogels based on chitosan and silk fibroin. Adjusting the polymer-to-gelling agent ratio and utilizing a chemical crosslinker developed hydrogel scaffolds with optimal gelling time and pH. Applying sodium hydrogen carbonate neutralizes chitosan while keeping its thermoresponsive characteristics and decreases glycerophosphate from 60% to 30%. Genipin boosts the mechanical properties of hydrogel without affecting the gel time. Due to their stable microstructure and lower amine availability, genipin-containing materials have a low swelling ratio, around six compared to eight for those without genipin. Hydrogels that are crosslinked degrade about half as fast as those that are not. The slowerr degradation of Silk fibroin compared to chitosan makes it an efficient degradation inhibitor in silk-containing formulations. All of the optimized samples showed less than 5% hemolytic activity, indicating that they lacked hemolytic characteristics. The acceptable cell viability in crosslinked hydrogels ranges from 72% to 91% due to the decreasing total salt concentration, which protects cells from hyperosmolality. The pH of hydrogels and their interstitial pores kept most encapsulated cells alive and functioning for 24 h. Urea levels are higher in the encapsulation condition compared to HepG2 cultivated alone, and this may be due to cell-matrix interactions that boost liver-specific activity. Urea synthesis in genipin crosslinked hydrogels increased dramatically from day 1 (about 4 mg dl^{-1}) to day 3 (approximately 6 mg dl^{-1}), suggesting the enormous potential of these hydrogels for cell milieu preparation. All mentioned findings represent that the optimized system may be a promising candidate for liver regeneration.

KEYWORDS

injectable hydrogel, chitosan, silk fibroin, genipin, glycerophosphate, sodium hydrogen carbonate, thermoresponsive

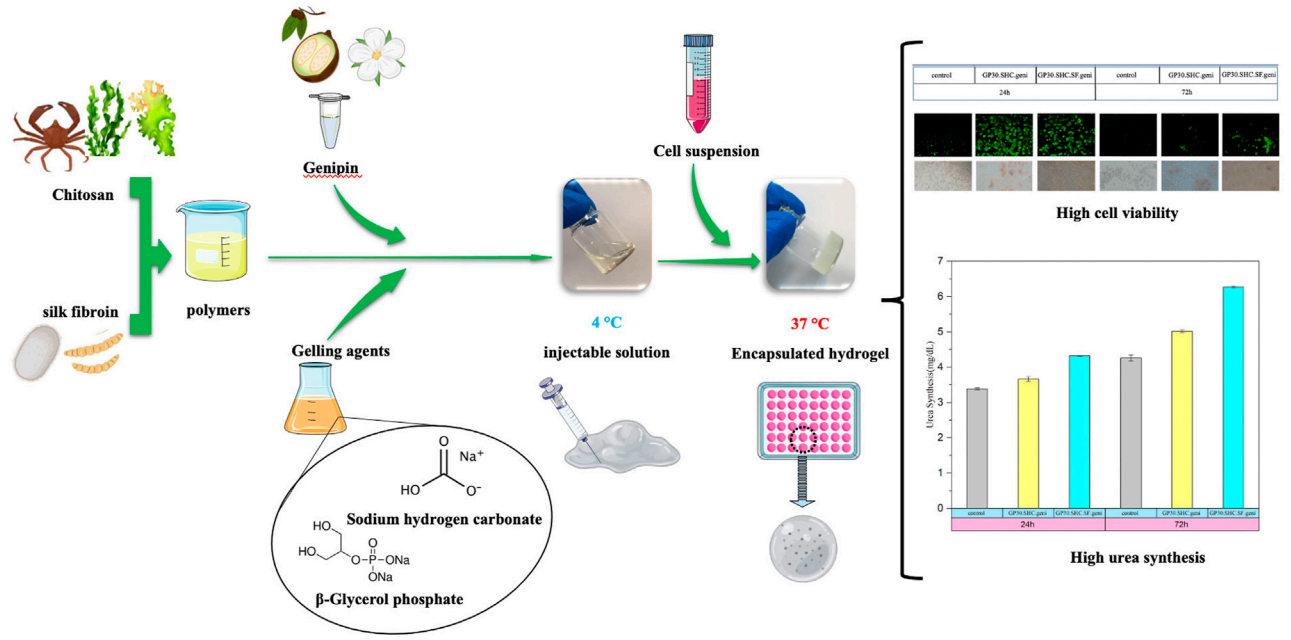

GRAPHICAL ABSTRACT

1 Introduction

As people age, their organs degenerate due to the normal human growth process. Various disorders and situations can also induce organ failure. Numerous treatments have been proposed, but none have been effective. Some illnesses are not drug-treatable, and in end-stage organ failure, the necessity for immunosuppression in organ transplantation may lead to infections and malignancies. Cell therapy, tissue engineering, and genetic manipulation have been studied to address aging, disease, and tissue and organ shortages (Ashammakhi et al., 2019). Improving cell survival and retention, tissue incorporation, and patient safety during cell therapy administration is essential. The most common cell transplantation methods are intravenous/intraarterial and intra-tissue injections. Most of these methods do not work because the cells that are transplanted die or migrate to the wrong place (De Pieri et al., 2021). When cells are transplanted *via* these routes, only around 1%–20% of them remain viable, which dramatically limits their therapeutic potential (Marquardt and Heilshorn, 2016). Tissue engineering was created to deal with these problems by introducing cells to biomaterials in a more integrated fashion. In particular, natural and synthetic compounds have been utilized to promote stem cell differentiation into target cells, alleviate direct cell delivery problems, and create applicable 3D tissue constructs (Ardeshirylajimi et al., 2018; De Pieri et al., 2021). Interdisciplinary research in tissue engineering attempts to develop biomaterials replacing damaged organs and encouraging cell proliferation (Hashemi et al., 2020).

In the case of liver and other soft tissues, the extracellular matrix (ECM)-derived hydrogel that forms the microenvironment of cell delivers various biochemical signals (Ijima et al., 2019; Lee et al., 2020). Every alteration in the ECM of liver affects its structure and function, highlighting the critical role of the surrounding ECM in preserving ability of hepatocytes to carry out their specialized hepatic roles (Saheli et al., 2018; Ye et al., 2019). When designing hydrogels, it is important to take into account the specific needs of hepatocytes for biocompatibility, biodegradability, thermoresponsiveness, and swelling (Ye et al., 2019). In order to create a microenvironment that is more similar to the liver, 3D scaffolds made from natural biomaterials are preferred (Lee et al., 2020). Anchorage-dependent hepatocytes modulate cell-matrix interactions. The matrix for cultivating hepatocytes should be extremely porous and mechanically stable, allowing nutrition, metabolite, and growth factor diffusion to stimulate vascularization and maintain liver functions (Janani et al., 2018). Encapsulated hepatocytes offer hepatic activities without immunosuppression, since they are shielded from activated immune cells (Iansante et al., 2018; Zhang et al., 2021).

Hydrogels, which emerged in the literature in 1894, are commonly employed in tissue engineering and regenerative medicine as a promising and encouraging candidate biomaterial. Hydrogels are a network of naturally occurring or synthesized hydrophilic polymer chains that are as flexible as natural tissues (Ye et al., 2019). By demonstrating structural similarities to biomacromolecules found in ECMs, hydrogels have played an important role in improving the permeability of oxygen, vitamins, and other water-soluble metabolites and stimulating biological activities (Afewerki et al., 2019). Hydrogels, with their adjustable porosity, changeable transpermeability, and appropriate mechanical properties, not only allow for the delivery of oxygen and nutrients and the release of depleted metabolites but also protect encapsulated cells from cytotoxic molecules, mechanical loads, and immune attacks (Wang et al., 2018). The recently coined phrase "injectable hydrogel" has gradually attracted researchers' interest in hydrogel-based biomaterials due to its capacity to fulfill biological tasks (Liao et al., 2020). Because of their minimally invasive nature and ability to develop a specific shape, injectable hydrogels might be the next hot topic for surgeons. Injectable hydrogels may also create minor frictional irritations in natural tissue and eliminate the need

for complex surgical procedures (Alinejad et al., 2018). To be used in medicine, an injectable hydrogel must be robust enough to withstand the stresses of its intended application but flexible enough to reach the correct site quickly (Pettinelli et al., 2020). Polysaccharides, proteins, and peptides, i.e., natural polymers, are often employed to create injectable hydrogels. Among them, as a result of their superior water solubility, biocompatibility, and biodegradability, polysaccharides are commonly employed to create hydrogels for injection (Thambi et al., 2016; Rijal et al., 2017).

As a deacetylated derivative of chitin, chitosan (Cs) is composed of β-(1-4) linked D-glucosamine and N-acetylglucosamine groups, the distribution of which varies with the degree of deacetylation (Jiang et al., 2015; Ahmed et al., 2018; Islam et al., 2020). Since chitosan mimics glycosaminoglycan, the foundational element of the ECM, it has been used as a scaffold for tissue engineering in recent years (Ardeshirylajimi et al., 2018). Temperature-responsive systems based on chitosan, a class of hydrogel systems that change their liquid state in response to the external temperature, are being investigated to help cell proliferation in tissue regeneration (Bhattarai et al., 2010; Saravanan et al., 2019). Chenite et al. (2000) and Pankongadisak and Suwantong (2019) previously introduced injectable thermogelling Cs/β-glycerol phosphate disodium salt (Cs/GP) hydrogels, which have a fluid shape at low temperatures but gel at 37°C. Glycerophosphate (GP) is generally identified in the body and utilized as a phosphate supply when phosphate absorption is unbalanced. Theoretically, the phosphates in GP salt neutralize the ammonium groups in chitosan, enabling greater hydrophobicity and hydrogen bonding between chitosan chains at higher temperatures. While the combination is still liquid at room temperature, it begins to gel around 37°C (Thambi et al., 2016).

As mentioned above, the ideal injectable hydrogel for tissue regeneration has a short gelation period, controlled degradation, and desirable pH stability. The concentration of GP may be adjusted to influence degradation and gelation durations, the greater the concentrations, the faster gelation. However, it has been shown that higher GP degrees cause hypertonicity and cell death. In order to decrease the concentration of GP, sodium hydrogen carbonate, $NaHCO_3$, is used, which results in improved thermal stability, reduced cytotoxicity, and shorter gelation times (Assaad et al., 2015; Saravanan et al., 2019).

Biocompatibility, hydrophilicity, and acceptable mechanical properties may all be achieved by combining silk fibroin (SF) and Cs (Li et al., 2018). Silkworm silk has two major components, i.e., silk fibroin and silk sericin; among them, silk fibroin has long been used in tissue engineering and regenerative medicine as a natural polymer, resulting in enhanced degrees of interconnection and increased surface area for cell attachment (Floren et al., 2016; Sun et al., 2016; Panjapheree et al., 2018). Fibroin is made up of a repeating amino acid sequence that includes glycine, serine, and alanine and could be obtained by removing cytotoxic silk sericin (Celikkin et al., 2017).

The crosslinkers, such as glutaraldehyde or genipin, have modified polymer components to stabilize the therapeutic system in a biological environment. Primary amines in protein-rich domains, such as chitosan and silk, may react with these crosslinkers (Sun et al., 2016). From the fruits of Gardenia jasminoides J. Ellis, genipin, a colorless monoterpene of the iridoid class, could be extracted. Genipin, rather than glutaraldehyde, is preferred to crosslink the hydrogel system because of its low toxicity, which allows it to be used directly in living tissue (Mirzaei et al., 2014; Neri-Numa et al., 2017). Thus, crosslinking agent based on genipin increases the mechanical characteristics of the scaffold while also helping to promote cell survival (Kwon et al., 2015).

The present study aims to investigate new formulations that enable the remarkable increase of mechanical properties and cytocompatibility of chitosan thermogels and rapid gelation. This was achieved by incorporating silk fibroin into the polymer section of hydrogel and combining GP with another weak base, i.e., sodium hydrogen carbonate (SHC), to reduce the concentration of the final gelling agent compound. Moreover, the hydrogel system, composed of chitosan-silk fibroin and gelling agent compounds, was crosslinked with genipin. Through optimizing parameters like pH, mechanical properties, gelation time, swelling behavior, biodegradability, and hemocompatibility, this research seeks to identify the best hydrogel to use as an injectable scaffold for minimally invasive therapeutic tissue engineering applications.

2 Experimental

2.1 Materials and methods

Chitosan (Cs, CAS NO. 9012-76-4), β-Glycerol phosphate disodium salt pentahydrate ($C_3H_7Na_2O_6P{\cdot}_5H_2O$, GP, CAS No. 13408-09-8), Sodium hydrogen carbonate ($NaHCO_3$, SHC, Cas No. 144-55-8), and also reagents that include acetic acid(AA), lithium bromide (LiBr), sodium carbonate (Na_2CO_3) and dimethyl sulfoxide (DMSO) were obtained from Sigma-Aldrich. Genipin ($C_{11}H_{14}O_5$, Geni, CAS No. 6902-77-8) was provided by Challenge Bioproducts Co. Ltd. (Touliu, Taiwan).

The cocoons of the silkworm (Bombyx mori) were provided by the University of Gilan. Dialysis bags (MWCO 12000) were supplied by Sigma-Aldrich. Dulbecco's Modified Eagle's Medium (DMEM), Dulbecco's Modified Eagle Medium/Nutrient Mixture F-12 (DMEM/F-12), penicillin-streptomycin antibiotics, trypsin-ethylenediaminetetraacetic acid (Trypsin- EDTA) and Fetal bovine serum (FBS) were purchased from Gibco™. 3-(4,5-Dimethylthiazol-2-yl)-2,5-diphenyl- tetrazolium bromide (MTT) were purchased from Sigma-Aldrich Co.

2.2 Hydrogel fabrication

2.2.1 Polymer solutions

2.2.1.1 Silk fibroin

The following instructions describe the preparation of silk fibroin solution that includes a degumming process. The degumming of fibers is performed to remove the glue-like sericin proteins of Bombyx mori silkworm cocoon fibers (Cárdena-Pérez et al., 2017).

The cocoons of Bombyx mori were boiled in a 0.05% Na_2CO_3 aqueous solution for 30 min at 98°C–100°C in triplicate in accordance with the technique mentioned somewhere else (Yin et al., 2017; Tao et al., 2021). The boiled cocoons were rinsed with deionized water throughout the process to eliminate the glue-like sericin proteins. The cleansed cocoons were then left to dry for almost half a day at 60°C. Degumming and drying the silk fiber allowed for a smoother

10.3389/fbioe.2022.1075166

TABLE 1 The preliminary studys' hydrogel compositions.

Sample number	Cs(%)	GP(%)	SF(%)	SHC(M)	Geni(μgr/ml)	Gel formation	Description
1	1.3	0	0	0.075	0	+	Basic pH
2	1.3	0	0	0.05	0	—	—
3	1.3	10	0	0	0	—	—
4	1.3	30	0	0	0	+	Lengthy gelation time
5	1.3	50	0	0	0	+	Appropriate gel
6	1.3	50	0	0.05	0	+	Low fluidity in the solution phase
7	1.3	50	0	0.075	0	+	Early gel formation
8	1.3	30	0	0.05	0	+	Appropriate gel
9	1.3	30	0	0.075	0	+	Early gel formation
10	1.3	10	0	0.05	0	—	—
11	1.3	10	0	0.075	0	+	Basic pH
12	1.3	30	1	0.05	0	+	Appropriate gel
13	1.3	30	2	0.05	0	+	Low fluidity in the solution phase
14	1.3	30	1	0.05	25	+	No color shift
15	1.3	30	1	0.05	50	+	Appropriate gel
16	1.3	30	0	0.05	25	+	No color shift
17	1.3	30	0	0.05	50	+	Appropriate gel

TABLE 2 Composition, pH, and gelling time of optimal synthesized hydrogels. The hydrogels had a Cs concentration of 1.3% (w/v).

Sample	Cs(%)	GP(%)	SHC)M(	SF(%)	geni(μgr/ml)	PH	Gelation time(Sec)
GP50	1.3	50	0	0	0	6.78 ± .02	382.3 ± 8.7
GP30.SHC	1.3	30	0.05	0	0	7.11 ± .09	230.6 ± 2.5
GP30.SHC.SF	1.3	30	0.05	1	0	7.31 ± .03	199.3 ± 4.1
GP30.SHC.SF.geni	1.3	30	0.05	1	50	7.34 ± .01	230.0 ± 3.2
GP30.SHC.geni	1.3	30	0.05	0	50	7.20 ± .02	220.0 ± 1.6

dissolution in a 9.3 M LiBr solution at 60°C for 1 h, yielding the purified aqueous silk fibroin solution. As a subsequent step, the SF solution with a 10% concentration (w/v) was dialyzed towards distilled water for 3 days at room temperature using a dialysis membrane (M_W cutoff: 12000). The last contaminants of silk fibroin solution were removed by centrifuging at 4,500 rpm for 10 min at 4°C. To be employed in subsequent formulations, silk fibroin has been lyophilized and then dissolved in deionized water to generate a 1% (w/v) SF solution (Li et al., 2018).

2.2.1.2 Chitosan

The chitosan powder (Cs) was dissolved in distilled water with 1% (by volume) acetic acid to produce a solution with a final chitosan concentration of 1.3% (w/v). The resulting solution was stirred at room temperature overnight. While stirring, 1 ml of SF 1% was then introduced to the chitosan solution so that the mixture of Cs/SF with a weight ratio of 1:1 was produced. The temperature of this solution was reduced to 4°C.

2.2.2 Gelling agent solutions

In terms of gelling agents (GA), GP alone, GP-SHC, or GP-SHC-Geni was used (genipin as crosslinker). The three types of gelling agent solutions are prepared by first preparing 30% (w/v) GP solution in distilled water, stirring in ice, then adding SHC powder with additional stirring until a final concentration of 0.05 M SHC is reached. The genipin solution was made by dissolving 10 mg of genipin in 1 ml of distilled water. This solution was then added to the GA solution until the final genipin concentration was 50 μg/ml. Gelling agents were filtered *via* 0.2 μm filters, sterilized, and then kept at 4°C.

2.2.3 Preparation of hydrogels for physicochemical characterization

To prepare each hydrogel at 4°C, dropwise additions of GA solutions were made to each of the sterilized polymer solutions with a volume-to-volume ratio of 1:1 (v/v). Further stirring was done to achieve homogeneous solutions. A list of all synthesized samples can be found in Table 1. Table 2 shows the samples

chosen for further research, representing the optimal pH and gelling time. Hydrogels are named based on their composition. Cs concentrations in all formulations were maintained at 1.3% (w/v); therefore, the name of the resulting hydrogels will be determined using the final concentration of the GA components. As an example, GP30.SHC.SF corresponds to a gel composed of 1.3% (w/v) of Cs, 0.05 M SHC, 1% (w/v) of SF and 30% GP Table 2.

2.2.4 Preparation of hydrogels for cell encapsulation

Two-step procedure was used for the cell encapsulation using two optimized hydrogel formulations, namely GP30.SHC.SF.geni and GP30.SHC.geni. First, dropwise additions of 2X concentrated filter-sterilized (0.22 μ) gelling agent to the stirred polymer solution on the ice were performed. Under aseptic conditions, the resultant mixture was stirred for 15 min. The cell suspensions in culture media, with concentrations of 5×10^5 cells/ml, were then inoculated into the polymer solutions at a volume ratio of 3:1 (3 for the cell suspensions and one for the polymer-GA). In each well of a 48-well plate, a volume of 500 μl gel solution containing cells was left to gel for 30 min at 37°C. After that, 400 μl of culture medium was added to the cell/hydrogel specimens, and they were incubated for another 24 h. The control was a culture medium with cells at the bottom of the 48-well plates (no scaffold).

2.3 Physicochemical characterization

2.3.1 Gel time and pH determination

For the aim of evaluating gel formation, an inverted tube test was performed. 1 ml of prepared polymer solutions mixed with gelling agents was kept at 4°C in 5 ml vials and kept in a 37°C water bath after 5 min of mixing in an ice/water bath. The time required for the sol-gel transition was measured by turning the vial upside down. The gelation time refers to the time when the gel did not flow. After incubating the hydrogels for 24 h at 37°C, they were pressed through 0.45 μ filters to yield an entrapped solution of hydrogel filtrates (Alinejad et al., 2018). Their pH was measured using a Denver Instrument UltraBasic pH meter.

2.3.2 Fourier transform infrared spectroscopy

In order to explore the effect of different gelling agents and crosslinker on the synthesis of hydrogels, the Fourier transform infrared (FTIR) spectra of freeze-dried samples of hydrogels were used. FTIR spectra were obtained using a Bruker TensorII FTIR spectrometer at wavenumbers ranging from 400 to 4,000 cm^{-1}.

2.3.3 SEM

A scanning electron microscope (SEM) was used to analyze the morphology and microstructure of the chitosan hydrogels. For this purpose, after 24 h of gelation, samples were frozen overnight at −20°C and then lyophilized for 24 h under the vacuum condition. Following dehydration, the samples were divided with a scalpel blade, gold-sputter coated, and examined using a scanning electron microscope (SEM; Hitachi S-3600).

2.3.4 Mechanical properties

After either 1 or 24 h of gelation at 37°C, 800 μl of each sample was deposited onto a 24-well plate and put in an incubator to assess the hydrogels' mechanical characteristics. Gel samples were prepared by using a sample punch to create cylinders with a diameter of 10 mm and a height of around 8 mm. A Bose ElectroForce® 3,200 instrument (Bose Corporation, United States) with a 22 N load cell is used to apply progressive compression up to 50% axial deformation (5%–50%) at a rate of 100% deformation/min, allowing for a complete characterization of the hydrogels. The Young secant moduli, defined as the slope of a line connecting the point of zero strain to a point at a specific deformation, were determined using displacement and load measurements.

2.3.5 Swelling measurement

Lyophilized samples were used to assess the swelling properties of the hydrogels. Each gel was immersed in PBS (phosphate buffer solution) at room temperature for a predetermined period of time to achieve its equilibrium swelling condition. After that, the hydrogels were delicately blotted using filter paper to wipe away any remaining PBS. Afterward, the gels were weighed (W_{wet}). The samples were re-immersed in fresh PBS. The swelling percentage was calculated using Eq. 1. All experiments were carried out three times (Alinejad et al., 2018).

$$\text{Swelling ratio} = \frac{\left(W_{wet} - W_{dry}\right)}{W_{dry}} \times 100 \quad (1)$$

W_{dry} is the initial mass of the lyophilized sample.

2.3.6 *In vitro* biodegradation study

For 4 weeks, at 37°C, in a pH 7.4 buffer solution, hydrogels were submerged in a 1000 U/ml lysozyme solution. Lysozyme concentrations like this, seen in human serum, may physiologically mimic the *in vivo* degradation process (Brouwer et al., 1984). The solution was refreshed every day. Hydrogels were taken out of the medium at regular intervals, gently dried using filter paper to remove surface water, and then weighed. Through the use of Eq. 2, the degree of *in vitro* degradation was quantified as a percentage of weight loss (Song et al., 2018).

$$\text{Weight loss (\%)} = \frac{(W_i - W_t)}{W_i} \times 100 \quad (2)$$

Here, W_i and W_t, respectively, denote the initial weight and the final weight of the samples.

2.4 Biological evaluation

2.4.1 MTT assay

The MTT assay was used to assess the *in vitro* cytotoxicity of the scaffolds in a human fibroblast cell line. An extraction test based on the ISO 10993-5 Standard (Kane et al., 2009) was used to assess the cytotoxicity of gel. Because fibroblast cells are the major cellular components of connective tissues, they are commonly utilized in biomaterial cytotoxicity investigations (De Souza et al., 2009). Fibroblast cells were cultured in DMEM/F-12 medium supplemented with 10% (v/v) heat-inactivated fetal bovine serum (FBS) and 1% (v/v) penicillin-streptomycin (100 U/ml penicillin G and 100 mg/mL streptomycin) at 37°C, under 5% CO_2.

This fibroblast cell line was expected to grow in a monolayer in a tissue culture flask that was kept at 90% relative humidity and incubated at 37°C. The media was changed every 3 days, and once the cells attained confluence, they were detached using a 0.25%

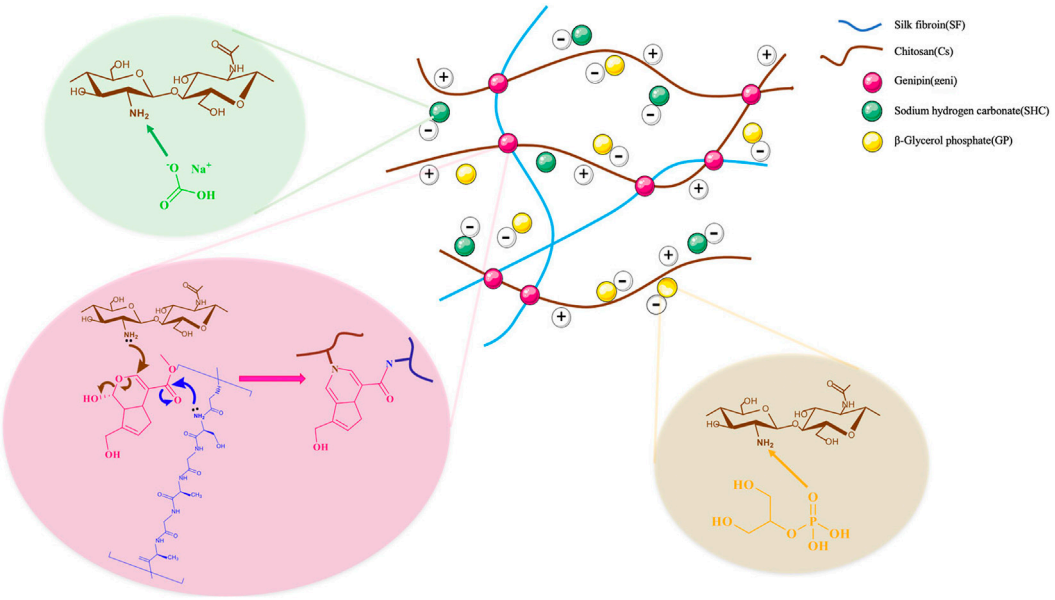

FIGURE 1
Illustrates the mechanism of production of the hydrogel network composed of polymer, and gelling agents, containing chitosan, silk fibroin, glycerophosphates, sodium hydrogen carbonate, and genipin as crosslinker. The electrostatic interactions between the positive charge of amine group of the polymer and the negative charge of the gelling agent are involved in the gelation mechanism. Between the polymer chains, there are additional hydrophobic interactions and hydrogen bond formation.

trypsin/EDTA solution. Cells were counted using a hemocytometer and seeded at a density of 7,000 cells/well in 96-well plates for the 24, 48, and 72-h MTT tests.

The gels were immersed in a culture medium at 1 ml per 1 g of sterilized hydrogels weight extraction ratio and kept at 37°C in a humidified environment of 5% CO_2 for 48 h. After 24 h, growth media was aspirated and replaced with 100 µl of 25, 50, and 100% concentrations of extraction medium produced based on the extract dilution method of cytotoxicity. Cell viability was assessed using the MTT test method after 24, 48, and 72 h of incubation.

Each well was filled with 100 µl of 5 mg/ml thiazolyl blue tetrazolium bromide solution (in culture media), and the plates were incubated for 3–4 h. MTT solution was taken away after incubation and substituted with 100 µl of DMSO. Finally, cell viability was determined using a Spectra Max Plus microplate reader and optical absorbance at 570 nm (Molecular Devices, CA, United States). Cells cultured with just a medium were used as a control, which was considered 100% cell viability.

2.4.2 Hemolysis

The degree to which the hydrogels caused hemolysis was determined by measuring the amount of hemoglobin that was released into the solution phase from hydrogel-exposed erythrocytes in whole blood. The process for making thermosensitive hydrogels was the same as that utilized for microscopic examination.

0.2 ml of anticoagulated whole blood was added to 10 ml of:

1) 0.9% NaCl solution comprising various hydrogel samples (0.25 g), allowing the samples to be soaked in an anticoagulant blood and saline solution for 120 min at 37°C with gentle agitation.
2) Physiological saline solution and distilled water served as negative and positive controls, respectively.

The samples were incubated for 2 h and centrifuged at 1,000 rpm for 10 min, and the absorbance of the supernatants from each tube was measured at 545 nm in a spectrophotometric plate reader. The tests were performed in triplicate on the samples. Eq. 3 was utilized to calculate the hemolysis ratio.

$$\text{Rate of hemolysis}\,(\%) = \frac{\text{OD}_{\text{sample}} - \text{OD}_{\text{negative}}}{\text{OD}_{\text{positive}} - \text{OD}_{\text{negative}}} \times 100 \qquad (3)$$

2.4.3 Cell viability assessment in hydrogels

HepG2 cells (human hepatocyte-like cell line) were cultured in Dulbecco's modified Eagle's medium (DMEM) supplemented with 10% fetal bovine serum, 100 U/ml penicillin, and .1 mg/ml streptomycin at 37°C in a CO_2 incubator. At 85% confluency, cells were removed from culture dishes using the trypsin-EDTA treatment and then suspended in culture media. Using moderate centrifugation, a cell pellet was formed.

The viability of cells after 24 h of entrapment in the hydrogel was determined using a fluorescence assay that simultaneously identifies live and dead cells using 5×10^{-2} µg/ml fluorescein diacetate (green) and propidium iodide (red), both from Sigma-Aldrich, in sterile PBS. The staining solution was applied to the cell-encapsulating hydrogels for 5 min at 37°C, and the cells were observed using an Olympus fluorescent microscope with a digital camera.

2.4.4 Urea synthesis

For the purpose of determining whether or not the encapsulated construct enhances hepatic cell functionality, the urea production level of HepG2 was measured. The encapsulated cells (HepG2 cells in blend gels) were put into a 24-well plate. The medium was changed regularly every day. Following each specific time interval (days 1 and 3), media from

3D culture systems was collected and stored at −80°C before being measured. The urea synthesis rate was measured using the commercial urea UV kit (Pars Azmon, Iran) according to the manufacturer's protocol. Absorbance at 430 nm was determined after incubating an equivalent volume of working reagents with the medium for 1 h at room temperature in a dark environment (MD SPECTRAMAX 190). A minimum of three replicates were conducted for each sample. The results were presented as mg dL^{-1} and compared to a standard curve.

2.4.5 Statistical analysis

At least three independent replicates of each experiment were conducted. The results of this investigation were presented as the mean SD of the obtained data (SD).

3 Result and discussion

3.1 Physicochemical characterization

3.1.1 Gel formation of hydrogel

The process of gel formation, as seen in Figure 1, will be thoroughly explained below. Since the -NH_2 groups are protonated in acidic environments, chitosan becomes a polyelectrolyte. Aqueous solution of chitosan solubility is accomplished through the protonation of its amine groups in acidic conditions. The condition of ionization was expressed by the equilibrium reaction, Eq. 4 (Rinaudo et al., 1999):

$$Cs - NH_2 + H_3O^+ \leftrightarrow Cs - NH_3^+ + H_2O \quad (4)$$

Physical linkages between the macromolecular chains of the polymers are formed when the positive charge density on chitosan chains is reduced, enabling the creation of physical hydrogels. As gelling agents, GP and SHC do not operate as crosslinkers but rather alter the quality of -CH chain interactions and entanglements by influencing the amount and rate of amino group deprotonation upon gelation (Ceccaldi et al., 2017).

At a pH of 6.2 or so, the dissolved chitosan might potentially stay stable in the solution. The production of a hydrated gel-like precipitate is consistently induced when chitosan aqueous solutions are neutralized to a pH greater than 6.2 (Chenite et al., 2000). To be clear, CS is not a thermosensitive polymer on its own; however, Chenite et al. (2000) and Supper et al. (2014) showed that by adding glycerophosphate (GP) to a CS solution, the polymer becomes thermoresponsive at physiological pH. It was mentioned that temperature plays an important role in this particular gel formation (Nilsen-Nygaard et al., 2015).

The influencing factors in the gelling process of the Cs-GP system have been explained as follows as a result of Cho et al. (2005) and Filion et al. (2007) studies. Several interactions may be contained in the gelation of chitosan-GP system, including electrostatic repulsion, ionic crosslinking, hydrophobic effect, and hydrogen bonding interactions. GP, a weak base (pKa 6.65 at 25°C), can raise the pH of chitosan solutions to near-neutral levels. Chitosan would be just soluble in acidic solutions, and when heated up to 37°C, it dissolved in glycerophosphate solutions at a pH close to neutral, resulting in a sol-gel transition. Glycerophosphate salt is an excellent proton receptor, and its temperature-insensitive pKa is close to that of chitosan (Cho et al., 2005). By increasing the temperature of a glycerophosphate and chitosan solution, protons were transferred from the chitosan to the GP, neutralizing the solution and reducing the electrostatic repulsion between the chitosan molecules. This allowed the hydrophobic and hydrogen-bonding interchain forces to initiate physical crosslinking, which resulted in gel formation (Filion et al., 2007). As mentioned above, GP may prevent electrostatic repulsion between chitosan molecules due to its negative charge in the solution. Hydrophobic (–CH_3) and hydrogen bonding favorable groups (-OH, -NH, and –C=O) are present in chitosan, allowing three-dimensional networks to form (Cho et al., 2005).

To neutralize the chitosan solution and reduce the GP concentration from 60% to 30%, $NaHCO_3$ can be used as a buffer. Although $NaHCO_3$ did not react with hydrophobic (-CH_3) or hydrogen bonding-favoring groups (-OH, -NH, and -C=O), it did react with the acid in the chitosan solution and partially replaced GP to neutralize the solution. Thus, the hydrogel system gels faster when $NaHCO_3$ is used as a buffer to neutralize the chitosan solution and lower the GP concentration (Huang et al., 2011). It should be noted that employing the weak SHC base as a gelling agent results in CO_2 production when mixed with the acidic chitosan solution, as described below (Assaad et al., 2015).

$$(1)\ Cs - NH_2 + H^+ \leftrightarrow Cs - NH_3^+ \quad (5)$$

$$(2)\ H^+ + HCO_3^- \leftrightarrow H_2CO_3 \rightarrow H_2O + CO_2 \quad (6)$$

$$(3)\ Cs - NH_3^+ + HCO_3^- \leftrightarrow Cs - NH_3^+ / HCO_3^- \rightarrow CH - NH_2 + H_2O + CO_2 \quad (7)$$

At 37°C, Eq. 6 proceeds between the H^+ related to amine group of chitosan and the HCO_3^- of the SHC salt. The reaction speeds up when the concentration of SHC rises, but the pH of the compound falls outside of the physiological range.

The physical properties of the scaffold could be enhanced by the beta-sheet region of SF content (She et al., 2008). Incorporating SF into a hydrogel system may alleviate steric hindrance between CS molecules and promote CS-gelling agent interaction, allowing for a quick gelation rate. Because hydrogen bonds can occur between the amino groups of CS and SF in these hydrogel systems at low temperatures, or water molecules can create hydrogen bonds with SF, the hydrogen bonding interaction was reduced as the temperature was raised. Meanwhile, water molecules have been eliminated from the molecular chains, allowing the hydrophobic CS and SF chains to migrate and entangle with each other (Pankongadisak and Suwantong, 2019).

Biomaterials containing amino groups, such as Cs and SF, have been crosslinked with Genipin. Strong intermolecular interactions and an improvement in the features of the resultant scaffold with regard to cell adhesion were supplied by the introduction of SF to Cs coupled with genipin crosslinking, which is a gentle reaction since they involve molecules containing amino groups (Silva et al., 2008). Crosslinks between primary amine groups were formed as a result of two reactions that transpired at distinct rates. The fastest reaction was a nucleophilic attack on genipin by a primary amine group, which led to the production of a heterocyclic genipin compound linked to the amine group of polymer. The second, slower reaction was the nucleophilic substitution of ester group of

10.3389/fbioe.2022.1075166

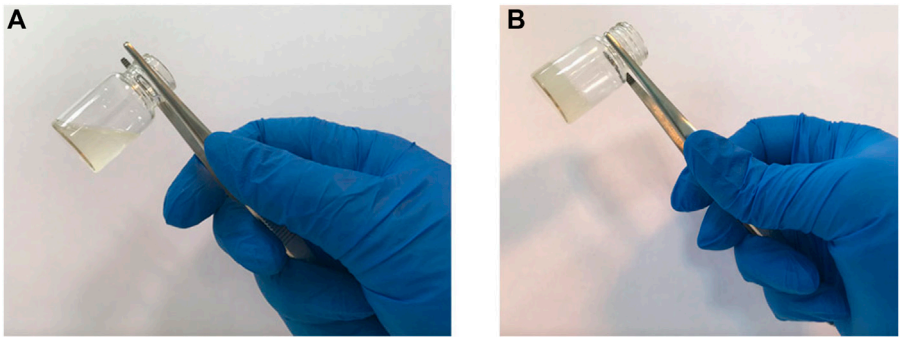

FIGURE 2
Inversion tube test of the samples to determine the gel time. **(A)** hydrogel at room temperature, and **(B)** hydrogel after incubation at 37°C.

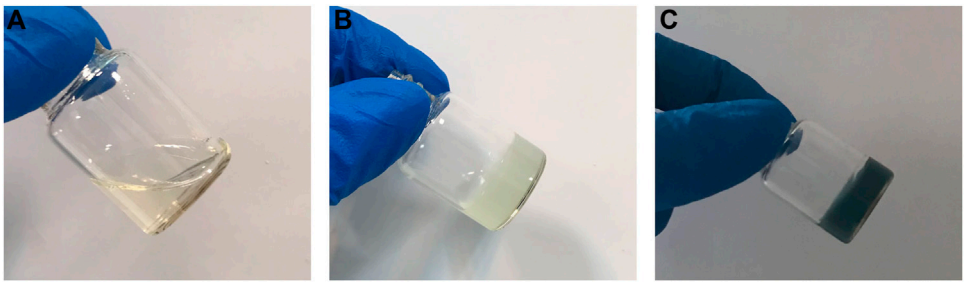

FIGURE 3
Hydrogel containing genipin in **(A)** room temperature **(B)** after incubation in 37 °C for 5 min and **(C)** after 24 h.

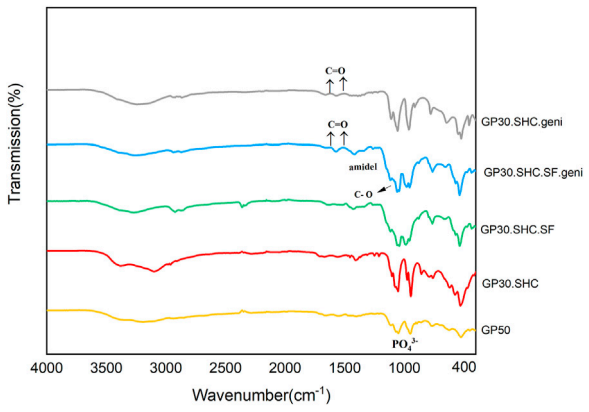

FIGURE 4
Fourier transform infrared (FTIR) spectra of chitosan hydrogels and the corresponding hydrogels.

genipin to generate a secondary amide link with polymer (Butler et al., 2003).

Finally, by varying the proportion of polymers in the hydrogel composition, as well as the amount of polymer to gelling agents and the use of chemical crosslinkers, hydrogel scaffolds with various properties can be created that can be used in a wide range of tissue engineering applications, including hard and soft tissues, as well as drug delivery.

3.1.2 Gel time and pH determination

As a consequence, from all of the designed samples (formulated in Table 1), hydrogel samples with the proper pH and gelation time, along with their components and concentrations, are identified and listed in Table 2.

The first crucial consideration in employing injectable hydrogels as a drug or cell carrier is to ensure that the pH is close to that of the human body and also that the gelation duration is optimal. The appropriate gel time for the hydrogel should neither be so quick that it gels prior to injection and reaching the target tissue nor should it be so lengthy that the solution does not gel and is translocated to the surrounding tissues after the hydrogel solution reaches the specified tissue. According to the MTT test, which will be further explained, the hydrogel itself is harmless and non-toxic, and it is also necessary to keep the pH of hydrogel within the body's physiological pH range, so that cells can remain within it.

A typical tube inversion test from a hydrogel sample can be seen in Figure 2. After being exposed to 37°C for a certain time period, the sample solution, which flows in a fluid form at room temperature, has the capacity to transfer to the gel form. When SHC is added to chitosan, carbon dioxide is produced, elevating the pH of scaffold over the physiological limit and rendering it unusable in medical settings. However, when utilizing the GP30.SHC sample, which contains both

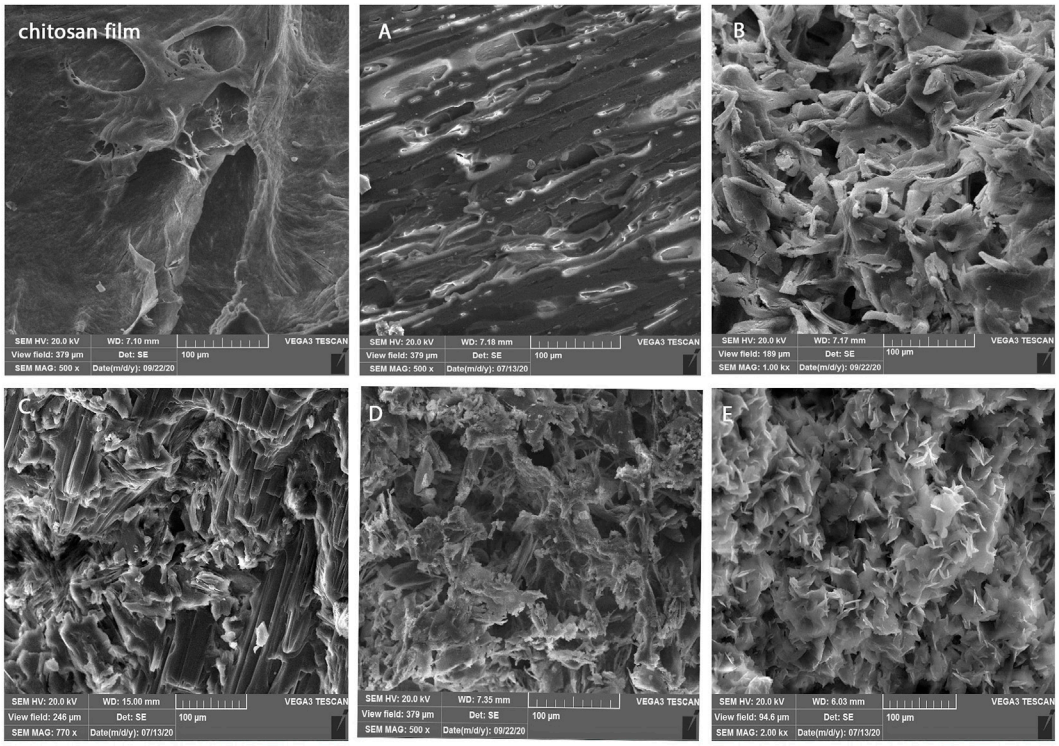

FIGURE 5
Morphology of chitosan films and hydrogels included **(A)** GP50, **(B)** GP30.SHC, **(C)** GP30.SHC.SF, **(D)** GP30.SHC.SF.geni, and **(E)** GP30.SHC.geni.

SHC and GP, gel times are shortened, and pH is maintained within the physiological range.

At 37°C, the effect of genipin on the hydrogel could be observed when the hydrogel turns blue, Figure 3. Actually, by inducing crosslinking in the structure of the hydrogel, genipin increases the mechanical properties of scaffold, and its usage has negligible effects on the gel time. Hydrogels containing these substances, as shown in Table 2, gel at a comparable rate and are temperature sensitive, like the body's physiology, leading to high cell viability in scaffolds.

3.1.3 FTIR

It was necessary to conduct FTIR analysis on hydrogel samples in order to determine whether functional groups related to hydrogel-forming compounds were present. The FTIR spectra of hydrogel samples are displayed in Figure 4. The 1,518 cm^{-1} signal in the GP50 spectra was attributed to protonated amino groups due to the presence of acetic acid in the solvent (Song et al., 2018). The absorption band at 1,630 cm^{-1} was assigned to the C=O stretch of the amide bond (Song et al., 2018). The broad band seen between 2,800 and 3,600 cm^{-1} was attributed to GP salt hydroxyl and alkyl group absorption. The strong absorption bands observed at 975 cm^{-1} were associated with the PO_4^{3-} (Pankongadisak and Suwantong, 2019).

It is possible that the decomposition of SHC in the acidic Cs solution reduces the intensity of the SHC bands at 1700–1,600 cm^{-1} and 1,400–1,300 cm^{-1} (Assaad et al., 2015; Saravanan et al., 2019). Intermolecular interactions between SF and CS during the blending process resulted in absorption bands at 1,627 cm^{-1} (amide I) and 1,521 cm^{-1} (amide II), as well as absorption bands at 1,060 cm^{-1} due to C–O stretching. It is worth noting that the combined ratio of the fibroin silk and chitosan linkages influences their specific adsorption (Li et al., 2018).

As a result of the stretching vibrations of C = O, genipin exhibits characteristic absorption bands at 1,645 and 1,679 cm^{-1} (Song et al., 2018). After crosslinking reaction of genipin in two hydrogel samples GP30.SHC.SF.geni and GP30.SHC.geni, the C = O peaks at 1,615 and 1,531 cm^{-1} show a shift related to the formation of amide bonds. It can be stated that the formation of amide bonds here is the result of a reaction between the amine groups of Cs-SF and the ester group genipin (Song et al., 2018).

3.1.4 SEM

Figure 5 displays the structure of lyophilized hydrogels, which shows a porous structure with varied sizes. Because the freeze-drying process causes artifacts, the porosity of the dried structure does not represent the porosity of the hydrated structure. Previous research has demonstrated that altering the type and concentration of the gelling agent can result in varied morphologies, as well as affect the amount of oxygen and nutrients available to the cells, and hence cell survival (Ceccaldi et al., 2017).

Here again, the observed difference between the gels indicates that the morphology can be defined by altering the type and concentration of gelling agent. The optimal morphology is selected depending on the application of scaffold. The amount of porosity and the size of the pore (larger or smaller) can be regulated by the application of scaffold, and the amount of porosity affects cell invasion, tissue differentiation, and drug release. By comparing the hydrogel to a poreless freeze-dried chitosan film, Figure 5 shows that the concentrations of GP and SHC may be

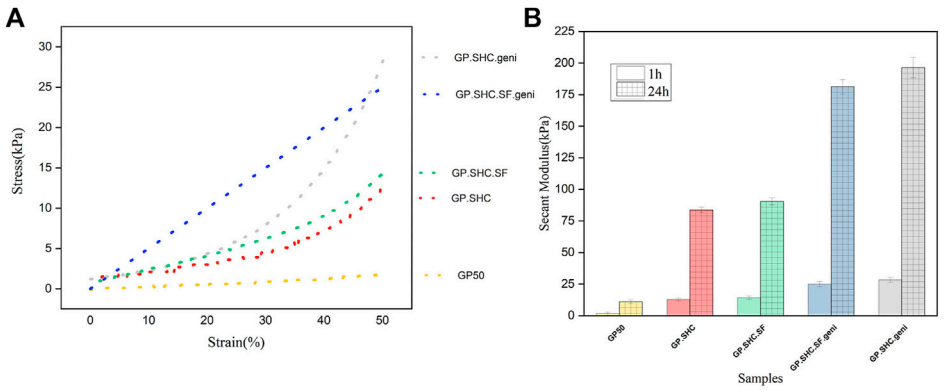

FIGURE 6
Mechanical properties of hydrogels. **(A)** Stress-strain diagram of hydrogels after 1 h of gelation and **(B)** Comparison of Secant modulus that measured at 50% of deformation after 1 and 24 h gelation, (mean + SD; *n* = 3).

adjusted to control the pore shape in scaffolds. In comparison to the GP50 sample, the porosity of the GP30.SHC sample increased. The existence of SF polymer in the hydrogel results in a layered structure with small pores. The GP30.SHC.The SF sample has a porous structure with pore sizes ranging from a few microns to more than 100 microns, as shown in Figure 5B–E. As shown in the study by Moura et al. (2013), gels crosslinked with genipin exhibit an open network structure that appears to be quite porous with the interconnecting macrodomains.

The pore structure is a crucial consideration in tissue engineering scaffolds' design. Cells, as well as water and biological fluids, can migrate within the interconnected porous structure of the hydrogel scaffold. Cell migration is restricted when pores are insufficiently large, leading to the creation of a cellular capsule around the borders of the scaffold. This can then lead to nutrition transport and waste removal, resulting in necrotic areas inside the construct. Overly large pores, on the other hand, reduce surface area, inhibiting cell adhesion (Murphy et al., 2010). The optimum porous structure of GP30.SHC.SF.geni and GP30.SHC.geni samples makes them useful as injectable scaffolds over a wide range of tissue engineering applications and cell types. As added benefits, these scaffolds also have desirable qualities like optimal biodegradability and sufficient mechanical strength.

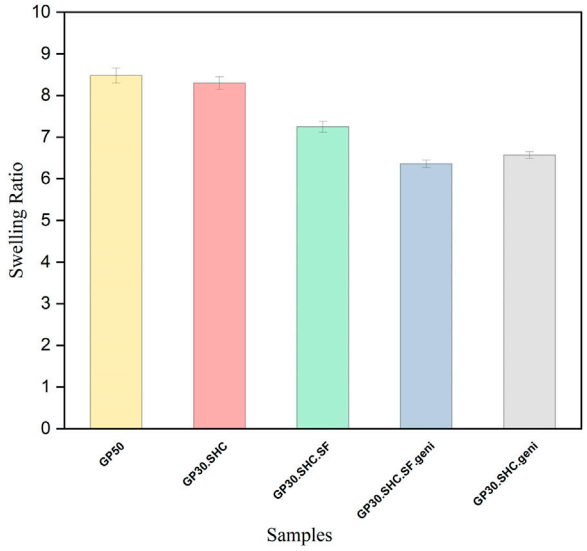

FIGURE 7
Swelling characteristicsof Hydrogel within the first 160 min of immersion in water. Error bars represent the mean ± standard deviation (*n* = 3).

3.1.5 Mechanical properties

Injectable scaffolds, with sufficient mechanical characteristics, maintain integrity in the face of *in vitro* stress. This indicates that hydrogels can be employed as a matrix for cell therapy applications. The elastic constant, E, of the matrix or microenvironment, is used to calculate the resistance that a cell experiences when deforming the ECM. Gelling agents, crosslinkers, and concentrations of hydrogels' components influence their mechanical properties and elasticity, resulting in controlled cell differentiation and tissue formation. Hydrogels also imitate the ECM and produce a microenvironment with mechanical cues closer to natural tissue (Kim et al., 2014).

Cell adhesion and growth in the hydrogel scaffold are affected by cell interaction with the surrounding microenvironment, and biochemical substances have varied impacts on cell behavior under different mechanical conditions of the microenvironment. In cell-cell and cell-matrix adhesions, actin and myosin filaments, as well as mechanical sensors that monitor the force acting on the matrix or cell, play a vital role. Through actin-myosin contractions, focal adhesions provide cells with the essential force transmission routes to "feel" their microenvironment (Engler et al., 2006). The stiffness of the scaffold can be tuned to different values regarding the target tissue and cell. The mechanical stimulation of the microenvironment by the scaffold stimulates the mechanical sensor of cells and initiates intracellular cascades, resulting in differentiated gene expression and cell function, such as proliferation, migration, or changes in how cells are arranged next to each other (Song et al., 2018).

Figure 6A shows stress-strain diagrams for hydrogels after 1 h of gelation. In addition, after 1 h and 24 h of gelation, Figure 6B demonstrates the Young secant moduli of hydrogels in compression (calculated at 50% deformation, showing their

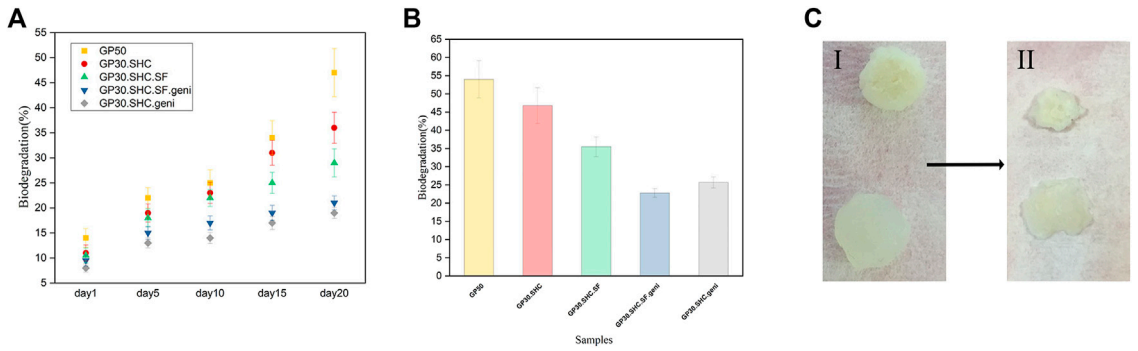

FIGURE 8
In vitro biodegradation of hydrogels. **(A)** biodegradation profiles of the hydrogels incubated within buffer solution at 37°C for 20 days. Error bars represent the mean ± standard deviation (n = 3) **(B)** biodegradation ratio of hydrogels after 28 days **(C)** hydrogels in (I) day 1 and (II) day 20.

mechanical characteristics). The secant modulus after 24 h of gelling is more than the amount after 1 h for all specimens, indicating that the gelling procedure continues even after 1 h, particularly in genipin-containing specimens, and is consistent with Assaad et al. (2015).

In comparison to the GP50, the strain–stress curves for GP30. SHC and GP30. SHC.SF gels were relatively steep with non-linear features; hence the results are displayed in secant modulus. The secant modulus increased as the hydrogel was deformed, indicating typical non-linear behavior (Assaad et al., 2015).

The low Young modulus (5 kPa) of GP50 gel shows its softness and weakness, but the GP30.SHC gel has higher secant moduli (8 kPa at 50% deformation). When these two samples are compared, it can be concluded that the presence of SHC and GP chemicals in the structure raises the sample modulus. The complete neutralization of polymer chains, the smaller size of the SHC molecule, and its degradation into CO_2 may explain the improved mechanical properties of SHC-containing gels compared to GP (Alinejad et al., 2018). The secant modulus increased from 8 kPa for GP50 to 14 kPa for GP30. SHC.SF after the addition of silk fibroin.

The genipin content increased the modulus of GP30.SHC.SF.geni and GP30.SHC.geni despite reduced salt concentrations compared to GP50, Figure 6B. The increased modulus of GP30.SHC.SF.geni and GP30.SHC.geni gels, in comparison with all samples, can be attributed primarily to the effects of genipin. On the other hand, when comparing these two samples, the SF component distinguishes GP30.SHC.SF from GP30.SHC.

Gelling agent salts will interact with the polar groups of SF and chitosan, which include free hydroxyl groups as well as terminated amino and carboxyl groups, to increase the strength of the hydrogels. On the other hand, silk fibroin chains can be converted into two different configurations: helixes and sheets, with the beta-sheet structure being more stiff and beneficial for reinforcing the composite or its compounds (Wu et al., 2016). Genipin crosslinker increase beta-sheet regions with crystalline domains, increasing stiffness and modulus (Silva et al., 2008; Wu et al., 2016). These findings indicate that these hydrogels could be employed as therapeutic cell delivery vehicles with desired mechanical properties.

3.1.6 Swelling measurement

Capacity for water retention in the ECM, which supports many cellular activities and functions, is a significant feature, according to Amorim et al. (2021). Swelling behavior is one of the most significant aspects of hydrogel hydrophilicity for evaluating hydrogels and determining their short-term durability following *in vivo* implantation. Because channels with large pores and significant porosity within the gel can help the hydrogel swell, the swelling index of dry hydrogel can also measure pore size and porosity (Yoshida et al., 1994). Three replications of each specimen were used to determine the swelling property of the hydrogel. The swelling capacity of scaffolds is affected by several parameters, including crosslink degree, pH, temperature, and the hydrophilicity of the polymer structure.

The swelling ratio in PBS for gels is shown in Figure 7. Degrees of swelling are highest in GP50 and GP30.SHC samples represent values of 8.2 and 8.4, respectively. Increased crosslinking of amine groups in chitosan and silk fibroin causes a compact and stable microstructure and fewer accessible amine groups, reducing the swelling ratio by 6.2 and 6.5, respectively, in genipin-containing samples, i.e., GP30.SHC.geni and GP30.SHC.SF.geni. Song et al. (2018) reported similar results when they investigated the properties of chitosan–gelatin scaffolds crosslinked with different genipin concentrations. The swelling capacity of the genipin crosslinked scaffolds was lower than that of the similar non-crosslinked scaffold, which was related to the increased degree of crosslinking.

The interchain polymer interactions as well as the formation of hydrogen bonds, are increased in GP30.SHC.SF.geni and GP30.SHC.SF compared to the GP50 and GP30.SHC without silk fibroin. Because newly formed hydrogen bonds constrain the mobility or relaxation of network chains in hydrogels, the swelling rate is decreased when internal and external polymer chain interactions produce a stronger network. When it comes to GP30.SHC.SF.geni, the synergistic actions of polymers and crosslinkers will further limit gel swelling, resulting in a reduction in the swelling index.

3.1.7 *In vitro* biodegradation study

The role of tissue engineering scaffolds after implantation is related to their resistance to biodegradation in the body; consequently, the hydrogel must be strong enough to operate correctly as a carrier for drug, bioactive molecule, or cell transport over a long period of time. However, the scaffold must degrade after the cells have been seeded onto the scaffold, proliferated, and begun to generate their ECM. Once new tissues have developed, it is crucial that

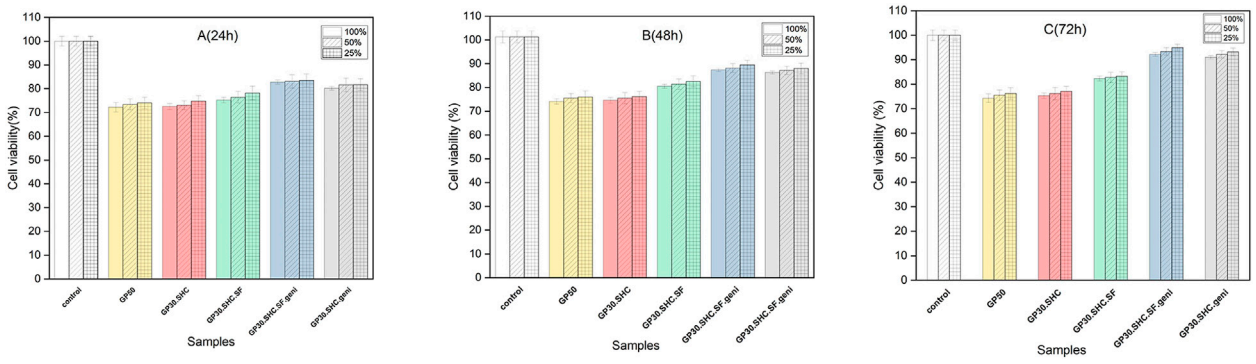

FIGURE 9
The MTT findings after exposing fibroblasts for **(A)** 24, **(B)** 48, and **(C)** 72 h to different dilutions of hydrogels' extraction medium (25, 50, 100%).

the scaffold material completely degrade and be safely absorbed by the body. The rate of hydrogel deterioration was determined by monitoring the weight loss of samples while they were stored in buffer at 37°C for a period of 30 days. In order to mimic the *in vivo* degradation mechanism, the gels were immersed in a pH 7.4 buffer solution containing 1,000 units of lysozyme per milliliter and incubated at 37 C for 3 days (Li et al., 2017). The lysozyme was utilized to investigate the enzymatic degradation of the scaffold. Weight loss was faster for hydrogels without genipin, as expected. Crosslinking the hydrogel network improves the stability of the scaffold. The degradation rate of the genipin crosslinked GP30.SHC.geni and GP30.SHC.SF.geni hydrogels are reduced to 29% and 23%, respectively, as shown in Figure 8B, while the hydrogel without genipin crosslinking has a biodegradability rate of around 54%. A recent study confirmed that hydrogels crosslinked with genipin represented a decreased *in vitro* hydrogel degradation (Song et al., 2018; Zafar et al., 2021).

Chitosan and silk fibroin are natural polymers with a structure that affects their degradation rate. The deacetylation degree (DD) of Cs is related to its degradation. The Cs with a lower DD has more acetyl groups ($NHCOCH_3$) and amorphous areas, which impacts the crystallinity of chitosan, resulting in faster *in vitro* degradation. Consequently, the deacetylation degree of the chitosan employed is 90%, influencing the biodegradability rate (Ahmed et al., 2018; Bakshi et al., 2020).

The binding of N-acetylglucosamine residues to the active site of lysozyme has been suggested as a reason for the degradation of chitosan by lysozyme. Horan's team (Horan et al., 2005) placed SF in PBS to monitor the degradation process and discovered that the SF mass remained constant after 10 days. In the current investigation, CS degradation likely contributed to the rapid initial rate of scaffold material degradation.

For silk-containing hydrogels to be effective as scaffolds that can withstand enzymatic degradation, the protein must undergo a conformational change from random coils to very stable sheets. Crystal-sheet conformation of repetitive amino acid sequences makes up the hydrophobic domain of silk polymeric chains, and the hydrophilic links between these hydrophobic domains consist of bulky and polar side chains that form the amorphous random coil conformation, as previously mentioned (Horan et al., 2005).

The weight of degraded gel samples was measured, and the results are shown in Figure 8A. It can be observed that 1) the GP50 gel lost a great deal of its weight after a 3-week degradation period, with a degradation ratio of roughly 46%, and 2) starting from day 10, the GP30.SHC.SF and GP30.SHC gels lost weight much slower than the GP50. The comparison in Figure 8A suggests that the silk fibroin content in GP30.SHC.SF and GP30.SHC.SF.geni hydrogels is effective in slowing down the degradation process since silk fibroin degrades more slowly than chitosan (Bhattarai et al., 2010). Intermolecular interactions are greater in these samples during gel formation, enhancing the strength of gel and postponing the degradation of the scaffold.

The size of the hydrogel specimens diminishes during the biodegradation process, as shown in Figure 8C, and the scaffold appears to have deteriorated through surface and interior erosion.

Finally, each of these scaffolds can be chosen for a specific application depending on the injection site of the target in the body and the amount of time required for the gel to remain in the body. However, genipin-containing scaffolds, namely GP30.SHC.SF.geni and GP30.SHC.geni, are the optimal solution in these hydrogels, with higher strength and degradation tolerance as well as improved injection performance.

3.2 Biological evaluation

3.2.1 MTT assay

The viability of fibroblast cells was assessed using MTT assays in varied concentrations of extraction media (25, 50, 100%) after 24, 48, and 72 h of incubation to assess the cytotoxicity of hydrogels using the extract dilution method. As predicted from the biodegradation data, day 1 of cell culture in GP50 resulted in decreased cell viability Figure 9. According to prior research, chitosan hydrogel produced at a concentration of 0.2 M GP or less exhibited no cytotoxic effects; non-etheless, its sluggish gelling rate limited its applicability in a variety of contexts. Hydrogels made from chitosan with GP concentrations high enough to induce quick gelation (0.4 M GP or more) caused considerable cell death due to the rapid release of a large quantity of GP upon immersion in the culture medium, leading to hypertonicity of the media extracts (Ahmadi and de Bruijn, 2008).

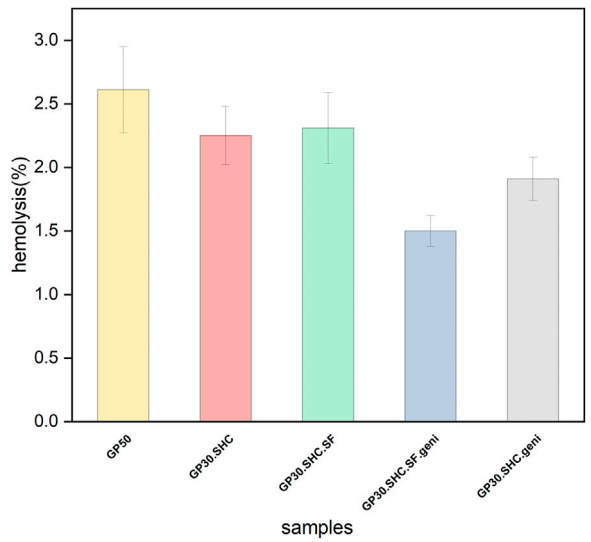

FIGURE 10
Hemolysis rate of scaffold samples.

Indirect cytotoxicity testing revealed that these new hydrogel formulations were more cytocompatible than GP50 hydrogel. No cytotoxic effect was seen in this investigation when extracts from the new formulations were used. This may be due to the fact that this innovative gelling agent system used to create the hydrogel lowers the total salt content of the hydrogel, saving cells from hyperosmolality that would otherwise damage or kill them. Furthermore, because SHC is an integral component of the blood chemical buffer system, it is biocompatible at low concentrations. SHC 0.1 M caused no damage to endothelial cells in previous studies (Hirsch and Haller, 2004), but it had a significant cytotoxic effect at high concentrations (2.4 M) (Assaad et al., 2015).

Chitosan structural units are structurally similar to glycosaminoglycans, making them biocompatible. They interact with growth factors, receptors, and adhesive proteins in cells. Thus, chitosan is believed to have a biocompatible structure for cells.

In 24 h, the viability of GP30.SHC.SF and GP30.SHC.SF.geni containing silk-fibroin polymer was higher (75% and 82%, respectively), and the number of dead cells was reduced. The biocompatibility properties of silk fibroin are determined by the conformation and structure of its amino acids. The formation of the beta-sheet structure increases the biocompatibility of silk fibroin scaffolds, confirming the findings of earlier studies (Yang et al., 2019; El-Fakharany et al., 2020). Silk fibroin has recently been discovered to diminish reactive oxygen species (ROS) created by activated neutrophils and macrophages (Yang et al., 2019; El-Fakharany et al., 2020). These ROS then stimulate the synthesis of a variety of non-specific mediators, including histamine, serotonin, and interleukin, which in turn attract even more inflammatory cells. Routine processes of the body, which include proteolytic enzymes and free radical scavenger chemicals, neutralize ROS and its byproducts (Kundu et al., 2013; Ezhilarasi et al., 2020).

In vitro biocompatibility of scaffolds containing genipin was excellent. In 24 h, the cell viability of the GP30.SHC.SF.geni and GP30.SHC.geni samples were about 82% and 80%, respectively, and increased to 91% and 89% in 72 h. All formulations significantly increased fibroblast vitality after 72 h, which may be attributable to the cells' adaptability *via* the release of growth factors, as mentioned in a previous study by Ahmadi and de Bruijn (2008).

The presence of genipin produces crosslinking in the hydrogel structure, which inhibits hydrogel biodegradation and leads to lower extract concentrations, which may reduce cytotoxicity. The cell viability was 72%–91% with genipin crosslinking, as shown in Figure 9 (Ye et al., 2019), demonstrating that the hydrogels had low cytotoxicity.

Two samples of injectable chitosan hydrogel with this novel formulation, GP30.SHC.SF.geni and GP30.SHC.geni, which incorporates polymers with a gelling agents-crosslinking system, were found to be promising carriers that did not compromise cell viability *in vitro* cytotoxicity tests and other assays. Thus, these two formulations were selected for 3D cell culture and urea testing.

3.2.2 Hemolysis

It is permissible to use *in vitro* hemolysis as a credible indicator method for determining the hemocompatibility of the scaffold. It is used as an indication of damage to the membrane of red blood cells. The hemolysis value is considered safe when it is below 5%, in accordance with the standard ISO document 10993-5 1992 (Seibert et al., 2003). According to the experimental approach, the scaffolds examined in this test were safe, and the hemolytic activity for all specimens was less than 5%, as shown in Figure 10. The lack of hemolytic properties of the chitosan-glycerophosphate scaffold was also confirmed in previous investigations by Zhou et al. (2011).

In the sol-gel phase transition, we have a wide range of molecular interactions between the aqueous solution of cationic chitosan and the anionic salt bases of the gelling agents, as discussed in the preceding sections. These interactions appear to decrease cationic density of chitosan, affecting hemolytic properties of the hydrogel structure. In reality, the hemolytic response is influenced by the interactions of the chitosan-related positive amine group with plasma proteins and blood cells. It appears that a hemocompatible polymer, as described by Ostuni et al. (2001), should be a hydrophilic material that is electrically neutral and has hydrogen-bond acceptors. When a polymer or scaffold comes into direct interaction with blood, it triggers a cascade of host responses. Protein adsorption to the surface, neutrophil and macrophage activation, coagulation cascade activation, platelet adhesion, complement system activation, antibody production, and cellular immune response are all related to these responses. These responses must be minimized or avoided by a hemocompatible system (Balan and Verestiuc, 2014).

Some polymers have the potential to break red blood cell membranes and release hemoglobin and other internal constituents after being exposed to them. The release of these components speeds up platelet accumulation and clot formation in that area. After the material is exposed to the blood, the protein adsorption on the interface of the material is the first event that occurs. Another group of proteins substitutes the absorbed proteins in the second step, irreversible changes in their conformation arise, and active platelet receptors detect the layer in which the protein is absorbed. Platelet adhesion and the clotting process are examples of subsequent reactions. Surface charge density of the material critically impacts the system (Balan and Verestiuc, 2014; Ashcraft et al., 2021).

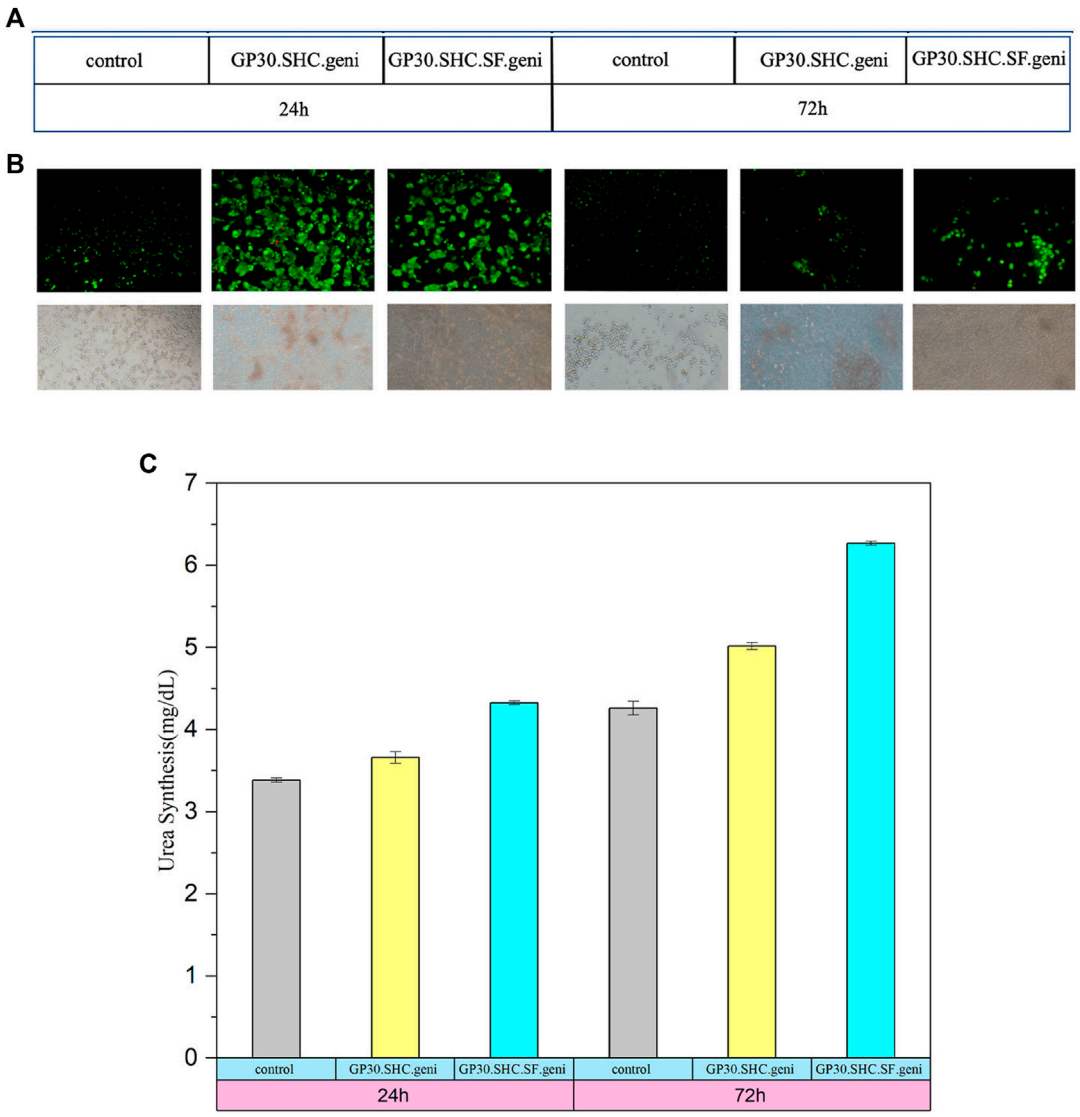

FIGURE 11
Evaluation of the HepG2 cells cultured in the hydrogels. **(A)** HepG2 cells encapsulated at day 1 and day 3. The cells were stained with FDA/PI (green) and (red) dyes, respectively. **(B)** encapsulated HepG2 cells on day 1 and day 3 visualized by optical microscopy. Scale bars: 200 μm **(C)** urea synthesis in the encapsulated HepG2 cell line. Secretion in 2D culture as control. Data represent value ± SD from three samples.

Chemical composition of the associated material, structure, and topography can also influence protein adsorption (Nonckreman et al., 2010). Chitosan and silk fibers are positively charged polymers of the hydrogel system; however, these hydrogels are created using glycerophosphate and sodium hydrogen carbonate gelling agents, as well as positive linkages between polymer constituents. It efficiently reduces the contact between blood cells and the material, hence the reaction of activated blood cells to the scaffold.

The presence of genipin, on the other hand, causes crosslinking in the structure, which reduces the size of the pores and reduces initial protein absorption. As a result, in hydrogels containing genipin, the hemolysis ratio decreases, and thus, the rate of hemocompatibility increases. The hemolysis test findings suggest that this chitosan-based injectable hydrogel system is safe and also has a modest hemolytic effect.

3.2.3 Cell viability assessment in hydrogels

The HepG2 cell line was encapsulated in two of the best hydrogel formulations previously selected (GP30.SHC.SF.geni and GP30.SHC.geni). The metabolic activity of the cells (urea synthesis) was also monitored for 24 and 72 h, as represented in Figure 11C, and live/dead labeling was done after 24 h of culture Figure 11A. The staining of living cells with fluorescein diacetate (FDA) causes them to fluoresce green following the response of intracellular esterase, whereas the staining of dead cells with propidium iodide (PI) results in a red coloration (Boyd et al., 2008).

Encapsulated cells are intended to be viable and functioning for implantation throughout the body. The quantification of live/dead cells by image analyses showed good cell survival and no difference between the two formulations evaluated, as shown in Figure 11A, B. After 24 h in culture, the majority of cells were alive (cells in green), and just a small percentage had died (cells in red). The

survival of encapsulated cells is influenced by the physiological pH of hydrogel and the existence of interconnecting pores inside the hydrogel, providing access to nutrients and oxygen (Ceccaldi et al., 2017; Hori et al., 2021). We also hypothesized that biodegradability of hydrogel would offer a nutrient-rich, favorable environment for the encapsulated cells, leading to increased cell viability. These three-dimensional hydrogel scaffolds, we hypothesized, would support significant cell-cell communication, leading to improved hepatocyte viability and functionality.

According to Capone et al. (2013), Hori et al. (2021), seeded cells have a spindle-like shape; however, encapsulated cells have a round morphology inside the hydrogel. The spherical shape of the encapsulated cells in the 3D gel suggests that the polymer chains did not adhere to the cells, which means that the cells were able to survive during the culture time. Finally, HepG2 cells encapsulated during the crosslinking procedure to create cell-hydrogel structures prove to be advantageous for cell survival and efficiency, which can be employed for cell therapy and tissue engineering applications. The same results for other formulations have been obtained by Lan et al.(2010), Hori et al, (2021)

3.2.4 Urea synthesis

One of the most crucial factors of hepatocyte health and function is urea secretion. The examination of a liver metabolic function will be the following step. On days 1 and 3, urea synthesis was investigated in supernatants to assess the hepatic functionality of beads. As a control, urea synthesis was measured in cells grown in collagen-coated 24-well plates.

Due to its importance in ammonia detoxication and pH control, ammonia metabolism is often used as a functional marker of hepatic phenotype (Godoy et al., 2013). The urea cycle, which converts extremely toxic ammonia to urea for excretion, is primarily carried out in the liver. As a result, urea production levels in blood or culture supernatant indicate liver functionality. Low urea levels, in particular, suggest liver dysfunction (Kang et al., 2021).

As shown in Figure 11, improved liver-specific functions are directly linked to increased cell viability in the encapsulation culture. Figure 11C demonstrates that the urea level under the encapsulation condition is much greater at each time point than HepG2 cultured alone, which could be due to cell-matrix interactions, which can increase liver-specific functions (Cui et al., 2019).

Between GP30.SHC.SF.geni and GP30.SHC.geni, no significant differences were detected. The difference between day 1 and day 3 was, however, more apparent than in the experimental groups. The synthesis of urea in GP30.SHC.SF.geni and GP30.SHC.geni was considerably higher on day 3 (6.269 ± 0.023 and 5.017 ± 0.042 mg dl^{-1}, respectively) than on day 1 (4.326 ± 0.021 and 3.659 ± 0.071 mg dl^{-1}).

Hepatocytes cultured in different 3D scaffolds of other studies showed similar enhancements in liver-specific activities (Wu et al., 2014; Wang et al., 2019). The improved microencapsulated cell viability outcomes are consistent with the liver-specific function data, suggesting the benefits of the 3D culture system (Khodabakhshaghdam et al., 2021). This indicates that the 3D culture system with a specific hydrogel combination had no cytotoxic effect on cell metabolic activity. Overall, our findings indicate that the 3D hydrogel provides an alternate method of cell growth, resulting in the formation of a functional microtissue *in vitro*.

4 Conclusion

Hydrogel scaffolds that rapidly solidify at body temperature have raised great interest in cell therapy and tissue engineering purposes. Previous studies demonstrate that chemical crosslinkers, compared to physical ones, result in strong mechanical properties of biological scaffolding systems. At the same time, due to the necessity for high-concentration usage, they induce increased cytotoxicity. In order to mimic *in vivo* situations, we designed and evaluated new *in-situ* gelling chitosan/silk fibroin hydrogels using the novel gelling agent system consisting of GP and SHC, crosslinked with genipin. These hydrogels, formulated using natural ingredients, are highly biocompatible (72%–85%) and sufficiently biodegradable (about 23% after 28 days), all allow the production of *in-situ* crosslinking systems with pH adjustments (range of natural pH). Furthermore, the thermoresponsive features of these hydrogels enable homogeneous mixing with cells and rapid gelling at 37°C (230 s), preventing cells from spreading out of the targeted area and maintaining matrix cohesiveness due to strong ultimate mechanical strength (185 kPa after 24 h of gelation). The stronger intermolecular interactions brought about by the novel gell agent-crosslinker system are responsible for the enhanced mechanical properties and prolonged degradation of the scaffold. Improved hemocompatibility and lower hemolysis ratios are the outcomes of genipin presence in crosslinked structures *via* decreasing pore size and delaying early protein absorption. By evaluating urea production, the positive effect of cell-matrix interactions and mimicking the extracellular matrix on the improvement of viability and, thus, liver-specific activities of encapsulated cells have been clearly observed. Genipin crosslinked hydrogels showed tremendous promise for use in 3D cell cultivation, with urea production increasing from 4 mg dl^{-1} on day 1 to roughly 6 mg dl^{-1} on day 3. The setting pH of hydrogel, close to the physiological one, and their interconnected pores, providing access to nutrients and oxygen, could describe the survival of encapsulated cells. High-throughput, minimally invasive surgery may have a promising future thanks to these kinds of injectable, thermoresponsive hydrogels.

Data availability statement

The original contributions presented in the study are included in the article/Supplementary Material, further inquiries can be directed to the corresponding author.

Author contributions

All authors contributed to the conception and design of the study. MG wrote the first draft of the manuscript. MT and MG wrote and revised sections of the manuscript. All authors read and approved the submitted version of the manuscript.

Conflict of interest

The authors declare that the research was conducted in the absence of any commercial or financial relationships that could be construed as a potential conflict of interest.

Publisher's note

References

Afewerki, S., Sheikhi, A., Kannan, S., Ahadian, S., and Khademhosseini, A. (2019). Gelatin-polysaccharide composite scaffolds for 3D cell culture and tissue engineering: towards natural therapeutics. *Bioeng. Transl. Med.* 4 (1), 96–115. doi:10.1002/btm2.10124

Ahmadi, R., and de Bruijn, J. D. (2008). Biocompatibility and gelation of chitosan–glycerol phosphate hydrogels. *J. Biomed. Mater. Res. Part A* 86 (3), 824–832. doi:10.1002/jbm.a.31676

Ahmed, S., Ali, A., and Sheikh, J. (2018). A review on chitosan centred scaffolds and their applications in tissue engineering. *Int. J. Biol. Macromol.* 116, 849–862. doi:10.1016/j.ijbiomac.2018.04.176

Alinejad, Y., Adoungotchodo, A., Hui, E., Zehtabi, F., and Lerouge, S. (2018). An injectable chitosan/chondroitin sulfate hydrogel with tunable mechanical properties for cell therapy/tissue engineering. *Int. J. Biol. Macromol.* 113, 132–141. doi:10.1016/j.ijbiomac.2018.02.069

Amorim, S., Reis, C. A., Reis, R. L., and Pires, R. A. (2021). Extracellular matrix mimics using hyaluronan-based biomaterials. *Trends Biotechnol.* 39 (1), 90–104. doi:10.1016/j.tibtech.2020.06.003

Ardeshirylajimi, A., Delgoshaie, M., Mirzaei, S., and Khojasteh, A. (2018). Different porosities of chitosan can influence the osteogenic differentiation potential of stem cells. *J. Cell. Biochem.* 119 (1), 625–633. doi:10.1002/jcb.26223

Ashammakhi, N., Ahadian, S., Darabi, M. A., El Tahchi, M., Lee, J., Suthiwanich, K., et al. (2019). Minimally invasive and regenerative therapeutics. *Adv. Mater.* 31 (1), 1804041. doi:10.1002/adma.201804041

Ashcraft, M., Douglass, M., Chen, Y., and Handa, H. (2021). Combination strategies for antithrombotic biomaterials: An emerging trend towards hemocompatibility. *Biomater. Sci.* 9 (7), 2413–2423. doi:10.1039/d0bm02154g

Assaad, E., Maire, M., and Lerouge, S. (2015). Injectable thermosensitive chitosan hydrogels with controlled gelation kinetics and enhanced mechanical resistance. *Carbohydr. Polym.* 130, 87–96. doi:10.1016/j.carbpol.2015.04.063

Bakshi, P. S., Selvakumar, D., Kadirvelu, K., and Kumar, N. (2020). Chitosan as an environment friendly biomaterial–a review on recent modifications and applications. *Int. J. Biol. Macromol.* 150, 1072–1083. doi:10.1016/j.ijbiomac.2019.10.113

Balan, V., and Verestiuc, L. (2014). Strategies to improve chitosan hemocompatibility: A review. *Eur. Polym. J.* 53, 171–188. doi:10.1016/j.eurpolymj.2014.01.033

Bhattarai, N., Gunn, J., and Zhang, M. (2010). Chitosan-based hydrogels for controlled, localized drug delivery. *Adv. drug Deliv. Rev.* 62 (1), 83–99. doi:10.1016/j.addr.2009.07.019

Boyd, V., Cholewa, O. M., and Papas, K. K. (2008). Limitations in the use of fluorescein diacetate/propidium iodide (FDA/PI) and cell permeable nucleic acid stains for viability measurements of isolated islets of Langerhans. *Curr. trends Biotechnol. Pharm.* 2 (2), 66–84.

Brouwer, J., van Leeuwen-Herberts, T., and Otting-van de Ruit, M. (1984). Determination of lysozyme in serum, urine, cerebrospinal fluid and feces by enzyme immunoassay. *Clin. Chim. Acta* 142 (1), 21–30. doi:10.1016/0009-8981(84)90097-4

Butler, M. F., Ng, Y. F., and Pudney, P. D. (2003). Mechanism and kinetics of the crosslinking reaction between biopolymers containing primary amine groups and genipin. *J. Polym. Sci. Part A Polym. Chem.* 41 (24), 3941–3953. doi:10.1002/pola.10960

Capone, S. H., Dufresne, M., Rechel, M., Fleury, M-J., Salsac, A-V., Paullier, P., et al. (2013). Impact of alginate composition: from bead mechanical properties to encapsulated HepG2/C3A cell activities for *in vivo* implantation. *PLoS One* 8 (4), e62032. doi:10.1371/journal.pone.0062032

Cárdena-Pérez, Y. C., Vera-Graziano, R., Muñoz-Prieto, EdJ., and Gómez-Pachón, E. Y. (2017). Preparation and characterization of scaffold nanofibers by electrospinning, based on chitosan and fibroin from Silkworm (*Bombyx mori*). *Ing. Compet.* 19 (1), 139–151.

Ceccaldi, C., Assaad, E., Hui, E., Buccionyte, M., Adoungotchodo, A., and Lerouge, S. (2017). Optimization of injectable thermosensitive scaffolds with enhanced mechanical properties for cell therapy. *Macromol. Biosci.* 17 (6), 1600435. doi:10.1002/mabi.201600435

Celikkin, N., Rinoldi, C., Costantini, M., Trombetta, M., Rainer, A., and Święszkowski, W. (2017). Naturally derived proteins and glycosaminoglycan scaffolds for tissue engineering applications. *Mater. Sci. Eng. C* 78, 1277–1299. doi:10.1016/j.msec.2017.04.016

Chenite, A., Chaput, C., Wang, D., Combes, C., Buschmann, M., Hoemann, C., et al. (2000). Novel injectable neutral solutions of chitosan form biodegradable gels *in situ*. *Biomaterials* 21 (21), 2155–2161. doi:10.1016/s0142-9612(00)00116-2

Cho, J., Heuzey, M-C., Bégin, A., and Carreau, P. J. (2005). Physical gelation of chitosan in the presence of β-glycerophosphate: the effect of temperature. *Biomacromolecules* 6 (6), 3267–3275. doi:10.1021/bm050313s

Cui, J., Wang, H., Shi, Q., Sun, T., Huang, Q., and Fukuda, T. (2019). Multicellular co-culture in three-dimensional gelatin methacryloyl hydrogels for liver tissue engineering. *Molecules* 24 (9), 1762. doi:10.3390/molecules24091762

De Pieri, A., Rochev, Y., and Zeugolis, D. I. (2021). Scaffold-free cell-based tissue engineering therapies: advances, shortfalls and forecast. *NPJ Regen. Med.* 6 (1), 18–15. doi:10.1038/s41536-021-00133-3

De Souza, R., Zahedi, P., Allen, C. J., and Piquette-Miller, M. (2009). Biocompatibility of injectable chitosan–phospholipid implant systems. *Biomaterials* 30 (23-24), 3818–3824. doi:10.1016/j.biomaterials.2009.04.003

El-Fakharany, E. M., Abu-Elreesh, G. M., Kamoun, E. A., Zaki, S., and Abd-El-Haleem, D. A. (2020). *In vitro* assessment of the bioactivities of sericin protein extracted from a bacterial silk-like biopolymer. *RSC Adv.* 10 (9), 5098–5107. doi:10.1039/c9ra09419a

Engler, A. J., Sen, S., Sweeney, H. L., and Discher, D. E. (2006). Matrix elasticity directs stem cell lineage specification. *Cell* 126 (4), 677–689. doi:10.1016/j.cell.2006.06.044

Ezhilarasi, S. S. V., Kothandaraman, R., Nesamani, R., Balasubramanian, S., and Mahalaxmi, S. (2020). *In vitro* assessment of cytotoxicity and anti-inflammatory properties of shilajit nutraceutical: A preliminary study. *J. Interdiscip. Dent.* 10 (1), 24. doi:10.4103/jid.jid_2_20

Filion, D., Lavertu, M., and Buschmann, M. D. (2007). Ionization and solubility of chitosan solutions related to thermosensitive chitosan/glycerol-phosphate systems. *Biomacromolecules* 8 (10), 3224–3234. doi:10.1021/bm700520m

Floren, M., Migliaresi, C., and Motta, A. (2016). Processing techniques and applications of silk hydrogels in bioengineering. *J. Funct. Biomater.* 7 (3), 26. doi:10.3390/jfb7030026

Godoy, P., Hewitt, N. J., Albrecht, U., Andersen, M. E., Ansari, N., Bhattacharya, S., et al. (2013). Recent advances in 2D and 3D *in vitro* systems using primary hepatocytes, alternative hepatocyte sources and non-parenchymal liver cells and their use in investigating mechanisms of hepatotoxicity, cell signaling and ADME. *Archives Toxicol.* 87 (8), 1315–1530. doi:10.1007/s00204-013-1078-5

Hashemi, S. S., Pourfath, M. R., Derakhshanfar, A., Behzad-Behbahani, A., and Moayedi, J. (2020). The role of labeled cell therapy with and without scaffold in early excision burn wounds in a rat animal model. *Iran. J. Basic Med. Sci.* 23 (5), 673–679. doi:10.22038/ijbms.2020.34324.8156

Hirsch, C., and Haller, C. (2004). Effect of extracellular hypertonicity and alkalosis on endothelial-derived EA. hy 926 cells *in vitro*. *Eur. J. Med. Res.* 9 (2), 71–77.

Horan, R. L., Antle, K., Collette, A. L., Wang, Y., Huang, J., Moreau, J. E., et al. (2005). *In vitro* degradation of silk fibroin. *Biomaterials* 26 (17), 3385–3393. doi:10.1016/j.biomaterials.2004.09.020

Hori, A., Utoh, R., Yamada, M., and Seki, M. (2021). "Preparation of microporous hydrogel sponges for 3D perfusion culture of mammalian cells," in MATEC Web of Conferences, Sapporo, Hokkaido, Japan, September 27, 2019. (EDP Sciences). doi:10.1051/matecconf/202133307004

Huang, Z., Yu, B., Feng, Q., and Li, S. (2011). Modification of an injectable chitosan scaffold by blending with NaHCO3 to improve cytocompatibility. *Polym. Polym. Compos.* 19 (9), 781–788. doi:10.1177/096739111101900908

Iansante, V., Dhawan, A., Masmoudi, F., Lee, C. A., Fernandez-Dacosta, R., Walker, S., et al. (2018). A new high throughput screening platform for cell encapsulation in alginate hydrogel shows improved hepatocyte functions by mesenchymal stromal cells co-encapsulation. *Front. Med.* 5, 216. doi:10.3389/fmed.2018.00216

Ijima, H., Nakamura, S., Bual, R. P., and Yoshida, K. (2019). Liver-specific extracellular matrix hydrogel promotes liver-specific functions of hepatocytes *in vitro* and survival of transplanted hepatocytes *in vivo*. *J. Biosci. Bioeng.* 128 (3), 365–372. doi:10.1016/j.jbiosc.2019.02.014

Islam, M. M., Shahruzzaman, M., Biswas, S., Sakib, M. N., and Rashid, T. U. (2020). Chitosan based bioactive materials in tissue engineering applications-A review. *Bioact. Mater.* 5 (1), 164–183. doi:10.1016/j.bioactmat.2020.01.012

Janani, G., Nandi, S. K., and Mandal, B. B. (2018). Functional hepatocyte clusters on bioactive blend silk matrices towards generating bioartificial liver constructs. *Acta biomater.* 67, 167–182. doi:10.1016/j.actbio.2017.11.053

Jiang, T., Singh, B., Choi, Y-J., Akaike, T., and Cho, C-S. (2015). "Liver tissue engineering using functional marine biomaterials," in *Functional marine biomaterials* (Elsevier), 91–106.

Kane, M. A., Kasper, C. E., and Kalinich, J. F. (2009). Protocol for the assessment of potential health effects FromEmbedded metal fragments. *Mil. Med.* 174 (3), 265–269. doi:10.7205/milmed-d-02-2808

Kang, H. K., Sarsenova, M., Kim, D-H., Kim, M. S., Lee, J. Y., Sung, E-A., et al. (2021). Establishing a 3D *in vitro* hepatic model mimicking physiologically relevant to *in vivo* state. *Cells* 10 (5), 1268. doi:10.3390/cells10051268

Khodabakhshaghdam, S., Khoshfetrat, A. B., and Rahbarghazi, R. (2021). Alginate-chitosan core-shell microcapsule cultures of hepatic cells in a small scale stirred bioreactor: Impact of shear forces and microcapsule core composition. *J. Biol. Eng.* 15 (1), 14–12. doi:10.1186/s13036-021-00265-6

Kim, J. K., Kim, H. J., Chung, J-Y., Lee, J-H., Young, S-B., and Kim, Y-H. (2014). Natural and synthetic biomaterials for controlled drug delivery. *Archives pharmacal Res.* 37 (1), 60–68. doi:10.1007/s12272-013-0280-6

Kundu, B., Rajkhowa, R., Kundu, S. C., and Wang, X. (2013). Silk fibroin biomaterials for tissue regenerations. *Adv. drug Deliv. Rev.* 65 (4), 457–470. doi:10.1016/j.addr.2012.09.043

Kwon, Y-S., Lim, E-S., Kim, H-M., Hwang, Y-C., Lee, K-W., and Min, K-S. (2015). Genipin, a cross-linking agent, promotes odontogenic differentiation of human dental pulp cells. *J. Endod.* 41 (4), 501–507. doi:10.1016/j.joen.2014.12.002

Lan, S-F., Safiejko-Mroczka, B., and Starly, B. (2010). Long-term cultivation of HepG2 liver cells encapsulated in alginate hydrogels: a study of cell viability, morphology and drug metabolism. *Toxicol. Vitro* 24 (4), 1314–1323. doi:10.1016/j.tiv.2010.02.015

Lee, H. J., Ahn, J., Jung, C. R., Jeung, Y. J., Cho, H. S., Son, M. J., et al. (2020). Optimization of 3D hydrogel microenvironment for enhanced hepatic functionality of primary human hepatocytes. *Biotechnol. Bioeng.* 117 (6), 1864–1876. doi:10.1002/bit.27328

Li, D-W., Lei, X., He, F-L., He, J., Liu, Y-L., Ye, Y-J., et al. (2017). Silk fibroin/chitosan scaffold with tunable properties and low inflammatory response assists the differentiation of bone marrow mesenchymal stem cells. *Int. J. Biol. Macromol.* 105, 584–597. doi:10.1016/j.ijbiomac.2017.07.080

Li, D-W., He, J., He, F-L., Liu, Y-L., Liu, Y-Y., Ye, Y-J., et al. (2018). Silk fibroin/chitosan thin film promotes osteogenic and adipogenic differentiation of rat bone marrow-derived mesenchymal stem cells. *J. Biomater. Appl.* 32 (9), 1164–1173. doi:10.1177/0885328218757767

Liao, Y., He, Q., Zhou, F., Zhang, J., Liang, R., Yao, X., et al. (2020). Current intelligent injectable hydrogels for *in situ* articular cartilage regeneration. *Polym. Rev.* 60 (2), 203–225. doi:10.1080/15583724.2019.1683028

Marquardt, L. M., and Heilshorn, S. C. (2016). Design of injectable materials to improve stem cell transplantation. *Curr. stem Cell Rep.* 2 (3), 207–220. doi:10.1007/s40778-016-0058-0

Mirzaei, E., Faridi-Majidi, R., Shokrgozar, M. A., and Asghari Paskiabi, F. (2014). Genipin cross-linked electrospun chitosan-based nanofibrous mat as tissue engineering scaffold. *Nanomed. J.* 1 (3), 137–146.

Moura, M., Gil, M., and Figueiredo, M. (2013). Delivery of cisplatin from thermosensitive co-cross-linked chitosan hydrogels. *Eur. Polym. J.* 49 (9), 2504–2510. doi:10.1016/j.eurpolymj.2013.02.032

Murphy, C. M., Haugh, M. G., and O'brien, F. J. (2010). The effect of mean pore size on cell attachment, proliferation and migration in collagen–glycosaminoglycan scaffolds for bone tissue engineering. *Biomaterials* 31 (3), 461–466. doi:10.1016/j.biomaterials.2009.09.063

Neri-Numa, I. A., Pessoa, M. G., Paulino, B. N., and Pastore, G. M. (2017). Genipin: A natural blue pigment for food and health purposes. *Trends food Sci. Technol.* 67, 271–279. doi:10.1016/j.tifs.2017.06.018

Nilsen-Nygaard, J., Strand, S. P., Vårum, K. M., Draget, K. I., and Nordgård, C. T. (2015). Chitosan: Gels and interfacial properties. *Polymers* 7 (3), 552–579. doi:10.3390/polym7030552

Nonckreman, C. J., Fleith, S., Rouxhet, P. G., and Dupont-Gillain, C. C. (2010). Competitive adsorption of fibrinogen and albumin and blood platelet adhesion on surfaces modified with nanoparticles and/or PEO. *Colloids Surfaces B Biointerfaces.* 77 (2), 139–149. doi:10.1016/j.colsurfb.2010.01.014

Ostuni, E., Chapman, R. G., Holmlin, R. E., Takayama, S., and Whitesides, G. M. (2001). A survey of structure– property relationships of surfaces that resist the adsorption of protein. *Langmuir* 17 (18), 5605–5620. doi:10.1021/la010384m

Panjapheree, K., Kamonmattayakul, S., and Meesane, J. (2018). Biphasic scaffolds of silk fibroin film affixed to silk fibroin/chitosan sponge based on surgical design for cartilage defect in osteoarthritis. *Mater. Des.* 141, 323–332. doi:10.1016/j.matdes.2018.01.006

Pankongadisak, P., and Suwantong, O. (2019). Enhanced properties of injectable chitosan-based thermogelling hydrogels by silk fibroin and longan seed extract for bone tissue engineering. *Int. J. Biol. Macromol.* 138, 412–424. doi:10.1016/j.ijbiomac.2019.07.100

Pettinelli, N., Rodriguez-Llamazares, S., Bouza, R., Barral, L., Feijoo-Bandin, S., and Lago, F. (2020). Carrageenan-based physically crosslinked injectable hydrogel for wound healing and tissue repairing applications. *Int. J. Pharm.* 589, 119828. doi:10.1016/j.ijpharm.2020.119828

Rijal, N., Adhikari, U., and Bhattarai, N. (2017). "Production of electrospun chitosan for biomedical applications," in *Chitosan based biomaterials* (Elsevier), Vol. 1, 211–237.

Rinaudo, M., Pavlov, G., and Desbrieres, J. (1999). Influence of acetic acid concentration on the solubilization of chitosan. *Polymer* 40 (25), 7029–7032. doi:10.1016/s0032-3861(99)00056-7

Saheli, M., Sepantafar, M., Pournasr, B., Farzaneh, Z., Vosough, M., Piryaei, A., et al. (2018). Three-dimensional liver-derived extracellular matrix hydrogel promotes liver organoids function. *J. Cell. Biochem.* 119 (6), 4320–4333. doi:10.1002/jcb.26622

Saravanan, S., Vimalraj, S., Thanikaivelan, P., Banudevi, S., and Manivasagam, G. (2019). A review on injectable chitosan/beta glycerophosphate hydrogels for bone tissue regeneration. *Int. J. Biol. Macromol.* 121, 38–54. doi:10.1016/j.ijbiomac.2018.10.014

Seibert, C. S., Shinohara, E. M. G., and Sano-Martins, I. S. (2003). *In vitro* hemolytic activity of Lonomia obliqua caterpillar bristle extract on human and Wistar rat erythrocytes. *Toxicon* 41 (7), 831–839. doi:10.1016/s0041-0101(03)00040-0

She, Z., Jin, C., Huang, Z., Zhang, B., Feng, Q., and Xu, Y. (2008). Silk fibroin/chitosan scaffold: Preparation, characterization, and culture with HepG2 cell. *J. Mater. Sci. Mater. Med.* 19 (12), 3545–3553. doi:10.1007/s10856-008-3526-y

Silva, S. S., Motta, A., Rodrigues, M. T., Pinheiro, A. F., Gomes, M. E., Mano, J. F., et al. (2008). Novel genipin-cross-linked chitosan/silk fibroin sponges for cartilage engineering strategies. *Biomacromolecules* 9 (10), 2764–2774. doi:10.1021/bm800874q

Song, Y., Nagai, N., Saijo, S., Kaji, H., Nishizawa, M., and Abe, T. (2018). *In situ* formation of injectable chitosan-gelatin hydrogels through double crosslinking for sustained intraocular drug delivery. *Mater. Sci. Eng. C* 88, 1–12. doi:10.1016/j.msec.2018.02.022

Sun, W., Incitti, T., Migliaresi, C., Quattrone, A., Casarosa, S., and Motta, A. (2016). Genipin-crosslinked gelatin–silk fibroin hydrogels for modulating the behaviour of pluripotent cells. *J. Tissue Eng. Regen. Med.* 10 (10), 876–887. doi:10.1002/term.1868

Supper, S., Anton, N., Seidel, N., Riemenschnitter, M., Curdy, C., and Vandamme, T. (2014). Thermosensitive chitosan/glycerophosphate-based hydrogel and its derivatives in pharmaceutical and biomedical applications. *Expert Opin. Drug Deliv.* 11 (2), 249–267. doi:10.1517/17425247.2014.867326

Tao, X., Jiang, F., Cheng, K., Qi, Z., Yadavalli, V. K., and Lu, S. (2021). Synthesis of pH and glucose responsive silk fibroin hydrogels. *Int. J. Mol. Sci.* 22 (13), 7107. doi:10.3390/ijms22137107

Thambi, T., Phan, V. G., and Lee, D. S. (2016). Stimuli-sensitive injectable hydrogels based on polysaccharides and their biomedical applications. *Macromol. rapid Commun.* 37 (23), 1881–1896. doi:10.1002/marc.201600371

Wang, L., Neumann, M., Fu, T., Li, W., Cheng, X., and Su, B-L. (2018). Porous and responsive hydrogels for cell therapy. *Curr. Opin. Colloid & Interface Sci.* 38, 135–157. doi:10.1016/j.cocis.2018.10.010

Wang, H., Liu, H., Liu, H., Su, W., Chen, W., and Qin, J. (2019). One-step generation of core–shell gelatin methacrylate (GelMA) microgels using a droplet microfluidic system. *Adv. Mater. Technol.* 4 (6), 1800632. doi:10.1002/admt.201800632

Wu, Y., Zhao, Z., Guan, Y., and Zhang, Y. (2014). Galactosylated reversible hydrogels as scaffold for HepG2 spheroid generation. *Acta biomater.* 10 (5), 1965–1974. doi:10.1016/j.actbio.2013.12.044

Wu, J., Liu, J., Shi, Y., and Wan, Y. (2016). Rheological, mechanical and degradable properties of injectable chitosan/silk fibroin/hydroxyapatite/glycerophosphate hydrogels. *J. Mech. Behav. Biomed. Mater.* 64, 161–172. doi:10.1016/j.jmbbm.2016.07.007

Yang, Q., Zhu, Z., Wang, L., Xia, H., Mao, J., Wu, J., et al. (2019). The protective effect of silk fibroin on high glucose induced insulin resistance in HepG2 cells. *Environ. Toxicol. Pharmacol.* 69, 66–71. doi:10.1016/j.etap.2019.04.001

Ye, S., Boeter, J. W., Penning, L. C., Spee, B., and Schneeberger, K. (2019). Hydrogels for liver tissue engineering. *Bioengineering* 6 (3), 59. doi:10.3390/bioengineering6030059

Yin, Z., Wu, F., Xing, T., Yadavalli, V. K., Kundu, S. C., and Lu, S. (2017). A silk fibroin hydrogel with reversible sol–gel transition. *RSC Adv.* 7 (39), 24085–24096. doi:10.1039/c7ra02682j

Yoshida, R., Kaneko, Yo, Sakai, K., Okano, T., Sakurai, Y., Bae, Y., et al. (1994). Positive thermosensitive pulsatile drug release using negative thermosensitive hydrogels. *J. Control. Release* 32 (1), 97–102. doi:10.1016/0168-3659(94)90229-1

Zafar, S., Hanif, M., Azeem, M., Mahmood, K., and Gondal, S. A. (2021). Role of crosslinkers for synthesizing biocompatible, biodegradable and mechanically strong hydrogels with desired release profile. *Polym. Bull.* 79, 9199–9219. doi:10.1007/s00289-021-03956-8

Zhang, Y., Lu, J., Li, Z., Zhu, D., Yu, X., and Li, L. (2021). Enhanced cellular functions of hepatocytes in the hyaluronate-alginate-chitosan microcapsules. *Int. J. Artif. Organs* 44 (5), 340–349. doi:10.1177/0391398820959345

Zhou, H. Y., Zhang, Y. P., Zhang, W. F., and Chen, X. G. (2011). Biocompatibility and characteristics of injectable chitosan-based thermosensitive hydrogel for drug delivery. *Carbohydr. Polym.* 83 (4), 1643–1651. doi:10.1016/j.carbpol.2010.10.022

frontiers | Frontiers in Bioengineering and Biotechnology

TYPE Review
PUBLISHED 22 February 2023
DOI 10.3389/fbioe.2023.1104126

OPEN ACCESS

EDITED BY
Filippo Rossi,
Politecnico di Milano, Italy

REVIEWED BY
Emanuele Mauri,
Politecnico di Milano, Italy
Fabio Pizzetti,
Politecnico di Milano, Italy

*CORRESPONDENCE
Seyed Morteza Naghib,
Naghib@iust.ac.ir
Wei Zhang,
wei.zhang@dlut.edu.cn

SPECIALTY SECTION
This article was submitted to Nanobiotechnology, a section of the journal Frontiers in Bioengineering and Biotechnology

RECEIVED 01 December 2022
ACCEPTED 09 February 2023
PUBLISHED 22 February 2023

CITATION
Salehi S, Naghib SM, Garshasbi HR, Ghorbanzadeh S and Zhang W (2023), Smart stimuli-responsive injectable gels and hydrogels for drug delivery and tissue engineering applications: A review. *Front. Bioeng. Biotechnol.* 11:1104126. doi: 10.3389/fbioe.2023.1104126

Smart stimuli-responsive injectable gels and hydrogels for drug delivery and tissue engineering applications: A review

Saba Salehi[1], Seyed Morteza Naghib[1]*, Hamid Reza Garshasbi[1], Sadegh Ghorbanzadeh[2] and Wei Zhang[2]*

[1]Nanotechnology Department, School of Advanced Technologies, Iran University of Science and Technology and Biomaterials and Tissue Engineering Department, Breast Cancer Research Center, Motamed Cancer Institute, Iran University of Science and Technology (IUST), ACECR, Tehran, Iran, [2]State Key Laboratory of Structure Analysis for Industrial Equipment, Department of Engineering Mechanics, Dalian University of Technology, Dalian, China

Hydrogels are widely used biomaterials in the delivery of therapeutic agents, including drugs, genes, proteins, etc., as well as tissue engineering, due to obvious properties such as biocompatibility and their similarity to natural body tissues. Some of these substances have the feature of injectability, which means that the substance is injected into the desired place in the solution state and then turns into the gel, which makes it possible to administer them from a way with a minimal amount of invasion and eliminate the need for surgery to implant pre-formed materials. Gelation can be caused by a stimulus and/or spontaneously. Suppose this induces due to the effect of one or many stimuli. In that case, the material in question is called stimuli-responsive because it responds to the surrounding conditions. In this context, we introduce the different stimuli that cause gelation and investigate the different mechanisms of the transformation of the solution into the gel in them. Also, we study special structures, such as nano gels or nanocomposite gels.

KEYWORDS

injectable, stimuli-responsive, hydrogel, drug delivery, tissue engineering

Introduction

Gels are polymer networks that are expanded by a fluid that occupies their entire volume (Veloso et al., 2021; Wang et al., 2022). Different gels with different fluid components are used in medical applications (Mohammad et al., 2021). Hydrogels with water fluid components are the most widely used type of materials, but there are other types, such as organogels, some members of this family that have low toxicity can be used in biological applications (Wang Y. et al., 2021). In other words, hydrogels are hydrophilic polymer networks that may absorb water up to thousands of times their dry weight (Ghazinezhad et al., 2022). The abundant use of hydrogels in medical applications is due to the extraordinary properties that these materials show (Zainal et al., 2021). For example, hydrogels are usually biocompatible. This characteristic is due to their high water content and similarity to the body's natural tissue in terms of chemical composition and mechanical properties (Pang et al., 2020). In addition, the target site may have damaging conditions for the cargo (Sabourian et al., 2020). Hydrogels can protect cells and sensitive

drugs such as peptides, proteins, oligonucleotides, and DNA inside them, preventing their association with enzymes and ROS (Gačanin et al., 2020).

Now, we will explain each application and the advantage of using hydrogels. First, we examine the application of tissue engineering. Tissue engineering uses biomaterials and, in some cases, cells and growth factors to improve the function, replace, restore or repair a lost or damaged body tissue. In tissue engineering, hydrogels are either made from the beginning with sufficiently large pores. Cells are placed in them, or the pores may be created by dissolving or destroying the hydrogel or releasing growth factors. The cells penetrate these places and, after growing and proliferating, secrete their extracellular matrix (ECM) and regenerate the tissue in this way.

Hydrogels work well in delivering nutrients and GF to cells and removing the products of cellular processes from them. Also, cell adhesive ligands can be easily attached to them. On the other hand, highly hydrated hydrogels mimic the physical and chemical environment of ECM; especially, injectable hydrogels have a microstructure similar to ECM, and for this reason, a good physical integration between these two is created. Also, hydrogels support cell proliferation due to their porous network.

The second application that is examined in this article is drug delivery. The advantage of using hydrogels in drug delivery mostly refers to regulating the processes' kinetics. For example, the network porosity can be easily adjusted to control the speed of drug penetration into the surrounding tissues. In addition, it is possible to deliver both hydrophilic and hydrophobic drugs with these materials.

Among the various gels, some formulations can be injected into the body in a sol state and turned into a gel after applying the stimulating effect *in situ*. These materials were highly regarded for the following reasons. (Huang et al., 2019; Ayoubi-Joshaghani et al., 2020; Bertsch et al., 2022).

- Cells and bioactive molecules can easily and, through a simple mixing process, be homogenously combined with the hydrogel precursor or the same solution, which also solves cell adhesion problems (Ishihara et al., 2020; Rajabi et al., 2021; Xue et al., 2021).
- In the application of tissue engineering, injecting biomaterials instead of invasive surgeries imposes less pain on the patient (Deus et al., 2020; Zeimaran et al., 2021).
- In addition, tissue recovery is faster and ultimately leaves a smaller scar. In addition, the injection of these materials into the defect area and its gelation makes the geometry of the implant perfectly match the defect and eliminate the need for pre-formed patient-specific scaffolds.
- On the other hand, in drug delivery, injection and local delivery of carriers reduce systemic toxicity (de Araújo et al., 2019; Sun et al., 2020).

Gelation of solutions occurs by creating cross-links between monomers, which this links can be chemical or physical (Marco-Dufort and Tibbitt, 2019; Peppas and Mikos, 2019). Chemical cross-links are created due to chemical reactions and are covalent bonds (Cao L. et al., 2019). These bonds are stronger than physical bonds and, as a result, are mechanically more stable, so these types of gels by chemical bonds are not diluted in environmental fluids and do not penetrate or move away from the intended site. In addition, they are physically compatible with more types of tissues and create a good and long-term connection with the surrounding tissue (Shen et al., 2023). These connections are permanent, and reversibility does not occur in them. In the past, these gels were mostly used for pre-formed implants, but with new techniques, it became possible to inject them.

Another type of cross-link is physical and non-covalent; chemical reactions do not play a role in their formation (Chen et al., 2019). The most important interactions that lead to gel production in this category are hydrogen bonding, dipolar-dipolar, and hydrophobic interactions (Anderson et al., 2020; Zhou et al., 2020; Yang et al., 2022). These relatively weak interactions have reversible nature, which means that the substance can turn into a gel in the environment outside the body, then during injection into the body, due to the shear stresses of the injection, the bonds are broken and turn into a sol, and after a while, it returns to the gel state again (Liu et al., 2020; Bai et al., 2022; Zou et al., 2022).

Nanogels and nanocomposite gels are two important examples of gels, which will be explained below. Nanogels are gels with a size of 1 to generally 200 nm, so in addition to the properties of hydrogels, due to their specific dimensions, they have characteristics that we will review below (Liu X. et al., 2022). These substances can escape the elimination process by the body's immune system. Also, due to the network structure after injection, they have a high circulation time in the bloodstream until they reach the target location, which increases the probability of targeting (Taghipour et al., 2022). In addition, the transfer of a hydrophilic surface to the nanogel increases the circulation time in the bloodstream and prevents particle absorption by immune mononuclear phagocytic cells (Rabiee et al., 2019). Due to their high surface-to-volume ratio, they have a large surface area for biological conjugation and cargo loading (Rabiee et al., 2019). The last item can be carried out without chemical reaction, effectively maintaining drug activity in drug delivery applications. Due to their small dimensions, they have a high response speed to the stimulus. Also, due to their small size and soft structure, they can reach small capillaries and penetrate the target tissues through transcellular and paracellular routes. Easy synthesis, the ability to adjust the size, stability in the presence of serum, the possibility of controlled release, and the ability to deliver hydrophobic drugs and sensitive compounds of protein or nucleic acids are some of the advantages of this class of materials (Amina and Guo, 2020; Curreri et al., 2021).

In addition, they can be used for targeted drug delivery, for example, to tumors. In this way, in addition to passive targeting, i.e., the inherent tendency of nanogels to accumulate in tumors, nanogels can perform active targeting by modifying the surface, for example, with a ligand. These substances can be injected intravenously, and after accumulating at the tumor site, they can be cross-linked by a stimulant and turned into a bulk gel (Cao et al., 2020). These substances overcome the challenges of conventional drug treatments, including low bioavailability. They reduce previous treatments' adverse reactions and side effects (Dalir Abdolahinia et al., 2022). However, despite the advances, the performance of nanocarriers usually has side effects. These structures generally have minimal toxicity.

Nevertheless, most synthetic nanogels have the risk of toxic compounds, so some of them have been prevented from using (Ma et al., 2022). Nanocomposite hydrogels are hydrogels in which nanomaterials are incorporated. Nanostructures can also be created *in situ* in the hydrogel matrix (Kuang et al., 2019). When nanoparticles can cause unwanted biological responses in the body (e.g., immune response), the hydrogel can prevent the two from directly interacting. In smart nanocomposite gels, the type of nanoparticle determines the type of stimulus (es) and enhances delivery in different body parts (Wen et al., 2020).

Reinforcing nanostructures form a strong link with many matrixes polymer chains because they have a high surface-to-volume ratio. This results in the composite having a high strength and toughness, which is crucial in the application of tissue engineering. The reinforcement can also give a kind of biological activity, such as angiogenesis or osteogenesis induction, to the hydrogel. In addition, it can improve the gelation time and biodegradation. In some systems, surface-modified nanoparticles can act as gelators and cause lateral chemical cross-linking of the network (Mellati et al., 2021). Conventional hydrogels are usually used to carry hydrophilic drugs and release hydrophobic drugs quickly, but nanocomposites can carry hydrophobic drugs. In addition, nanocomposites have a higher swell/deswell rate and mimic natural tissues more (Kurian et al., 2022).

Endogenous stimuli

Internal stimuli are the conditions applied by the environment inside the body after injection to the gel and inducing gelation. All the gels mentioned in this category are physical.

Temperature

The temperature at which gelation occurs depends on the concentration of monomers in the fluid. For each substance in a specific concentration, gelation occurs at the lowest temperature, called the lower critical solution temperature or (LCST); this temperature point is called the cloud point (Figure 2A). These gels have a negative temperature dependence, which means that they shrink with increasing temperature, and for example, if they contain drugs, the release of the drug from them is limited. These gels are widely used because they can be dissolved at room temperature (25°C) and turned into a gel by injecting them into the body and reaching the temperature of the material to about 37°C (Nguyen et al., 2019). The gelation mechanism in this category of materials is that the hydrogen bond between the side groups of monomers and water in the solution weakens with increasing temperature, and gelation and contraction occur with the strength of hydrophobic interactions of the main chain, and the dehydrated polymer is formed (Figure 1) (Le et al., 2018). PNIPAM Poly (N-isopropyl acrylamide) is the most famous member of this family with an LCST of about 32°C, and its shrinking behavior occurs with a state transition from the extended helix to the coiled-coil. It is possible to increase the gelation temperature by copolymerizing this polymer with hydrophilic monomers and decreasing this temperature with hydrophobic monomers. The first case is used because the gelation temperature close to body temperature are desirable. One disadvantage of this gel is its possibility of being toxic and non-degradable (Litowczenko et al., 2021).

b) The second category of materials, contrary to the previous case, turns into a gel with a decrease in temperature (Figure 2B). The use of these materials is limited because the solution must have a high temperature before injection, in which biomolecules and sensitive drugs may be damaged (Ward and Georgiou, 2011).

c) In the third category, known as thermoreversible gels, both of these behaviors are seen, that is, with the increase in temperature, first a conversion of sol to gel, and then at higher temperatures, a conversion of gel to sol is observed in them (Figure 2C). The mechanism of gelation in some amphiphile members (substances with both hydrophilic and hydrophobic properties) of this class of materials is that when the temperature rises above the LCST of the gel, the monomers self-assemble due to the polymer-polymer interaction and turn into micelles, after their fraction exceeds a certain limit and the micell packing and knots reach such a level that the micelles cannot move, so the system turns into a gel (Xin and Naficy, 2022).

One of the important formulas in this field is triblock copolymers, the most important part of this family is poloxamer or pluronic with the chemical formula PEO-PPO-PEO. Whose central block is hydrophobic, and the side blocks are hydrophilic. Meanwhile, poloxamer407 or pluronicF127 has the least toxicity and the most use. However, due to the weakness of the cross-links between the micelles, the mechanical properties of this material are weak, and in addition, in a short time, the structure is separated, and release from them happens. In addition, these materials are not biodegradable, and these items can be improved by modifying the structure (Matanović et al., 2014).

To check gelation from a thermodynamic point of view, the formula $\Delta G = \Delta H\text{-}T\Delta S$ should be referred to. For polymers with LCST, gelation proceeds mainly due to increased entropy, especially in the water component, which reduces the Gibbs free energy. However, in polymers with UCST, the driving force of gelation is enthalpy type. Despite all the mentioned advantages, this method also has its disadvantages. For example, suppose the speed of gelation is high. In that case, there is a possibility of gelation of the substance inside the syringe needle and blocking it during injection, or with slow gelation, the release of these substances has a burst state for a while. The speed of gelation in tissue engineering applications is effective in cell distribution.

In general, in the case of block copolymers such as poloxamer and polymers containing PANIPAAM, to modify characteristics such as gelation time, temperature/pH of gelation, mechanical strength, biocompatibility, it is possible to work on copolymer composition, hydrophobic-hydrophilic balance, two-component block length, weight molecular, polymer architecture. Chenite and co-workers added polyol phosphate salts to chitosan to add temperature-sensitive gelation properties to a pH-sensitive solution and to prepare a biodegradable and biocompatible gel with a good residence time for the delivery of cells and therapeutic proteins (Chenite et al., 2000).

Cho and colleagues proposed a water-soluble chitosan-g-NIPAAm copolymer to treat bladder or gastric reflux during a single-injection endoscopic procedure (without a double-injection

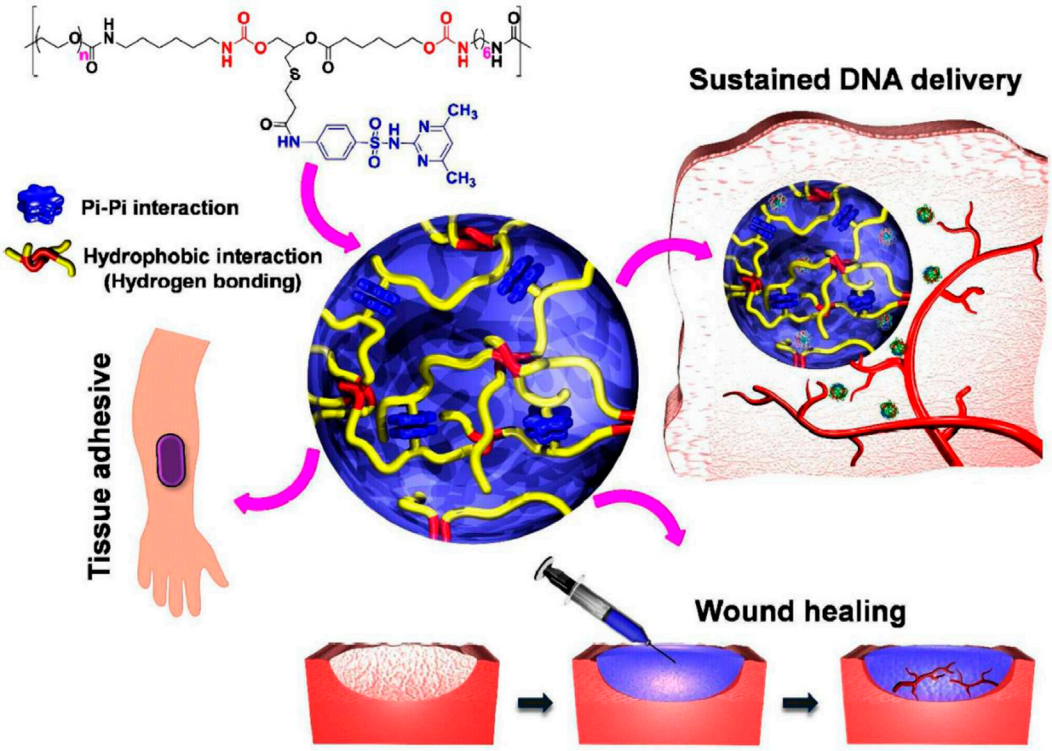

FIGURE 1
The idea of PEG-PSMEU copolymers' sol-to-gel phase transition and their numerous biomedical applications. i) Following subcutaneous delivery of PEG-PSMEU copolymer sols containing polyplex, a viscoelastic gel was created that controlled the release of the polyplex. ii) Similar to adhesives inspired by mussels, the PEG-PSMEU copolymer hydrogel easily penetrates onto the skin's surface. iii) The hydrogels' tissue adhesion properties are used in wound healing to close wounds and restore tissue structure and function. Reprinted with permission from (Le et al., 2018). Copyright 2018 American Chemical Society.

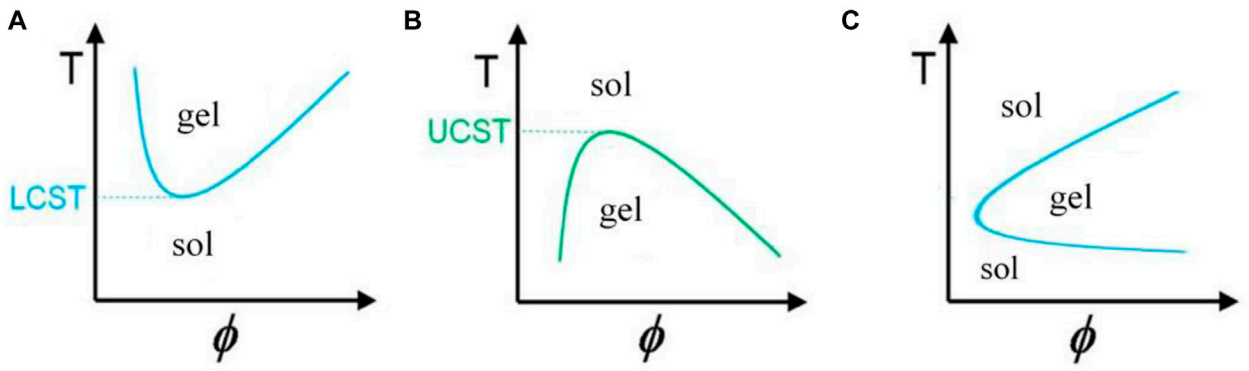

FIGURE 2
Graph of temperature changes with volume fraction of polymer in solution for gels with **(A)** negative, **(B)** positive (Ward and Georgiou, 2011), and **(C)** reversible temperature behavior.

system). Human mesenchymal stem cells were placed and differentiated into chondrocytes inside this gel. Lowering the polymer's temperature from 32°C or LCST allowed the cells to be revived. With the use of this gel, it was possible to study the development of cartilage in the submucosa layer of rabbits' bladders (Cho et al., 2004).

Shou created the thermosensitive, injectable, tissue-adhesive, biodegradable, biocompatible, and wound hemostasis multifunctional HBCS-C hydrogels (Figure 3). They exhibit an excellent liquid-gel transition at different temperatures because of differences in the hydrophilic-hydrophobic interaction and hydrogen bonds created by the hydroxybutyl groups. The

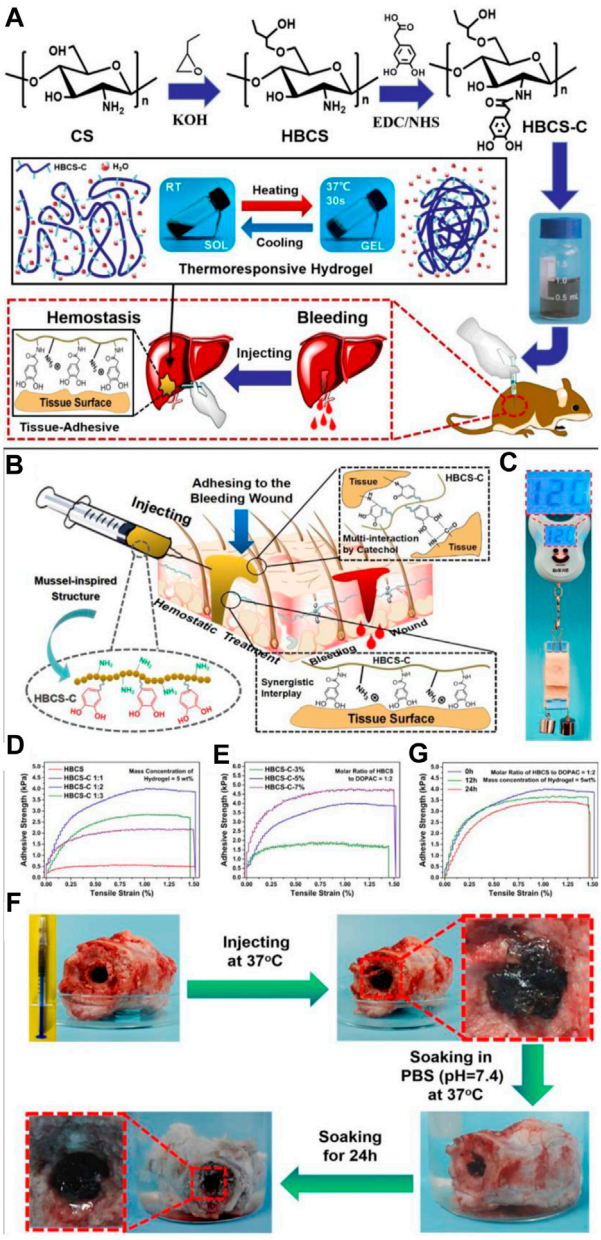

FIGURE 3
(A) HBCS-C thermoresponsive sticky hydrogels shown schematically. **(B–G)** Tissue adhesive behaviors of HBCS-C hydrogels. **(B)** Mussel-inspired HBCS-C hydrogels' possible tissue-adhesive mechanism is depicted schematically; **(C)** The image demonstrated the HBCS-C hydrogel's strong adhesive ability on pig skin; lap shear tests of the HBCS-C hydrogels **(D)** at different molar feed ratios of HBCS to DOPAC and **(E)** at different mass concentrations; **(F)** Photos captured the HBCS-C hydrogel's wet bioadhesive activity and stability in an aqueous environment at 37°C. The HBCS-C hydrogel was still firmly adhered in the hole after 24 h of immersion in PBS, demonstrating its excellent tissue-adhesion and stability; **(G)** Lap shear tests at a different immersing time in PBS. Reprinted with permission from (Shou et al., 2020). Copyright 2020 American Chemical Society.

interactions between tissues and catechol/amino groups, which occur often, allow biocompatible hydrogels to cling firmly to tissue surfaces (Shou et al., 2020).

Chung and colleagues prepared Pluronic stereo complex hydrogels linked by D-lactide and L-lactide oligomers for sustained and zero-order release of human growth factor with two mechanisms of diffusion and erosion, which had a linear mass erosion profile. The concentration and critical gelation temperatures were much lower than uncomplexed formulas or pluronic homopolymers. This degradable gel had higher strength than the previous samples, probably due to the spontaneous formation of stereo-complex crystal regions and more cross-links. It was also more resistant to being dissolved in water environments. This gel can be used for gene or cell delivery (Chung et al., 2008).

Yu and colleagues investigated the ability of thermoreversible PLGA–PEG–PLGA for sustained release of PEGylated drugs and used camptothecin as a hydrophobic antitumor model drug (Yu et al., 2008).

Lee and colleagues used a methylcellulose hydrogel to encapsulate spherical aggregates of cells instead of injecting single cells into muscle tissues, which would remain in that area due to their larger size. By using this technique, ECM and intercellular connections were preserved due to not using any proteolytic enzymes during their implantation. In addition, most of the cells were viable; they maintained their aggregate state after injection and maintained their activity by moving to another growth surface. The gel was injected into rabbit skeletal muscle and showed that the aggregates were large enough to stay in the muscle spaces and form a good ECM (Lee et al., 2009).

Choi and co-workers synthesized a polyalanine-poloxamer-polyalanine hydrogel in which the polypeptide end blocks were made using L-polyalanine and D-polyalanine and a mixture of the two and controlled their secondary structure in terms of the β-sheet fraction, which It was effective on the population and nanostructure of the fibrous hydrogel, and as a result, the proliferation and expression of the chondrocyte protein that was encapsulated in it, and it also performed well in their differentiation (Choi et al., 2010).

Hsiao and his colleagues partially substituted chitosan with the hydrophilic carboxymethyl group to increase chitosan water solubility and with the hydrophobic hexanoyl group to increase amphiphilicity. This material was self-assembled and created nanocapsules, which created a gel by combining it with a polyol salt. This degradable substance is used to release therapeutic agents. These substances showed little host inflammation and toxicity on human retinal epithelial cells and had good drug loading (Hsiao et al., 2012).

Chen and his colleagues used hexamethylene diisocyanate to create cross-links in pluronic F127, which increased its mechanical stability and biocompatibility. These nanostructures were used to prepare a composite with a hyaluronic acid matrix. This substance was used to bring the anticancer drug DOX to the zero-order state, which had a negative effect on cancer cell viability and tumor size. In addition, it was shown that the regulation of degradation time could be achieved with the concentration parameter of nanostructures (Chen et al., 2013).

Gelation of temperature-sensitive polymers with increasing temperature can occur due to the rotation of. superparamagnetic iron oxide nanoparticles (SPIONs) in an alternating magnetic field. Zhang and his colleagues proposed using SPIONs in chitosan and β-glycerophosphate hydrogels to deliver *Bacillus* Calmettee Guérin, an immunotherapy drug for bladder cancer (Zhang et al., 2013).

Boustta and his colleagues synthesized Poly (N-acryloyl glycinamide) UCST gel in which the burst release was minimized and could deliver neutral and ionic drugs, especially soluble in an aqueous medium, salts, charged macromolecules, and proteins (Boustta et al., 2014).

Redox reactions

Utilizing a water-soluble initiator for redox-polymerization. For redox/photopolymerization, synthetic hydrophilic macromers containing acrylate/methacrylate groups were developed. Using similar methods, semi-synthetic macromers derived from natural polymers were studied.

In order to create a hydrogel, functionalized macromers with acrylate/methacrylate groups can be polymerized using free radicals created in water by redox processes. As a redox-initiating system, ammonium persulfate/N, N, N-tetramethyl ethylene diamine (APS/TEMED) or APS/ascorbic acid have typically been employed. The biocompatibility of oxidizing or reducing substances can be a problem in the *in situ* gelling system based on redox reactions. When catechol-containing polymers are oxidized, quinine, an oxidized catechol, may react with the amino groups of the medication absorbed during the gel-forming process. The cysteine groups of the protein medicines can obstruct the thiol-disulfide process. The potential inclusion complex between cyclodextrin and the medication or a portion of the drug should be carefully followed in the event that an inclusion complex forms to create a gel.

Oxidative stress, which is caused by reactive oxygen species (ROS) such superoxide and hydroxyl radicals, has a significant impact on aging and a number of diseases. We created redox polymers with covalent bonds to antioxidants. These polymers, which have the ability to self-assemble, create redox nanoparticles (RNPs) in aqueous media, which limit absorption into healthy cells, build up at regions of inflammation, and successfully fend off diseases caused by ROS. As a result, RNPs are successful in stopping disorders that involve ROS, including cancer, myocardial and brain ischemia-reperfusion injuries, ulcerative colitis, and ulcerative colitis. We created injectable redox gels (RIGs), which, when exposed to physiological circumstances, change from a flowable solution at room temperature to a gel at body temperature. RIGs can be used to reduce localized inflammation, such as those caused by periodontitis. Anti-tissue adhesion sprays used following physical surgery can also contain RIGs.

The electron transport pathway in the mitochondria of healthy cells generates a lot of ROS. Small molecular antioxidants reach healthy cells and their mitochondria, where they have an unfavorable influence on the critical redox processes involved in electron transfer chains. It is impossible to provide enough LMW antioxidants because ROS are “double-edged swords” in this way; these antioxidants have a small or non-existent therapeutic window. We created a different type of antioxidant nanomedicine. This is a covalent compound of a typical antioxidant and a metabolizable, moderately-molecular-weight polymer. An amphiphilic block copolymer with a self-assembling property was covalently conjugated with a nitroxide radical (TEMPO) with catalytic ROS scavenging capabilities [8]. In an aqueous solution, the amphiphilic redox polymer self-assembles to produce nanoparticles (Ko et al., 2013; Nagasaki, 2018).

Numerous cardiovascular illnesses are impacted by nitric oxide (NO), but its therapeutic use is constrained by its short half-life and low absorption. Overproduced reactive oxygen species (ROS) quickly react with endogenous NO in inflamed tissues, lowering its bioavailability. When there has been a myocardial infarction, the infiltration of inflammatory cells like macrophages and the ensuing inflammatory response are crucial for tissue repair. However, if the inflammatory response becomes excessive, it will slow wound healing and lead to persistent heart failure.

The inducible NO synthase (iNOS) enzymatic process can produce NO by using L-Arg as a substrate since these activated macrophages lead to a considerable rise in iNOS expression and activity.

Vong et al. (2018) designed a formulation based on PArg-PEG-PArg and PMNT-PEG-PMNT coupled with PAAcs for preventing and treating cardiovascular diseases, in which the polyion complex (PIC) micelle was formed in the flower-type and turned into a gel by changing the temperature during the injection. This substance spread homogeneously and remained in the myocardial tissue, releasing NO and scavenging overproduced ROS. This redox-responsive gel caused angiogenesis, reduced infarction size, and good heart function after infarction.

Cao and his colleagues produced a thermally reversible gel that contained self-assembled peptide nanofibrils and PNIPAM, and when the temperature passed from the LCST of PNIPAM, the globules formed from it acted as a cross-linker of the fibrils and a gel was created. The release rate can be adjusted by the concentration of the peptide due to the affinity between them. To remove this material, the temperature can be reduced below the LCST and removed from the site with slight mechanical pressure. This gel can be used in drug delivery, and due to its fibrillar structure similar to ECM, it can potentially be used for tissue engineering (Cao M. et al., 2019).

Shou and colleagues used a chitosan-based gel for the hemostasis of bleeding wounds. Unlike the previous samples, this gel had very good tissue adhesion, which resulted in excellent homeostatic properties, and was biocompatible and biodegradable (Figure 4) (Shou et al., 2020).

Tan and colleagues developed a PLGA-PEG-PLGA-based nanocomposite gel containing metal-organic frameworks, DOX, and the anti-angiogenic agent celecoxib for treating oral cancer, which has high drug loading capacity, sustained release, and pH-responsiveness of both types of drugs was one of its benefits (Tan et al., 2020).

pH

pH stimulus is mostly used to induce volume change and drug release in gels, but cases of gelation induction have also been reported by applying this stimulus (Figure 5). Chitosan, the N-deacetylated derivative of chitin and the only natural cationic polysaccharide, is known to gelate due to pH change. This substance is a polybase that is protonated in a mild acid, and the dangling primary amine groups receive a positive charge; that is, they are converted from the formula $-NH_2$ to $-NH_3^+$, which creates a repulsive force in it and causes its dissolution and transformation to sol. Nevertheless, it turns into a gel again after crossing the Pka point, removing the positive charges and creating a hydrogen bond between the amine groups (Yuan et al., 2022). This substance has an acidic pH in the sol state that causes inflammation in the host tissue, which subsides with the

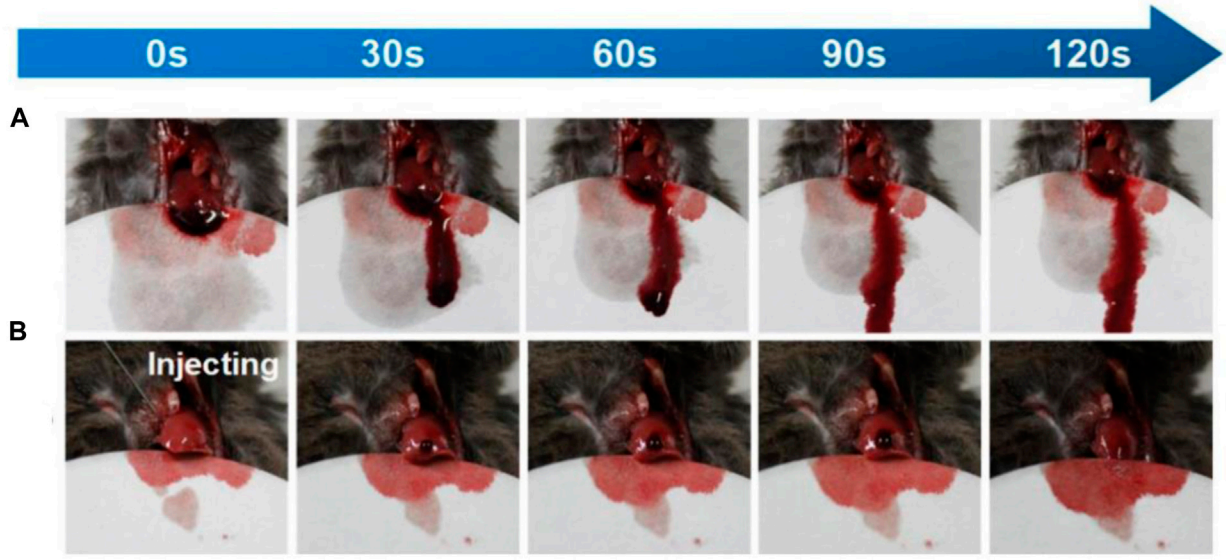

FIGURE 4
The amount of bleeding in the mouse liver over time **(A)** without and **(B)** with gel. Reprinted with permission from (Shou et al., 2020). Copyright 2020 American Chemical Society.

degradation of the gel. To increase the strength of polymers in general, it is possible to use hydrophobic modification and polymer blends. The gel's strength depends on the polymer's crystallinity and, as a result, the porosity of the gel (Podgórski et al., 2020). Due to the acidic pH of inflamed areas or tumors, these gels can be used in cancer treatment with chemotherapy, gene therapy, or immunotherapy. For example, nanogels containing anticancer drugs can be injected intravenously so that they accumulate in the tumor area and become a bulk gel, which can be designed with target ligands for this purpose. Formation of gel and then releasing the drug in the target area helps to prevent systemic side effects. Gels of other categories, for example, thermo-responsive, can be modified with ph-responsive groups and create a dual-responsive gel (Huang et al., 2021). To create more intermolecular forces and enhance gelation in chitosan, Chiu and colleagues modified it with a hydrophobic palmitoyl group and obtained N-palmitoyl chitosan (NPCS). In which gelation occurs in a narrow pH range of 6.5–7. This non-toxic and degradable gel can be used for drug and cell delivery (Chiu et al., 2009).

Li and colleagues reacted to PEG derivatives and α, β-polyaspartylhydrazide during the injection. The resulting gel was able to transform into a sol in the tumor tissue with an acidic pH, release the anticancer drug DOX, and return to the gel state with an increase in pH. The resulting material was biocompatible and biodegradable and was tested on mice with human fibrosarcoma (Li et al., 2015).

The work of Wu et al. (2020) Aldehyde-functionalized polymers and amine-modified silica nanoparticles interact through Schiff base interactions to create injectable, self-healing, and pH-responsive nanocomposite hydrogels (Figure 6). The hydrogel gelates in 10 s, is injectable and has quick self-healing capabilities. Additionally, the hydrogel demonstrated amazing stability in physiologically neutral conditions, but a mildly acidic environment caused a quick gel-sol transition, which was suitable for regulated drug delivery. The hydrogel's pH responsiveness was extremely sensitive; when subjected to a 0.2 pH shift, mechanical properties, hydrolytic breakdown, and drug release behaviors all changed significantly.

Moreover, the composition of the hydrogel might easily alter its mechanical and pH-responsive capabilities. Cytotoxicity testing on human dermal fibroblast cells (HDFa) demonstrated good biocompatibility.

Hybrid hydrogels that are injectable, self-healing, and pH-responsive are prospective biomaterials for the gradual release of therapeutic chemicals during the course of cancer treatment. Cimen et al. (2021) Hydrazone linkages were produced using aldehyde- and hydrazide-functionalized gelatin (Gel-ADH) and PEG (diBA-PEG) polymers. They have developed an injectable hybrid hydrogel that responds to pH (Figure 7). By assimilating the resulting Pregele with Laponite (LAP) nanodiscs loaded with the anticancer medication doxorubicin (DOX) during the gelation process, an ADH/diBA-PEG/LAP@DOX hybrid hydrogel was created. The hybrid hydrogel's observed gelation time was 80 s, and the finished product had outstanding injectability and quick self-healing. The injectable hybrid hydrogels had a very efficient and pH-dependent long-term drug release profile. Human breast cell line (SVCT) and endothelial cell line (HUVEC) were used to assess the hydrogel's components for biocompatibility. The hybrid hydrogel's components are entirely biocompatible and even encourage cell growth. In addition, human breast cancer cell lines and triple-negative breast cancer cell lines were used to test the hydrogels' cytotoxicity.

Ion

Certain polyelectrolytes, such as alginate and pectin, which become anions by dissolving in water and, for example, loses H

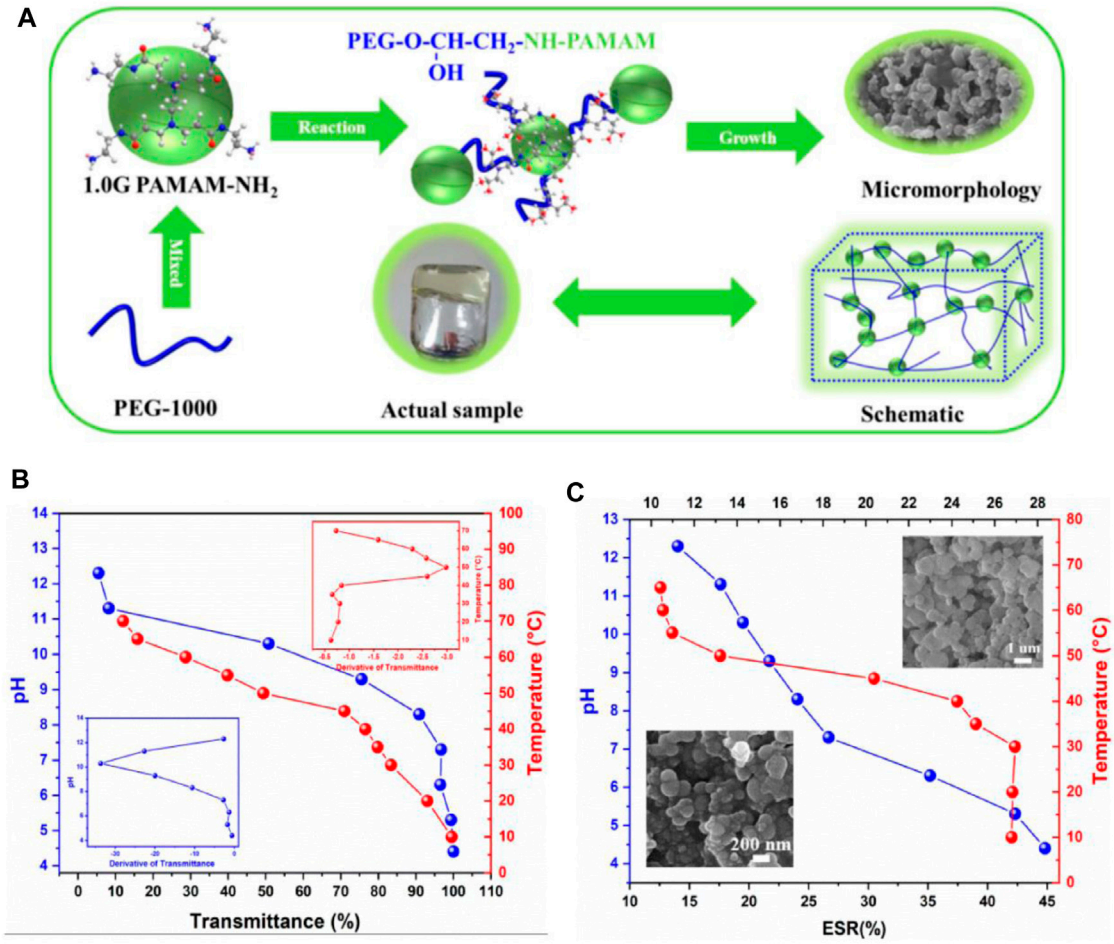

FIGURE 5
(A) Diagram of PEG/PAMAM hydrogel gelation. **(B)** Transmittance and phase transition temperature and pH curves of PEG/PAMAM hydrogels. **(C)** Equilibrium swelling ratio curves of PEG/PAMAM hydrogels under different temperatures and pHs (Liu X. et al., 2022).

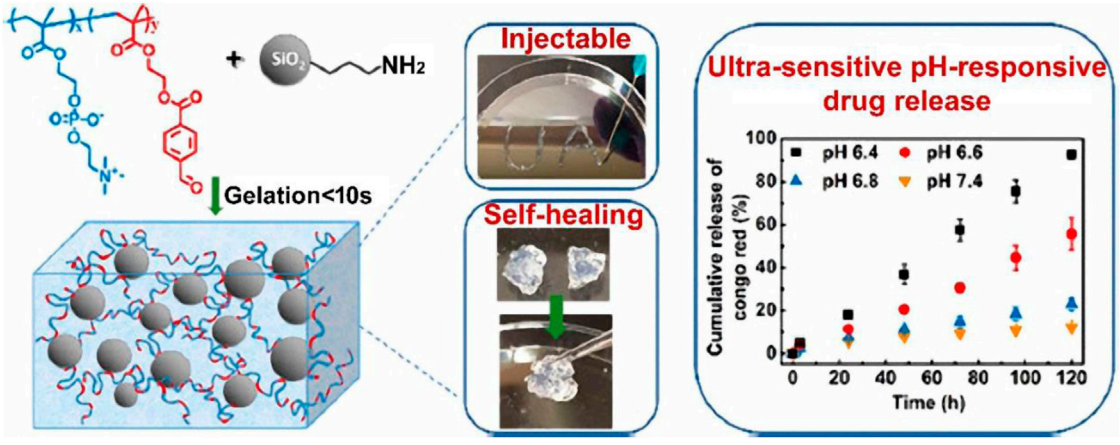

FIGURE 6
Illustration of injectable and self-healing nanocomposite hydrogels with ultrasensitive pH-responsiveness and tunable mechanical properties. Reprinted with permission from (Wu et al., 2020). Copyright 2020 American Chemical Society.

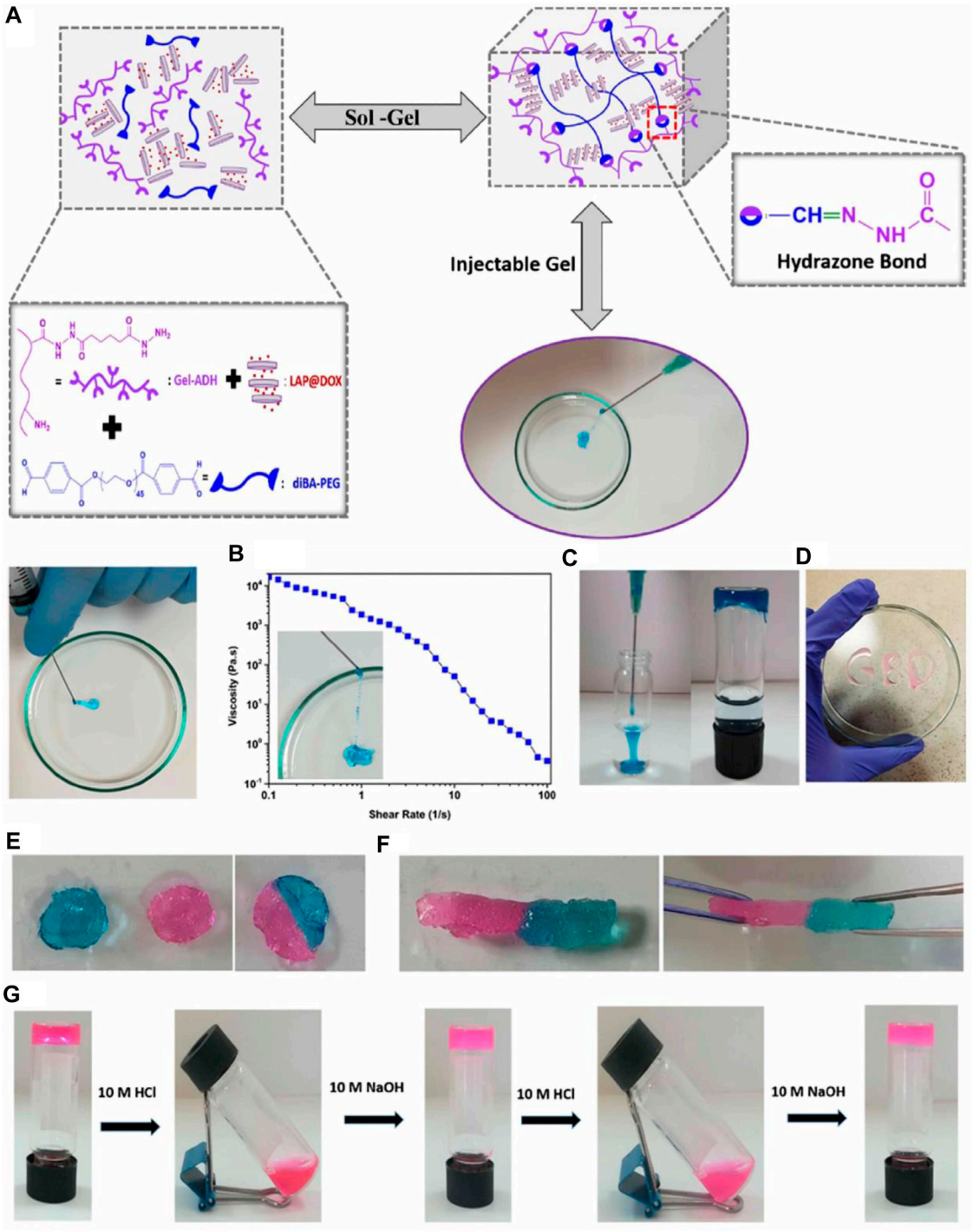

FIGURE 7
Injectability of the hybrid hydrogel: **(A)** hybrid hydrogel was injected through a 21-gauge needle, **(B)** diagram of the apparent viscosity rheology as a function of the shear rate of the hybrid hydrogels. **(C)** Injection of the Gel-ADH/diBA-PEG/LAP hybrid hydrogels into the PBS buffer and the photograph of the formed hydrogel into the PBS solution **(D)** Gel-ADH/diBA-PEG/LAP hybrid hydrogels injected from a 21-gauge needle onto a Petri dish. Self-healing behavior of the Gel-ADH/diBA-PEG/LAP hybrid hydrogels: the hybrid hydrogel was prepared in two colors, that is, pink and blue, separately, and these two-hybrid hydrogels were allowed to make contact with each other **(E)** photograph of the self-healed hydrogel after 1 h, and **(F)** stretching behavior of the self-healing hydrogel after 1 h **(G)** pH-dependent decomposition–composition behavior of the hybrid hydrogels. Reprinted with permission from (Cimen et al., 2021). Copyright 2021 American Chemical Society.

of its carboxyl group, are connected by 2- or 3-valent counterions such as Ca_2^+ and become a gel. In this way, $CaCl_2$ solution or an aqueous slurry of Ca salts is injected into the desired area with a polymer solution using a two-syringe applicator. Adjusting the cross-link density and, consequently, the gel's mechanical properties can be achieved by adjusting the number of counter ions. However, the excessive concentration of opposite ion causes toxicity and damage cell life and therapeutic effect. Therefore, this parameter has an optimal value. To avoid increasing the Ca^{2+} concentration too much, salts of this ion with lower solubility can be used. For example, α-TCP releases Ca ions in water. Another solution is to use calcium-free gels.

Alginate and pectin do not have good cell adhesion, but this issue can be solved with some measures. In addition, the degradation of alginate gels occurs slowly because hydrolysis or enzymatic degradation is not performed on these materials. However, hydrolysis becomes possible with partial oxidation, and the degradation rate increases (Van Tomme et al., 2005). Except for ionic cross-linkers, charged small molecules have also been used for this type of gelation. These agents create similar bonds, but there are differences in penetration speed, etc. Of course, there are other types of ionic gelation, for example, the combination of two polyelectrolytes with opposite charges, which creates a polyelectrolyte complex. Gelation by ion and pH stimuli is performed with a mass transfer mechanism, which is slower compared to temperature gelation through a heat transfer mechanism, and as a result, the problem of rapid gelation and syringe blockage does not occur in these methods.

Tomme and colleagues mixed dispersions of oppositely charged dextran gel microspheres. The gel network was degraded under low pH and high ionic strength. This gel was used in drug delivery and tissue engineering (Van Tomme et al., 2005).

Douglas and colleagues prepared a composite gel containing pectin derived from citrus peel and apple pomace and calcium-rich bioactive glass particles derived from the gel. These glass particles, releasing calcium ions for pectin gelation, caused an antibacterial property as well as mineralization of the gel in the simulated biological environment, which the last item was related to the particle size. Glass with smaller particle size caused a higher ion release rate and thus higher gelation speed. The distribution of glass particles in the gel was not uniform. This gel could be used in bone tissue engineering and showed good cell compatibility with MC3T3-E1 osteoblast cells (Douglas et al., 2018).

Wang J. H. et al. (2021) prepared a hybrid gel with interpenetrate network composed of pectin methacrylate and methacryloyl gelatin for skin hemostasis. In this gel, cross-links were created by light and ions. The high porosity of the gel network caused blood absorption and coagulation at high speed. The characteristics of the gel were easily adjustable and easily removed from the site.

Biological stimuli

Enzyme

Enzymes are the only important biological and internal factors that can cause gelation. Some protein hydrogels, such as fibrin, collagen, and gelatin hydrogels, can be formed with transglutaminase enzymes, known as bioadhesives; This enzyme creates an isopeptide chemical bond, which is an amide bond between two protein molecules. This bond is highly resistant to proteolysis and has good stability in the body. FactorXIIIa enzyme is one such type of enzyme that catalyzes the gelation of fibrin hydrogels. Another enzyme widely used in the gelation of polysaccharide-based polymers is the horseradish peroxide (HRP) enzyme, which works in the presence of an oxidant such as H_2O_2 as a substrate. This enzyme is stable, has an easy purification process, and creates strong gels. This type of gelation is widely used in tissue engineering applications and interaction with cells due to the biocompatibility of the reaction. In addition, the reaction is carried out at neutral pH and mild temperature, and due to the specificity of the function between the enzyme and the substrate and the absence of side reactions, no toxicity is caused.

Sanborn and his colleagues developed a system consisting of phospholipid vesicles containing calcium, thrombin, and factorXIII along with a four-armed PEG with a 20-mer peptide derived from fibrin γ chain attached to an N-terminal cysteine. By changing the temperature at 37°C, the liposomes changed phase, and calcium was released from them, which, along with thrombin, activated factorXIII, which catalyzed the gelation and created a strong and elastic gel that It could not be cut under oscillating cutting and of course it was degradable. This type of gelation was inspired by the cross-link that is done in blood coagulation. This gel is used in drug and gene delivery and tissue adhesion (Sanborn et al., 2002).

Mchale and his colleagues performed genetic engineering on an elastin-like polypeptide, which turns into a gel in the presence of tissue transglutaminase (tTG). This gel can differentiate cells and promote chondrogenesis and control mechanical properties. This material can be used both with and without cells. If used with cells and encapsulation of chondrocyte cells and bioactive factors, the cells had good viability, the phenotype of the cells was maintained, and the increase in the mechanical integrity of the gel indicated ECM deposition. The gel showed good cell penetration if used without cells (McHale et al., 2005).

Jin and co-workers found the formation of dextran-tyramine conjugated gels by HRP enzymes in the presence of H_2O_2, which was used for cartilage tissue engineering. Dextran molecular weight and tyramine substitution degree were effective on gelation time and storage modulus. Chondrocyte cells had good survival and proliferation in this gel, maintained their spherical shape, and produced a cartilage-specific matrix, namely GAG and type II collagen. GAG accumulation gradually increased inside the gel (Jin et al., 2010b).

The same group developed a hyaluronic acid gel grafted with a dextran-tyramine conjugate (Figure 8A) for bone tissue engineering application. That the HRP enzyme, in the presence of H_2O_2, accelerated the establishment of the cross-link of tyramine. The use of this gel led to good cell survival, proliferation, matrix production (collagen and GAG), and differentiation. The proteoglycan of the natural cartilage ECM inspired the molecular structure of this gel (Figure 8B). The gel was degraded in the presence of hyaluronidase enzyme. The degree of tyramine substitution and polymer concentration was effective on gelation time, equilibrium swelling, and storage modulus (Jin et al., 2010a).

Ren and co-workers constructed a glycopolypeptide by conjugating poly (g-propargyl-Lglutamate) with azide-modified mannose and 3-(4-hydroxyphenyl) propanamide, which HRP and H_2O_2 gelled. The concentration of these two was effective on the gelation time,

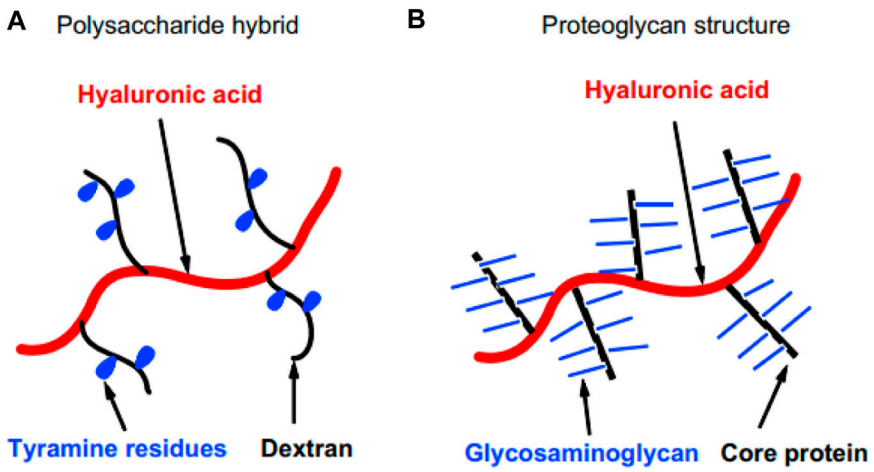

FIGURE 8
Schematic illustration of **(A)** the molecular structure of the material and its similarity to **(B)** proteoglycan of cartilage ECM.

storage modulus, and degradation and swelling time. This gel had useful features such as fast gelation and degradability, and when used with cells, it caused cell survival, cell compatibility, phenotype preservation, cell proliferation, and type II collagen production. In the construction of this gel, natural glycopolypeptides and glycoproteins were mimicked, and their function was similar to the proteoglycans of natural cartilage ECM (Ren et al., 2015).

Inspired by platelets blood coagulation and using serotonin, Zhang et al. (2021) prepared a gel for hemostasis and then wound healing. Chondroitin sulfate was also present in that gel, which regulated cell behavior and wound healing. The HRP enzyme did gelation in this material, and it caused biocompatibility, proper cross-linking, and degradability. Table 1 represents examples of gels formed by enzymes in the literature.

Exogenous stimuli

External stimuli are applied to induce gelation from outside the body.

Photo

This stimulus is used to form and destroy the gel network. The formation of the network by this method under UV or visible light includes three stages initiation, propagation, and termination. At first, there are monomers or oligomers of the substance and a substance called photoinitiator, which uses free radical type photoinitiators with a controlled concentration that does not cause significant toxicity. Usually, UV light irradiation causes the excitation and breaking of a specific bond in the photoinitiator molecule and the formation of a free radical (a particle that has at least one unpaired valence electron), which this free radical separates the double bonds of the main chain of monomers, and create new free radicals. In the propagation stage, which occurs rapidly, these continue the same process on the monomers around them, and the interaction between the two radicals creates a long polymer chain with chemical bonds. This type of polymerization is widely used in tissue engineering (Jiang et al., 2022). Having control over the time and place of radiation is one of the outstanding advantages of this method, and for this reason, it is possible to create micropatterns on the surface and adjust cell behavior, including adhesion, migration, and differentiation in the field of tissue engineering or setting the release rate in different places in the field of therapeutic agent delivery. Of course, these techniques are mostly used for pre-formed gels and not for injectable gels.

In addition, in this method, the gelation speed is higher than other methods, such as gelation induced by temperature, due to the high energy of UV light and the light speed compared to heat transfer in bulk. The high rate of polymerization can cause a great increase in temperature and damage to cells and biomolecules; In this regard, to control the speed of gelation, it is possible to change the intensity of light or the type and concentration of photoinitiator or to irradiate light at intervals during gelation, and also to adjust the amount of reactive double bonds. A long irradiation time leads to an increase in the cross-link density in the gel. It is effective on the gel's mechanical properties, swelling or degradation, and cargo release. It limits the diffusion of nutrients and O_2 and the migration of encapsulated and host cells. This problem can also be solved by surface polymerization, not and not by bulk (Liu Y. et al., 2022). Liu et al. reported a hydrogel-coated upconversion cyanobacterium nanocapsule (UCCy@Gel) for MI prevention and therapy (Figure 9): upconversion nanoparticles (?- NaErF 4@NaLuF4 nanocrystals, UCNPs), which could absorb deeper tissue penetrable near-infrared (NIR) photons and emit shorter wavelength photons (upconversion luminescence, UCL), was conjugated to the surface of cyanobacteria. Besides, a methacrylate outer hydrogel layer was formed to enhance stability and provide stable tissue adhesion. When necessary, through the excitation of 980 nm NIR light, a blend of visible light emitted by UCNPs were used for photosynthesis in cyanobacteria to achieve appropriate oxygen liberation. By this means, a flexible NIR-controllable oxygen-modulating cyanobacterium nanocapsule could be realized for both MI hypoxic prevention and local oxygen therapy (Liu Y. et al., 2022).

In this method, there is a possibility of damaging DNA and cell function and changing gene expression due to the presence of UV light and free radicals. On the other hand, the penetration depth of UV light in the body tissue is low, and therefore this method is mostly used for subcutaneous applications and at shallow depths of the body; Of course, the use of laparoscopic radiation tools is a possible way to use this method for areas that are far away from the surface of the skin. The limited penetration of UV also causes a rigid gel not usually obtained, and to solve these problems, high-intensity visible light can be used, which has deeper penetration and causes less damage to the tissues. Elisseeff and his colleagues realized the possibility of penetration of UV and visible light in living tissues such as skin and polymerization under indirect light irradiation and investigated the potential of this material for the application of cartilage tissue engineering and the release of a protein drug, which led to the creation of collagen and proteoglycan in the first application (Elisseeff et al., 1999).

Such gels can be obtained by modifying materials with functional groups capable of cross-linking by light, such as acrylate groups and their derivatives. For example, Nettles and his colleagues synthesized a methacrylate hyaluronan gel based on natural hyaluronan and thus plays an important role in the development and function of cartilage and has good mechanical properties. Chondrocyte cells were encapsulated in this gel and kept their spherical shape. This resulted in the accumulation of a large amount of matrix and infiltration of cells from the gel into the defect, which resulted in a good integration (Nettles et al., 2004). Light-induced gelation can occur in temperature-sensitive solutions in which photothermal agents are present. In this way, photothermal agents produce heat with light radiation, and as a result, the gel is formed. In this context, Kawano and his colleagues designed a system consisting of several PNIPAM nanogels, each of which contained a gold nanorod, which was systemically injected and circulated, and then by absorbing NIR light at the target site, the hydrophobic surface of the nanorod changed, formed aggregates and accumulated in that place, and then produced heat and caused the reversible phase transformation of PNIPAM (Kawano et al., 2009).

Wu and his colleagues designed a system containing graphene oxide nanosheets and a peptide consisting of glycine-alanine (GA) repeats flanked by a motif for binding to the former and a motif for cross-linking by light for drug delivery (Wu et al., 2014). This gel was self-assembled by creating a β-sheet from the juxtaposition of GA components. Then, a cross-link was formed by light irradiation and with the help of a ruthenium catalyst. The resulting gel had high mechanical stability and a low erosion rate. The radiation of NIR light and the generation of heat by the graphene oxide sheets caused the β-sheets of the structure to unfold partially, the interaction between the two components of the structure was weakened, and the drug contained in it was released (Wu et al., 2015).

Qi and his colleagues extracted sericin from silk industry waste and meta-acrylate it, which turned into a gel in the presence of UV. By changing the degree of network modification, the mechanical properties and degradation speed were adjusted, which is necessary for different needs. This biocompatible gel was used for cartilage tissue engineering, and the chondrocyte had good adhesion and growth. It also had a photoluminescent property that made its location traceable at any moment. This gel was biomimetic and, for example, resulted in the accumulation of cartilage-specific ECM compounds or the expression of more of its genes (Qi et al., 2018).

Lim and co-workers used visible light in the 400–450 nm range for the gelation of Gel-MA by ruthenium and sodium persulfate photoinitiators. Despite having comparable properties to gels created by conventional primers, this gel has fewer side effects on the survival and metabolic activity of articular chondrocyte cells, causes more glycosaminoglycan formation, cells show a higher re-differentiation ability in it. Moreover, the light has a higher penetration depth, which makes possible the formation of gels with a higher thickness (Lim et al., 2019).

Chang et al. (2021) used the combination of methacryloyl gelatin and phenyl isothiocyanate-modified gelatin and developed a gel for rapid hemostasis of oral and dental wounds. The resulting gel has biological activity properties due to the presence of GelMA and good toughness due to the presence of Gel-Phe.

An injectable, near-infrared (NIR)/pH-responsive poly (NIPAm-co-MPCD)/GNRs nanocomposite hydrogel was created using the copolymerization of N-isopropyl acrylamide (NIPAm) and methacrylate poly-cyclodextrin (MPCD)-based macromer. This hydrogel could be used as a long-acting implant for chemophotothermal synergistic cancer (Figure 10). The hydrogel had excellent gelation characteristics, NIR responsiveness, and acceptable mechanical and swelling properties. A doxorubicin prodrug modified with adamantane and hydrophobic acid-labile was successfully loaded into the hydrogel by the host-guest interaction. The hydrogel showed prolonged drug release and could maintain a modest, constant flow of DOX for over a month. The acid-labile hydrazone link between DOX and adamantyl groups was seen to break in an acidic environment, revealing the pH-dependent release of DOX from nanocomposite hydrogels. The release of DOX from the hydrogel network that was accelerated by NIR irradiation was controlled by the hydrogel network collapse brought on by the photothermal action of GNR. *In vitro* cytotoxicity experiments on nanocomposite hydrogels showed their good biocompatibility and photothermal effect.

Additionally, the mouse model study showed good tissue biocompatibility. The nanocomposite hydrogels' capacity to deliver chemo photothermal synergistic therapy with fewer adverse effects was proven by the *in vivo* anticancer test. So, as a long-term drug delivery system, this injectable, NIR/pH responsive nanocomposite hydrogel showed great promise (Xu et al., 2017).

Shear stress

These materials are known as shear-thin and self-heal materials. Applying shear stress during injection reduces their viscosity; they become an injectable sol, and after the injection is completed and the shear stress is removed, they repair themselves and return to the gel state. These materials are a subset of self-healing materials in which the self-healing process occurs by a stimulus and not by itself. These materials have shape memory characteristics, meaning they leave their original shape in memory and return to their original state after changing the shape. The components of self-healing materials are placed next to each other with reversible physical links, and if a crack is formed in them, it will be repaired by itself, which increases the lifetime of these

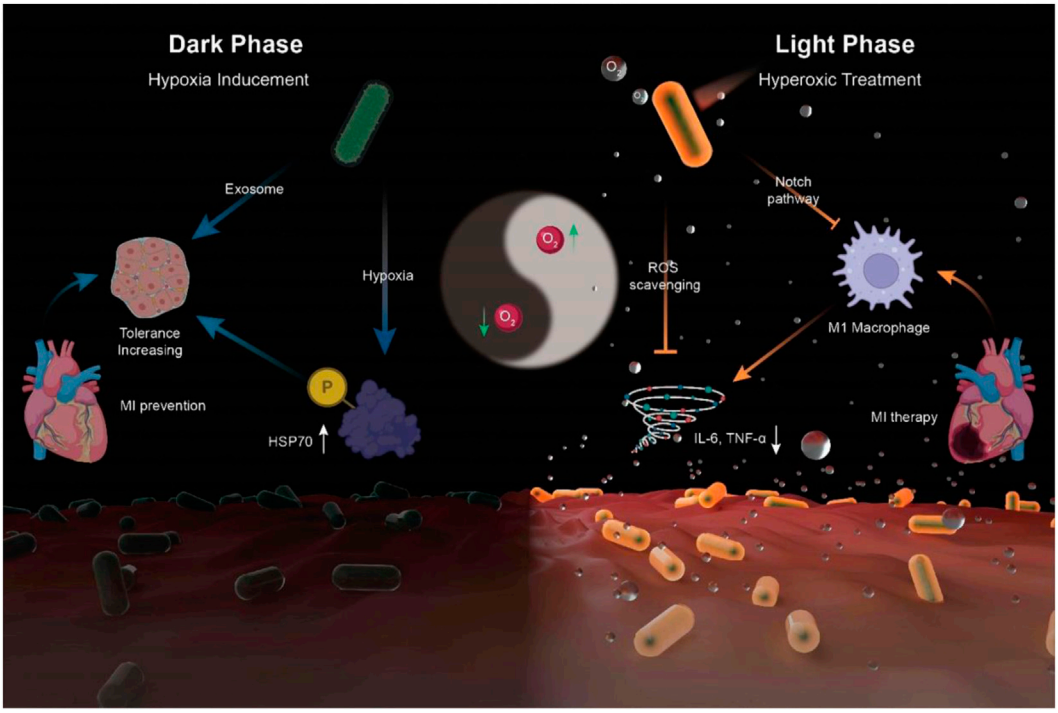

FIGURE 9
Synthesis of UCCy@Gel for acute MI prevention (dark phase) and therapy (light phase): the UCCy@Gel consumes oxygen *via* respiration to generate a hypoxic microenvironment, resulting in the upregulation of HSP70, which enhanced the tolerance of CMs for MI (left); Under 980 nm NIR irradiation, the UCCy@Gel releases photosynthetic oxygen through UCL to inhibit macrophage M1 polarization and downregulated proinflammatory cytokines IL-6 and TNF-α to repair myocardial injury (right) (Liu Y. et al., 2022).

materials. This method also has a very good gelation speed, so the problems of fast and slow gelation mentioned in the temperature section do not exist for this method. Another advantage of such gels is that they reduce the effect of shear force on cells.

The network structure of the hydrogel in these cases comprises stimuli-responsive moieties that permit prompted and reversible conversion from hydrogel to sol or solid states. For instance, metal ion cross-linked poly (acrylic acid) (pAAc) forms a metal–carboxylate hydrogel that exhibited a light-induced transformation into the sol state. Likewise, a pH-sensitive hydrogel was synthesized using the interaction between the polymer chains functionalized with catechol and boronic acid moieties. Under alkaline conditions, a three-dimensional hydrogelator network was generated by the crosslinking of polymeric chains with boronate–catechol complexes, whereas upon acidification of the hydrogel phase separation took place as a result of the hydrolysis of the boronate ester. Furthermore, the mechanical properties of stimuli-sensitive hydrogels and nanogels can be tuned. The covalent crosslinking of polymeric chains with various bridging molecules or with stimuli sensitive crosslinkers produces stable hydrogels. The dissociation of the crosslinker using various stimuli decreases the stiffness of the hydrogel. Hence by the reversible association and dissociation of the stimuli-sensitive crosslinkers, the hydrogels can be reversibly swapped between upper and lower rigidity (Roy et al., 2022).

Another significant and readily measurable method to represent the self-healing ability is the dynamic rheology test. The amplitude sweep measurement was performed firstly in order to ascertain the linear viscoelastic region of the hydrogel and find out the critical strain value required to break the hydrogel network (Chen et al., 2020). An important factor for injectability from the rheology data is whether the hydrogel is shear-thinning. Shear-thinning hydrogels experience decreases in viscosity upon application of shear, which are enabled by reversible cross-linking mechanisms. Hydrogels with a lower viscosity and lower storage and loss moduli are typically easier to inject than hydrogels of a high viscosity and high storage and loss moduli (Chen et al., 2017).

These materials have many potential applications in the field of tissue engineering. Yan and colleagues studied how shear-thinning and self-healing occur in β-hairpin peptide-based gels. During the injection, the network was divided into gels larger than 200 nm, which penetrated quickly after the shear was completed, and thus the gel was restored. It was also found that the period and speed of shear are effective on the speed of repair and the stiffness of the gel afterward, and in addition, the injection has little effect on cell viability and distribution (Yan et al., 2010).

The repair process in some materials can occur by a mechanism called Dock and Lock. In the complex, the component derived from the R subunit of the protein kinase A family (which can exist in two types, I and II, in PKA isozymes, and each type has two isoforms, α, and β) dimerizes during the docking phase. And then another component derived from A-kinase anchoring protein that anchors them with high specificity is called the lock stage.

Lu and his colleagues conducted research in this field in which the primary component was attached to both ends of a polypeptide,

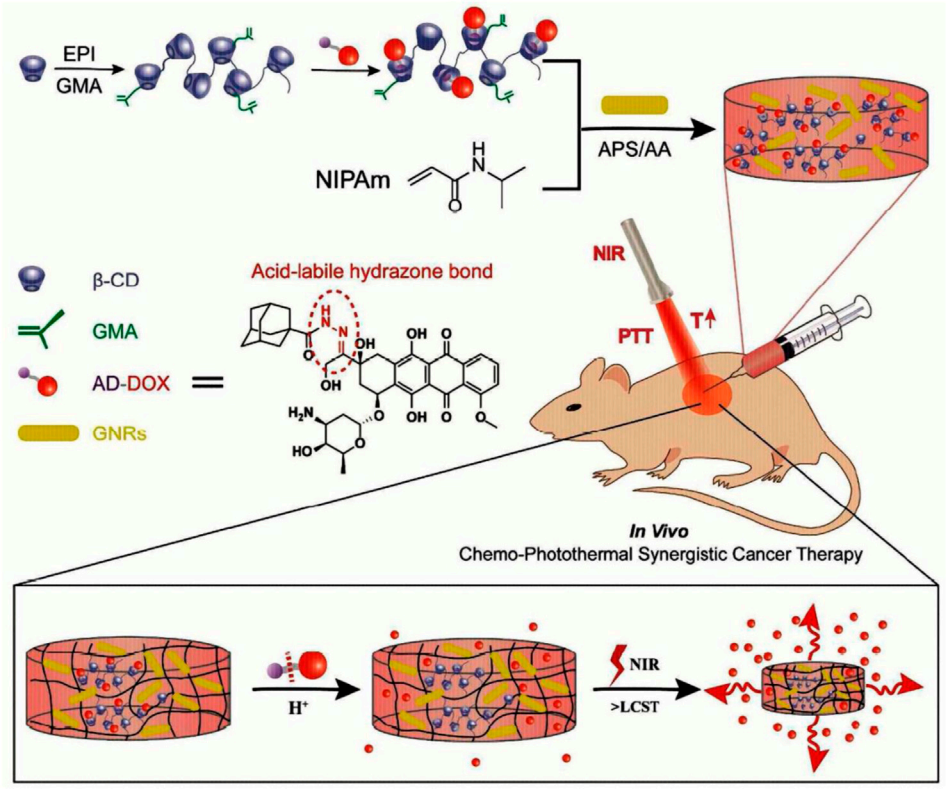

FIGURE 10
Formation of injectable, NIR/pH-responsive nanocomposite hydrogel and chemo-photothermal synergistic cancer therapy. Reprinted with permission from (Xu et al., 2017). Copyright 2017 American Chemical Society.

and the secondary component was attached to the ends of a 4- or 8-arm PEG cross-linker by mixing the two a strong gel formed with physical links between two components. This gel was used to deliver stem cells and large molecules during erosion, and it had a high percentage of survival and compatibility for the cells. The gels' mechanical properties and erosion speed could be adjusted with the peptide sequence of the second component, the concentration and ratio of each component, and the number of peptides in the cross-linking polymer. Adequate gelation speed, homogeneous encapsulation of the cargo, and repeatability of the reaction were among the advantages of this system (Lu et al., 2012).

Zhang and his colleagues created a stable ferrofluid by dispersing Fe_3O_4 nanoparticles in a chitosan solution, which was mixed with an organic solution of PEG to form a gel by creating a Schiff-Base dynamic side bond between the two. The link was broken during the injection and then repaired in this material. Collecting parts for repair could be done by magnetic force. Also, by magnetic conduction, the gel could pass through the channels by changing its shape while maintaining its integrity (Zhang et al., 2012).

Wang and his colleagues prepared a material based on elastin-like protein (ELP) and hyaluronic acid, in which the formation of the secondary network of ELP by changing the temperature during injection reduced the erosion rate and long-term stability. This gel provided good mechanical protection of stem cells during injection, had good cell adhesion, and was degradable (Wang et al., 2017).

Qu and his colleagues developed a shear thin-self-heal hydrogel based on chitosan and PEG for the treatment of liver cell cancer, which was established between the two components of the Schiff-base bond, which was dissociated by changing the pH, the gel was degraded, and as a result, the DOX drug content was released. The drug-free gel was non-toxic to L929 and HepG2 cells. Gelation time, storage modulus, and degradation were adjustable with cross-linker concentration (Qu et al., 2017).

Wang and colleagues developed a diabetic wound-healing gel (FEMI) susceptible to multidrug-resistant bacterial infection, hyperglycemia, and an oxidative environment. They used MnO_2 nanosheets coated with ε-polylysine (EPL) and self-assembled micelles of Pluronic F127 aldehyde containing insulin (FCHO), which formed a Schiff-base bond between them (Figure 11). During reaction $H_2O_2 + MnO_2 \rightarrow H_2O + O_2 + Mn^{2+}$, MnO_{2s} nano-enzymes continuously supplied O_2 by converting endogenous H_2O_2 to O_2 while reducing the intensity of environmental oxidation. The pH- and redox-responsive gel had long-term insulin release with temporal and spatial control in oxidative and acidic skin conditions. Coated nanoplates in the gel and their interaction with the matrix caused the material's rapid gelation and stable rheological properties. Fast gelation and tissue adhesion properties caused a good hemostatic application in the gel. Also, the presence of ε-polylysine with a positive charge and nano-enzymes brings antimicrobial properties to the gel. This gel accelerated cell proliferation, facilitated angiogenesis, increased granulation tissue

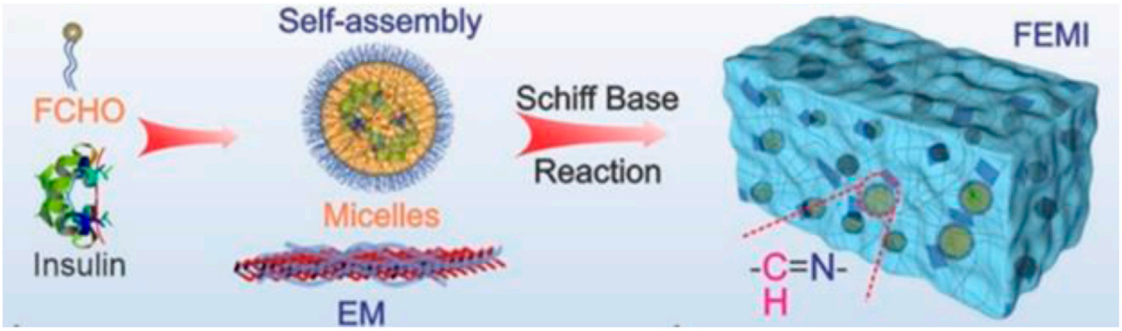

FIGURE 11
Components of the gel (Wang et al., 2020b). Reprinted with permission from (Wang et al., 2020b). Copyright 2020 American Chemical Society.

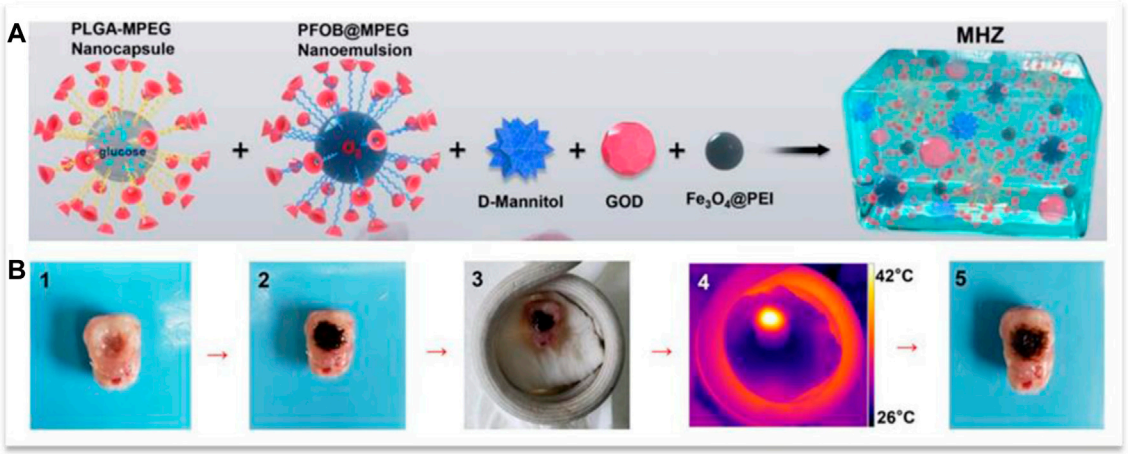

FIGURE 12
(A) the components of the gel and **(B)** its penetration into an isolated tumor during the application of a magnetic field. Reprinted with permission from (Wu et al., 2019). Copyright 2019 American Chemical Society.

formation and ECM deposition, re-epithelialization, and diabetic wound healing (Wang et al., 2020b).

Wu and his colleagues developed a gel containing PLGA nanocapsules containing glucose and perfluorooctyl bromide nanoemulsion containing O_2, which were connected to α-CD through methoxy polyethylene glycol blocks, D-Mannitol, GOD, and Fe3O4@PEI nanoparticles (Figure 12A). This gel produced heat by being placed under an alternating magnetic field by existing nanoparticles, which, in addition to the hyperthermia effect, led to a gel-sol phase transition and penetration into tumor cell spaces (Figure 12B), which is due to the presence of D-Mannitol, which causes Dehydration of the cell and its contraction could be intensified. Then, glucose and O_2 in the components and GOD together produced H_2O_2 during reaction $glucose + O_2 + H_2O \rightarrow gluconic\ acid + H_2O_2$. Then nanoparticles in this acidic environment accelerate the production of ·OH according to the Fenton $2H_2O_2 \rightarrow HO. + HOO. + H_2O$ reaction, which increases the oxidative stress of the tumor and damages the heat shock protein 70, which is highly expressed in hyperthermia. Hyperthermia itself increases the activity of nanoenzymes (Wu et al., 2019).

Wang et al. (2020a) developed a gel based on catechol functionalized chitosan and MnO2 nanosheets for treating skin cancer and multidrug-resistant (MDR) bacteria wound healing, which could self-assemble, and in addition, the nanosheets created an oxidative cross-link in it. This redox-responsive gel reduces the hypoxia in tumor areas with a high concentration of H2O2 by converting it to O2. In addition, increasing the level of O2 improves the effect of the DOX drug contained in the gel. On the other hand, nanosheets with a photothermal effect with good temporal and spatial control cause hyperthermia in the tumor, which can almost completely remove the tumor. In addition, due to the presence of positively charged chitosan and nano-knife-like MnO2 nanosheet, this gel can remove bacteria long-term by contacting them. In addition, with the destruction of the gel and due to the enzymatic effect of nanoplates, the consumption of ROS reduces inflammation and accelerates the proliferation of fibroblasts, and as a result, wound healing improves.

TABLE 1 Examples of gels formed by enzymes in the literature.

Enzyme	Gel	Example	Ref
transglutaminase	Protein hydrogels	a peptide derived from fibrin and factorXIII	Sanborn et al. (2002)
		elastin-like polypeptide	McHale et al. (2005)
HRP	Polysacharide hydrogels	dextran-tyramine	Jin et al. (2010a)
		hyaluronic acid-g-dextran-tyramine	Jin et al. (2010a)
		poly (g-propargyl-Lglutamate)-azide-modified mannose-3-(4-hydroxyphenyl) propanamide	Ren et al. (2015)
		Serotonin-Chondroitin sulfate	Zhang et al. (2021)

TABLE 2 A summary of the characteristics of the gels formed by the action of different stimuli.

Type of stimuli	Gelation mechanism	Advantage	Disadvantage	Gelation speed	Most used polymers
temperature	LCST: Reduction of polymer-water interaction and increase of polymer-polymer hydrophobic interaction with increasing temperature	Control of drug release with volume changes	The possibility of toxicity and non-degradability of the gel and blocking the syringe during injection	high	LCST: PNIPAM
	Thermoreversible: micellization due to polymer-polymer interaction and then establishing a link between micelles				Thermoreversible: pluronic
pH	Removal of positive covalent charges and formation of hydrogen bonds between amine groups with increasing pH	The possibility of using to treat cancer and inflammation due to the special ph of these diseases	The possibility of inflammation due to the acidic pH of the sol	less than the temperature stimulus	chitosan
ion	Establishing an ionic bond between the anion resulting from the dissolution of polymers and some special cations		Low cell adhesion	less than the temperature stimulus	Alginate, pectin
			Low degradation rate of alginate		
enzyme	Accelerating the creation of bonds between biomolecules by enzymes	Biocompatibility			Some protein and polysaccharide polymers
		Mild temperature and ph conditions			
		Low toxicity			
photo	The transformation of the primary substance into a free radical and its propagation	Controlling the time and place of radiation	The possibility of damage to the cargo due to the increase in temperature caused by the high gelation speed, damage to the DNA of the cell due to the presence of UV light and free radicals, and the limitation of use due to the low penetration depth of UV light	Too high	Some acrylated polymers
Shear stress	Viscosity increase and heal with the end of injection shear stress	Long life of gel due to self-healing, the low effect of injection shear stress on cells		good	

As an alternative to conventional surgical closure or implant fixation methods (sutures, staples, meshes, and grafts), Zhou and colleagues prepared surgical sealants based on ECM-derived biopolymers gelatin and chondroitin sulfate, which have a Schiff-base dynamic bond under shear and adhesive properties. This gel can reattach torn tissues, close bleeding wounds, leak fluids, and laparoscopic surgery sealant in elastic tissues. This gel had good biocompatibility, biodegradability, and elasticity. Besides, it was economical and easy to synthesize and use. The Schiff-Base bond and hydrogen bond between gel and tissue at body temperature could be weakened by lowering the temperature to 20°C and causing gel separation. The concentration of the gel and the degree of oxidation of chondroitin sulfate could adjust the hydrogel's mechanical properties and adhesion strength (Zhou et al., 2021). Table 2 presents a summary of the characteristics of the gels formed by the action of different stimuli.

Summary, challenges and future perspective

Smart injectable gels are polymer networks containing a fluid that can be injected into the body in a solution state and then turned into a gel due to the effect of a stimulus *in situ*. The most important advantage of these materials is the delivery of therapeutic agents in a process with minimal invasiveness. The process of gelation of these materials can be under changing conditions inside the body, that is, with hydrophobic interactions during temperature changes, ionization of polymer side chains with pH changes, creation of ionic bonds with changes in the concentration of polyvalent ions, Or the application of external stimuli, i.e., light radiation, reduction of shear stress and increase of gel viscosity, generation of heat in the temperature-responsive gel by nanoparticles under magnetic field, or biological stimulation of transglutaminase enzymes can cause gel formation. Each method has its characteristics, advantages, and disadvantages, which this article discusses.

Despite the many advantages of these materials in medical applications, their properties can be improved by considering some things. First of all, like other biomaterials, in the design of gels, we must pay attention to the compatibility of the gel with sensitive cells to remain healthy and maintain their proliferation, as well as compatibility with sensitive molecules such as DNA, oligonucleotides, proteins, and peptides to maintain activity them and not to denature them. Also, degradation products, remaining components, and catalysts or cross-linkers that have not reacted should be investigated in terms of causing cytotoxicity. Also, the interactions between the material and the host tissue should be considered to prevent inflammation. To help the proteolytic degradation of the gel, the remodeling phenomenon, and the penetration of cells due to the signals secreted from the cell, it is possible to use peptides sensitive to matrix metalloproteinase in the gel, inspired by the biological phenomena. In addition, regarding degradable materials, it should be noted that the rate of degradation in the drug delivery application should be adjusted according to the rate of release of the drug in our consideration and the application of tissue engineering according to the rate of formation of new tissue.

Rheology is the following important parameter in the development of gels. If the viscosity of the material is lower than a certain limit, the gelation speed decreases. On the other hand, gels with high viscosity require more force for injection, which is unpleasant for both the patient and the operator. Also, using this method for deep target locations that require long transportation of materials in the catheter is impossible. In this context, using a two-syringe tool shortens the transfer distance, but there is a possibility of accidental changes in viscoelasticity or phase separation due to the reaction or interaction of the mixing components in this case. The rheology of these materials must be carefully adjusted so that the material flow is homogeneous. Mechanical properties are one of the other challenging areas, and to strengthen this property in gels, stronger gels, which probably have more compact networks, can be used. However, in this case, it is harder to penetrate the interface of the extruded flows, and the possibility of creating a homogeneous network is less. On the other hand, the desired gel must have good flexibility to remain intact after reorganizing the infiltrating cells.

The phase transition behavior of a copolymer system may change upon the addition of drugs, cells, or even a cell culture medium. In addition, the release of cells and GFs, and drugs at the desired place and time is still a remarkable field. Among the shortcomings of the hydrogels made so far, we can mention their short half-life. Also, delivery to the target location will not be suitable for multiple injections. In addition, in natural polymers, there is a possibility of changes between different batches and, as a result, properties with a change of origin. Increasing the concentration of GF for human use is another challenge.

Developing these materials leads to producing new materials with complex formulations that have safety risks and low repeatability of properties. Therefore, it is always necessary to use simple formulations along with simple manufacturing methods. Despite this issue, hybrid hydrogels, composite systems with nano or microparticles containing drugs or proteins, materials responsive to multiple stimuli, and hydrogels with the ability to identify biomolecules have unique properties that can be used to solve many challenges have been mentioned.

Recent publications on hydrogel research reveal complex polymers with several parts. In the envisioned application, each component has a specific function. A hydrogel, for example, having diverse properties (e.g., hydrophilic and hydrophobic monomers) exhibits distinct surface qualities. Another polymer can be grafted onto the surface of a hydrogel to alter its surface characteristics. Another method to change surface properties is to physically alter the gel surface. The order of the monomer units in a hydrogel can also be altered, as can the cross-linking process. The mechanical properties of a hydrogel are directly affected by cross-linking. These alterations can have an impact on the hydrogel's physical qualities as well as its biodegradability. Combinatorial synthesis can be employed because it might be challenging to find the ideal monomer sequence or the right combination of cross-links to produce the required properties. In combinatorial synthesis, a wide range of monomers, modifiers, cross-linkers, and other components can be used. The majority of current research, as shown by recently published studies, integrates various modification procedures to produce a single hydrogel with as many desired properties as possible. Due to compatibility issues, however, it is not straightforward or simple to combine different approaches. The absence of commercially viable hydrogel products necessitates new research efforts and the continuation of existing hydrogel programs.

Author contributions

SS, SN, and HG wrote the manuscript. SG and WZ revised and enriched the paper.

Funding

This work was supported by the National Key R&D Project of China (2018YFA0704103, 2018YFA0704104) and Fundamental Research Funds for the Central Universities (DUT22YG123, DUT21TD105).

Conflict of interest

The authors declare that the research was conducted in the absence of any commercial or financial relationships that could be construed as a potential conflict of interest.

Publisher's note

References

Amina, S. J., and Guo, B. (2020). A review on the synthesis and functionalization of gold nanoparticles as a drug delivery vehicle. *Int. J. Nanomedicine* 15, 9823–9857. doi:10.2147/ijn.s279094

Anderson, A. J., Culver, H. R., Bryant, S. J., and Bowman, C. N. (2020). Viscoelastic and thermoreversible networks crosslinked by non-covalent interactions between "clickable" nucleic acid oligomers and DNA. *Polym. Chem.* 11, 2959–2968. doi:10.1039/d0py00165a

Ayoubi-Joshaghani, M. H., Seidi, K., Azizi, M., Jaymand, M., Javaheri, T., Jahanban-Esfahlan, R., et al. (2020). Potential applications of advanced nano/hydrogels in biomedicine: Static, dynamic, multi-stage, and bioinspired. *Adv. Funct. Mat.* 30, 2004098. doi:10.1002/adfm.202004098

Bai, X., Sun, Q., Cui, H., Guerzoni, L. P. B., Wuttke, S., Kiessling, F., et al. (2022). Controlled covalent self-assembly of a homopolymer for multiscale materials engineering. *Adv. Mat.* 34, 2109701. doi:10.1002/adma.202109701

Bertsch, P., Diba, M., Mooney, D. J., and Leeuwenburgh, S. C. G. (2022). Self-healing injectable hydrogels for tissue regeneration. *Chem. Rev.* 123, 834–873. doi:10.1021/acs.chemrev.2c00179

Boustta, M., Colombo, P. E., Lenglet, S., Poujol, S., and Vert, M. (2014). Versatile UCST-based thermoresponsive hydrogels for loco-regional sustained drug delivery. *J. Control. Release* 174, 1–6. doi:10.1016/j.jconrel.2013.10.040

Cao, J., Huang, D., and Peppas, N. A. (2020). Advanced engineered nanoparticulate platforms to address key biological barriers for delivering chemotherapeutic agents to target sites. *Adv. Drug Deliv. Rev.* 167, 170–188. doi:10.1016/j.addr.2020.06.030

Cao, L., Fan, J., Huang, J., and Chen, Y. (2019). A robust and stretchable cross-linked rubber network with recyclable and self-healable capabilities based on dynamic covalent bonds. *J. Mat. Chem. A* 7, 4922–4933. doi:10.1039/c8ta11587g

Cao, M., Wang, Y., Hu, X., Gong, H., Li, R., Cox, H., et al. (2019). Reversible thermoresponsive peptide-PNIPAM hydrogels for controlled drug delivery. *Biomacromolecules* 20, 3601–3610. doi:10.1021/acs.biomac.9b01009

Chang, W., Tai, A., Tsai, N., and Li, Y. E. (2021). 可注射性明胶甲基丙烯酰基(GelMA)/苯基杂化材料.

Chen, J., Li, F., Luo, Y., Shi, Y., Ma, X., Zhang, M., et al. (2019). A self-healing elastomer based on an intrinsic non-covalent cross-linking mechanism. *J. Mat. Chem. A* 7, 15207–15214. doi:10.1039/c9ta03775f

Chen, M. H., Wang, L. L., Chung, J. J., Kim, Y. H., Atluri, P., and Burdick, J. A. (2017). Methods to assess shear-thinning hydrogels for application as injectable biomaterials. *ACS Biomater. Sci. Eng.* 3, 3146–3160. doi:10.1021/acsbiomaterials.7b00734

Chen, Y. Y., Wu, H. C., Sun, J. S., Dong, G. C., and Wang, T. W. (2013). Injectable and thermoresponsive self-assembled nanocomposite hydrogel for long-term anticancer drug delivery. *Langmuir* 29, 3721–3729. doi:10.1021/la400268p

Chen, Y., Zhang, R., Zheng, B., Cai, C., Chen, Z., Li, H., et al. (2020). A biocompatible, stimuli-responsive, and injectable hydrogel with triple dynamic bonds. *Molecules* 25, 3050. doi:10.3390/molecules25133050

Chenite, A., Chaput, C., Wang, D., Combes, C., Buschmann, M. D., Hoemann, C. D., et al. (2000). Novel injectable neutral solutions of chitosan form biodegradable gels *in situ*. *Biomaterials* 21, 2155–2161. doi:10.1016/S0142-9612(00)00116-2

Chiu, Y. L., Chen, S. C., Su, C. J., Hsiao, C. W., Chen, Y. M., Chen, H. L., et al. (2009). pH-triggered injectable hydrogels prepared from aqueous N-palmitoyl chitosan: *In vitro* characteristics and *in vivo* biocompatibility. *Biomaterials* 30, 4877–4888. doi:10.1016/j.biomaterials.2009.05.052

Cho, J. H., Kim, S. H., Park, K. D., Jung, M. C., Yang, W. I., Han, S. W., et al. (2004). Chondrogenic differentiation of human mesenchymal stem cells using a thermosensitive poly(N-isopropylacrylamide) and water-soluble chitosan copolymer. *Biomaterials* 25, 5743–5751. doi:10.1016/j.biomaterials.2004.01.051

Choi, B. G., Park, M. H., Cho, S. H., Joo, M. K., Oh, H. J., Kim, E. H., et al. (2010). *In situ* thermal gelling polypeptide for chondrocytes 3D culture. *Biomaterials* 31, 9266–9272. doi:10.1016/j.biomaterials.2010.08.067

Chung, H. J., Lee, Y., and Park, T. G. (2008). Thermo-sensitive and biodegradable hydrogels based on stereocomplexed Pluronic multi-block copolymers for controlled protein delivery. *J. Control. Release* 127, 22–30. doi:10.1016/j.jconrel.2007.12.008

Cimen, Z., Babadag, S., Odabas, S., Altuntas, S., Demirel, G., and Demirel, G. B. (2021). Injectable and self-healable pH-responsive gelatin–PEG/laponite hybrid hydrogels as long-acting implants for local cancer treatment. *ACS Appl. Polym. Mat.* 3, 3504–3518. doi:10.1021/acsapm.1c00419

Curreri, A. M., Mitragotri, S., and Tanner, E. E. L. (2021). Recent advances in ionic liquids in biomedicine. *Adv. Sci.* 8, 2004819. doi:10.1002/advs.202004819

Dalir Abdolahinia, E., Barati, G., Ranjbar-Navazi, Z., Kadkhoda, J., Islami, M., Hashemzadeh, N., et al. (2022). Application of nanogels as drug delivery systems in multicellular spheroid tumor model. *J. Drug Deliv. Sci. Technol.* 68, 103109. doi:10.1016/j.jddst.2022.103109

de Araújo, D. R., Ribeiro, L. N., and de Paula, E. (2019). Lipid-based carriers for the delivery of local anesthetics. *Expert Opin. Drug Deliv.* 16, 701–714. doi:10.1080/17425247.2019.1629415

Deus, I. A., Mano, J. F., and Custódio, C. A. (2020). Perinatal tissues and cells in tissue engineering and regenerative medicine. *Acta Biomater.* 110, 1–14. doi:10.1016/j.actbio.2020.04.035

Douglas, A. T. E. L., Dziadek, M., Boone, M., Declercq, H. A., Coenye, T., Vervaet, C., et al. (2018). Pectin-bioactive glass self-gelling, injectable composites with high antibacterial activity. *Carbohydr. Polym.* 205, 427–436. doi:10.1016/j.carbpol.2018.10.061

Elisseeff, J., Anseth, K., Sims, D., Mcintosh, W., Randolph, M., and Langer, R. (1999). Transdermal photopolymerization for minimally invasive implantation. *Proc. Natl. Acad. Sci. U. S. A.* 96, 3104–3107. doi:10.1073/pnas.96.6.3104

Gačanin, J., Synatschke, C. V., and Weil, T. (2020). Biomedical applications of DNA-based hydrogels. *Adv. Funct. Mat.* 30, 1906253. doi:10.1002/adfm.201906253

Ghazinezhad, M., Bozorgian, A., and Gholami Dastnaei, P. (2022). A review of frontal polymerization in the chemical industry. *Int. J. New Chem.* 9, 623–646. doi:10.22034/IJNC.2022.4.12

Hsiao, M. H., Larsson, M., Larsson, A., Evenbratt, H., Chen, Y. Y., Chen, Y. Y., et al. (2012). Design and characterization of a novel amphiphilic chitosan nanocapsule-based thermo-gelling biogel with sustained *in vivo* release of the hydrophilic anti-epilepsy drug ethosuximide. *J. Control. Release* 161, 942–948. doi:10.1016/j.jconrel.2012.05.038

Huang, C., Hu, X., Hou, Z., Ji, J., Li, Z., and Luan, Y. (2019). Tailored graphene oxide-doxorubicin nanovehicles via near-infrared dye-lactobionic acid conjugates for chemo-photothermal therapy. *J. Colloid Interface Sci.* 545, 172–183. doi:10.1016/j.jcis.2019.03.019

Huang, J., Zhang, X., Fu, K., Wei, G., and Su, Z. (2021). Stimulus-responsive nanomaterials under physical regulation for biomedical applications. *J. Mat. Chem. B* 9, 9642–9657. doi:10.1039/D1TB02130C

Ishihara, K., Oda, H., and Konno, T. (2020). Spontaneously and reversibly forming phospholipid polymer hydrogels as a matrix for cell engineering. *Biomaterials* 230, 119628. doi:10.1016/j.biomaterials.2019.119628

Jiang, B., Liu, X., Yang, C., Yang, Z., Luo, J., Kou, S., et al. (2022). Injectable, photoresponsive hydrogels for delivering neuroprotective proteins enabled by metal-directed protein assembly. *Sci. Adv.* 6, eabc4824. doi:10.1126/sciadv.abc4824

Jin, R., Moreira Teixeira, L. S., Dijkstra, P. J., van Blitterswijk, C. A., Karperien, M., and Feijen, J. (2010a). Enzymatically-crosslinked injectable hydrogels based on biomimetic dextran-hyaluronic acid conjugates for cartilage tissue engineering. *Biomaterials* 31, 3103–3113. doi:10.1016/j.biomaterials.2010.01.013

Jin, R., Moreira Teixeira, L. S., Dijkstra, P. J., Zhong, Z., Van Blitterswijk, C. A., Karperien, M., et al. (2010b). Enzymatically crosslinked dextran-tyramine hydrogels as injectable scaffolds for cartilage tissue engineering. *Tissue Eng. - Part A* 16, 2429–2440. doi:10.1089/ten.tea.2009.0764

Kawano, T., Niidome, Y., Mori, T., Katayama, Y., and Niidome, T. (2009). PNIPAM gel-coated gold nanorods for targeted delivery responding to a near-infrared laser. *Bioconjug Chem.* 20, 209–212. doi:10.1021/bc800480k

Ko, D. Y., Shinde, U. P., Yeon, B., and Jeong, B. (2013). Recent progress of *in situ* formed gels for biomedical applications. *Prog. Polym. Sci.* 38, 672–701. doi:10.1016/j.progpolymsci.2012.08.002

Kuang, L., Ma, X., Ma, Y., Yao, Y., Tariq, M., Yuan, Y., et al. (2019). Self-assembled injectable nanocomposite hydrogels coordinated by *in situ* generated CaP nanoparticles for bone regeneration. *ACS Appl. Mat. Interfaces* 11, 17234–17246. doi:10.1021/acsami.9b03173

Kurian, A. G., Singh, R. K., Patel, K. D., Lee, J.-H., and Kim, H.-W. (2022). Multifunctional GelMA platforms with nanomaterials for advanced tissue therapeutics. *Bioact. Mat.* 8, 267–295. doi:10.1016/j.bioactmat.2021.06.027

Le, T. M. D., Duong, H. T. T., Thambi, T., Giang Phan, V. H., Jeong, J. H., and Lee, D. S. (2018). Bioinspired pH- and temperature-responsive injectable adhesive hydrogels

with polyplexes promotes skin wound healing. *Biomacromolecules* 19, 3536–3548. doi:10.1021/acs.biomac.8b00819

Lee, W. Y., Chang, Y. H., Yeh, Y. C., Chen, C. H., Lin, K. M., Huang, C. C., et al. (2009). The use of injectable spherically symmetric cell aggregates self-assembled in a thermo-responsive hydrogel for enhanced cell transplantation. *Biomaterials* 30, 5505–5513. doi:10.1016/j.biomaterials.2009.07.006

Li, L., Gu, J., Zhang, J., Xie, Z., Lu, Y., Shen, L., et al. (2015). Injectable and biodegradable pH-responsive hydrogels for localized and sustained treatment of human fibrosarcoma. *ACS Appl. Mat. Interfaces* 7, 8033–8040. doi:10.1021/acsami.5b00389

Lim, K. S., Klotz, B. J., Lindberg, G. C. J., Melchels, F. P. W., Hooper, G. J., Malda, J., et al. (2019). Visible light cross-linking of gelatin hydrogels offers an enhanced cell microenvironment with improved light penetration depth. *Macromol. Biosci.* 19, 1900098. doi:10.1002/mabi.201900098

Litowczenko, J., Gapiński, J., Markiewicz, R., Woźniak, A., Wychowaniec, J. K., Peplińska, B., et al. (2021). Synthesis, characterization and *in vitro* cytotoxicity studies of poly-N-isopropyl acrylamide gel nanoparticles and films. *Mat. Sci. Eng. C* 118, 111507. doi:10.1016/j.msec.2020.111507

Liu, J.-D., Du, X.-Y., Wang, C.-F., Li, Q., and Chen, S. (2020). Construction of triple non-covalent interaction-based ultra-strong self-healing polymeric gels via frontal polymerization. *J. Mat. Chem. C* 8, 14083–14091. doi:10.1039/d0tc02986f

Liu, X., Wang, S., Shi, W., and Liu, H. (2022). Thermo-/pH-Dual-Sensitive PEG/PAMAM nanogel: Reaction dynamics and plugging application of CO2 channeling. *Gels* 8, 683. doi:10.3390/gels8100683

Liu, Y., Zhong, D., He, Y., Jiang, J., Xie, W., Tang, Z., et al. (2022). Photoresponsive hydrogel-coated upconversion cyanobacteria nanocapsules for myocardial infarction prevention and treatment. *Adv. Sci.* 9, 2202920. doi:10.1002/advs.202202920

Lu, H. D., Charati, M. B., Kim, I. L., and Burdick, J. A. (2012). Injectable shear-thinning hydrogels engineered with a self-assembling Dock-and-Lock mechanism. *Biomaterials* 33, 2145–2153. doi:10.1016/j.biomaterials.2011.11.076

Ma, X., Li, S.-J., Liu, Y., Zhang, T., Xue, P., Kang, Y., et al. (2022). Bioengineered nanogels for cancer immunotherapy. *Chem. Soc. Rev.* 51, 5136–5174. doi:10.1039/D2CS00247G

Marco-Dufort, B., and Tibbitt, M. W. (2019). Design of moldable hydrogels for biomedical applications using dynamic covalent boronic esters. *Mat. Today Chem.* 12, 16–33. doi:10.1016/j.mtchem.2018.12.001

Matanović, M. R., Kristl, J., and Grabnar, P. A. (2014). Thermoresponsive polymers: Insights into decisive hydrogel characteristics, mechanisms of gelation, and promising biomedical applications. *Int. J. Pharm.* 472, 262–275. doi:10.1016/j.ijpharm.2014.06.029

McHale, M. K., Setton, L. A., and Chilkoti, A. (2005). Synthesis and *in vitro* evaluation of enzymatically cross-linked elastin-like polypeptide gels for cartilaginous tissue repair. *Tissue Eng.* 11, 1768–1779. doi:10.1089/ten.2005.11.1768

Mellati, A., Hasanzadeh, E., Gholipourmalekabadi, M., and Enderami, S. E. (2021). Injectable nanocomposite hydrogels as an emerging platform for biomedical applications: A review. *Mat. Sci. Eng. C* 131, 112489. doi:10.1016/j.msec.2021.112489

Mohammad, N. F., Ahmad, R. N., Rosli, N. L. M., Manan, M. S. A., Marzuki, M., and Wahi, A. (2021). Sol gel deposited hydroxyapatite-based coating technique on porous titanium niobium for biomedical applications: A mini review. *Mat. Today Proc.* 41, 127–135. doi:10.1016/j.matpr.2020.11.1023

Nagasaki, Y. (2018). Design and application of redox polymers for nanomedicine. *Polym. J.* 50, 821–836. doi:10.1038/s41428-018-0054-6

Nettles, D. L., Vail, T. P., Morgan, M. T., Grinstaff, M. W., and Setton, L. A. (2004). Photocrosslinkable hyaluronan as a scaffold for articular cartilage repair. *Ann. Biomed. Eng.* 32, 391–397. doi:10.1023/B:ABME.0000017552.65260.94

Nguyen, D. T., Phan, V. H. G., Lee, D. S., Thambi, T., and Huynh, D. P. (2019). Bioresorbable pH- and temperature-responsive injectable hydrogels-incorporating electrosprayed particles for the sustained release of insulin. *Polym. Degrad. Stab.* 162, 36–46. doi:10.1016/j.polymdegradstab.2019.02.013

Pang, M., Huang, Y., Meng, F., Zhuang, Y., Liu, H., Du, M., et al. (2020). Application of bacterial cellulose in skin and bone tissue engineering. *Eur. Polym. J.* 122, 109365. doi:10.1016/j.eurpolymj.2019.109365

Peppas, N. A., and Mikos, A. G. (2019). "Preparation methods and structure of hydrogels," in *Hydrogels in medicine and pharmacy* (Florida: CRC Press), 1–26.

Podgórski, M., Fairbanks, B. D., Kirkpatrick, B. E., McBride, M., Martinez, A., Dobson, A., et al. (2020). Toward stimuli-responsive dynamic thermosets through continuous development and improvements in covalent adaptable networks (CANs). *Adv. Mat.* 32, 1906876. doi:10.1002/adma.201906876

Qi, C., Liu, J., Jin, Y., Xu, L., Wang, G., Wang, Z., et al. (2018). Photo-crosslinkable, injectable sericin hydrogel as 3D biomimetic extracellular matrix for minimally invasive repairing cartilage. *Biomaterials* 163, 89–104. doi:10.1016/j.biomaterials.2018.02.016

Qu, J., Zhao, X., Ma, P. X., and Guo, B. (2017). pH-responsive self-healing injectable hydrogel based on N-carboxyethyl chitosan for hepatocellular carcinoma therapy. *Acta Biomater.* 58, 168–180. doi:10.1016/j.actbio.2017.06.001

Rabiee, N., Rabiee, M., Bagherzadeh, M., and Hamblin, M. R. (2019). "Stimuli-responsive polymers: Recent advances," in *Stimuli-responsive polym. Nano-Dimension* (Bristol: IOPscience). 44.

Rajabi, M., McConnell, M., Cabral, J., and Ali, M. A. (2021). Chitosan hydrogels in 3D printing for biomedical applications. *Carbohydr. Polym.* 260, 117768. doi:10.1016/j.carbpol.2021.117768

Ren, K., He, C., Xiao, C., Li, G., and Chen, X. (2015). Injectable glycopolypeptide hydrogels as biomimetic scaffolds forcartilage tissue engineering. *Biomaterials* 51, 238–249. doi:10.1016/j.biomaterials.2015.02.026

Roy, A., Manna, K., and Pal, S. (2022). Recent advances in various stimuli-responsive hydrogels: From synthetic designs to emerging healthcare applications. *Mat. Chem. Front.* 6, 2338–2385. doi:10.1039/d2qm00469k

Sabourian, P., Tavakolian, M., Yazdani, H., Frounchi, M., van de Ven, T. G. M., Maysinger, D., et al. (2020). Stimuli-responsive chitosan as an advantageous platform for efficient delivery of bioactive agents. *J. Control. Release* 317, 216–231. doi:10.1016/j.jconrel.2019.11.029

Sanborn, T. J., Messersmith, P. B., and Barron, A. E. (2002). *In situ* crosslinking of a biomimetic peptide-PEG hydrogel via thermally triggered activation of factor XIII. *Biomaterials* 23, 2703–2710. doi:10.1016/S0142-9612(02)00002-9

Shen, X., Li, S., Zhao, X., Han, J., Chen, J., Rao, Z., et al. (2023). Dual-crosslinked regenerative hydrogel for sutureless long-term repair of corneal defect. *Bioact. Mat.* 20, 434–448. doi:10.1016/j.bioactmat.2022.06.006

Shou, Y., Zhang, J., Yan, S., Xia, P., Xu, P., Li, G., et al. (2020). Thermoresponsive chitosan/DOPA-based hydrogel as an injectable therapy approach for tissue-adhesion and hemostasis. *ACS Biomater. Sci. Eng.* 6, 3619–3629. doi:10.1021/acsbiomaterials.0c00545

Sun, Z., Song, C., Wang, C., Hu, Y., and Wu, J. (2020). Hydrogel-based controlled drug delivery for cancer treatment: A review. *Mol. Pharm.* 17, 373–391. doi:10.1021/acs.molpharmaceut.9b01020

Taghipour, Y. D., Zarebkohan, A., Salehi, R., Rahimi, F., Torchilin, V. P., Hamblin, M. R., et al. (2022). An update on dual targeting strategy for cancer treatment. *J. Control. Release* 349, 67–96. doi:10.1016/j.jconrel.2022.06.044

Tan, G., Zhong, Y., Yang, L., Jiang, Y., Liu, J., and Ren, F. (2020). A multifunctional MOF-based nanohybrid as injectable implant platform for drug synergistic oral cancer therapy. *Chem. Eng. J.* 390, 124446. doi:10.1016/j.cej.2020.124446

Van Tomme, S. R., Van Steenbergen, M. J., De Smedt, S. C., Van Nostrum, C. F., and Hennink, W. E. (2005). Self-gelling hydrogels based on oppositely charged dextran microspheres. *Biomaterials* 26, 2129–2135. doi:10.1016/j.biomaterials.2004.05.035

Veloso, S. R. S., Andrade, R. G. D., and Castanheira, E. M. S. (2021). Review on the advancements of magnetic gels: Towards multifunctional magnetic liposome-hydrogel composites for biomedical applications. *Adv. Colloid Interface Sci.* 288, 102351. doi:10.1016/j.cis.2020.102351

Vong, L. B., Bui, T. Q., Tomita, T., Sakamoto, H., Hiramatsu, Y., and Nagasaki, Y. (2018). Novel angiogenesis therapeutics by redox injectable hydrogel - regulation of local nitric oxide generation for effective cardiovascular therapy. *Biomaterials* 167, 143–152. Elsevier Ltd. doi:10.1016/j.biomaterials.2018.03.023

Wang, H., Zhu, D., Paul, A., Cai, L., Enejder, A., Yang, F., et al. (2017). Covalently adaptable elastin-like protein–hyaluronic acid (ELP–HA) hybrid hydrogels with secondary thermoresponsive crosslinking for injectable stem cell delivery. *Adv. Funct. Mat.* 27, 1605609–1605611. doi:10.1002/adfm.201605609

Wang, J. H., Tsai, C. W., Tsai, N. Y., Chiang, C. Y., Lin, R. S., Pereira, R. F., et al. (2021). An injectable, dual crosslinkable hybrid pectin methacrylate (PECMA)/gelatin methacryloyl (GelMA) hydrogel for skin hemostasis applications. *Int. J. Biol. Macromol.* 185, 441–450. doi:10.1016/j.ijbiomac.2021.06.162

Wang, S., Zheng, H., Zhou, L., Cheng, F., Liu, Z., Zhang, H., et al. (2020a). Injectable redox and light responsive MnO2 hybrid hydrogel for simultaneous melanoma therapy and multidrug-resistant bacteria-infected wound healing. *Biomaterials* 260, 120314. doi:10.1016/j.biomaterials.2020.120314

Wang, S., Zheng, H., Zhou, L., Cheng, F., Liu, Z., Zhang, H., et al. (2020b). Nanoenzyme-reinforced injectable hydrogel for healing diabetic wounds infected with multidrug resistant bacteria. *Nano Lett.* 20, 5149–5158. doi:10.1021/acs.nanolett.0c01371

Wang, Y., Zhang, S., and Wang, J. (2021). Photo-crosslinkable hydrogel and its biological applications. *Chin. Chem. Lett.* 32, 1603–1614. doi:10.1016/j.cclet.2020.11.073

Wang, Z., Cui, H., Liu, M., Grage, S. L., Hoffmann, M., Sedghamiz, E., et al. (2022). Tough, transparent, 3D-printable, and self-healing poly (ethylene glycol)-gel (PEGgel). *Adv. Mat.* 34, 2107791. doi:10.1002/adma.202107791

Ward, M. A., and Georgiou, T. K. (2011). Thermoresponsive polymers for biomedical applications. *Polym. (Basel)* 3, 1215–1242. doi:10.3390/polym3031215

Wen, N., Jiang, B., Wang, X., Shang, Z., Jiang, D., Zhang, L., et al. (2020). Overview of polyvinyl alcohol nanocomposite hydrogels for electro-skin, actuator, supercapacitor and fuel cell. *Chem. Rec.* 20, 773–792. doi:10.1002/tcr.202000001

Wu, H., Liu, L., Song, L., Ma, M., Gu, N., and Zhang, Y. (2019). Enhanced tumor synergistic therapy by injectable magnetic hydrogel mediated generation of

hyperthermia and highly toxic reactive oxygen species. *ACS Nano* 13, 14013–14023. doi:10.1021/acsnano.9b06134

Wu, J., Chen, A., Qin, M., Huang, R., Zhang, G., Xue, B., et al. (2014). Hierarchical construction of a mechanically stable peptide-graphene oxide hybrid hydrogel for drug delivery and pulsatile triggered release *in vivo*. *Nanoscale* 7, 1655–1660. doi:10.1039/C4NR05798H

Wu, J., Chen, A., Qin, M., Huang, R., Zhang, G., Xue, B., et al. (2015). Hierarchical construction of a mechanically stable peptide-graphene oxide hybrid hydrogel for drug delivery and pulsatile triggered release *in vivo*. *Nanoscale* 7, 1655–1660. doi:10.1039/c4nr05798h

Wu, M., Chen, J., Huang, W., Yan, B., Peng, Q., Liu, J., et al. (2020). Injectable and self-healing nanocomposite hydrogels with ultrasensitive pH-responsiveness and tunable mechanical properties: Implications for controlled drug delivery. *Biomacromolecules* 21, 2409–2420. doi:10.1021/acs.biomac.0c00347

Xin, H., and Naficy, S. (2022). Drug delivery based on stimuli-responsive injectable hydrogels for breast cancer therapy: A review. *Gels* 8, 45–17. doi:10.3390/gels8010045

Xu, X., Huang, Z., Huang, Z., Zhang, X., He, S., Sun, X., et al. (2017). Injectable, NIR/pH-Responsive nanocomposite hydrogel as long-acting implant for chemophotothermal synergistic cancer therapy. *ACS Appl. Mat. Interfaces* 9, 20361–20375. doi:10.1021/acsami.7b02307

Xue, X., Hu, Y., Deng, Y., and Su, J. (2021). Recent advances in design of functional biocompatible hydrogels for bone tissue engineering. *Adv. Funct. Mat.* 31, 2009432. doi:10.1002/adfm.202009432

Yan, C., Altunbas, A., Yucel, T., Nagarkar, R. P., Schneider, J. P., and Pochan, D. J. (2010). Injectable solid hydrogel: Mechanism of shear-thinning and immediate recovery of injectable β-hairpin peptide hydrogels. *Soft Matter* 6, 5143–5156. doi:10.1039/c0sm00642d

Yang, J., Chen, Y., Zhao, L., Zhang, J., and Luo, H. (2022). Constructions and properties of physically cross-linked hydrogels based on natural polymers. *Polym. Rev.*, 1–39. doi:10.1080/15583724.2022.2137525

Yu, L., Chang, G. T., Zhang, H., and Ding, J. D. (2008). Injectable block copolymer hydrogels for sustained release of a PEGylated drug. *Int. J. Pharm.* 348, 95–106. doi:10.1016/j.ijpharm.2007.07.026

Yuan, Z., Ding, J., Zhang, Y., Huang, B., Song, Z., Meng, X., et al. (2022). Components, mechanisms and applications of stimuli-responsive polymer gels. *Eur. Polym. J.* 177, 111473. doi:10.1016/j.eurpolymj.2022.111473

Zainal, S. H., Mohd, N. H., Suhaili, N., Anuar, F. H., Lazim, A. M., and Othaman, R. (2021). Preparation of cellulose-based hydrogel: A review. *J. Mat. Res. Technol.* 10, 935–952. doi:10.1016/j.jmrt.2020.12.012

Zeimaran, E., Pourshahrestani, S., Fathi, A., bin Abd Razak, N. A., Kadri, N. A., Sheikhi, A., et al. (2021). Advances in bioactive glass-containing injectable hydrogel biomaterials for tissue regeneration. *Acta Biomater.* 136, 1–36. doi:10.1016/j.actbio.2021.09.034

Zhang, D., Sun, P., Li, P., Xue, A., Zhang, X., Zhang, H., et al. (2013). A magnetic chitosan hydrogel for sustained and prolonged delivery of Bacillus Calmette-Guérin in the treatment of bladder cancer. *Biomaterials* 34, 10258–10266. doi:10.1016/j.biomaterials.2013.09.027

Zhang, X., Ma, Z., Ke, Y., Xia, Y., Xu, X., Liu, J., et al. (2021). An injectable serotonin-chondroitin sulfate hydrogel for bio-inspired hemostatic adhesives with high wound healing capability. *Mat. Adv.* 2, 5150–5159. doi:10.1039/d1ma00137j

Zhang, Y., Yang, B., Zhang, X., Xu, L., and Tao, L. (2012). A magnetic self-healing hydrogel. *Chem. Comm.* 48, 9305–9307. doi:10.1039/c2cc34745h

Zhou, L., Dai, C., Fan, L., Jiang, Y., Liu, C., Zhou, Z., et al. (2021). Injectable self-healing natural biopolymer-based hydrogel adhesive with thermoresponsive reversible adhesion for minimally invasive surgery. *Adv. Funct. Mater.* 31, 2007457. doi:10.1002/adfm.202007457

Zhou, L., Pei, X., Fang, K., Zhang, R., and Fu, J. (2020). Super tough, ultra-stretchable, and fast recoverable double network hydrogels physically crosslinked by triple non-covalent interactions. *Polym. Guildf.* 192, 122319. doi:10.1016/j.polymer.2020.122319

Zou, W., Monterroza, A. M., Yao, Y., Millik, S. C., Cencer, M. M., Rebello, N. J., et al. (2022). Extending BigSMILES to non-covalent bonds in supramolecular polymer assemblies. *Chem. Sci.* 13, 12045–12055. doi:10.1039/d2sc02257e

frontiers | Frontiers in Molecular Biosciences

TYPE Original Research
PUBLISHED 04 April 2023
DOI 10.3389/fmolb.2023.1071376

OPEN ACCESS

EDITED BY
Luca Menichetti,
National Research Council (CNR), Italy

REVIEWED BY
Baolong Zhou,
Weifang Medical University, China
Amir Rostami,
Persian Gulf University, Iran

*CORRESPONDENCE
Rahmatollah Rahimi,
rahimi_rah@iust.ac.ir
Fatemeh Molaabasi,
molaabasi.fatemeh@yahoo.com

SPECIALTY SECTION
This article was submitted to Nanobiotechnology, a section of the journal Frontiers in Molecular Biosciences

RECEIVED 16 October 2022
ACCEPTED 26 January 2023
PUBLISHED 04 April 2023

CITATION
Gharehdaghi Z, Naghib SM, Rahimi R, Bakhshi A, Kefayat A, shamaeizadeh A and Molaabasi F (2023), Highly improved pH-Responsive anticancer drug delivery and T2-Weighted MRI imaging by magnetic MOF CuBTC-based nano/microcomposite.
Front. Mol. Biosci. 10:1071376.
doi: 10.3389/fmolb.2023.1071376

Highly improved pH-Responsive anticancer drug delivery and T2-Weighted MRI imaging by magnetic MOF CuBTC-based nano/microcomposite

Zahra Gharehdaghi[1], Seyed Morteza Naghib[2], Rahmatollah Rahimi[1]*, Atin Bakhshi[3], Amirhosein Kefayat[3], Armin shamaeizadeh[2] and Fatemeh Molaabasi[3]*

[1]Department of Chemistry, Iran University of Science and Technology, Tehran, Iran, [2]Nanotechnology Department, School of Advanced Technologies, Iran University of Science and Technology (IUST), Tehran, Iran, [3]Biomaterials and Tissue Engineering Research Group, Department of Interdisciplinary Technologies, Breast Cancer Research Center, Motamed Cancer Institute, ACECR, Tehran, Iran

Cu-BTC framework has received a considerable attention in recent years as a drug carrier candidate for cancer treatment due to its unique structural properties and promising biocompatibility. However, its intrinsic deficiency for medical imaging potentially limits its bioapplications; To address this subject, a magnetic nano/microscale MOF has been successfully fabricated by introducing Fe_3O_4 nanoparticles as an imaging agent into the porous isoreticular MOF $[Cu_3(BTC)_2]$ as a drug carrier. The synthesized magnetic MOFs exhibits a high loading capacity (40.5%) toward the model anticancer DOX with an excellent pH-responsive drug release. The proposed nanocomposite not only possesses large surface area, high magnetic response, large mesopore volume, high transverse relaxivity (r^2) and good stability but also exhibits superior biocompatibility, specific tumor cellular uptake, and significant cancer cell viability inhibitory effect without any targeting agent. It is expected that the synthesized magnetic nano/microcomposite may be used for clinical purposes and can also serve as a platform for photoactive antibacterial therapy ae well as pH/GSH/photo-triple-responsive nanocarrier.

KEYWORDS

magnetic, metal-organic framework, controlled release, pH-responsive doxorubicin release, magnetic resonance imaging, multifunctional nanocomposite

Introduction

An important challenge for cancer therapy is to design a smart nanocarrier with pH-sensitive drug-releasing property and high loading capacity of therapeutic molecules like chemotherapy agents while being able to act as a contrast agent for making a multimodal drug delivery system (DDS) (Chowdhuri et al., 2016a). Porous magnetic microspheres with a porous shell and a magnetic core have been of great interest due to the shell and core functions which induce desired properties, including high drug loading efficacy, considerable biocompatibility, and controllable drug release. In particular anticancer DDS, magnetic nanomaterials possess other diverse properties relation to the photothermal activity, magnetically targeted hyperthermia, and MRI contrast agent resulting in the capability to real-time monitoring tumor tissue treatment (Sun et al., 2008; Liu et al., 2011). In this regard, a variety of porous magnetic core–shell structures include carbon materials, polymers,

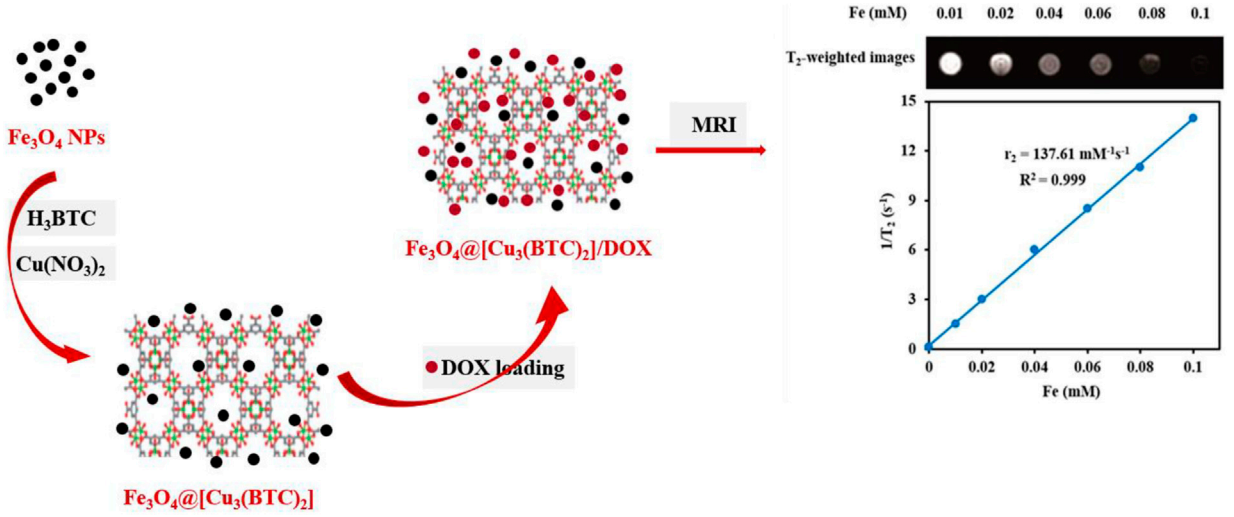

SCHEME 1
Schematic demonstration of the stepwise synthesis process of Fe_3O_4@$[Cu_3(BTC)_2]$ and DOX loading into the Fe_3O_4@$[Cu_3(BTC)_2]$ nanocarrier.

mesoporous oxides, and zeolites. On the other hand, issues such as long fabrication process, low surface area and high reaction temperature, have resulted in high fabrication cost and low scalability (Deng et al., 2009).

As an efficient porous material, Metal Organic Frameworks (MOFs) has received a highly interest in many areas including catalysis (Lee et al., 2009), gas separation and storage (Rosi et al., 2003), drug delivery (Horcajada et al., 2010), biosensing (Allendorf et al., 2009), and especially developing DDSs (Horcajada et al., 2010) due to their high porosity and surface area, various available structures, adjustable pore sizes and functionalities (Eddaoudi et al., 2001). Compared to the typical porous nanomaterials (e.g., silica), the synthesis of MOFs is simpler and more efficient (Wu et al., 2014). Moreover, MOFs can carry metal nanoparticles in for delivering organic materials and drugs with therapeutic purposes (Dhakshinamoorthy and Garcia, 2012), act as a pH/GSH/photo-triple-responsive carrier in developing multimodal chemo/photothermal/chemodynamic therapy (Lou et al., 2022a), serve as an artificial enzyme to create a pH sensitive (Mandal et al., 2022) (Lou et al., 2022b) (Xu et al., 2022) DDS and as a photoactive dual-cationic covalent MOF to construct a cation/photothermal/NO antibacterial therapy system (Luo et al., 2022a) (Luo et al., 2022b). Ferey and coworkers first studied the ability of MIL-100(Fe) and MIL-101(Cr) to encapsulate ibuprofen molecules for sustained drug delivery (Horcajada et al., 2006). Furthermore, Rahimi et al. used porous multifunctional GO/Cu (II)-porphyrin MOF biocompatible nanocomposite (CuG) to produce a pH-responsive drug carrier to treat breast cancer (Gharehdaghi et al., 2021). Recently, metal organic frameworks with core–shell structures have been also employed in biomedicine and optic fields. Studies on MOF-based core–shell (e.g., MOF@MOF microporous core-shell architectures (Koh et al., 2009), MOF@SiO_2 nanocomposites (Rieter et al., 2007), MOF-cored molecular imprinted polymers (Qian et al., 2011) and polystyrene@MOF photonic films (Wu et al., 2011) are very limited, and porous magnetic MOF-based core–shell structures have not been significantly explored.

Regarding MOFs with MRI property could be referred to Lin's group that has synthesized a novel MRI contrast agent based on Gd-MOFs (Rieter et al., 2006). Gd-based MOFs had a high longitudinal relaxivity though the leaching Gd^{3+} ions caused nephrogenic systemic fibrosis (Broome et al., 2007), which challenges their clinical applications. Magnetic nanoparticles may be embedded into MOFs to overcome the issue and maximize drug encapsulation capacity (Vakilinezhad et al., 2018). Iron oxide nanoparticles are widely used in MRI as they can shorten transverse relaxation time and also due to biocompatibility (Lee and Hyeon, 2012). Therefore, Fe_3O_4 magnetic nanoparticles may be used to produce multifunctional biocompatible MOF-based composites with high drug load capacity and relaxivity. In this regard, researchers produced multifunctional Fe_3O_4@PAA/AuNCs/ZIF-8 NPs (Bian et al., 2015) and RITCFe_3O_4@IRMOF-3/FA NPs (Chowdhuri et al., 2016b) by coating Fe_3O_4 with different types of Zn-based MOFs for cell imaging and drug delivery.

In this study, Fe_3O_4at $[Cu_3$ $(BTC)_2]$ magnetic metal organic framework composite was produced using $[Cu_3(BTC)_2]$ and Fe_3O_4 (Scheme 1). Benzene-1,3,5-tricarboxylate is referred to as BTC and $[Cu_3$ $(BTC)_2]$, is called "HKUST-1". $[Cu_3(BTC)_2]$ has an excellent chemical and solvent stability and therefore has been greatly used for drug delivery. The Cu (II)-cluster coordination and linear ligands form a rigid cubic 3D porous structure with octahedral and tetrahedral cavities. Properties such as numerous open cavities, presence of Cu-O clusters, amphiphilic character and metal sites have made $[Cu_3(BTC)_2]$ a candidate for capturing and releasing a variety of anticancer agents. These properties are a result of the coordination bonds of the DOX hydroxyl groups with Cu II) in $[Cu_3(BTC)_2]$ (Chui et al., 1999). Moreover, the DOX loaded Fe_3O_4@$[Cu_3(BTC)_2]$ has shown a sustainable and pH-responsive drug meanwhile having the T_2-MR contrast property of Fe_3O_4 nanospheres. As a result, Fe_3O4@$[Cu_3(BTC)_2]$ composites have high drug loading capacity, low cytotoxicity and high transverse relaxivity, which have made them a candidate for theranostic applications.

Experimental section

Materials. Benzene-1,3,5-tricarboxylic acid (H_3BTC), ferric chloride hexahydrate ($FeCl_3.6H_2O$), copper II) nitrate trihydrate ($Cu\ (NO_3)_2.3H_2O$, 99%), ethylene glycol (EG), sodium acetate (CH_3COONa), ethanol (C_2H_6O, 99%), and phosphate buer (PBS pH 5, 6 and 7.4) was supplied from Merck. Doxorubicin was supplied from Ebewe Pharma Company. Dulbecco's modified Eagle's medium (DMEM), trypsin/EDTA and FBS were supplied from Gibco (Grand Island, NY, United States of America). All solutions were prepared using deionized water.

Synthesis of MAA-Fe_3O_4 nanoparticles. Fe_3O_4 particles were produced using solvothermal process. 2.7 g of $FeCl_3.6H_2O$ and 4.8 g of NaAc were stirred in 75 ml of ethylene glycol for 30 min using a magnetic stirrer. The mixture was poured in a sealed Teflon-lined stainless-steel container and heated to a temperature of 200°C in an autoclave for 16 h. Then, the Teflon lined container was cooled down to reach room temperature. The resulted Fe_3O_4 nanospheres were collected, washed several times using ethanol, and dried under vacuum conditions at a temperature of 50°C (Zeng et al., 2012). 0.5 g Fe_3O_4 was added to a 100 ml solution of mercapto-acetic acid in ethanol (2.9 mM) and then was collected by an external magnetic field and finally washed to obtain Mercapto-acetic acid (MAA)-functionalized Fe_3O_4 nanoparticles (Wang et al., 2013).

Synthesis of Fe_3O_4at$[Cu_3(BTC)_2]$ magnetic nanocomposites. Firstly, 0.25 g of MAA- Fe_3O_4 particles were dissolved in 150 ml of ethanol and 1.83 g of $Cu\ (NO_3)_2.6H_2O$ was added to it and treated using ultrasonic for 30 min. Further, 100 ml of 0.875 g H_3BTC was added to previous solution with a rate of 1 ml/min under mechanical stirring for 3 h. The Fe_3O_4@$[Cu_3(BTC)_2]$ particles were extracted from the mixture using a magnetic field, rinsed with ethanol three times, and then dried at a temperature of 60°C and vacuum conditions (Zhao et al., 2015).

Characterization. XRD method was used to assess the phase purity of the synthesized products. A Philips PW 1730 X-ray diffractometer (Philips PW 1730/10, Holland) with Cu-Kα radiation was used for this purpose. FTIR test was carried out with IR spectrometer (8500S SHIMADZU, Japan) to identify functional groups. BET method was used to observe the surface area of the materials from N_2 adsorption and desorption. The measurements were observed on a Micrometritics ASAP2020 system (ASAP 2020; Japan). The distribution of the pore size was found from desorption branches of the N_2 isotherms with BJH method. Vibrating sample magnetometer (VSM, MDKB, Magnetic Daghigh Kavir Co., Iran) was applied to observe the magnetic properties of as-prepared nanocomposites at room temperature. The transverse relaxivity times and T_2-weighted MR images were taken with a Siemens Prisma 3.0 TMR scanner (Siemens 3.0 T MAGNETOM Prisma, Germany) having a gradient strength up to 80 mT/m under the following sequence (multi spin-echo, FOV of 100 × 100 mm, TR/TE = 2000/60 m, slices = 1, and a matrix of 192 × 256, 0.55 T, 32.0°C). Tescan Mira3 FE-SEM was used to observe the morphology of synthesized samples (TESCAN MIRA3, Australia). The UV-Visible characterization of the samples was carried out by Shimadzu UV-1700 (Shimadzu UV-1700, Japan) spectrophotometer.

***In vitro* loading and release of DOX.** DOX was loaded into Fe_3O_4@$[Cu_3(BTC)_2]$ nano/microcomposites *via* adding 2 ml of 2 mg/ml DOX solution to a 5 mg of Fe_3O_4@$[Cu_3(BTC)_2]$ (2.5 mg/ml). The solution was mixed for 24 h at room temperature using a 180-rpm shaker in a dark room. The Fe_3O_4@$[Cu_3(BTC)_2]$ particles loaded with drug and then were removed from the solution using magnetic decantation. The DLC of the magnetic nanocomposite was determined from UV-Vis absorbance at 480 nm using to the following formula:

$$\text{DLC (wt. \%)} = \text{weight of loaded DOX} \,/\, (\text{total weight of loaded DOX and } Fe_3O_4@[Cu_3(BTC)_2]) \times 100\%. \quad (1)$$

The DOX release profile from the Fe_3O_4@$[Cu_3(BTC)_2]$/DOX was investigated *via* dialysis. 3 mg of DOX-loaded nanocomposite was dissolved in 5 ml of a number of buffer solutions with different pHs and placed in a dialysis membrane with MWCO of 14 kDa. The mixture was then dialyzed in 100 ml of PBS at 37°C. At each time point, 2 ml of the release medium was sampled to observe the DOX percentage released in intervals, using UV-Vis with a wavelength of 480 nm. The DOX release percentage was found using the following formula:

$$Er = \frac{Ve\sum_{i=1}^{n-1} Ci + VoCn}{m} \quad (2)$$

In this formula, Er refers to the DOX release percentage (%); Ve is the volume which was taken out (2 ml); Ci refers to the concentration in μg/mL at time i, wherein i = n − 1; Vo is the total volume of PBS outside the dialysis bag (100 ml); Cn representates the concentration at a certain time (μg/ml); and m refers to the total amount of DOX in Fe_3O_4@$[Cu_3(BTC)_2]$/DOX (mg).

Drug release data were plotted and fitted to the drug release kinetics models to propose a release mechanism as follows (Nie et al., 2011):

$$\text{Higuchi model: } M_t/M_\infty = Kt^{1/2} \quad (3)$$

$$\text{Zero} - \text{order model: } M_t/M_\infty = Kt \quad (4)$$

$$\text{First} - \text{order model: } M_t/M_\infty = 1 - e^{-Kt} \quad (5)$$

The correlation coefficient was then calculated to find the best fit. The release data were also fitted to the Korsmeyer–Peppas model to reveal the release mechanism according to the formula below:

$$\text{Korsmeyer–Peppas model: } M_t/M_\infty = Kt^n \quad (6)$$

In all of the above-mentioned formulas, M_t/M_∞ shows the drug fraction released at time t, K refers to the rate constant and the exponent "n" shows the drug transport mechanism to evaluate the diffusion mechanism (Reddy et al., 2014) (Mosallanezhad et al., 2022).

Transverse relaxivity and T_2-weighted images. The samples with different Fe concentrations (0.00, 0.02, 0.04, 0.06, 0.08, 0.10 mM) were prepared using Fe_3O_4@$[Cu_3(BTC)_2]$ composites. T_2-weighted images and transverse relaxivity time (T_2) of the materials were obtained, using a Siemens Prisma 3.0 T MR scanner (Erlangen, Germany) having a gradient strength of 80 mT/m. The transverse relaxivity (r_2) of Fe_3O_4@$[Cu_3(BTC)_2]$ was found by linear fitting of $1/T_2$ *versus* Fe concentration.

***In vitro* MTT assessments.** The MTT assay for evaluation of cytotoxicity was used towards 3 cell lines including 3T3 (mouse embryonic fibroblasts) as normal cells, MCF-7 (breast cancer cell line) and HeLa (human cervical cancer cells) as cancer cell lines. 3T3, MCF-7 and Hela (7×10^3 cells per well) cells were seeded in 96-well assay plates with 100 μl of culture medium (DEMEM) and placed in an incubator for 24 h. The cells were kept in a 5% CO_2 at 37 °C and in a humidified incubator. In the next step, 100 μl of various concentrations of Fe_3O_4@$[Cu_3(BTC)_2]$, Fe_3O_4@

10.3389/fmolb.2023.1071376

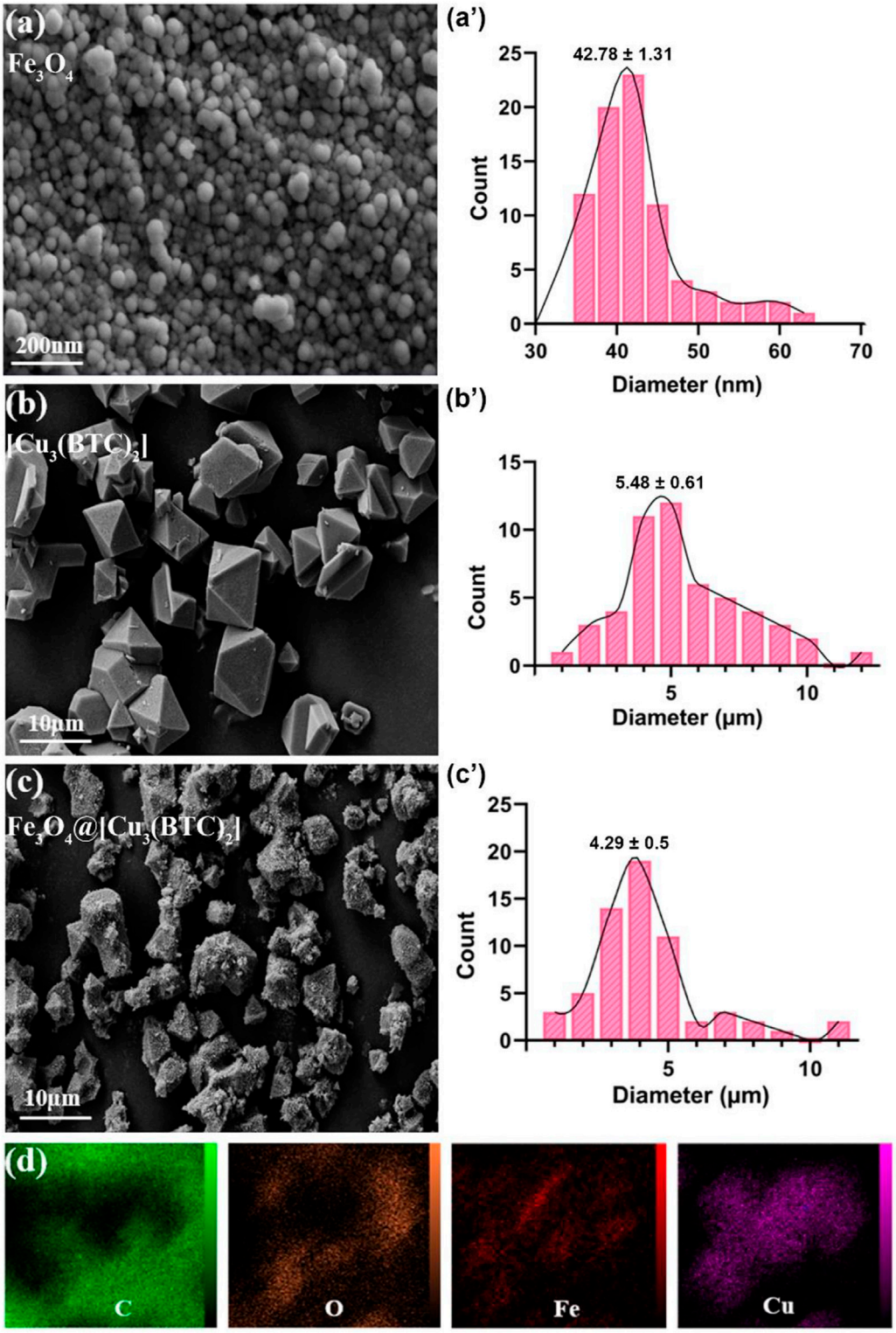

FIGURE 1
FE-SEM analysis for **(A)** Fe_3O_4, **(B)** $[Cu_3(BTC)_2]$ and **(C)** Fe_3O_4@$[Cu_3(BTC)_2]$, respectively. **(D)** The elemental mapping of magnetic Fe_3O_4@$[Cu_3(BTC)_2]$ nanocomposite.

$[Cu_3(BTC)_2]$/DOX and free DOX were added and placed in the incubator for 24 h. 100 μl of 3- (4, 5dimethylthiazol-2-yl) -2, 5-diphenyl tetrazolium bromide (MTT) (0.5 mg/ml in PBS) were added to the media containing Fe_3O_4@$[Cu_3(BTC)_2]$, Fe_3O_4@$[Cu_3(BTC)_2]$/DOX, and free DOX. The plate was placed in an incubator and cultured for 4 h to achieve the purple formazan product. At the final stage, 50 μl of DMSO was replaced with the medium in each well to dissolve formazan. A BioTek plate reader

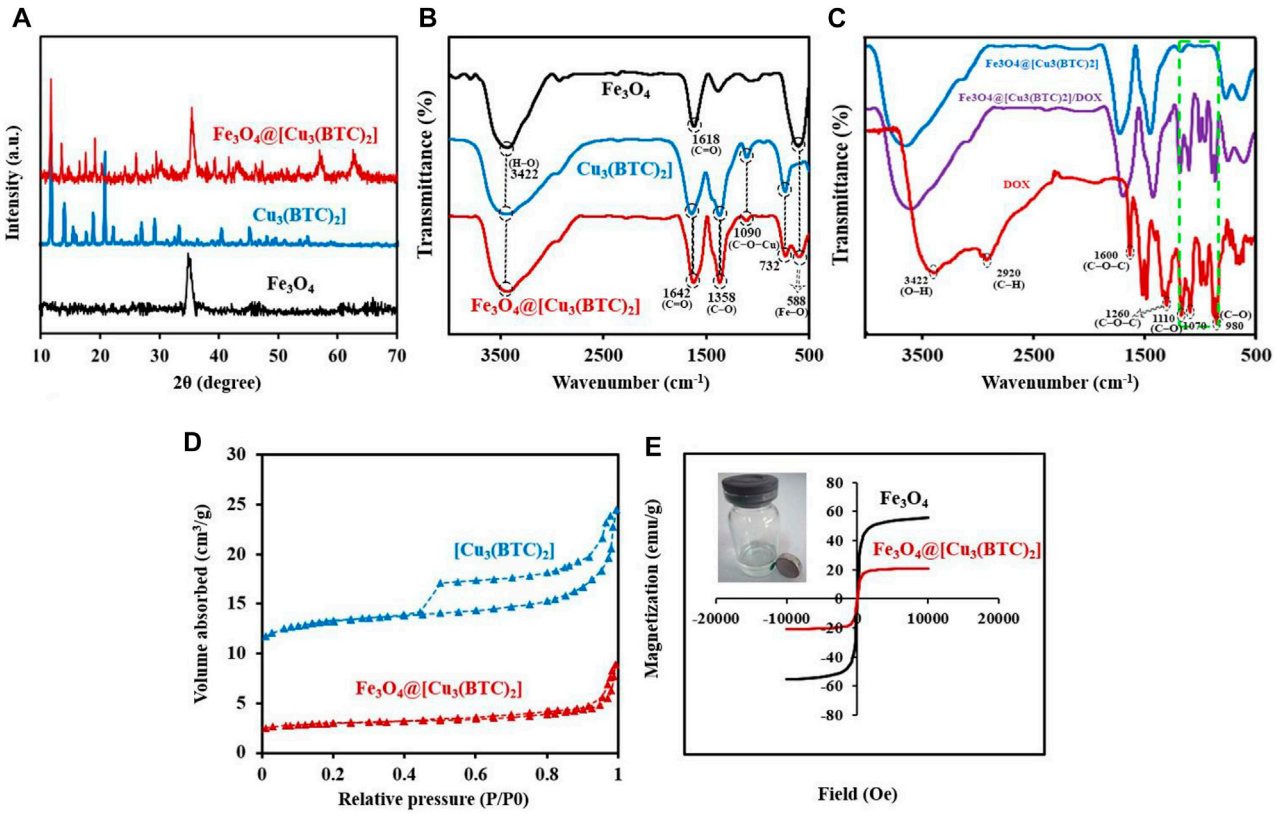

FIGURE 2
(A) PXRD patterns for Fe_3O_4, $[Cu_3(BTC)_2]$ and Fe_3O_4@$[Cu_3(BTC)_2]$. **(B)** FT-IR analysis for the materials produced: Fe_3O_4, $[Cu_3(BTC)_2]$ and Fe_3O_4@$[Cu_3(BTC)_2]$. **(C)** FT-IR spectra for Fe_3O_4@$[Cu_3(BTC)_2]$, Fe_3O_4@$[Cu_3(BTC)_2]$/DOX and free DOX **(D)** N_2 adsorption-desorption isotherms of $[Cu_3(BTC)_2]$ and Fe_3O_4@$[Cu_3(BTC)_2]$. **(E)** VSM analysis for Fe_3O_4 and Fe_3O_4@$[Cu_3(BTC)_2]$.

with a wavelength of 570 nm was used to observe the absorbance of each well. The cell viability percentage was calculated compared with untreated control cells. The results were shown as mean value ±standard deviation (SD).

Annexin V-FITC apoptosis **assessment.** The Effect of Fe_3O_4@$[Cu_3(BTC)_2]$/DOX and free DOX on apoptosis and necrosis in HeLa cells was studied *via* Annexin V-FITC apoptosis method. Cells were seeded in a 6 well plate (1×10^5 cells/well) and placed in a CO_2 incubator at 37°C for 24 h. Cells were treated with Fe_3O_4@$[Cu_3(BTC)_2]$/DOX of concentration equivalent to 8 μg/ml of DOX and free DOX in an incubator at a temperature of 37°C for 7 h. Cells were then rinsed twice with PBS and after centrifuging for 5°min, was resuspended in 100 μl Annexin V binding buffer and were placed in an incubator for 20 min with Annexin V-FITC (5 μl) and propidium iodide solution in a dark environment. 400°μl of Annexin V binding buffer was added in FACS tube. Then the cells were observed in a Flow Cytometer. Data analyzed by Flowing Software (Version 2.5.1, Turku Centre for Biotechnology, Finland).

Results and discussion

FESEM study. The morphology and structure of the produced samples were studied in this section. According to the FESEM images, Fe_3O_4 NPs are mono-dispersed with a spherical shape and an average diameter of 45 nm (Figure 1A). Moreover, size of $[Cu_3(BTC)_2]$ was obtained 5.48 μm with an octahedral structure made of dimer Cu paddle wheels linked with BTC (Figure 1B) (Wee et al., 2012). Cu^{2+} ions have weak bindings wherein the residual axial coordination sites are filled by water molecules with a weak bond. The primary building blocks were combined using BTC ligands to produce a 3D octahedral structure with an open-pore system (Schlichte et al., 2004). As seen, Fe_3O_4@$[Cu_3(BTC)_2]$ also shows an octahedral morphology similar to $[Cu_3(BTC)_2]$ together with Fe_3O_4 NPs on its surface (Figure 1C). In this regard, Cu^{2+} ions and functional MAA- Fe_3O_4 were combined with free state and the $[Cu_3(BTC)_2]$ nucleation rate is controlled by manipulating the organic ligand addition speed. The distribution of Fe and Cu elements in the nanocomposite were observed using elemental mapping analysis as well (Figure 1D). The obtained results verified the production of magnetic Fe_3O_4@$[Cu_3(BTC)_2]$ nano/microcomposite.

X-ray diffraction study. The crystal structure of the obtained composite was studied *via* powder X-ray diffraction (PXRD) (Figure 2A). The Fe_3O_4 diffraction peaks were appeared at 2θ = 34.70° (311), 41.45° (400), 51.75° (422), 56.94° (511) and 62.45° related to the (440) plan (JCPDS No.19–0629, magnetite) (Yang et al., 2017). The resulting XRD peaks of Fe_3O_4@$[Cu_3(BTC)_2]$ belong to the crystalline Fe_3O_4 and $[Cu_3(BTC)_2]$ (Zeng et al., 2014), suggesting crystalline structure formation of the Fe_3O_4@$[Cu_3(BTC)_2]$ composite. Moreover, no impurities were detected according to the peaks. Or there is not a physical mixture of two separate phases of Fe_3O_4 and $[Cu_3(BTC)_2]$.

TABLE 1 BET surface area, total pore volume, and pore diameter of $[Cu_3(BTC)_2]$ and Fe_3O_4@$[Cu_3(BTC)_2]$ based on N_2 adsorption isotherms at 77K.

Samples	BET surface area (m2g−1)	Total pore volume (x106m3g−1)	Pore diameter (nm)
[CU3(BTC)2]	800	0.4	4.2
Fe3O4at[Cu3(BTC)2]	301.69	0.2	3.2

FT-IR spectra. The FT-IR spectra of Fe_3O_4 nanospheres, $[Cu_3(BTC)_2]$ and the magnetic nanocomposite Fe_3O_4@$[Cu_3(BTC)_2]$ are illustrated in Figure 2B. The FTIR spectrum of $[Cu_3(BTC)_2]$ shows the characteristic peaks at 732 and 1090 cm^{-1} related to the C–O–Cu stretching vibrations, and two sharp peaks at 1358 and 1642 cm^{-1} attributed to the C–O and C=O stretching vibrations, respectively. Moreover, a broad band is observed about 3500 cm^{-1} which could be assigned to O–H stretching vibration or adsorbed water. MAA-Fe_3O_4 NPs exhibits the characteristic FT-IR peak specially at 588 belonged to the Fe–O vibration, a small peak at 2693 cm^{-1} related to S–H stretching vibration and a sharp peak at 1618 cm^{-1} as well as a broad peak at 3422 cm^{-1} attributed to the starching C=O and H–O vibrations of MAA located on the surface of Fe_3O_4, respectively (Bandosz and Petit, 2011; Zeng et al., 2013). Notably, the peaks at 1090 and 732 cm−1 (C–O–Cu), as well as the other 588 (Fe–O), 1358 (C–O) and 1642 cm^{-1} (C=O) intensified in the FT-IR spectrum of Fe_3O_4@$[Cu_3(BTC)_2]$ indicate the successful formation of Fe_3O_4@$[Cu_3(BTC)_2]$ composites (Varghese et al., 2022). The peak intensity was lower in Fe_3O_4@$[Cu_3(BTC)_2]$ due to the immobilization caused by coating $[Cu_3(BTC)_2]$.

The IR spectra of Fe_3O_4@$[Cu_3(BTC)_2]$ as a new proposed pH-responsive platform was also compared before and after adding DOX as a commercially anticancer drug model. The FT-IR spectrum of DOX illustrated characteristics peaks including C–O stretching primary alcohol (980 cm^{-1}), C–O stretching secondary alcohol (1070 cm^{-1}), C–O stretching tertiary alcohol (1110 cm^{-1}), C–O–C stretch (1260 cm^{-1}), C=O stretch (1600 cm^{-1}), C=O stretch ketone (1730 cm^{-1}), C–H stretch aromatic (2920 cm^{-1}), and O–H and N–H stretches (2500–3600 cm^{-1}). As shown in Figure 2C, the characteristic sorption bonds at 980, 1070, and 1110 cm^{-1} of DOX labelled with green dash rectangle in the spectra of Fe_3O_4@$[Cu_3(BTC)_2]$/DOX confirmed the successful loading of DOX in the Fe_3O_4@$[Cu_3(BTC)_2]$ nanocomposite (Figure 2C).

Nitrogen adsorption–desorption isotherms. In order to calculate the surface area and study the porosity of the materials and pore volumes, nitrogen adsorption-desorption isotherms were recorded (Figure 2D). As seen, the adsorption-desorption isotherms intermediate between type I and IV were observed for Fe_3O_4@$[Cu_3(BTC)_2]$ as well as $[Cu_3(BTC)_2]$. This indicates that there is the copresence of micropores and mesopores in materials (Ke et al., 2014) (Zhang et al., 2016). Table 1 shows the BET pore volumes and surface areas. The BET total pore volume and surface area of Fe_3O_4@$[Cu_3(BTC)_2]$ were 0.236 × 10^{-6} m^3g^{-1} and 301.69 m^2g^{-1}, respectively, which is lower than that of $[Cu_3(BTC)_2]$ MOF (Table 1). This can be due to the presence of Fe_3O_4 NPs on the octahedral structure of MOF. Average pore size was 3.2 nm which was calculated from N_2 isotherm desorption using BJH method. Really, the high porosity and specific surface area may result in multiple channels for drug loading.

VSM measurements. The magnetic hysteresis loops of magnetic nanocomposite Fe_3O_4@$[Cu_3(BTC)_2]$ and Fe_3O_4 nanospheres were measured at 300 K by a VSM with a field ranging from -20000 to +20,000 Oe; wherein the results are depicted in Figure 2E.

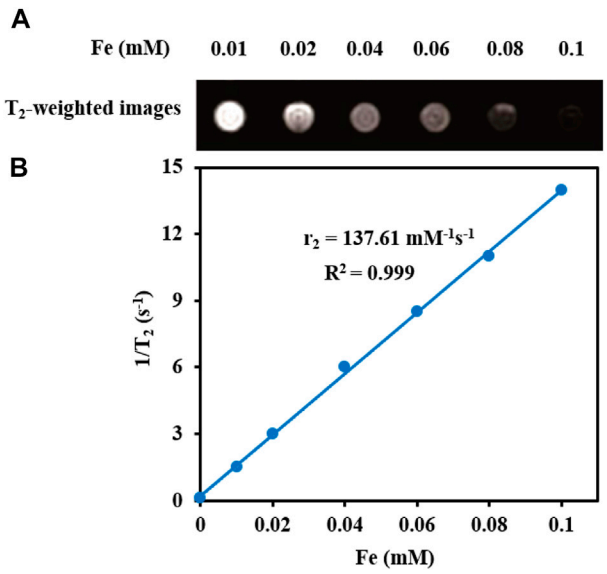

FIGURE 3
(A) T_2-Weighted MRI images of Fe_3O_4@$[Cu_3(BTC)_2]$ at various Fe concentrations **(B)** Plot of inverse transverse relaxation time ($1/T_2$) *versus* Fe concentrations. The slope indicates the relaxivity value, r_2.

The Ms (saturation magnetization) values for Fe_3O_4@$[Cu_3(BTC)_2]$ nanoparticles were 20.87 emu/g which were lower than that of Fe_3O_4 nanospheres (55.58 emu/g) (Figure 2E). A large surface area to volume ratio magnetic anisotropy energy of nanocomposite caused that the magnetization reduction of nanocomposite could be comparable to the thermal energy. The thermal fluctuations can significantly reduce the magnetic moment in a specific field (Spaldin, 2010; Ghosh et al., 2011). The high Ms value allows the Fe_3O_4@$[Cu_3(BTC)_2]$ nanocomposites to be used in MRI, magnetic targeted drug carriers, adsorption and many other applications.

T_2-weighted MRI. The application of Fe_3O_4@$[Cu_3(BTC)_2]$ nanocomposite as an MRI contrast agent is evaluated using T_2-weighted MR imaging with a 3T clinical MRI instrument. To evaluate the T_2 effect, the concentration-dependent darkening of the Fe_3O_4@$[Cu_3(BTC)_2]$ nanocomposite was recorded and shown in Figure 3. Accordingly, the T_2 contrast depended on the concentration of Fe. Figure 3 shows T_2 relaxation rates ($1/T_2$) of Fe_3O_4a@$[Cu_3(BTC)_2]$ nanocomposites with different concentrations of iron. Moreover, the transverse relaxivity (r_2) of Fe_3O_4@$[Cu_3(BTC)_2]$ was reported 137.61 mM/s. Thus, the results indicate that the Fe_3O_4@$[Cu_3(BTC)_2]$ composites with very low concentrations may be applicable as MRI contrast agents. Furthermore, the r_2 value of

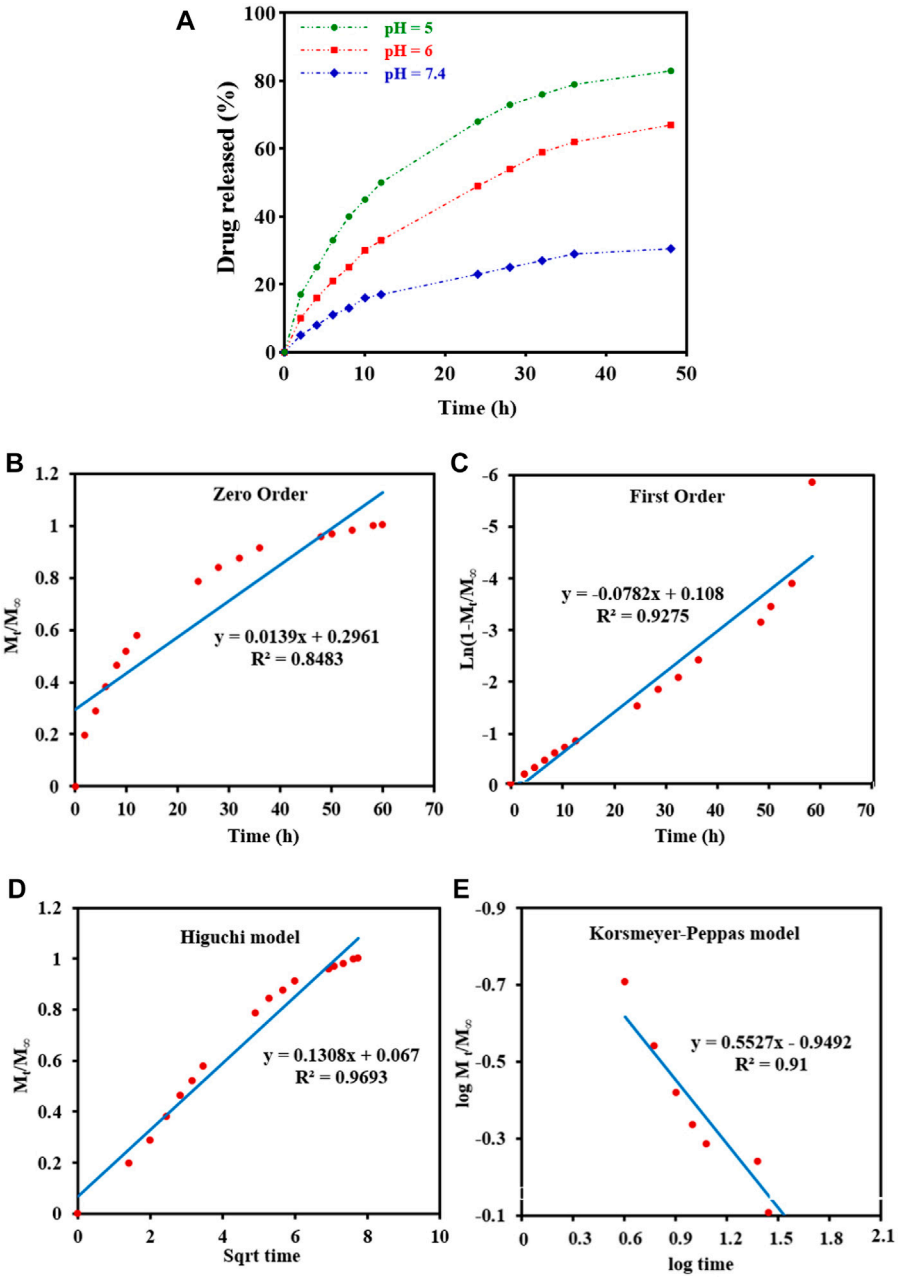

FIGURE 4
(A) *In vitro* DOX release of the Fe_3O_4@$[Cu_3(BTC)_2]$/DOX at different pH 5,6, and 7.4. **(B–E)** Drug release data fitted to various kinetic models. **(B)** Zero order; **(C)** First order; **(D)** Higuchi model; and **(E)** Korsmeyer-Peppas drug diffusion model.

the prepared Fe_3O_4@$[Cu_3(BTC)_2]$ was much higher than that of PDA-ICG-PEG/DOX (Mn) (39.2 mM/s) (Dong et al., 2016) and clinical Fe-based T_2-weighted contrast agents such as ferumoxide (98.3 mM/s) and ferumoxsil (72 mM/s). According to the results, Fe_3O_4@$[Cu_3(BTC)_2]$ could be applicable as a strong MRI contrast agent in T_2-MR imaging.

***In vitro* drug load/release of nanomagnetic Fe_3O_4at $[Cu_3(BTC)_2]$.** Because of the unique properties of the as-prepared magnetic MOF composite, we designed a targeted drug delivery nano/microcarrier for cancer treatment based on applying and loading DOX into magnetic composite. In this sense, DOX was added to Fe_3O_4@$[Cu_3(BTC)_2]$ in PBS for 24 h at a pH of 7.4. Then, the unloaded DOX was removed to obtain Fe_3O_4@$[Cu_3(BTC)_2]$/DOX and as-above mentioned the IR spectra were used to confirm DOX loading in Fe_3O_4@$[Cu_3(BTC)_2]$ composite (Figure 2C). With the appearance of peaks related to DOX in as-prepared MOF composite, the drug loading of Fe_3O_4@$[Cu_3(BTC)_2]$/DOX was calculated and found around 40.5 wt%. This high drug loading of Fe_3O_4@$[Cu_3(BTC)_2]$ nanocomposite is due to the high surface area of $[Cu_3(BTC)_2]$ and the interactions between DOX and $[Cu_3(BTC)_2]$. Interactions include π-π stacking effect between the $[Cu_3(BTC)_2]$ aromatic porous walls and the DOX aromatic anthracycline, hydrogen bonding between the $[Cu_3(BTC)_2]$ carboxyl groups and the DOX oxygen atoms, electrostatic interactions, Van Der Waals forces, and coordination

TABLE 2 Kinetic models for drug release.

Kinetic models	Fitting equation	R2	K (h−1)
Mt/M∞ = Kt	Mt/M∞ = 0.0139t	0.848	0.0139
Mt/M∞ = 1—e−Kt	Mt/M∞ = 1—e−0.0782t	0.927	0.0782
Mt/M∞ = Kt1/2	Mt/M∞ = 0.13t1/2	0.969	0.130
Mt/M∞ = Ktn	Mt/M∞ = 0.11t0.552	0.910	0.11

bonds (Horcajada et al., 2012). The coordination bonds between DOX deprotonated hydroxyls and the Cu sites in $[Cu_3(BTC)_2]$ had a major impact in drug delivery (Zhao et al., 2016).

DOX-release experiments were performed in PBS buffer solutions (pH 5,6 and 7.4 at 37°C) and characterized by UV-Vis to evaluate the drug delivery properties of DOX-loaded Fe_3O_4@$[Cu_3(BTC)_2]$ in different physiological environments (Figure 4A). As can be seen in Figure 4A, the released amount of drug after 48 h was about 83% at a pH of 5.0, and around 30.5% at a pH of 7.4. Therefore, drug release from Fe_3O_4@$[Cu_3(BTC)_2]$/DOX was slower at a pH of 7.4 in comparison with a pH of 5, due to the electrostatic interaction between framework rings and drug molecules with pH change. According to the results, small amounts of DOX are released at normal cell pH and therefore the normal cells are not affected by the undesirable side effects of the drug; while, in an acidic pH (cancer cells environment), the drug release is increased to eliminate tumor cells. Therefore, Fe_3O_4@$[Cu_3(BTC)_2]$ nano/microcomposite had pH-responsive properties which may be used to adjust DOX release and prevent premature release in physiological conditions. Notably, two variation of drug molecules existed in the release process. The drug was released with a high rate during the first 10 h followed by gradual drug dissolution. The guest molecules near the boundaries had host–guest interactions, such as π–π interactions and hydrogen bonds between the framework organic part and the DOX aromatic rings. Meanwhile, drug molecules far from the walls had guest-guest interactions. The molecules with weak bonds were dissolved in the primary stage of the delivery (Lin et al., 2016).

To study drug release from nanoparticles *in vitro*, the results are verified with a mathematical model (Gandhi et al., 2014) (Figure 4 b-e) (Table 2). As shown in Figure 4D, Higuchi model exhibited the best fit of all data points (up to 100% of release curves), since R_h was the best match compared to other coefficients. The Higuchi release model is represented as:

$$M_t/M_\infty = K_h t^{1/2}$$

Wherein M_t refers to the DOX release amount at time t, M_∞ shows the maximum DOX release, and k_h is the Higuchi constant for DOX release. R^2 was reported to be 0.9693, according to an "n" value (diffusion exponent) in the range of 0.45–0.89, found from the Korsmeyer–Peppas model. Therefore, it can be concluded that the DOX release was non-Fickian model, with an anomalous transport diffusional release, suggesting both swelling- and diffusion-controlled drug release.

***In vitro* cytotoxicity tests.** The effect of Fe_3O_4@$[Cu_3(BTC)_2]$ and Fe_3O_4@$[Cu_3(BTC)_2]$/DOX on the viability of two cancer cell lines, human cervical cancer HeLa and breast cancer MCF-7 cells (Madej et al., 2022), was investigated in the range of 2.0–64 μg/ml. The results showed significant cell survival due to the low cytotoxicity of Fe_3O_4at$[Cu_3(BTC)_2]$, so that the viability remained above ca. 80% for HeLa cells and 95% for MCF-7 cells after 24 h of incubation time. This result verified the high biocompatibility of Fe_3O_4@$[Cu_3(BTC)_2]$ even with a high concentration 64 μg/ml of magnetic nano/microcomposite (Figure 5). The inhibitory effect of DOX released from Fe_3O_4at$[Cu_3(BTC)_2]$/DOX on the growth of HeLa and MCF-7 cells was also examined and compared to the cytotoxicity of free DOX as a control experiment. The results depict that Fe_3O_4@$[Cu_3(BTC)_2]$/DOX was much higher cytotoxic to cancer cell lines than free DOX (Figures 5C,D). The IC_{50} of Fe_3O_4@$[Cu_3(BTC)_2]$/DOX on HeLa cells (4.45 μg/ml) and MCF-7 cells (6.8 μg/ml) was obtained about 4.0 and 2.6 times more than that of free DOX state (17.74 μg/ml), respectively (Table 3). This observation can be attributed to more uptake of Fe3O4at[Cu3(BTC)2]/DOX by cancer cells, which allows pH-responsivity mediated specific endocytosis and thus a growth inhibition and cell death. Consequently, the DOX released from DOX-loaded Fe3O4@[Cu3(BTC)2] possess an anticancer potential and tumor-targeting activity (Shamsipur et al., 2018).

To further confirm the pH responsivity of proposed magnetic nano/microcomposite, one normal cell line, mouse embryonic fibroblasts 3T3 cells was selected and incubated with various concentrations of the as-synthesized magnetic composite same as above to investigate their cell viability. As shown in Figures 5A, B, both Fe3O4at[Cu3(BTC)2] and Fe3O4at[Cu3(BTC)2]/DOX displayed low cytotoxic activity at even high concentrations, since the viability remained above ca. 80% by composite and 70% by Dox-loaded composite after 24 h incubation time, revealing that both nano/microcomposites are of high biocompatibility toward normal cells and thus promising ability for use in tumor treatment with a minimum side effect. Fe_3O_4@$[Cu_3(BTC)_2]$/DOX was also showed a much lower cytotoxicity to normal 3T3 cells compared to free DOX (~3.5 times). This further demonstrates the pH responsivity of developed nano/micro magnetic composite because the structural properties of [Cu3(BTC)2] MOFs play an absolutely crucial role in their toxicity to cells. Overall, it can be said that the proposed nano/microcomposte magnetic [Cu3(BTC)2] MOF can act as a selective dual functional targeted nanocarrier-assisted pH-responsive drug delivery system with potential of **MRI** property. Therefore, the Fe_3O_4@$[Cu_3(BTC)_2]$/DOX DDS may be a potential substitute for targeted cancer therapy, as the system uses lower dose of DOX to achieve similar cytotoxicity to tumor cells, while decreases the side effects on normal cells (Shahrousvand et al., 2022).

Annexin V-FITC apoptosis assay

Induction of apoptosis is proposed as the main the mechanism in most anticancer drugs (Chen et al., 2010). For this reason, the apoptotic impact of Fe_3O_4@$[Cu_3(BTC)_2]$/DOX on the HeLa cell line was evaluated *via* flow cytometry using PI and Annexin-V FITC double-staining method (Figure 6). For this purpose, HeLa cells were treated with 8 μg/ml Fe_3O_4@$[Cu_3(BTC)_2]$/DOX, free DOX and Fe_3O_4@$[Cu_3(BTC)_2]$ for 12 h and after that the percentages of necrotic, early and late apoptotic, and live cells after treatments were investigated. According to the results, cells exposed to free DOX (12.21%) had a lower apoptosis percentage compared to when HeLa cells exposed to Fe_3O_4at$[Cu_3(BTC)_2]$/

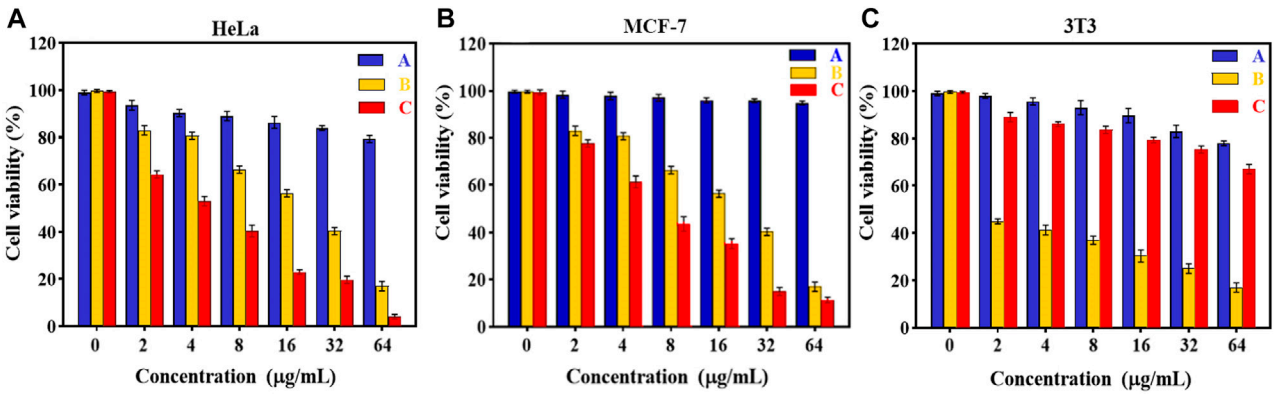

FIGURE 5
Cell viability of **(A)** HeLa, **(B)** MCF-7 and **(C)** 3T3 cells after incubating with various amounts of **(A)** Fe_3O_4@[Cu_3(BTC)$_2$] and **(B)** free DOX, **(C)**Fe_3O_4@[Cu_3(BTC)$_2$]/DOX for 24 h (Data were given as mean ± SD, n = 3).

TABLE 3 IC50 values on HeLa, MCF-7 and 3T3 cells were calculated using non-linear regression analysis in Graph Pad Prism 8.0.2 software (+SD; n = 3).

Cell lines	IC_{50}(μg/mL)		
	Fe_3O_4@[Cu_3(BTC)$_2$]	Fe_3O_4@[Cu_3(BTC)$_2$]/DOX	DOX
HeLa	3109	4.45	17.74
MCF-7	7530	6.8	18.01
3T3	410.5	431.5	1.45

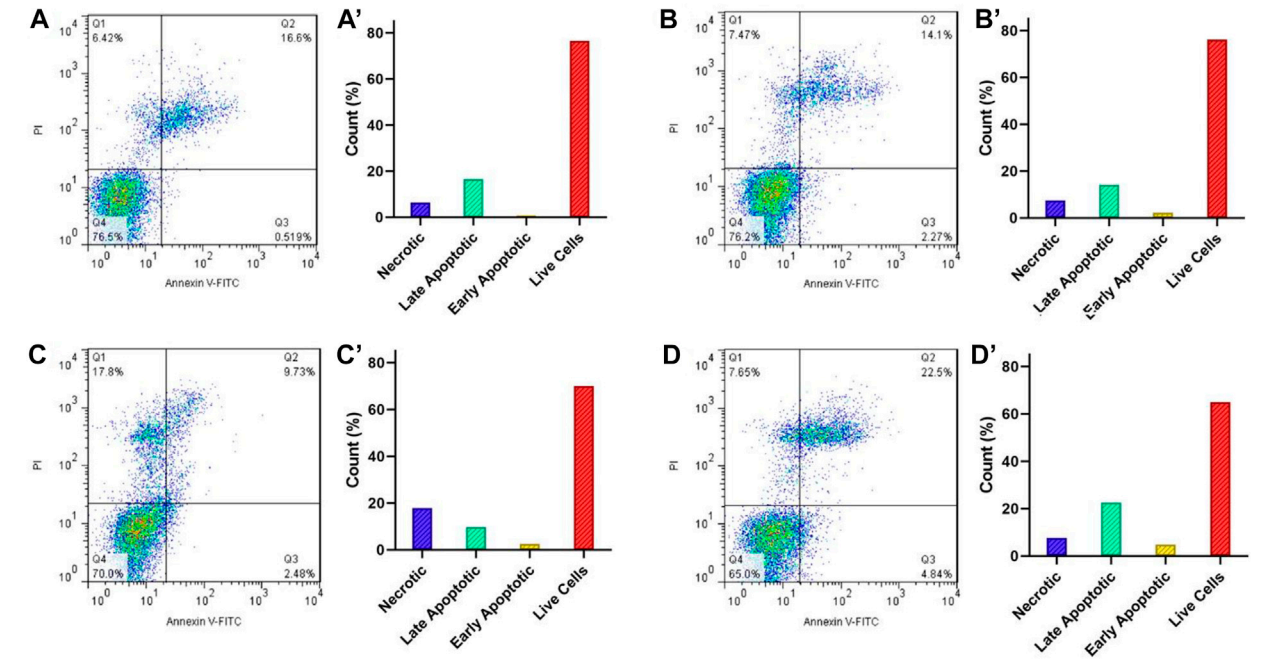

FIGURE 6
Flow cytometry analysis of the apoptotic and necrotic HeLa cells at pH 7.4 after 6 h incubation with the control group **(A)**, Fe_3O_4@[Cu_3(BTC)$_2$] **(B)**, free DOX **(C)**, and Fe_3O_4@[Cu_3(BTC)$_2$]/DOX **(D)**. The results are expressed as mean ± standard deviation (n = 3). Q1–Q4 represent the necrotic, late apoptotic, early apoptotic, and live cells, respectively.

DOX (27.34%). As a conclusion, it can be mentioned that Fe_3O_4at $[Cu_3(BTC)_2]$/DOX triggered a significantly higher amount of apoptosis in the HeLa cells compared to free DOX state.

Conclusion

In summary, a multifunction magnetic nano/microcomposite has been synthesized using a novel convenient method, consisting $[Cu_3(BTC)_2]$ as a targeted drug delivery system with enhanced antitumor efficacy and Fe_3O_4 as T_2-weighted MR imaging agent. DOX was loaded into the prepared magnetic nanocomposite as a model drug, which provided high drug loading capacity. Moreover, according to *in vitro* studies, the DOX released from Fe_3O_4@$[Cu_3(BTC)_2]$/DOX was 83.0% at a pH of 5 while this amount reduced to 30.5% at a physiological pH (7.4). These results showed that multifunctional magnetic nano/microcomposite had a high DOX release rate under acidic conditions of tumor cells, and a low release rate at a physiological condition of healthy cells with a pH 7.4. Additionally, the cytotoxicity assay studies demonstrated that the magnetic composites have lower toxicity and higher biocompatibility, while DOX-loaded Fe_3O_4@$[Cu_3(BTC)_2]$ caused higher toxicity in cancer cells and lower toxicity in normal cells compared to free DOX due to the pH-responsive behavior. Furthermore, the transverse relaxivity of Fe_3O_4@$[Cu_3(BTC)_2]$ was found to be 137.61 mM/s, showing its high ability to be used as a contrast agent for MR imaging. Further, flow cytometry was used to study the apoptosis amount induced by the Fe_3O_4@$[Cu_3(BTC)_2]$/DOX. Really, the Fe_3O_4@$[Cu_3(BTC)_2]$ magnetic nano/microcomposites exhibited a significantly higher drug loading capacity, high transverse relaxivity, and lower cytotoxicity. Therefore, it can be said that developed Fe_3O_4@$[Cu_3(BTC)_2]$ magnetic nano/microcomposites may be used as a strong potential drug delivery system in biomedicine and as a promising theranostic agent for MR imaging.

Data availability statement

The raw data supporting the conclusions of this article will be made available by the authors, without undue reservation.

Author contributions

ZG performed experimental procedure. SN, RR, and FM supervised the student, edited and revised the paper.

Acknowledgments

The authors gratefully acknowledge the support of this work by Iran University of Science and Technology and Motamed Cancer Institute. The authors gratefully acknowledge the Support Grant by the Iran National Science Foundation (INSF-4000890).

Conflict of interest

The authors declare that the research was conducted in the absence of any commercial or financial relationships that could be construed as a potential conflict of interest.

Publisher's note

All claims expressed in this article are solely those of the authors and do not necessarily represent those of their affiliated organizations, or those of the publisher, the editors and the reviewers. Any product that may be evaluated in this article, or claim that may be made by its manufacturer, is not guaranteed or endorsed by the publisher.

References

Allendorf, M. D., Bauer, C. A., Bhakta, R. K., and Houk, R. J. T. (2009). Luminescent metal–organic frameworks. *Chem. Soc. Rev.* 38 (5), 1330–1352. doi:10.1039/b802352m

Bandosz, T. J., and Petit, C. (2011). MOF/graphite oxide hybrid materials: Exploring the new concept of adsorbents and catalysts. *Adsorption* 17 (1), 5–16. doi:10.1007/s10450-010-9267-5

Bian, R., Wang, T., Zhang, L., Li, L., and Wang, C. (2015). A combination of tri-modal cancer imaging and *in vivo* drug delivery by metal–organic framework based composite nanoparticles. *Biomaterials Sci.* 3 (9), 1270–1278. doi:10.1039/c5bm00186b

Broome, D. R., Girguis, M. S., Baron, P. W., Cottrell, A. C., Kjellin, I., and Kirk, G. A. (2007). Gadodiamide-associated nephrogenic systemic fibrosis: Why radiologists should be concerned. *Am. J. Roentgenol.* 188 (2), 586–592. doi:10.2214/ajr.06.1094

Chen, T., Liu, Y., Zheng, W. J., Liu, J., and Wong, Y. S. (2010). Ruthenium polypyridyl complexes that induce mitochondria-mediated apoptosis in cancer cells. *Inorg. Chem.* 49 (14), 6366–6368. doi:10.1021/ic100277w

Chowdhuri, A. R., Bhattacharya, D., and Sahu, S. K. (2016). Magnetic nanoscale metal organic frameworks for potential targeted anticancer drug delivery, imaging and as an MRI contrast agent. *Dalton Trans.* 45 (7), 2963–2973. doi:10.1039/c5dt03736k

Chowdhuri, A. R., Singh, T., Ghosh, S. K., and Sahu, S. K. (2016). Carbon dots embedded magnetic nanoparticles @chitosan @metal organic framework as a nanoprobe for pH sensitive targeted anticancer drug delivery. *ACS Appl. Mater. Interfaces* 8 (26), 16573–16583. doi:10.1021/acsami.6b03988

Chui, S., Lo, AG., Charmant, JP., Orpen, AG., and Williams, ID. (1999). A chemically functionalizable nanoporous material. *Science* 283 (5405), 1148–1150. doi:10.1126/science.283.5405.1148

Deng, Y., Deng, C., Qi, D., Liu, C., Liu, J., Zhang, X., et al. (2009). Synthesis of core/shell colloidal magnetic zeolite microspheres for the immobilization of trypsin. *Adv. Mater.* 21 (13), 1377–1382. doi:10.1002/adma.200801766

Dhakshinamoorthy, A., and Garcia, H. (2012). Catalysis by metal nanoparticles embedded on metal–organic frameworks. *Chem. Soc. Rev.* 41 (15), 5262–5284. doi:10.1039/c2cs35047e

Dong, Z., Gong, H., Gao, M., Zhu, W., Sun, X., Feng, L., et al. (2016). Polydopamine nanoparticles as a versatile molecular loading platform to enable imaging-guided cancer combination therapy. *Theranostics* 6 (7), 1031–1042. doi:10.7150/thno.14431

Eddaoudi, M., Moler, D. B., Li, H., Chen, B., Reineke, T. M., O'Keeffe, M., et al. (2001). Modular chemistry: Secondary building units as a basis for the design of highly porous and robust metal– organic carboxylate frameworks. *Accounts Chem. Res.* 34 (4), 319–330. doi:10.1021/ar000034b

Gandhi, A., Jana, S., and Sen, K. K. (2014). *In-vitro* release of acyclovir loaded Eudragit RLPO® nanoparticles for sustained drug delivery. *Int. J. Biol. Macromol.* 67, 478–482. doi:10.1016/j.ijbiomac.2014.04.019

Gharehdaghi, Z., Rahimi, R., Naghib, S. M., and Molaabasi, F. (2021). Cu (II)-porphyrin metal–organic framework/graphene oxide: Synthesis, characterization, and application as a pH-responsive drug carrier for breast cancer treatment. *JBIC J. Biol. Inorg. Chem.* 26, 689–704. doi:10.1007/s00775-021-01887-3

Ghosh, S., Badruddoza, A. Z. M., Uddin, M. S., and Hidajat, K. (2011). Adsorption of chiral aromatic amino acids onto carboxymethyl-β-cyclodextrin bonded Fe3O4/SiO2 core–shell nanoparticles. *J. colloid interface Sci.* 354 (2), 483–492. doi:10.1016/j.jcis.2010.11.060

Horcajada, P., Chalati, T., Serre, C., Gillet, B., Sebrie, C., Baati, T., et al. (2010). Porous metal–organic-framework nanoscale carriers as a potential platform for drug delivery and imaging. *Nat. Mater.* 9 (2), 172–178. doi:10.1038/nmat2608

Horcajada, P., Gref, R., Baati, T., Allan, P. K., Maurin, G., Couvreur, P., et al. (2012). Metal–organic frameworks in biomedicine. *Chem. Rev.* 112 (2), 1232–1268. doi:10.1021/cr200256v

Horcajada, P., Serre, C., Vallet-Regi, M., Sebban, M., Taulelle, F., and Ferey, G. (2006). Metal–organic frameworks as efficient materials for drug delivery. *Angew. Chem.* 118 (36), 5974–5978. doi:10.1002/anie.200601878

Ke, F., Qiu, L.-G., and Zhu, J. (2014). Fe_3O_4@MOF core-shell magnetic microspheres as excellent catalysts for the Claisen-Schmidt condensation reaction. *Nanoscale* 6 (3), 1596–1601. doi:10.1039/c3nr05051c

Koh, K., Wong-Foy, A. G., and Matzger, A. J. (2009). MOF@ MOF: Microporous core–shell architectures. *Chem. Commun.* 2009 (41), 6162–6164. doi:10.1039/b904526k

Lee, J., Farha, O. K., Roberts, J., Scheidt, K. A., Nguyen, S. T., and Hupp, J. T. (2009). Metal–organic framework materials as catalysts. *Chem. Soc. Rev.* 38 (5), 1450–1459. doi:10.1039/b807080f

Lee, N., and Hyeon, T. (2012). Designed synthesis of uniformly sized iron oxide nanoparticles for efficient magnetic resonance imaging contrast agents. *Chem. Soc. Rev.* 41 (7), 2575–2589. doi:10.1039/c1cs15248c

Lin, W., Hu, Q., Jiang, K., Yang, Y., Yang, Y., Cui, Y., et al. (2016). A porphyrin-based metal–organic framework as a pH-responsive drug carrier. *J. Solid State Chem.* 237, 307–312. doi:10.1016/j.jssc.2016.02.040

Liu, J., Qiao, S. Z., Hu, Q. H., and Lu, G. Q. M. (2011). Magnetic nanocomposites with mesoporous structures: Synthesis and applications. *small* 7 (4), 425–443. doi:10.1002/smll.201001402

Lou, H., Chu, L., Zhou, W., Dou, J., Teng, X., Tan, W., et al. (2022). A diselenium-bridged covalent organic framework with pH/GSH/photo-triple-responsiveness for highly controlled drug release toward joint chemo/photothermal/chemodynamic cancer therapy. *J. Mater. Chem. B* 10 (39), 7955–7966. doi:10.1039/d2tb01015a

Lou, H., Fang, H., Wang, T., Wang, D., Han, Q., Zhou, W., et al. (2022). Biodegradable porous polymeric drug with pH-stimuli-responsive delivery capacity for combined cancer therapy. *ACS Appl. Polym. Mater.* 4 (1), 714–724. doi:10.1021/acsapm.1c01502

Luo, H., Huang, T., Li, X., Wang, J., Lv, T., Tan, W., et al. (2022). Synergistic antibacterial and wound-healing applications of an imidazole-based porous organic polymer encapsulated silver nanoparticles composite. *Microporous Mesoporous Mater.* 337, 111925. doi:10.1016/j.micromeso.2022.111925

Luo, H., Ji, W., Guo, W., Chen, P., Zhang, Z., Xu, X., et al. (2022). A photoactive Dual-cationic Covalent Organic Framework Encapsulated Sodium Nitroprusside as controllable NO-releasing material for joint cation/photothermal/NO antibacterial therapy. *Microporous Mesoporous Mater.* 346, 112281. doi:10.1016/j.micromeso.2022.112281

Madej, M., Kurowska, N., and Strzalka-Mrozik, B. (2022). Polymeric nanoparticles—tools in a drug delivery system in selected cancer therapies. *Appl. Sci.* 12, 9479. doi:10.3390/app12199479

Mandal, W., Fajal, S., Samanta, P., Dutta, S., Shirolkar, M. M., More, Y. D., et al. (2022). Selective and sensitive recognition of specific types of toxic organic pollutants with a chemically stable highly luminescent porous organic polymer (POP). *ACS Appl. Polym. Mater.* 4 (11), 8633–8644. doi:10.1021/acsapm.2c01538

Mosallanezhad, P., Nazockdast, H., Ahmadi, Z., and Rostami, A. (2022). Fabrication and characterization of polycaprolactone/chitosan nanofibers containing antibacterial agents of curcumin and ZnO nanoparticles for use as wound dressing. *Front. Bioeng. Biotechnol.* 10, 1027351. doi:10.3389/fbioe.2022.1027351

Nie, S., Hsiao, W. L. W., Pan, W., and Yang, Z. (2011). Thermoreversible pluronic F127-based hydrogel containing liposomes for the controlled delivery of paclitaxel: *In vitro* drug release, cell cytotoxicity, and uptake studies. *Int. J. Nanomedicine* 6, 151–166. doi:10.2147/IJN.S15057

Qian, K., Fang, G., and Wang, S. (2011). A novel core–shell molecularly imprinted polymer based on metal–organic frameworks as a matrix. *Chem. Commun.* 47 (36), 10118–10120. doi:10.1039/c1cc12935j

Reddy, N. S., Sowmya, S., Bumgardner, J. D., Chennazhi, K. P., Biswas, R., and JayakumaR, R. (2014). Tetracycline nanoparticles loaded calcium sulfate composite beads for periodontal management. *Biochimica Biophysica Acta (BBA)-General Subj.* 1840 (6), 2080–2090. doi:10.1016/j.bbagen.2014.02.007

Rieter, W. J., Taylor, K. M., and Lin, W. (2007). Surface modification and functionalization of nanoscale metal-organic frameworks for controlled release and luminescence sensing. *J. Am. Chem. Soc.* 129 (32), 9852–9853. doi:10.1021/ja073506r

Rieter, W. J., Taylor, K. M. L., Lin, W., and Lin, W. (2006). Nanoscale metal– organic frameworks as potential multimodal contrast enhancing agents. *J. Am. Chem. Soc.* 128 (28), 9024–9025. doi:10.1021/ja0627444

Rosi, N. L., Eckert, J., Eddaoudi, M., Vodak, D. T., Kim, J., O'Keeffe, M., et al. (2003). Hydrogen storage in microporous metal-organic frameworks. *Science* 300 (5622), 1127–1129. doi:10.1126/science.1083440

Schlichte, K., Kratzke, T., and Kaskel, S. (2004). Improved synthesis, thermal stability and catalytic properties of the metal-organic framework compound Cu3 (BTC) 2. *Microporous Mesoporous Mater.* 73 (1-2), 81–88. doi:10.1016/j.micromeso.2003.12.027

Shahrousvand, M., Hajikhani, M., Nazari, L., Aghelinejad, A., Shahrousvand, M., Irani, M., et al. (2022). Preparation of colloidal nanoparticles PVA-PHEMA from hydrolysis of copolymers of PVAc-PHEMA as anticancer drug carriers. *Nanotechnology* 33 (27), 275603. doi:10.1088/1361-6528/ac6089

Shamsipur, M., Molaabasi, F., Sarparast, M., Roshani, E., Vaezi, Z., Alipour, M., et al. (2018). Photoluminescence mechanisms of dual-emission fluorescent silver nanoclusters fabricated by human hemoglobin template: From oxidation- and aggregation-induced emission enhancement to targeted drug delivery and cell imaging. *ACS Sustain. Chem. Eng.* 6 (8), 11123–11137. doi:10.1021/acssuschemeng.8b02674

Spaldin, N. A. (2010). *Magnetic materials: Fundamentals and applications*. Cambridge, United Kingdom: Cambridge University Press.

Sun, C., Lee, J. S., and Zhang, M. (2008). Magnetic nanoparticles in MR imaging and drug delivery. *Adv. drug Deliv. Rev.* 60 (11), 1252–1265. doi:10.1016/j.addr.2008.03.018

Vakilinezhad, M. A., Alipour, S., and Montaseri, H. (2018). Fabrication and *in vitro* evaluation of magnetic PLGA nanoparticles as a potential Methotrexate delivery system for breast cancer. *J. Drug Deliv. Sci. Technol.* 44, 467–474. doi:10.1016/j.jddst.2018.01.002

Varghese, A. M., Reddy, K. S. K., and Karanikolos, G. N. (2022). An in-situ-grown Cu-BTC metal–organic framework/graphene oxide hybrid adsorbent for selective hydrogen storage at ambient temperature. *Industrial Eng. Chem. Res.* 61 (18), 6200–6213. doi:10.1021/acs.iecr.1c04710

Wang, L., Liang, J., Zhu, Y., Mei, T., Zhang, X., Yang, Q., et al. (2013). Synthesis of Fe 3 O 4@ C core–shell nanorings and their enhanced electrochemical performance for lithium-ion batteries. *Nanoscale* 5 (9), 3627–3631. doi:10.1039/c3nr00353a

Wee, L. H., Lohe, M. R., Janssens, N., Kaskel, S., and Martens, J. A. (2012). Fine tuning of the metal–organic framework Cu 3 (BTC) 2 HKUST-1 crystal size in the 100 nm to 5 micron range. *J. Mater. Chem.* 22 (27), 13742–13746. doi:10.1039/c2jm31536j

Wu, Y.-n., Li, F., Xu, Y., Zhu, W., Tao, C. a., Cui, J., et al. (2011). Facile fabrication of photonic MOF films through stepwise deposition on a colloid crystal substrate. *Chem. Commun.* 47 (36), 10094–10096. doi:10.1039/c1cc12563j

Wu, Y.-n., Zhou, M., Li, S., Li, Z., Li, J., Wu, B., et al. (2014). Magnetic metal–organic frameworks: γ-Fe2O3@MOFs via confined *in situ* pyrolysis method for drug delivery. *Small* 10 (14), 2927–2936. doi:10.1002/smll.201400362

Xu, Z., Wang, T., Li, J., Zhang, F., Lou, H., Zhang, J., et al. (2022). Nanosized porous artificial enzyme as a pH-sensitive doxorubicin delivery system for joint enzymatic and chemotherapy towards tumor treatment. *New J. Chem.* 46 (30), 14565–14577. doi:10.1039/d2nj02031a

Yang, Y., Xia, F., Yang, Y., Gong, B., Xie, A., Shen, Y., et al. (2017). Litchi-like Fe 3 O 4@ Fe-MOF capped with HAp gatekeepers for pH-triggered drug release and anticancer effect. *J. Mater. Chem. B* 5 (43), 8600–8606. doi:10.1039/c7tb01680h

Zeng, T., Zhang, X. l., Ma, Y. r., Niu, H. y., and Cai, Y. q. (2012). A novel Fe 3 O 4–graphene–Au multifunctional nanocomposite: Green synthesis and catalytic application. *J. Mater. Chem.* 22 (35), 18658–18663. doi:10.1039/c2jm34198k

Zeng, T., Zhang, X. l., Niu, H. y., Ma, Y. r., Li, W. h., and Cai, Y. q. (2013). *In situ* growth of gold nanoparticles onto polydopamine-encapsulated magnetic microspheres for catalytic reduction of nitrobenzene. *Appl. Catal. B Environ.* 134, 26–33. doi:10.1016/j.apcatb.2012.12.037

Zeng, T., Zhang, X., Wang, S., Ma, Y., Niu, H., and Cai, Y. (2014). Assembly of a nanoreactor system with confined magnetite core and shell for enhanced fenton-like catalysis. *Chemistry–A Eur. J.* 20 (21), 6474–6481. doi:10.1002/chem.201304221

Zhang, Y., Dai, T., Zhang, F., Zhang, J., Chu, G., and Quan, C. (2016). Fe3O4@UiO-66-NH2 core–shell nanohybrid as stable heterogeneous catalyst for Knoevenagel condensation. *Chin. J. Catal.* 37 (12), 2106–2113. doi:10.1016/s1872-2067(16)62562-7

Zhao, H.-X., Zou, Q., Sun, S. K., Yu, C., Zhang, X., Li, R. J., et al. (2016). Theranostic metal–organic framework core–shell composites for magnetic resonance imaging and drug delivery. *Chem. Sci.* 7 (8), 5294–5301. doi:10.1039/c6sc01359g

Zhao, X., Liu, S., Tang, Z., Niu, H., Cai, Y., Meng, W., et al. (2015). Synthesis of magnetic metal-organic framework (MOF) for efficient removal of organic dyes from water. *Sci. Rep.* 5 (1), 11849–11910. doi:10.1038/srep11849

Frontiers in
Bioengineering and Biotechnology

Accelerates the development of therapies, devices, and technologies to improve our lives

A multidisciplinary journal that accelerates the development of biological therapies, devices, processes and technologies to improve our lives by bridging the gap between discoveries and their application.

Discover the latest Research Topics

See more →

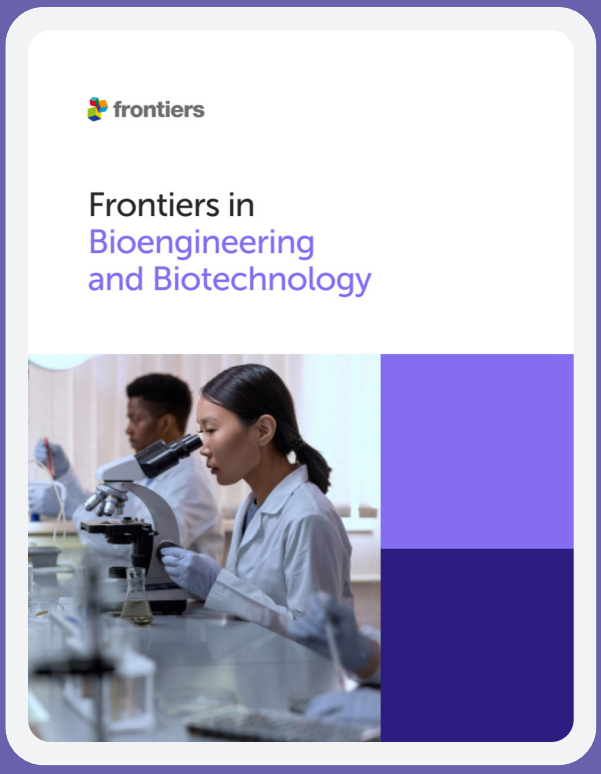

Frontiers

Avenue du Tribunal-Fédéral 34
1005 Lausanne, Switzerland
frontiersin.org

Contact us

+41 (0)21 510 17 00
frontiersin.org/about/contact